SANDIA REPORT

SAND90-1615 • UC-261
Unlimited Release
Printed February 1992

Selected Papers on Wind Energy Technology

January 1989–January 1990
Sandia National Laboratories Staff

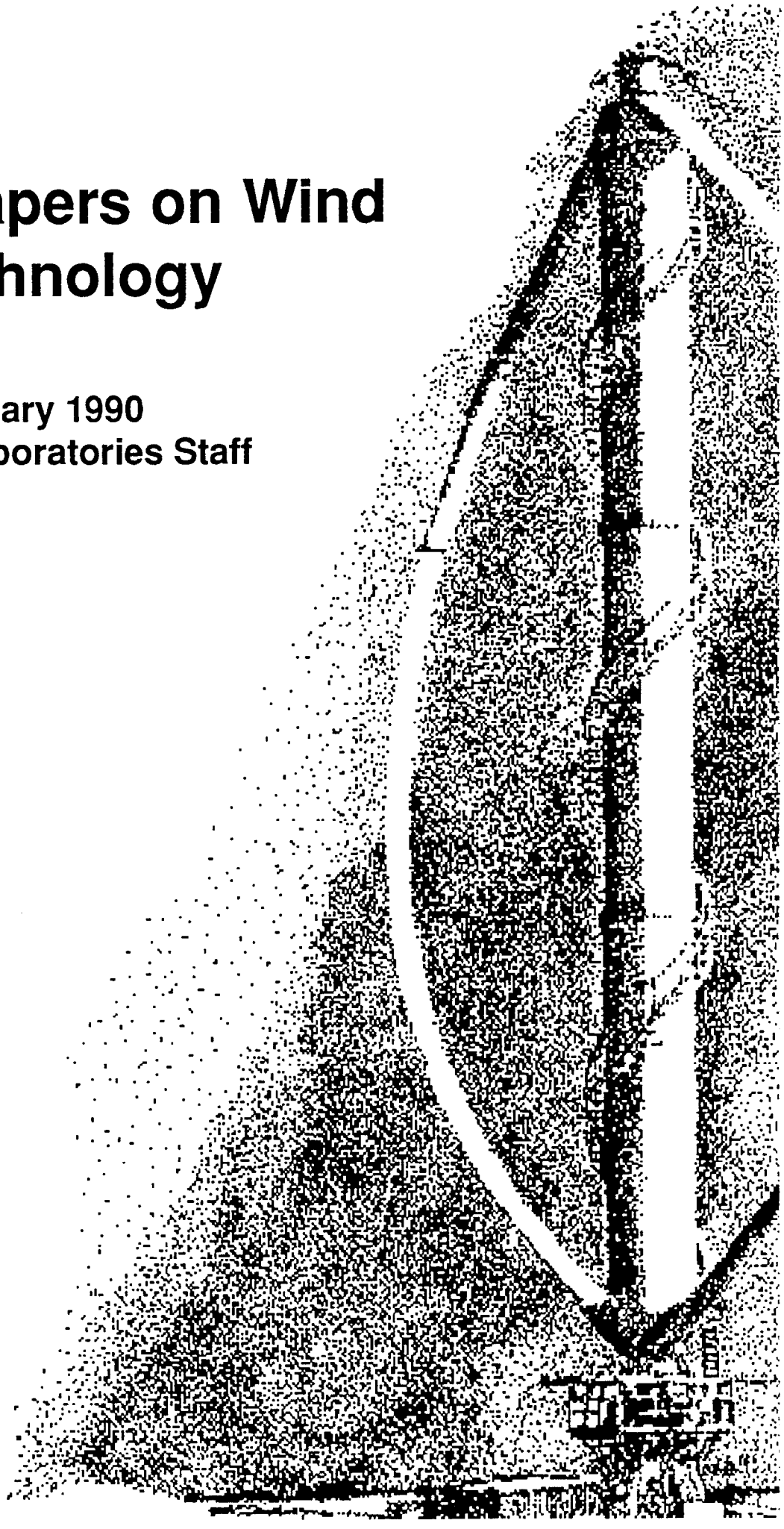

Prepared by
Sandia National Laboratories
Albuquerque, New Mexico 87185 and
Livermore, California 94550
for the United States Department of Energy
under Contract DE-ACO4-76DP00789

Issued by Sandia National Laboratories, operated for the United States Department of Energy by Sandia Corporation.

FOREWORD

The Sandia National Laboratories Wind Energy Research Division and supporting staff in aerodynamics, applied and experimental mechanics, and metallurgy have worked for 15 years to advance wind turbine technology, with special emphasis on vertical axis wind turbines (VAWTs). In the last few years, analytical tools and improved analysis techniques have been documented, most of them in conference proceedings. A selection of these papers has been brought together here in a single, comprehensive format to illustrate the scope of recent Sandia wind energy research and development. Twelve papers have been selected from the last two years of the annual forum provided by the ASME Wind Energy Symposium. Three papers are included from the proceedings of conferences in the United States, Canada and Europe.

Many of the papers in this volume focus on the DOE/Sandia 34-Meter Test Bed, a research VAWT. The 34-Meter Test Bed, dedicated in May 1988, has been used to validate analysis techniques and demonstrate the improved aerodynamic and structural performance of advanced components, including natural laminar flow airfoils, step tapered blades, and a variable speed generator. The Test Bed clearly emerges as a stepping stone in the VAWT development process and serves as an important benchmark in software evaluation efforts. Building and operating the Test Bed has thrown the harsh light of reality on the technical predictions made during the design effort; the results shown here are most encouraging.

Advances in fatigue analysis, structural dynamics, variable speed control, and aerodynamic performance are also shown in these papers. It is our intent that this compilation of past work serve as a milestone marking our current position and guiding future efforts to advance the state of the art in wind turbine technology.

Paul S. Veers

This Page Intentionally left Blank

Selected Papers on Wind Energy Technology January 1989-January 1990

By Sandia National Laboratories Staff

Contents

Proceedings of the Eighth ASME Wind Energy Symposium, Houston, Texas, January 1989

Three-Dimensional Wind Simulation
P. S. Veers *1*

Time Domain Structural Response Calculations for Vertical Axis Wind Turbines
C. R. Dohrmann and P. S. Veers *11*

Fatigue Characterization of a VAWT Blade Material
J. A. Van Den Avyle and H. J. Sutherland *19*

Simplified Fatigue Damage and Crack Growth Calculations for Wind Turbines
P. S. Veers *25*

Crack Propagation Analysis of WECS Components Using the LIFE2 Computer Code
H. J. Sutherland and L. L. Schluter *33*

Model Validation of the Sandia 34-Meter Test Bed Turbine Using Substructured Modal-Testing
T. G. Carne, J. P. Lauffer, A. J. Gomez, and T. D. Ashwill *39*

Initial Structural Response Measurements for the Sandia 34-Meter VAWT Test Bed
T. D. Ashwill *47*

Proceedings of the European Wind Energy Conference (EWEC '89), Glasgow, Scotland, July 1989

Damage Predictions for Wind Turbine Components Using the LIFE2 Computer Code
H. J. Sutherland *55*

Proceedings of the American Wind Energy Association Conference (Windpower '89), San Francisco, California, September 1989

Control of the Variable Speed Generator on the Sandia 34-Metre Vertical Axis Wind Turbine
M. E. Ralph *61*

Proceedings of the Canadian Wind Energy Association Conference, Charlottetown, PEI, Canada, September 1989

Test Results and Status of the DOE/Sandia 34-M VAWT Test Bed
H. M. Dodd et al. 73

Proceedings of the Ninth ASME Wind Energy Symposium, New Orleans, Louisiana, January 1990

Aerodynamic Design and Initial Performance Measurements for the Sandia 34-M Diameter Vertical-Axis Wind Turbine
D. E. Berg, P. C. Klimas and W. A. Stephenson 93

Structural Response Measurements and Predictions for the Sandia 34-Meter Test Bed
T. D. Ashwill and P. S. Veers 101

Fatigue Analysis of the Sandia 34-Meter Vertical Axis Wind Turbine
T. D. Ashwill, H. J. Sutherland and P. S. Veers 109

Rainflow Counting Algorithm for the LIFE2 Fatigue Analysis Code
L. L. Schluter and H. J. Sutherland 117

Smart Control Algorithms for Operation of Variable-Speed Wind Turbines
W. A. Vachon 121

Performance Predictions for an Intermediate-Sized VAWT Based on Performance of the 34-M VAWT Test Bed
H. M. Dodd 131

Proceedings of the Eighth ASME Wind Energy Symposium
D. E. Berg and P. C. Klimas (ed.), SED-Vol. 7, ASME, January 1989

THREE-DIMENSIONAL WIND SIMULATION*

P. S. Veers
Sandia National Laboratories
Albuquerque, New Mexico

*This work was supported by the U.S. Department of Energy under Contract DE-AC04-76DP000789

ABSTRACT

A method for numerically simulating a three-dimensional field of turbulent wind-speed (the "Sandia method") for use in the aerodynamic and structural analyses of wind turbines is presented. The required inputs are single point power spectral densities (PSDs) and the coherence function. Suggestions for appropriate inputs and an example calculation are included. The simulation method is used to obtain "rotationally sampled" PSDs, which are compared with measurements obtained by Pacific Northwest Laboratories. The results show that the Sandia method is capable of producing simulations that agree with the measurements, especially when the coherence function is augmented from the usual form to include the ratio of spatial separation over height, raised to the 0.25 power. The method is specialized for horizontal axis wind turbine analysis by phase lagging the simulations at each point in space so that wind speeds are simulated only when the turbine blade passes the point, reducing storage requirements and computation time by nearly an order of magnitude. For vertical axis applications, where interpolation will be required, the loss of variance induced by the interpolation is estimated and eliminated by the addition of appropriate white noise.

INTRODUCTION

Wind simulation has become an important part of both vertical and horizontal axis wind turbine structural analysis. Because of the highly nonlinear relationship between atmospheric turbulence and aerodynamic loads on wind turbine blades, there continues to be interest in numerically simulating the winds and then calculating time series of blade loads. For mid-to-large size wind turbines, spatial variations in the turbulence must be considered and three-dimensional wind simulation is required.

The basic approach of the *Sandia method* [1] is to simulate wind-speed time series at several points in a plane perpendicular to the mean wind direction and to propagate the time series in the mean wind direction at the mean wind speed (i.e., using Taylor's frozen turbulence hypothesis). This is a "full-field" method in that it completely fills a three-dimensional block of space with a grid of instantaneous wind speeds. This is especially useful for VAWT applications where the blades sweep back and forth through the turbulence as it propagates through the rotor. Even one-dimensional turbulence inputs have been shown to produce some unexpected aerodynamic effects on VAWT loads [2]. By contrast, each point on a HAWT blade follows a simpler path tracing a circle in a vertical plane. An improvement to the Sandia method is obtained (for HAWT applications) by specializing the simulation for the points in space and time occupied by rotating HAWT blades.

The Sandia method for full-field wind simulation has already been applied to both HAWT [3,4] and VAWT [5,6] structural analysis. Very little computer time is needed to produce a full field of simulated winds. The limiting factor is the rather hefty storage requirement. To simulate a time series of length M at N points in space requires more than $M(N^2 + N)/2$ storage locations. For HAWT applications, this storage requirement can be significantly reduced by using the efficient simulation technique described in this report.

The required input includes the single point turbulence PSDs for all N points and the coherence function, which describes how turbulence is correlated as a function of spatial separation, mean wind speed, and frequency. The coherence is assumed to be isotropic in the cross-wind plane and the cross spectral densities are assumed to be real valued. Neither of these assumptions are *necessary* for the method to work, but they both simplify implementation and are consistent with current knowledge of turbulence statistics. If improved turbulence descriptions are found, they could be included with minor modifications.

REVIEW OF THE SIMULATION METHOD

The three-dimensional wind simulation method described in Ref. 1 and reviewed in this section is based on a method developed by Shinozuka and Jan [7] and more clearly outlined by

Smallwood [8]. It creates N correlated time series based on the spectral matrix, $\mathbf{S}$. The diagonals of $\mathbf{S}$ are the power spectral densities (PSDs). Each off-diagonal term, S_{jk}, is the cross spectral density between points j and k.

For the purpose of numerical simulation, a discrete representation of each element in the spectral matrix is required. The continuous, one-sided PSD at point j, $G_{jj}(f)$, is discretized by dividing it into frequency bands Δf Hertz wide with the center frequency of each band designated as f_m. The correct variance is maintained by letting $S_{jj}(f_m) = G_{jj}(f_m)\Delta f/2$.[1] Each entry in the spectral matrix must contain $M/2$ frequency components to get a time series of length M using an FFT.

The magnitude of the cross spectrum between points j and k can be defined in terms of the PSDs and the coherence function, Coh_{jk}, by

$$|S_{jk}(f_m)| = Coh_{jk}(f_m, \Delta r_{jk}, U_{jk})\sqrt{S_{jj}(f_m)S_{kk}(f_m)} \qquad (1)$$

where the coherence is a function of frequency (f_m), distance between points j and k (Δr_{jk}), and mean wind speed at points j and k (U_{jk}). By assuming that there is an average phase of zero between any two points, the imaginary parts of the cross spectra are zero. Thus, the entire spectral matrix is defined by the PSDs and the coherence.

The N correlated time series are generated by linear combinations of N independent, white-noise processes. In this case, $\mathbf{S}$ can be written as the product of a transformation matrix, $\mathbf{H}$, and the transpose of its complex conjugate [7].

$$\mathbf{S}(f_m) = \mathbf{H}(f_m)\mathbf{H}^{*T}(f_m) \qquad (2)$$

where each entry in $\mathbf{S}$ and $\mathbf{H}$ is a function of frequency.

Because $\mathbf{S}$ is real, $\mathbf{H}$ must also be real and $\mathbf{H} = \mathbf{H}^*$. Because $\mathbf{S}$ is symmetric, it contains $(N^2+N)/2$ independent entries while the full $\mathbf{H}$ contains N^2 entries; $\mathbf{H}$ is therefore not uniquely defined. If $\mathbf{H}$ is assumed to be lower triangular, however, the nonzero entries will be uniquely defined and can be determined by a simple recursive set of equations:

$$\begin{aligned}
H_{11} &= S_{11}^{1/2} \\
H_{21} &= S_{21}/H_{11} \\
H_{22} &= (S_{22} - H_{21}^2)^{1/2} \\
H_{31} &= S_{31}/H_{11} \\
&\vdots \\
H_{jk} &= \left(S_{jk} - \textstyle\sum_{l=1}^{k-1} H_{jl}H_{kl}\right)/H_{kk} \\
H_{kk} &= \left(S_{kk} - \textstyle\sum_{l=1}^{k-1} H_{kl}^2\right)^{1/2}
\end{aligned} \qquad (3)$$

The elements of the $\mathbf{H}$ matrix can be thought of as the weighting factors for the linear combination of N independent, unit-magnitude, white-noise inputs that will yield N correlated outputs with the correct spectral matrix. Each row of $\mathbf{H}$ gives the contributions of all the inputs to the output at point k. Each column gives the contributions of the j^{th} input to all of the outputs.

[1] $S_{jj}(f_m)$ is the two-sided Fourier amplitude of the f_m^{th} frequency component. The normalisation factor (1/2 in this case) must be unity if your FFT routine assumes a one-sided input.

The independent, unit-magnitude, white-noise inputs are contained in an $N \times N$ diagonal matrix $\mathbf{X}$ such that

$$X_{jk}(f_m) = \begin{cases} e^{i\theta_{km}} & j = k \\ 0 & j \neq k \end{cases} \qquad (4)$$

where i is $\sqrt{-1}$ and θ_{km} is the phase angle associated with the k^{th} input point and the m^{th} frequency component. θ_{km} is a uniformly distributed random variable on the interval $(0, 2\pi)$. This insures that the time series will approach a Gaussian process as the number of frequency components becomes large.

The matrix equation for the $N \times 1$ vector of complex Fourier coefficients of the simulated wind speed, $\mathbf{V}$, is given by

$$\mathbf{V} = \mathbf{H}\mathbf{X}\mathbf{1} \qquad (5)$$

where $\mathbf{1}$ is an $N \times 1$ vector of ones.

The operations may be more easily visualized in summation notation where it is evident that the vector $\mathbf{1}$ is only present for the purpose of summing across each row of $\mathbf{HX}$.

$$V_j(f_m) = \sum_{k=1}^{j} H_{jk}(f_m)X_{kk}(f_m) = \sum_{k=1}^{j} H_{jk}(f_m)\, e^{i\theta_{km}} \qquad (6)$$

Because $\mathbf{X}$ has all unit magnitude entries, the only effect it has is to apply a random phase to each column of $\mathbf{H}$. The summation form shows that the V_j depend on the inputs from all the earlier points ($k \leq j$), which are weighted by the H_{jk}. The fact that each output does not depend on *all* the inputs is an artifact of selecting a lower triangular form for $\mathbf{H}$. Assuming that $\mathbf{H}$ has other forms (e.g., symmetric) could eliminate the order dependence, but would also eliminate the simple recursive method of solving for the elements of $\mathbf{H}$.

The time series are obtained by taking the inverse Fourier transform of each element of $\mathbf{V}$, resulting in a simulated wind speed at every time step for all N points in space. While this "full-field" representation may be necessary for VAWT applications, it produces many unused data for HAWT applications. These extra data are eliminated by an efficient rotational sampling technique employed in HAWT applications.

TURBULENCE POWER SPECTRAL DENSITY

The basic input to any method of three-dimensional turbulence simulation is the wind speed PSD. Many models of turbulence PSDs have been proposed, starting with von Karman in 1948 [9]. Reference 1 used the PSD suggested by Frost, et al. [10] while Powell and Connell [11] suggest (rightly) that the Kaimal spectrum [12] is a more accurate representation. The Frost ($G_F(f)$), Kaimal ($G_K(f)$), and von Karman ($G_V(f)$) models are shown in Fig. 1, in the traditional form of logarithmic spectra ($fG(f)$ vs f). The formulas for these PSDs are:

$$G_F(f) = \frac{12.3U_{10}z[\ln(\frac{10}{z_0}+1)\ln(\frac{z}{z_0}+1)]^{-1}}{1 + 192[(\frac{fz}{U_{10}})\ln(\frac{10}{z_0}+1)/\ln(\frac{z}{z_0}+1)]^{\frac{5}{3}}} \qquad (7)$$

$$G_K(f) = \frac{105u_*^2 z/U}{(1+33(fz/U))^{\frac{5}{3}}} \qquad (8)$$

$$G_V(f) = \frac{4(5.7u_*^2)L_x/U}{1.339(1+39.48(fL_x/U)^2)^{\frac{5}{6}}} \qquad (9)$$

where:

f is the frequency in Hertz

z is the height above ground in meters

z_0 is the surface roughness coefficient in meters

U_{10} is the mean wind speed in m/s at a height of 10 meters

U is the mean wind speed in m/s at a height of z meters

L_x is the integral length scale

u_*, the shear velocity, is related to U and z_o by $u_* = \frac{0.4U}{\ln(z/z_0)}$

(The shear velocity is related to the turbulence variance, σ_u^2, in the von Karman spectrum by $\sigma_u^2 \approx 5.7u_*^2$.)

Figure 1 shows that all three PSDs have the same slope in the *inertial subrange* (high frequency). The Frost spectrum is significantly different than the other two because it is derived from the Kaimal spectrum with a *stable* atmosphere while the others apply to *neutral* atmospheres. The Kaimal and von Karman spectra are quite similar except that the Kaimal spectrum is slightly lower in the important region below one Hertz and, therefore, results in a turbulence intensity about 15% lower than the von Karman spectrum, for the parameter values used in Ref. 11 ($z_0 = .01m$, $L_x = 120m$, $U_{10} = 8m/s$, and $z = 30m$). These values result in different variances for all three PSDs, as shown in Fig. 1.

A recent review of the wind turbulence literature by Solari [13] highlights the uncertainty in determining the coefficients of any PSD model of atmospheric turbulence. Solari suggests that a deterministic representation for the turbulence PSD is *illusory*. He suggests that the basic form of the von Karman and Kaimal PSDs be retained, but that the parameter of the PSD be a random variable. Solari's PSD ($G_S(f)$) is of the form

$$G_S(f) = \frac{2.21u_*^2\beta^{2.5}z/U}{(1+3.31(f\beta^{1.5}z/U))^{\frac{5}{3}}} \qquad (10)$$

where

$$\beta = \beta_m + \mu_\beta \Delta\beta$$

in which

$$\beta_m = \begin{cases} 7.5 & z_0 \le 0.03 \\ 4.5 - 0.856\ln(z_0) & 0.03 \le z_0 \le 1.0 \\ 4.5 & 1.0 \le z_0 \end{cases}$$

$$\Delta\beta = \begin{cases} 2.5 & z_0 \le 0.03 \\ 2.0 - 0.143\ln(z_0) & 0.03 \le z_0 \le 1.0 \\ 2.0 & 1.0 \le z_0 \end{cases}$$

and μ_β is a uniformly distributed random variable on the interval (-1,1).

When β is varied in this way, it represents the scatter that is found in measured turbulence spectra. The two extremes of the Solari PSD are shown in Fig. 2 for the case of $z_0 \le 0.03$. The variance of the turbulence, σ_u^2, is roughly βu_*^2. It may be argued that a uniform distribution on μ_β is artificial; one simple improvement would be to preserve the mean and standard deviation while substituting a continuous, one-sided distribution (e.g., Weibull). The important change is that β, and therefore the low frequency part of the PSD, is a random variable. The high frequency part matches both the von Karman and Kaimal PSDs.

COHERENCE

The coherence function is a frequency dependent measure of the amount of correlation between the wind speeds at two points in space. The usual form of the coherence function is exponential; the one given by Frost, et al. [10] (and previously suggested for use in the Sandia method [1]) is

$$Coh_{jk} = \exp\left(-\frac{C\Delta r_{jk} f}{U}\right) \qquad (11)$$

where Δr_{jk} is the distance (in meters) between points j and k.

The constant, C, (called the *coherence decrement*) has been estimated often for cross-wind separations without much agreement on any single value. Solari reports values ranging from 2 to

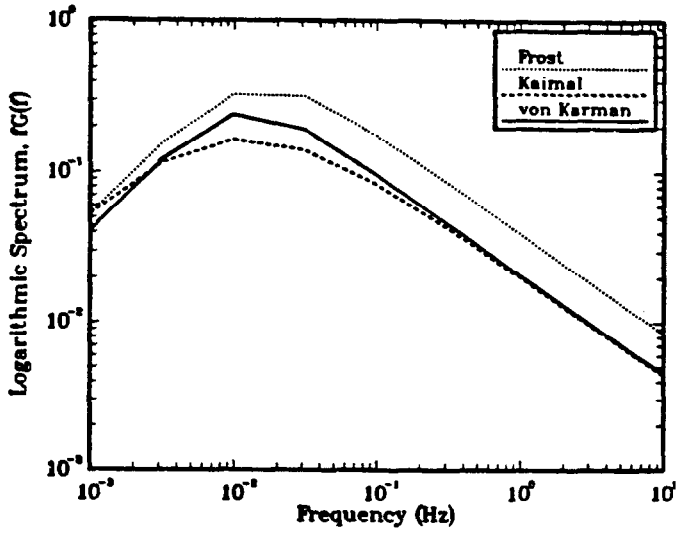

Figure 1: Turbulence PSD models by Frost [10], Kaimal [12], and von Karman [9] for $z_0 = .01m$, $L_x = 120m$, $U_{10} = 8m/s$, and $z = 30m$.

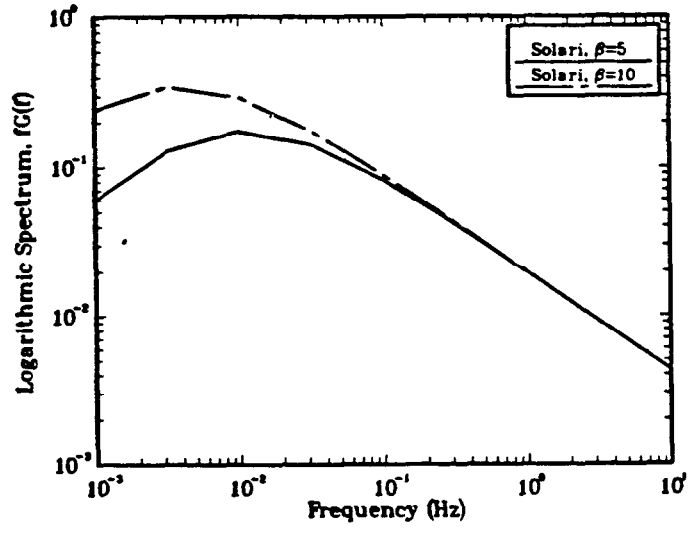

Figure 2: Turbulence PSDs by Solari [13] with the minimum and maximum values of the random variable β.

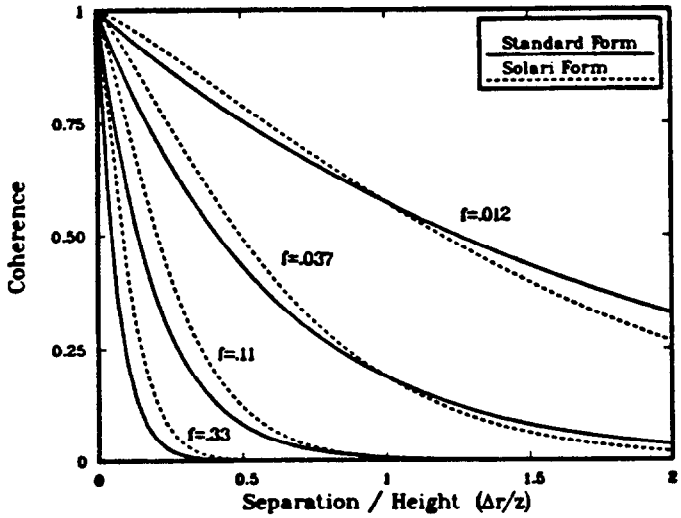

Figure 3: Coherence is plotted as a function of spatial separation at four different frequencies. The solid lines are the standard exponential form and the dashed lines are Solari's suggested form (with $U = 8$m/s, $b = 12$, and $z = 30$m).

27 (Frost suggested $C = 7.5$ for lateral spacing) with the larger values of C tending to be associated with larger ratios of $\Delta r/z$, which suggests that the exponential form may not be capable of representing the full range of possible spacings of points. The form suggested by Solari is the same as Eq. (11) except that $U = U_{jk}$ is defined as the average of the mean wind speeds at points j and k (a minor revision) and that $C = C_{jk}$ is a function of the spacing between points, Δr_{jk}, and the mean height of the two points, $z_m = (z_j + z_k)/2$, given by

$$C_{jk} = b\left(\frac{\Delta r_{jk}}{z_m}\right)^{0.25} \tag{12}$$

in which

$$b = 12 + 5\mu_b$$

As in the case of the spectral density, the coherence decrement is modeled as a random variable by defining μ_b to be uniformly distributed on the interval (-1,1).

The most important change is that the coherence function has been augmented by the dimensionless parameter $(\Delta r/z_m)^{0.25}$, thereby increasing the coherence when $(\Delta r/z_m) < 1$ and decreasing the coherence at greater spacings, as shown in Fig. 3 for four different frequencies. The selection of the 0.25 exponent in Eq. (12) provides a good fit to the data, but seems to be somewhat arbitrary.

ROTATIONAL SAMPLING

The term *rotational sampling* was born out of an experiment in which anemometers were arranged around a circle in a vertical plane perpendicular to the mean wind direction. Wind speeds were then sampled successively from each anemometer to form a composite time series made up of wind speeds as seen by a rotating HAWT blade [14]. Experiments were later conducted with an anemometer on a rotating boom and with a LIDAR scanner (laser anemometer). Rotational sampling is one method of checking simulations of spatially distributed turbulence. Unlike the PSD observed at a stationary point, the rotational PSD has peaks at the integer multiples of the rotating frequency. [2]

Rotational sampling with the Sandia method is accomplished by selecting wind speeds out of the full field at points in space and time that correspond to positions of a rotating HAWT blade. A rotationally sampled PSD can then be estimated from the sampled time series with the aid of a Fourier transform.

Simulation techniques have been devised by Pacific Northwest Laboratory (PNL) to generate the wind speeds for a point on rotating HAWT [14] and VAWT [15] blades. The PNL method analytically derives a rotationally sampled PSD and then uses the inverse Fourier transform to produce a time series. The major shortcoming of this method is that it can only simulate the wind speed at a single point on one turbine blade, while structural response is sensitive to the distribution of wind speed over the entire blade. The Sandia method, by simulating the wind speed at many points in space for all time steps and then sampling at the moving position of the turbine blade, can provide wind speed at many points on several blades. The disadvantage is that wind speeds are also generated at points in space and time that the blades will never occupy. The cost of obtaining wind speed at many points along the blades is therefore a large increase in the required storage space for simulation program execution.

Any input functions describing turbulence PSD and coherence can be used to drive the Sandia simulation method. To illustrate the effects of changes in turbulence PSD and coherence, simulations using the Sandia method, with various spectral and coherence inputs, are compared to the test case of Ref. 11. Rotational sampling is done about a circle with a 20m radius centered 30m above the ground at a rotational speed of (2/3)Hz. The sampling interval is 0.125sec (12 points per revolution) and the record length is 1024 points (128sec). The mean wind speed is 8m/s and the surface roughness coefficient (z_0) is 0.01m.

Table 1 lists the total variance of the turbulence and the distribution of variance in the per rev peaks for the *exact* PNL results (from Ref. 11) and for several different inputs to the Sandia method. The *exact* results are the PNL method results adjusted by empirical corrections that make the per rev variances agree with measured data [16]. Variances are listed in units of meters per second squared and (in parenthesis) normalized by the *exact* results, which are listed in the first line of the table. (The *exact* total variance was not published.) The results flagged with an asterisk are from Powell and Connell [11].

The Sandia method results reported by PNL in Ref. 11, using both the Frost and Kaimal PSDs, have far from the desired distribution of variance, especially at one per rev (1P), as can be seen in Table 1. The SNL estimates using the Sandia method with the Frost and Kaimal PSDs are substantially better. The only apparent difference is that PNL used only one record (125 seconds long) to estimate the rotationally sampled PSD, while the SNL results are the ensemble average of 100 records. The variability in per rev variance from record to record is surprisingly large; the coefficient of variation (standard deviation divided by the mean) is about 0.2 for the higher per revs and 0.25

[2] Integer multiples of the rotating frequency are abbreviated as *per rev* frequencies — i.e., 1 per rev (1P) is the rotational frequency; 2 per rev (2P) is twice the rotational frequency, etc...

at one per rev. It is therefore likely that most of the difference is due to PNL's failure to account for statistical variations in the per rev variances.

The von Karman PSD has slightly more low frequency variance than the Kaimal PSD (see Fig. 1), which is reflected in a higher total rotationally sampled variance, and a better fit to the *exact* results. The von Karman PSD is consistent with the PNL method for estimating rotationally sampled PSDs. This is another reason that the PNL method results, which are based on the von Karman PSD, did not match the Sandia method results, which had been based on the Kaimal PSD, in Ref. 11.

The Solari PSD is about the same as the Kaimal PSD when the random parameter β is at its minimum value of 5, and has more low frequency variance when β is high (see Fig. 2). Table 1 shows the rotationally sampled per rev variances for the Solari PSD with β fixed at the mean value ($\beta = 7.5$) and with the same exponential form of the coherence as used in all the above results. The one per rev variance is still too low and the higher per rev variances are too high. Augmenting the coherence by $(\Delta r/z_m)^{0.25}$, as Solari suggests, makes a substantial improvement on the match between simulated and *exact* results. Randomizing the parameters β and C has a minor influence on the results. Because augmenting by $(\Delta r/z_m)^{0.25}$ fills the need to increase the coherence at small separations and decrease it at large separations, while the choice of 0.25 appears somewhat arbitrary, a power of 0.50 was also tried, resulting in an improved fit to the *exact* results (see Table 1).

The results in Table 1 indicate that a wide variety of rotationally sampled PSDs can be obtained with the Sandia method depending on the input models of turbulence PSD and coherence. The Solari models produce a good fit to the *exact* results, better than the uncorrected PNL method. An even better fit is possible by using $(\Delta r/z_m)^{0.50}$ instead of $(\Delta r/z_m)^{0.25}$ in the coherence model. However, a better fit for this one application may not be a sufficient reason to override Solari's choice of 0.25. It is also not clear that the goal should be to match the *exact* results precisely. There is a great deal of variability in per rev variance in any given wind sample; even the *exact* results may not be perfectly representative.

EFFICIENT SIMULATION FOR HAWTs

In HAWT applications the wind speed is simulated at points arranged around the circular path followed by the blades. With the method described above, the time series at each point is simulated at a rate of the number of points per revolution, N_{pr}, times the rotating frequency in Hertz, Ω (i.e., $\Delta t = 1/N_{pr}\Omega$). The time series at each point is only sampled once per revolution by each blade, making the sampling rate equal to the number of blades, N_b, times Ω. Because N_{pr} is always much greater than N_b, most of the data is wasted. It is therefore more efficient to simulate data at each point at a rate of $N_b\Omega$ with the time of the samples shifted to correspond to the time of blade passage.

The trick is to make each simulated data point correspond to

PSD Model	Coherence Model	Coh. Dec. C	Total Variance	Per Rev Variance 1P	2P	3P	4P	5P
Exact (corrected) PNL Results*			—	.263	.097	.054	.038	.033
Uncorrected PNL Results*			.837	.359 (1.37)	.111 (1.14)	.055 (1.02)	.034 (0.90)	.024 (0.73)
Frost* (PNL)	Standard	3.75	1.10	.152 (0.58)	.089 (0.92)	.060 (1.11)	.052 (1.38)	.047 (1.42)
Frost (SNL)	Standard	3.75	1.17	.201 (0.76)	.090 (0.93)	.058 (1.07)	.045 (1.19)	.041 (1.24)
Kaimal* (PNL)	Standard	10.0	.532	.086 (0.33)	.065 (0.67)	.044 (0.82)	.043 (1.14)	.040 (1.21)
Kaimal (SNL)	Standard	10.0	.607	.129 (0.49)	.070 (0.72)	.049 (0.91)	.040 (1.06)	.038 (1.15)
von Karman (SNL)	Standard	12.0	.776	.171 (0.65)	.085 (0.88)	.059 (1.09)	.048 (1.27)	.042 (1.27)
Solari ($\beta = 7.5$)	Standard	12.0	1.00	.215 (0.82)	.104 (1.07)	.069 (1.28)	.055 (1.46)	.048 (1.45)
Solari ($\beta = 7.5$)	$(\Delta r/z_m)^{0.25}$	12.0	1.00	.237 (0.90)	.105 (1.08)	.064 (1.19)	.047 (1.25)	.039 (1.18)
Solari (Random β)	$(\Delta r/z_m)^{0.25}$	Random	1.04	.239 (0.91)	.111 (1.14)	.069 (1.28)	.053 (1.41)	.045 (1.36)
Solari (Random β)	$(\Delta r/z_m)^{0.50}$	Random	1.04	.259 (0.98)	.111 (1.14)	.064 (1.19)	.046 (1.22)	.038 (1.15)
Solari	$(\Delta r/z_m)^{0.25}$	Random	1.09	.237 (0.90)	.098 (1.01)	.057 (1.06)	.041 (1.09)	.033 (1.00)
Simulating one sample per rev								
* Results taken from Powell and Connell, Ref. 11.								

Table 1. The Distribution of variance over the per rev harmonics are shown for the PNL method (first two rows) and for the Sandia method using various PSD and coherence models. Variance is in units of $(m/s)^2$; the numbers in parentheses are the per rev variances normalized by the *exact* (corrected) values given in the first row.

the exact time that the wind turbine blade occupies that point in space. For evenly spaced points around a circle and constant rotational speed, there must be an equal time lag between simulations at each point. The time lag is implemented by shifting the phase of each frequency component in the PSD by the appropriate amount before transforming into the time domain.

The method may be illustrated by taking the specific example in Fig. 4, which has $N_{pr} = 12$, $N_b = 2$, and only one radial set of points ($N = N_{pr}$). The N_{pr} points are divided into N_b groups with a location index, l_j, ranging from 0 to $(N_{pr}/N_b) - 1$ in each group. The blades are initially located at the $l_j = 0$ points.

Simulating as above at a frequency of $N_b\Omega$ will produce one wind speed value at each point in space every time the blades are at the $l_j = 0$ locations. The wind speed at the $l_j > 0$ points must be lagged in time to correspond to the time of blade passage. The time lag is implemented by applying a phase shift, ϕ_{jm}, that depends on the location index, l_j, and the frequency component, f_m.

$$\phi_{jm} = l_j \left(\frac{2\pi}{N_{pr}}\right)\left(\frac{f_m}{\Omega}\right) \tag{13}$$

Equation (6) then becomes

$$V_j(f_m) = \sum_{k=1}^{j} H_{jk}(f_m) e^{i(\theta_{km} - \phi_{jm})} \tag{14}$$

The time domain representation is again obtained by taking the inverse Fourier transform of V. The odd samples (1,3,5,...) in the Group 1 time series belong to Blade 1 and the even samples belong to Blade 2. The reverse is true of the Group 2 time series. Every data sample in the time series of every point is therefore sampled by one of the blades so there are no longer any *spurious* data. The reduction in storage requirements and computation time is a factor of N_{pr}/N_b.

The rotationally sampled PSD with the full-field approach using the Solari model for turbulence and coherence (with random parameters) is shown in Fig. 5. The PSD estimated with

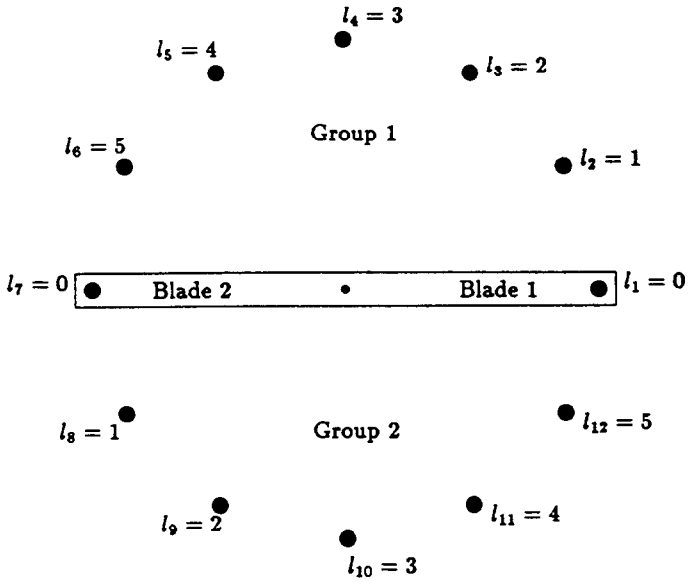

Figure 4: Example of the locations of points for wind simulation with application to HAWTs.

the *one sample per rev* method (simulating wind for only one blade) is shown in Fig. 6. The integrated per rev variance is about the same at 1P and is slightly reduced (about 15%) at higher per revs, as shown in Table 1. The per rev variance from the one sample per rev method is within 10% of the *exact* results for the first five per revs — a better fit than any other known method.

The greatest difference between simulating the full field and only simulating those data points that will be sampled is the minimum level of the PSD. Figure 5 shows a minimum level of PSD content at about .05 $(m/s)^2/Hz$, while the one sample per rev PSD has minima around .02 $(m/s)^2/Hz$. This *background* level comes from the high frequency portion of the input turbulence where the coherence is very small (see Eq. (11) and Fig. 3). The high frequency input is therefore nearly uncorrelated, even at closely spaced points, and shows up as a white-noise background on the rotational PSD. The one sample per rev method

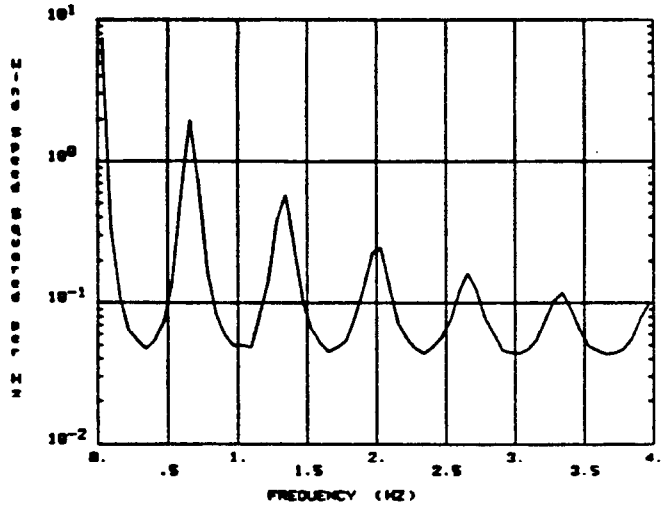

Figure 5: Rotationally sampled PSD based on the Solari PSD and coherence using the full-field Sandia method.

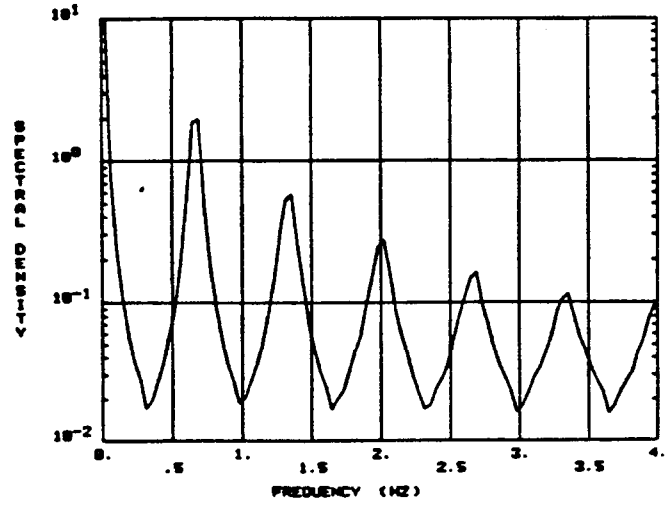

Figure 6: Rotationally sampled PSD based on the Solari PSD and coherence simulating one sample per revolution for each input point.

has a maximum frequency (Nyquist frequency) of one half per rev ($\Omega/2$) so the white background is omitted. When the full-field method is supplied an input PSD that has zero spectral content at frequencies above $\Omega/2$, the same decrease in the minima of the roatationally sampled PSD is observed.

The improved fit to the *exact* per rev variances when simulating only one point per rev is due to the elimination of the background, uncorrelated, high-frequency input. It is not clear that this is desirable, because the *exact* results could also be suffering from a lack of high-frequency input, which could even occur in measurements (i.e., due to insufficient anemometer frequency response). The full-field method includes all of these high frequencies and may therefore be more accurate. The uncorrelated input could be added to the one sample per rev simulation by simply adding white noise with variance equal to the spectral content of the turbulence above a frequency of $\Omega/2$. When simulating wind speeds for N_B blades, the missing spectral content is above $N_B\Omega/2$.

The structural implications of the missing spectral content between per rev frequencies is not obvious for two reasons: (1) the *aerodynamic loads* on the blades are often nonlinearly related to the incident wind speed, and (2) the blades may not respond *aerodynamically* to fluctuations of such high frequency and small scale. The per rev spectral content is between 2 times (at 5P) and 40 times (at 1p) greater than the background level (see Fig. 5) and is therefore the most important part of the PSD to match.

SPATIAL INTERPOLATION

The efficient simulation for HAWT applications in the previous section can not be used for VAWT applications because of the looping paths that VAWT blades trace out in the moving field of turbulence. It is therefore necessary to minimize the number of input points over the swept area of the wind turbine and interpolate wind speed values between those points. For example, a 4x4 rectangular grid of 16 points was used to cover the swept area of the 25 meter diameter VAWT in Ref. 6. Obtaining wind speed values at locations in space lying between simulation points can result in a loss of variance due to the averaging inherent in interpolation. Simulating wind speed for arbitrary locations on a moving VAWT blade therefore requires that this lost variance be replaced before the aerodynamic loads are calculated.

The wind speed, Y, at a location not at a grid point can be estimated by an interpolated value, $\tilde{Y}$, by taking a weighted sum of the n surrounding simulated values, Y_j;

$$\tilde{Y} = \sum_{j=1}^{n} W_j Y_j \tag{15}$$

The variance of $\tilde{Y}$ is the expected value of $\tilde{Y}^2$ (assuming a zero mean), given by

$$E[\tilde{Y}^2] = \sum_{j=1}^{n}\sum_{k=1}^{n} W_j W_k E[Y_j Y_k] \tag{16}$$

The actual variance of Y, $E[Y^2]$, may be known a priori, or may be interpolated from the grid points by the same scheme as given in Eq. (15).

If Y_j and Y_k are perfectly correlated (and have the same variance), then $E[Y_jY_k] = E[Y_j^2] = E[Y_k^2]$ and there is no loss of variance. However, there will usually be some difference in variance and lack of correlation in wind speed reflected in the coherence function and quantified by the cross spectral density, G_{jk}. (See also Eq. (1) and recall that because $G_{jk}(f)$ is real valued, $\int_0^\infty G_{jk}(f)df = E[Y_jY_k]$.) The normalized error is the missing variance divided by the correct variance, $E[Y^2]$, and can therefore be expressed as

$$Error = 1 - \frac{\sum_{j=1}^{n}\sum_{k=1}^{n} W_j W_k \int_0^\infty G_{jk}(f)df}{E[Y^2]} \tag{17}$$

The potential loss of variance for each pair of points can be expressed by defining the parameter ϵ_{jk},

$$\epsilon_{jk} = 1 - \frac{\int_0^\infty G_{jk}(f)df}{E[Y^2]} \tag{18}$$

The potential (or maximum) loss of variance, ϵ_{jk}, is therefore a function of the level of correlation between points j and k, which is in turn a function of the distance between the points, Δr. The value of ϵ_{jk} is plotted as a function of the point spacing in Fig. 7 (using the Solari PSD and coherence with average values for the random parameters). This potential for loss of variance is also the integrated difference between the PSD and the CSD of any two points, if the points have identical PSDs. Figure 8 shows how ϵ_{jk} is distributed over frequency in this case by plotting the turbulence CSDs for point spacings of 10, 20, and 30 meters. The actual PSD of the interpolated data will lie between the CSD and the "Original PSD," shown in Fig. 8.

The normalized error is the fraction of ϵ_{jk} actually lost, as shown by substituting Eq. 18 into Eq. 17.

$$Error = 1 - \sum_{j=1}^{n}\sum_{k=1}^{n} W_j W_k (1 - \epsilon_{jk}) \tag{19}$$

Using the fact that $\epsilon_{jj} = 0$ and assuming the interpolation weights have the usual property that

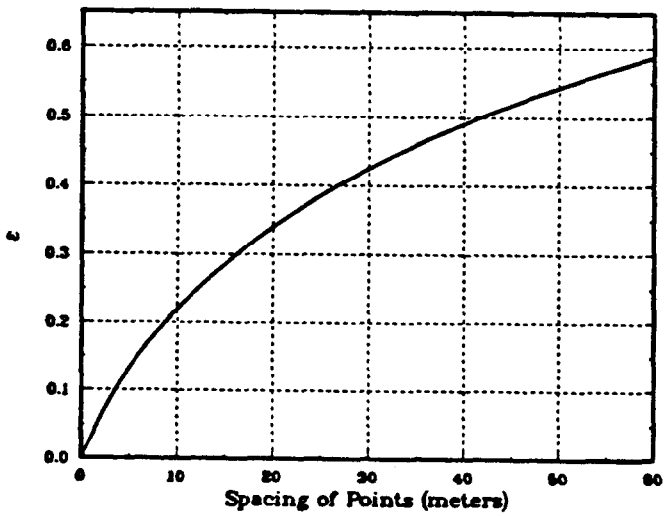

Figure 7: Potential loss of variance, ϵ, as a function of the distance between points for interpolating wind speed (using Solari's PSD and coherence).

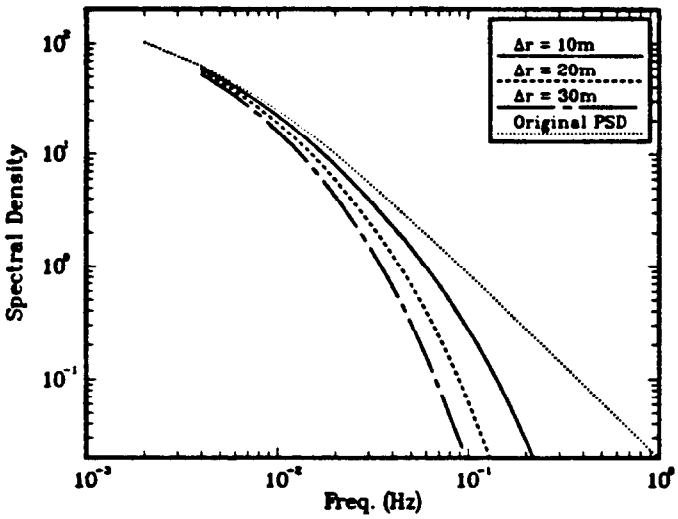

Figure 8: CSDs of turbulence for points with 10, 20, and 30 meter spacings compared with the PSD at each point (Original PSD).

$$\sum_{j=1}^{n}\sum_{k=1}^{n} W_j W_k = 1$$

the expression for the error can be reduced to

$$Error = 2\sum_{j=1}^{n-1}\sum_{k=j+1}^{n} W_j W_k \, \epsilon_{jk} \qquad (20)$$

The error therefore depends on the weights used in the interpolation scheme.

For example, consider a square region to be interpolated from the four corner values with a bilinear interpolation. Let $\epsilon = \epsilon_{jk}$, where j and k are adjacent corners, be the characteristic potential loss of variance for the region. Figure 9 shows approximately how the error, as a fraction of ϵ, will be distributed over the region. There will be no loss of variance at each corner. The maximum error, about $3\epsilon/4$, is at the center. The error at the center of each side is $\epsilon/2$.

The lost variance represents the portion of the process that is uncorrelated between adjacent simulation points. To simulate a time series at some location inside the region, an interpolated time series could first be generated from the corner points. The missing part could be simulated *independently* by taking an inverse Fourier transform of a weighted sum of the differences between the PSDs and CSDs in Fig. 8 (replace ϵ_{jk} with the (PSD - CSD) for each pair of points in Eq. 20). The two time series could then be added together to obtain a result with the correct variance.

For VAWT applications, however, complete time series at intermediate locations are not needed, only samples of time series at intermediate locations are needed. Each wind speed sample on the moving blade is taken from a different location in space where the missing high frequency variance (see Fig. 8) is relatively uncorrelated. The missing variance can therefore be replaced by adding uncorrelated Gaussian increments (white noise) to the wind speed samples, where the variance of the added increment is equal to the missing part at that location in space. The effect is the same as in the previous section where

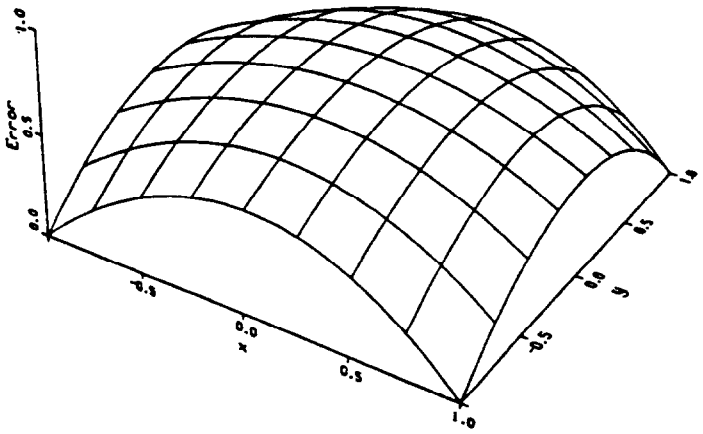

Figure 9: Distribution in error (loss of variance), as a fraction of ϵ, for bilinear interpolation over a square region.

there is missing high frequency content when only N_B points per revolution of a HAWT are simulated. In both cases, the missing frequency content is well approximated by white noise when applied to a blade moving through the turbulence field.

There are two cases in which the white noise approximation may be in error: (1) where the blade is moving slowly (near the attachments to the tower), and (2) when simulating at very closely spaced points on the blade. In case (1), the error may be neglected because points where the blade is moving slowly are also points where the aerodynamic loads are small. In case (2), there is potential for slightly underestimating the contribution of the resulting aerodynamic loads to the lower modes of the structure. Care must be taken to avoid refining the spacing of locations at which loads are calculated beyond the level at which the winds can be accurately simulated. Similarly, too small an interval in blade azimuth position can cause case (1) type errors, even at the equator. A practical limit on the spacing of points on the blade would be the distance that the blade equator travels between time steps.

CONCLUSIONS

1. The Sandia method for three-dimensional turbulence simulation is capable of matching the best estimates of rotationally sampled PSDs better than any other simulation method currently available. The input models of turbulence PSD and coherence are what determine the accuracy of the method (see Table 1).

2. Models for atmospheric turbulence PSD and coherence with coefficients that are modeled as random variables (Eqs. (10), (11), and (12)) provide good results for rotational sampling. The recent paper by Solari [13] provides estimates of the distributions of these coefficients.

3. A coherence that is exponential in Δr, as previously assumed, is not capable of matching the suggested distribution of variance in rotationally sampled PSDs. Solari's suggestion of augmenting by $(\Delta r/z_m)^{0.25}$ is a definite improvement; simulations using $(\Delta r/z_m)^{0.50}$ give even better results for this one test case. It is recommended that Solari's suggestion (Eq. (12)) be followed.

4. An improvement to the Sandia method for full-field wind simulation permits simulation of only those samples that are actually used in rotational sampling. This reduces the storage requirement and computation time by a factor of the number of divisions per rev divided by the number of blades. The match between published rotationally sampled PSDs and the simulation results is excellent (see Table 1). This improvement is useful for HAWT analysis, but not for VAWT analysis.

5. When interpolating simulated wind speeds, there will be a reduction in variance of the interpolated data. The error is quantified in terms of the cross spectral density functions, permitting an estimate of the missing variance at any location in space. Because the missing part is uncorrelated over the region of the interpolation, simulations of wind speed at a point on a rotating VAWT blade can be generated by adding uncorrelated Gaussian variates, with the appropriate variance for each location, to the interpolated values.

ACKNOWLEDGEMENTS

Special thanks are due to David Powell and James Connell of Pacific Northwest Laboratories, who provided assistance in discovering the sources of modeling discrepancies. Gregory Homicz of the Sandia Aerodynamics Department provided extensive editorial comments, and Clark Dohrmann of the Applied Mechanics Department carefully checked the equations.

REFERENCES

1. Veers, P.S., "Modeling Stochastic Wind Loads on Vertical Axis Wind Turbines," SAND83-1909, Sandia National Laboratories, Albuquerque, NM, September, 1984.

2. Homicz, G.F., "VAWT Stochastic Loads Produced by Atmospheric Turbulence," Proc., 7th *ASME Wind Energy Symposium*, New Orleans, LA, January 10–14, 1988.

3. Lobitz, D.W., "NASTRAN-based Software for the Structural Analysis of Vertical and Horizontal Axis Wind Turbines," Proc., *European Wind Energy Conference*, Hamburg, F.R. Germany, October 22-26, 1984, ed. W. Palz, *Commission of the European Communities*, H.S. Stephens and Associates, Bedford, England, 1985.

4. Oscar, D.S. and T.L. Paez, "Analysis of Wind Turbines on Offshore Support Structures Excited by Random Wind and Random Waves," Proc., 7th *ASME Wind Energy Symposium*, New Orleans, LA, January 10–14, 1988.

5. Anderson, M.B., S.J.R. Powles, and E.A. Bossanyi, "The Response of a Vertical Axis Wind Turbine to Fluctuating Aerodynamic Loads," Proc., 7th *British Wind Energy Association Conference*, Oxford University, March 27–29, 1985.

6. Malcolm, D.R., "A Model for the Response of Vertical Axis Wind Turbines to Turbulent Flow: Parts 1 and 2," Sandia National Laboratories Contractor Report SAND88-7021, Prepared by Indal Technologies Inc., Mississauga, Ontario, Canada, July, 1988.

7. Shinozuka, M. and C.-M. Jan, "Digital Simulation of Random Processes and Its Applications," *J. Sound and Vibration*, Vol. 25, No. 1, pp. 111-128, 1972.

8. Smallwood, D.O., "Random Vibration Testing of a Single Test Item with a Multiple Input Control System," Proc., *Institute of Environmental Sciences*, April, 1982.

9. von Karman, T. "Progress in the Statistical Theory of Turbulence," *Proc. National Academy of Science*, Vol. 34, 1948.

10. Frost, W., B.H. Long, and R.E. Turner, "Engineering Handbook on the Atmospheric Environmental Guidelines for Use in Wind Turbine Development," NASA Tech. Paper 1359, December, 1978.

11. Powell, D.C. and J.R. Connell, "Review of Wind Simulation Methods for Horizontal-Axis Wind Turbine Analysis," PNL–5903, Battelle Pacific Northwest Laboratory, Richland, WA, June, 1986.

12. Kaimal, J.C., J.C. Wyngaard, Y. Izumi, and O.R. Cote, "Spectral Characteristics of Surface-Layer Turbulence," *Quart. J. Royal Met. Soc.*, 98, 1972.

13. Solari, G., "Turbulence Modeling for Gust Loading," *J. Structural Engrg., ASCE*, Vol. 113, No. 7, July, 1987.

14. Connell, J.R., "The Spectrum of Wind Speed Fluctuations Encountered by a Rotating Blade of a Wind Energy Conversion System," PNL–4083, Battelle Pacific Northwest Laboratory, Richland, WA, November, 1981.

15. George, R.L., "Simulation of Winds as Seen by a Rotating Vertical Axis Wind Turbine Blade," PNL–4914, Battelle Pacific Northwest Laboratory, Richland, WA, February, 1984.

16. Powell, D.C., J.R. Connell, and R.L. George, "Verification of Theoretically Computed Spectra for a Point Rotating in a Vertical Plane," PNL–5440, Battelle Pacific Northwest Laboratory, Richland, WA, 1985.

Proceedings of the Eighth ASME Wind Energy Symposium
D. E. Berg and P. C. Klimas (ed.), SED-Vol. 7, ASME, January 1989

TIME DOMAIN STRUCTURAL RESPONSE CALCULATIONS FOR VERTICAL AXIS WIND TURBINES

C. R. Dohrmann and P. S. Veers, Members of Technical Staff
Applied Mechanics Division IV
Sandia National Laboratories
Albuquerque, New Mexico

ABSTRACT

Structural response of Vertical Axis Wind Turbines (VAWTs) during transient events such as starting and stopping or during variable speed operation cannot be estimated with existing frequency domain techniques. Time domain simulation is presented, including the effects of changes in rotation speed on turbine response. The method for predicting the structural response of VAWTs during variable speed events differs from that used to analyze constant speed operation in two ways: (1) the equations of motion no longer have constant coefficients and (2) additional terms contribute to the stiffness matrix and loading vector. The structural matrices are obtained at several discrete rotor speeds using NASTRAN and interpolated for intermediate speeds. The equations of motion are then numerically integrated in a separate program. Results for constant speed operation in turbulence-free winds agree favorably with those from a frequency domain analysis. Reasonable results are obtained for a change in rotor speed which passes through a structural resonance.

INTRODUCTION

The primary objective of wind turbine dynamic structural analysis is to evaluate the fatigue susceptibility of the rotor. The first goal is to determine the natural frequencies of vibration, and adjust the design to keep them from coinciding with the inherent harmonic excitation at integer multiples of the operating speed. Fatigue life estimates, however, require statistics of the steady-state stress response to stochastic-wind loading and of the transients, such as start-up and shut-down. Steady-state forced-response calculations can be done either in the time domain, using direct time integration, or in the frequency domain, using frequency response analysis.

Frequency domain techniques have been used to predict the dynamic response of VAWTs operating at constant speeds in both steady winds (1) and turbulent winds (2). Typically, the steady centrifugal and gravitational loads are applied to the wind turbine in a geometric nonlinear static analysis to determine the static stresses and the stiffness matrix of the structure at the specified operating speed. The geometric nonlinearity arises due to significant tension stiffening of the relatively flexible VAWT blades. Once the revised stiffness matrix is obtained, linear techniques are used to predict the dynamic response. Motions are assumed to be small perturbations about the static prestressed state. The stress at a point in the turbine is then obtained by adding the dynamic response to the static results. Frequency domain techniques are particularly efficient for stochastic-wind applications because loading statistics can be transformed directly to structural response statistics, without repeatedly calculating response (2).

During variable speed operation, or for transient events such as start-up and shut-down, the structural equations of motion have time-varying coefficients. Frequency domain techniques require constant coefficients and are therefore no longer applicable. The approach outlined here is to integrate the equations of motion in the time domain, simulating structural response to stochastic-wind loading, control system inputs, and braking transients. The main difficulty in obtaining meaningful results for fatigue-life estimates using time-domain stress analysis lies in the stochastic nature of the response. Stress statistics can only be estimated by repeated simulation of turbine response to stochastic-wind excitation. Therefore, it is especially important that the procedure outlined here is efficient, minimizing the number of times that structural matrices must be updated and refactored.

The purpose of this work is to describe a computational technique that efficiently and accurately evaluates the equations of motion in the time domain for the above events. Turbine stresses are then estimated from the displacements. This paper builds on the work of Lobitz and Sullivan (1), and includes the additional

terms necessary to simulate variable rotor speed. Where possible, new terms are related to existing quantities to minimize additional computations. A method for including a generator control system in the analysis is derived. Short examples are included for illustration, but the statistical analysis necessary to apply the results to fatigue life prediction is left for future work.

THEORY

The formulation of the governing equations of motion for VAWTs operating at either constant or variable speeds makes use of a reference frame that follows the overall motion of the structure. The reference frame is fixed at the base of the wind turbine and rotates about the vertical axis with angular velocity $\Omega = \Omega \mathbf{n}_3$ (see Fig. 1). In the finite element formulation, all displacements and rotations are with respect to this rotating frame, in contrast to conventional structural dynamics where there are small structural deformations in a fixed Newtonian frame. Because deformations are given in the rotating frame, the standard dynamical equations of motion must be modified.

To illustrate rotating frame effects, consider the acceleration of a point on the turbine in a Newtonian frame:

$$\mathbf{a} = \ddot{\mathbf{u}} + 2\Omega \times \dot{\mathbf{u}} + \Omega \times (\Omega \times (\mathbf{r} + \mathbf{u})) + \dot{\Omega} \times (\mathbf{r} + \mathbf{u}) \qquad (1)$$

In Eq. (1), $\mathbf{u}, \dot{\mathbf{u}}, \ddot{\mathbf{u}}$ are the displacement, velocity, and acceleration of the point in the rotating frame, $\mathbf{r}$ is the original position of the point, and $\dot{\Omega} = \dot{\Omega}\mathbf{n}_3$ is the angular acceleration of the rotating frame. For constant speed operation ($\dot{\Omega} = 0$) the final term in Eq. (1) drops out, and the governing equations of motion take the form

$$M\ddot{u} + (B + C)\dot{u} + (K - S)u = f_e \qquad (2)$$

where u is a vector of displacements, f_e is a vector of external loads, and M and B are the standard mass and damping matrices. The static stiffness matrix, K, is obtained from a nonlinear static analysis, where the steady centrifugal and gravitational loads are applied to the structure. The vector of displacements, u in Eq. (2), is the deformation of the structure about the static prestressed state. Rotating coordinate system effects are taken into account by the Coriolis matrix, C, and the centrifugal softening matrix, S, which may be expressed as

$$C = \Omega C_0 \qquad (3)$$

$$S = \Omega^2 S_0 \qquad (4)$$

where C_0 and S_0 are the Coriolis and softening matrices for $\Omega = 1$ rad/sec (1).

For constant speed operation, the Coriolis and softening matrices are included in the NASTRAN model with DMIG (Direct Matrix Input) cards in the Bulk Data Deck as described in Ref. (1). If steady winds are assumed, the frequency content of the wind loads is limited to frequencies at integer multiples of the rotation speed, referred to as the "per rev" harmonics. The dynamic response of the turbine at the per rev harmonics is obtained in a frequency response analysis (NASTRAN solution 68).

For variable-speed operation ($\dot{\Omega} \neq 0$), two more terms must be included in the equations of motion, resulting in

$$M\ddot{u} + (B + C)\dot{u} + (K - S + A)u = f_e + f_a \qquad (5)$$

The matrix A and load vector f_a originate from the $\dot{\Omega} \times \mathbf{u}$ and $\dot{\Omega} \times \mathbf{r}$ acceleration terms in Eq. (1), respectively.

Because both the Ω and $\dot{\Omega}$ vectors lie in the $\mathbf{n}_3$ direction, A and f_a can be calculated from existing quantities. Noting that the term $2\Omega \times \dot{u}$ leads to the Coriolis matrix, C, the matrix A may be expressed as

$$A = \frac{\dot{\Omega}}{2\Omega} C = \dot{\Omega} \frac{C_0}{2} \qquad (6)$$

The load vector f_a may be obtained using standard finite element techniques; however, a comparison of the terms $\dot{\Omega} \times \mathbf{r}$ and $\Omega \times (\Omega \times \mathbf{r})$ reveals the relationship between f_a and the centrifugal load vector used in the static analysis. These two load vectors are identical except for a scale factor $(\dot{\Omega}/\Omega^2)$ and a rotation (due to the extra cross product in the centrifugal loading). The load vector f_a may be constructed by calculating the centrifugal loads for $\Omega = 1$ rad/sec, rotating the loads -90 degrees about the vertical axis, and storing the result in the vector f_{a0}. Then f_a may be written as

$$f_a = \dot{\Omega} f_{a0} \qquad (7)$$

The matrices C, K, and S are all functions of Ω, and the matrix A and vector f_a are functions of $\dot{\Omega}$. Eq. (5) therefore has

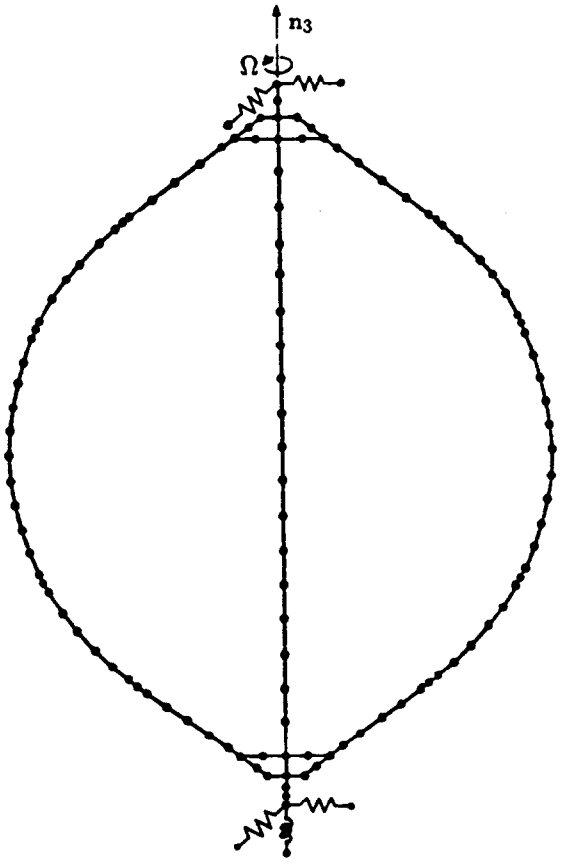

Figure 1: Finite element model of the 34-m Test Bed.

time-varying coefficients for variable-speed operation because both Ω and $\dot{\Omega}$ are functions of time.

This analysis assumes centrifugal loads do not produce any dynamic response. The centrifugal loads for constant speed operation of the VAWT (see Eq. 2) remain constant and are accounted for in the static analysis. For variable-speed operation, however, the centrifugal loads are no longer constant and could have some dynamic effect. It is assumed that the dynamic response induced by the slowly varying centrifugal loads is negligible and that motion between the different prestressed states of the turbine is quasi-steady. The frequency of the first mode that could possibly be excited by the centrifugal loads is the controlling factor in the quasi-steady assumption. The lowest frequency mode for a VAWT is typically the propeller mode where the entire rotor oscillates as a rigid body about the vertical axis, resulting in displacements entirely *out of the plane* of the rotor. The propeller mode, however, is not excited by the centrifugal loads because these loads lie *in the plane* of the rotor. Limiting changes in centrifugal loads to 5 percent over the period of the lowest in-plane mode restricts the rate of change of rotor speed to

$$\dot{\Omega} \leq 0.025\Omega_0 f_{min} \tag{8}$$

where Ω_0 is the nominal operating speed and f_{min} is the lowest natural frequency (in Hertz) of any mode that contains an in-plane component.[1] As $\Omega_0 \rightarrow 0$, the restriction imposed on $\dot{\Omega}$ by Eq. (8) is no longer necessary because the centrifugal loads approach zero as well.

Another assumption is that the motions about the prestressed state at any operating speed are small enough that a linear theory is valid. As a check of this assumption, a frequency response calculation was done for the 34-m Test Bed operating at 37.5 rpm in 45 mph winds. The magnitudes of predicted displacements and rotations were within the bounds of linear beam theory, and the additional tension in the blades, which causes stiffening effects, was small in comparison to the static tension (see Fig. 2).

[1]Throughout this development, Ω has units of rad/sec and $\dot{\Omega}$ units of rad/sec^2. If Ω and $\dot{\Omega}$ are expressed in units of rpm and rpm per minute, the constant in Eq. (8) is 1.5 rather than 0.025.

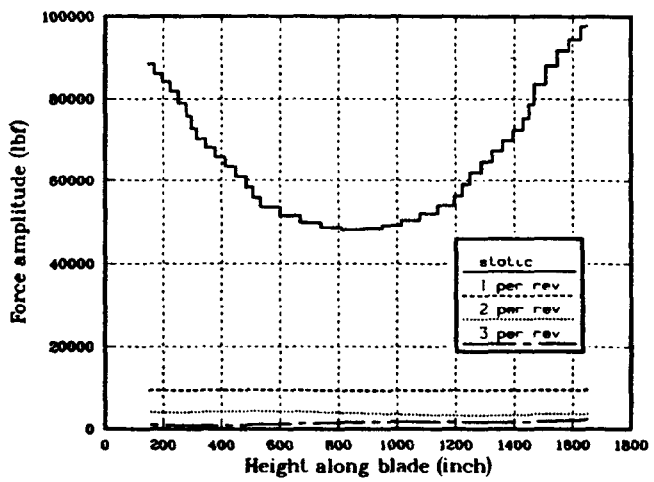

Figure 2: Comparison of static and dynamic blade tension at 37.5 rpm in 45 mph winds.

Specified Variation of Operating Speed

One possibility for variable speed operation is a control system that specifies the operating speed at all times. A typical scenario involves ramping the rotational rate, Ω, up or down at constant $\dot{\Omega}$ to control output power. An essential requirement in analyzing variable-speed operation of a VAWT is the availability of the mass, damping, and stiffness matrices at different values of Ω. The approach taken herein is to generate the structural matrices at several discrete values of Ω ranging from 0 to the maximum rpm and interpolate these matrices for intermediate values of Ω. The steps taken to generate the matrices at discrete values of Ω are outlined in Figure 3 and described below.

1. Perform a geometric nonlinear static analysis of the wind turbine at the specified operating speed using NASTRAN (solution 64) by applying the steady centrifugal and gravitational loads, creating a data base that includes the static stiffness matrix, K.

2. Generate a NASTRAN input deck for transient analysis (solution 69) including the Coriolis and centrifugal softening terms.

3. Use the data base created in Step 1 and the input deck from Step 2 in transient analysis (solution 69) to assemble and write out the structural matrices.

4. Translate the matrices stored in the NASTRAN format into a format readable by the dynamic simulation program VSFEVD.

Interpolation of the matrices in Eq. (5) for general operating conditions Ω and $\dot{\Omega}$, where $\Omega_i < \Omega < \Omega_{i+1}$, is done using the equations

$$\begin{aligned}(K-S+A)_{\Omega,\dot{\Omega}} &= (1-\xi)(K-S)_{\Omega_i} + \xi(K-S)_{\Omega_{i+1}} \\ &\quad +\dot{\Omega}C_0/2 \qquad (9)\\ (B+C)_{\Omega} &= B+\Omega C_0 \qquad (10)\end{aligned}$$

where $\xi = (\Omega^2 - \Omega_i^2)/(\Omega_{i+1}^2 - \Omega_i^2)$. The mass matrix remains the same regardless of the value of Ω or $\dot{\Omega}$.

Static stresses and displacements for intermediate values of Ω are obtained using the same interpolation given in Eq. (9). The apparent loads caused by the angular acceleration of the rotating frame are given by Eq. (7).

The numerical time integration scheme used for Eq. (5) is of the Newmark-β family (3). Integration parameters $\gamma = 0.50$ and $\beta = 0.25$ gave the best agreement with previous frequency domain results. The Newmark-β method is an implicit integrator that treats the displacements, velocities, and accelerations at the end of each time step as a pseudo-force at the beginning of the next time step. The displacement vector at time $t + \Delta t$ is obtained by solving the system of linear equations

$$\hat{K}u_{t+\Delta t} = f_e + \dot{\Omega}f_{ao} + g(u_t, \dot{u}_t, \ddot{u}_t) \tag{11}$$

where $\hat{K}$ is the effective stiffness matrix, and g is a vector that depends on displacements, velocities, and accelerations at time

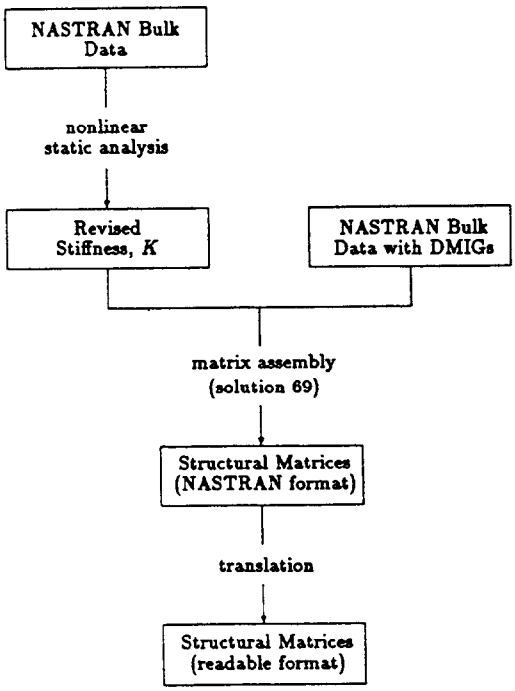

Figure 3: Flowchart of the method used to extract structural matrices.

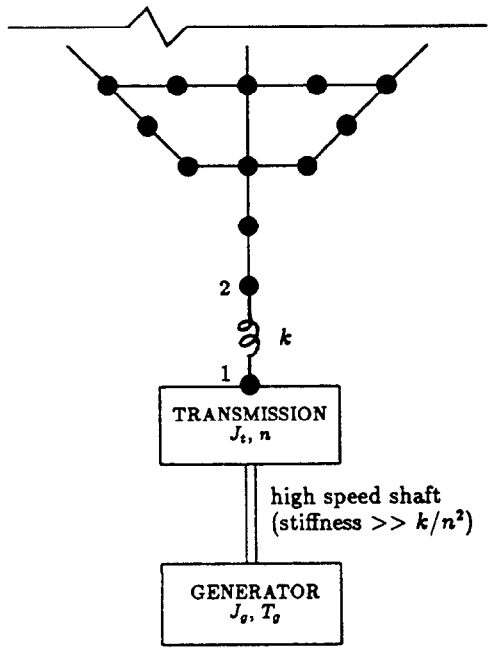

Figure 4: Schematic showing the connection of the finite element model to the low speed side of the transmission.

t (see Ref. 3 for a complete explanation of $\hat{K}$ and g).

For constant speed operation, the coefficient matrix, $\hat{K}$, needs to be factored just once; incrementing the solution through time requires only back substitution at each time step. In contrast, the coefficient matrix for variable-speed operation is continually changing and must be factored many times. Since factoring a matrix requires more computational effort than back substitution, it is undesirable to factor the coefficient matrix at each time step. Numerical experiments indicated that sufficient accuracy is retained if the coefficient matrix is refactored whenever the operating speed, Ω, changes by more than 1 rpm.

Torque Control of Operating Speed

For normal variable-speed operation, the control system may be able to directly specify the operating speed, Ω, and its rate of change, $\dot{\Omega}$. Under other control strategies, the system may be controlling other quantities such as generator torque. If there is a loss of grid resistance, generator torque must be zero and an emergency shutdown, using only braking torque, would result. Direct control of $\dot{\Omega}$ is not possible under such conditions, requiring the analyst to determine the behavior of $\dot{\Omega}$ with time. Once $\dot{\Omega}$ is determined for the current time step, the method for calculating structural response is the same as in the previous section for specified variation of operating speed.

The key to understanding the behavior of $\dot{\Omega}$ lies in the coupling between the finite element model and the generator (see Figure 4). In the finite element model, point 1 is fixed; i.e., the rotating frame moves about the vertical axis at precisely the same rate as the low speed side of the transmission. For purposes of modeling drive train dynamics, the torsional inertia of the generator and transmission may almost always be combined at point 1 because the shaft connecting them is relatively stiff. The combined torsional inertia, referred to the low speed side of the transmission, is given by

$$J_1 = n^2 J_g + J_t \tag{12}$$

where n is the speed ratio of the transmission, J_g is the torsional inertia of the generator, and J_t is the torsional inertia of the transmission referred to the low speed side. Letting k denote the stiffness of the shaft between points 1 and 2 (see Fig. 4), the equation of motion for the reference frame is given by

$$J_1\dot{\Omega} = nT_g + k\theta_2 \tag{13}$$

where T_g is the torque applied by the generator and θ_2 is the rotation of point 2 relative to point 1. Equation (13) must be satisfied at each time step in the simulation for the boundary condition at the base of the tower to be satisfied. For specified $\dot{\Omega}$, Eq. (13) may be used to determine the generator torque, but is not needed to solve the equations of motion. In situations such as emergency shutdown or torque controlled operation, Eq. (13) governs the behavior of $\dot{\Omega}$.

The equations of motion can be integrated using the Newmark-β method, just as in the specified $\dot{\Omega}$ case. The only difference

for torque control is that the $\dot{\Omega}$ appearing in Eqs. (11) and (13) is now an unknown. Equation (13) cannot be used to explicitly solve for $\dot{\Omega}$ because θ_2 is an element of $u_{t+\Delta t}$. The approach for solving the coupled sets of equations is to express $u_{t+\Delta t}$ as the sum of the displacement with $\dot{\Omega} = 0$ and the displacement due solely to $\dot{\Omega}$ loading:

$$u_{t+\Delta t} = (u_{t+\Delta t})_{\dot{\Omega}=0} + \dot{\Omega} u_{a0} \tag{14}$$

where

$$\hat{K}(u_{t+\Delta t})_{\dot{\Omega}=0} = f_e + g(u_t, \dot{u}_t, \ddot{u}_t) \tag{15}$$

$$\hat{K}(\dot{\Omega} u_{a0}) = \dot{\Omega} f_{a0} \tag{16}$$

The rotation of point 2 is then described by the superposition $\theta_2 = a + \dot{\Omega} b$, where a and b are the elements of $(u_{t+\Delta t})_{\dot{\Omega}=0}$ and u_{a0} corresponding to the θ_2 degree of freedom. An expression for $\dot{\Omega}$ is obtained by substituting $\theta_2 = a + \Omega b$ into Eq. (13) and solving for $\dot{\Omega}$.

$$\dot{\Omega} = \frac{nT_g + ka}{J_1 - kb} \tag{17}$$

The steps necessary to advance the solution from t to $t + \Delta t$ are summarized below:

1. Solve Eqs. (15) and (16) for $(u_{t+\Delta t})_{\dot{\Omega}=0}$ and u_{a0} ($\hat{K}$ and therefore u_{a0} only change when the structural matrices are updated).
2. Set the scalars a and b equal to the elements of the vectors $(u_{t+\Delta t})_{\dot{\Omega}=0}$ and u_{a0} corresponding to the θ_2 degree of freedom.
3. Solve Eq. (17) for $\dot{\Omega}$.
4. Calculate $u_{t+\Delta t}$ from Eq. (14).

The rate of rotation at the end of the time step is: $\Omega_{t+\Delta t} = \Omega_t + \dot{\Omega} \Delta t$.

The control system can specify T_g in any way without affecting the linearity of the structural equations of motion. Not only can the simple case of zero torque associated with loss of grid resistance be modeled, but highly complicated, even nonlinear, control rules can be included. The only restrictions are that the above assumptions be satisfied: small displacements about the prestressed state and $\dot{\Omega}$ satisfies Eq. (8).

EXAMPLES

The first check of the program VSFEVD is a comparison of the calculated per rev harmonics of the 34-m Test Bed, operating at a constant speed of 37.5 rpm in steady 20 mph winds, using both frequency domain and time domain methods. The frequency domain method uses NASTRAN solution 68 (1) to conduct a frequency response analysis at each per rev frequency. The time domain analysis integrates Eq. (2) through time until a steady-state response is achieved (about 45 seconds). Initial transients are minimized by including a small amount of damping and gradually ramping from zero to the full wind loads over several revolutions of the turbine. One revolution of the steady-state history is then Fourier transformed to determine the per rev harmonics.

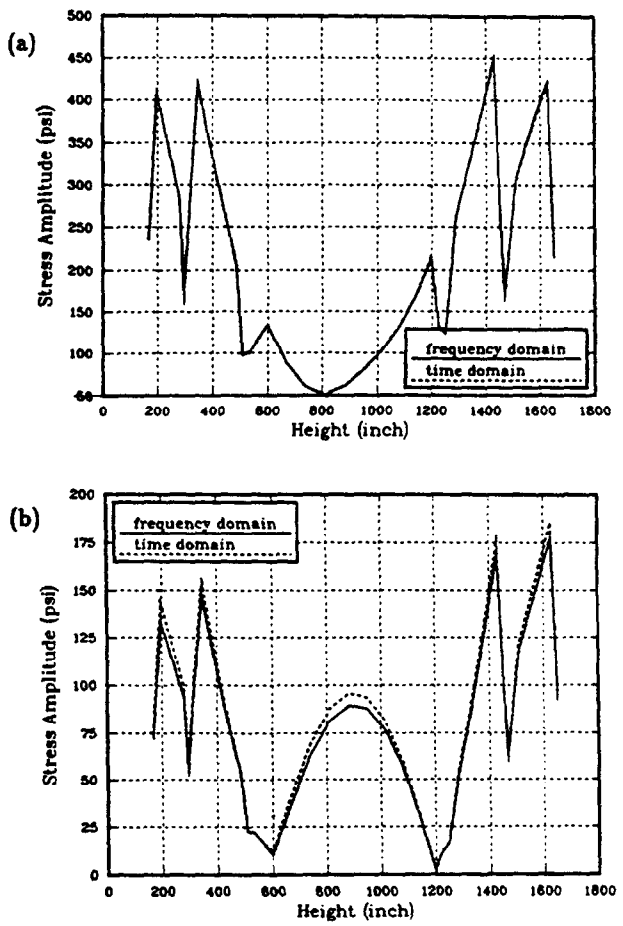

Figure 5: Comparison of leading edge stresses: (a) 1 per rev, (b) 3 per rev.

The distributions of leading edge stress amplitudes along the turbine blade are plotted for the first and third per rev harmonics in Figure 5. Agreement in stress amplitudes is excellent at 1 per rev and always within 5 percent at 3 per rev. Part of the error at 3 per rev is due to remaining start up transients that keep the time series from being exactly periodic. The good agreement provides a valuable check on the temporal approximation of the equations of motion, the time integration, and stress recovery procedures in VSFEVD.

Variable speed wind turbines are capable of operating over a fairly wide range of rotation rates. Once the wind turbine begins generating power, operating speed may be controlled directly by altering the electrical load at the generator. In some situations it might be necessary to pass through a structural resonance when changing from one speed to another. Under these circumstances it is important to pass through the resonance quickly in order to avoid excessive stress levels.

Operating speeds at which the per rev harmonic loading excites structural modes are readily identified with the use of fan plots (see Figure 6). For example, the 1B (first butterfly[2]) mode

[2]The 1B mode is characterized by out of plane blade displacements resembling the motion of a butterfly's wings.

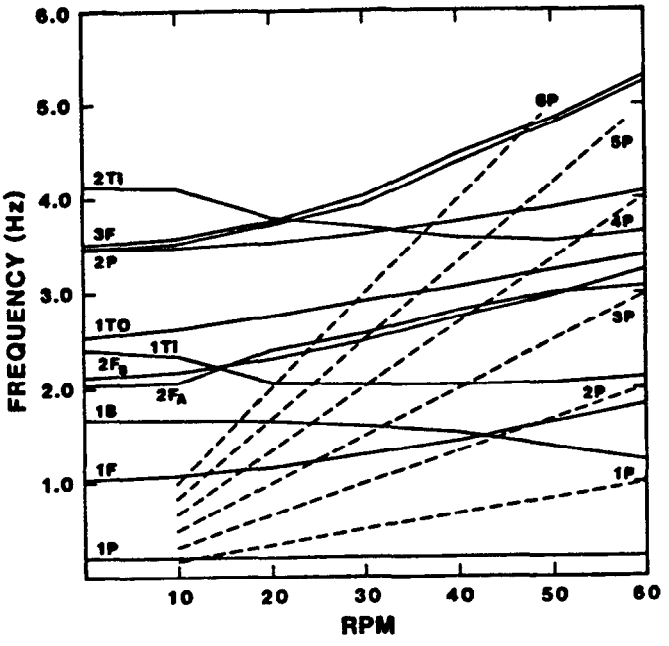

Figure 6: Plot of natural frequencies (solid lines) and per rev harmonic excitations (dashed lines) versus operating speed for the 34-m Test Bed with brakes released.

of the 34-m Test Bed is excited by the 3P (3 per rev) loads at 31.5 rpm. To demonstrate the effects of passing through a resonance, Ω is ramped from 28 to 34 rpm at a rate of $\dot{\Omega}$=7 rpm/min, as shown in Figure 7. The resulting leading edge blade stresses near the base of the tower are shown in Figure 8 for 40 mph winds with a 10 percent turbulence intensity. Stress amplitudes clearly increase as the operating speed passes through the resonance, but then drop off quickly after the resonance is passed. Flatwise stresses on the inner surface of the blade (see Figure 9) are only slightly affected by the 1B mode and do not exhibit the same growth in amplitude; stress amplitudes tend to decrease during ramping because of a diminished excitation of the 1F (first flatwise) mode by the 3P loading. Both leading edge and inner surface mean stresses change during ramping because of increased centrifugal loads. The increase in mean stress at the leading edge is due to increased axial tension. A decrease at the inner surface is due to a change in the in-plane bending as the blade is forced into troposkein shapes that vary as the centrifugal loads change. Flatwise stresses are affected to a greater extent by in-plane bending than by tension.

SUMMARY

The change from constant speed operation to variable speed operation affects the structural analysis in two ways: (1) the structural matrices are time varying and (2) additional terms must be included in the stiffness matrix and loading vector. Time varying matrices are modeled as piecewise constant; updating occurs when the speed changes by more than 1 rpm. The additional terms are simple multiples of existing terms and therefore require minimal additional computations.

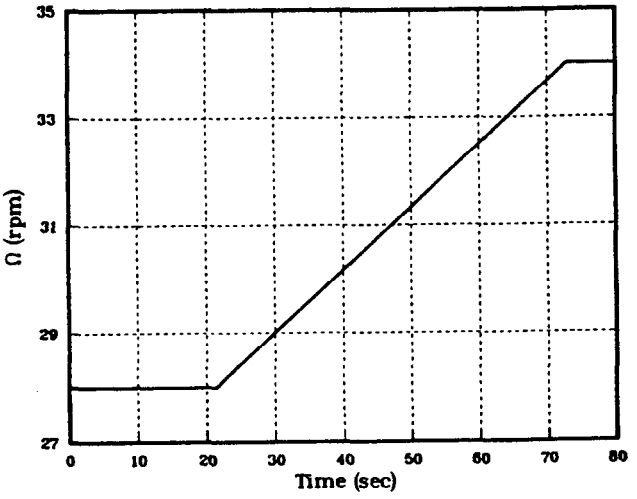

Figure 7: Variation of Ω during ramping maneuver.

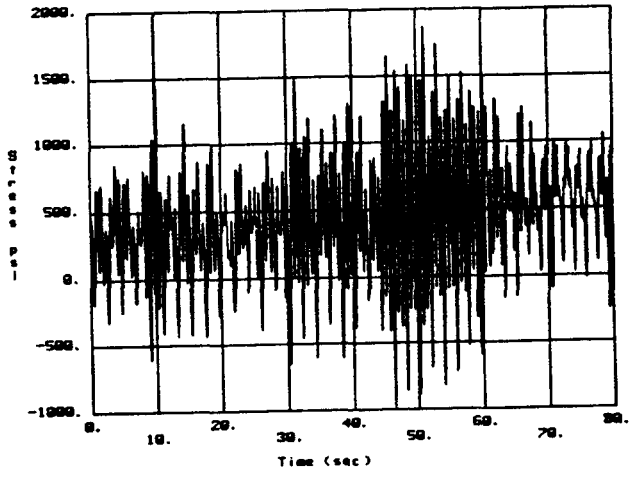

Figure 8: Leading edge stresses at lower blade root during ramping maneuver.

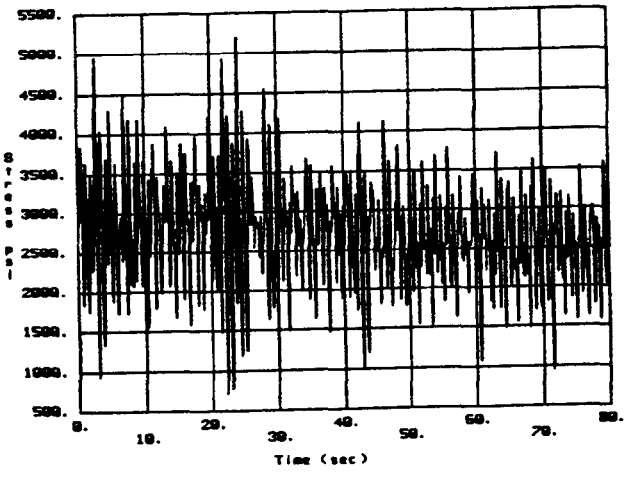

Figure 9: Inner surface stresses at lower blade root during ramping maneuver.

The equations of motion are formulated by using NASTRAN to assemble the structural matrices at a few preselected constant speeds. Operation at intermediate speeds is modeled by interpolating the structural matrices. The Newmark-β method is used to integrate the equations of motion, advancing the solution through time with the program VSFEVD. The cumbersome data management overhead of NASTRAN is eliminated, streamlining the solution procedure and making the use of smaller computers possible.

Various control systems can be incorporated into the analysis. When the rotating speed is specified (controlling both Ω and $\dot{\Omega}$) results are obtained by a direct substitution into the equations of motion. Other control systems that specify torque, perhaps through some intermediate generator parameters, are included through Eq. (13) and the steps following. Any programmable control system, even a highly nonlinear one, can be simulated with this method without the need for linearization or iterative solutions.

VAWT blade stress predictions using VSFEVD and frequency domain techniques agree very well for the case of constant speed operation. Reasonable results were also obtained for variable speed operation; however, future comparisons need to be made with measured test data as it becomes available.

ACKNOWLEDGEMENTS

The authors wish to extend their appreciation to Don Lobitz of the Applied Mechanics Division at SNLA for sharing his knowledge of VAWT structural dynamics during numerous informal discussions. Thanks are also extended to Tom Ashwill of the Wind Energy Research Division for the frequency domain results and fan plot, and to Greg Homicz of the Computational Aerodynamics Division for the code used to generate wind loads for the turbine blades.

REFERENCES

1. Lobitz, D.W. and Sullivan, W.N., "A Comparison of Finite Element Predicitons and Experimental Data for the Forced Response of the DOE 100 kW Vertical Axis Wind Turbine," SAND82-2534, Sandia National Laboratories, Albuquerque, NM, February, 1984.

2. Malcolm, D.J., "Dynamic Response of a Darrieus Rotor Wind Turbine Subject to Turbulent Flow," *Eng. Struct.*, Vol. 10, pp. 125–134, 1988.

3. Bathe, K.J. and Wilson, E.L., *Numerical Methods in Finite Element Analysis*, Prentice-Hall, Inc., Englewood Cliffs, NJ, pp. 322–323.

Proceedings of the Eighth ASME Wind Energy Symposium
D. E. Berg and P. C. Klimas (ed.), SED-Vol. 7, ASME, January 1989

FATIGUE CHARACTERIZATION OF A VAWT BLADE MATERIAL*

J. A. Van Den Avyle, Mechanical Metallurgy Division
H. J. Sutherland, Wind Energy Research Division
Sandia National Laboratories
Albuquerque, New Mexico

ABSTRACT

The fatigue analysis of Wind Energy Conversion System blades has been limited by the lack of fatigue data for typical blade materials, including 6063 aluminum, an alloy commonly used for Vertical Axis Wind Turbine (VAWT) blades. This paper reports results to date of a testing program to establish a fatigue properties database for this alloy. Two types of fatigue response data were measured: 1) stress versus number of cycles to failure (S-n) and 2) fatigue crack growth rates. S-n experiments have been conducted on 6063 aluminum blade extrusion material using approximately 100 bend specimens cycled at five alternating stress amplitudes and at four mean stress levels. Data have been analyzed using an equivalent alternating stress based on Goodman's rule to describe mean stress effects on fatigue life. Cyclic crack growth rates have been measured using three loading ratios.

NOMENCLATURE

a,b	-	constants in linear regression fit to Goodman analysis
A,m	-	constants in crack growth rate equation
da/dn	-	cyclic crack propagation rate, mm/cycle
K_{max}	-	maximum applied stress intensity factor in fatigue loading cycle, $MPa\sqrt{m}$
K_{min}	-	minimum applied stress intensity factor in fatigue loading cycle, $MPa\sqrt{m}$
ΔK	-	$K_{max}-K_{min}$, $MPa\sqrt{m}$
n	-	number of loading cycles in fatigue
n_f	-	number of cycles to failure
R	-	loading ratio, K_{min}/K_{max}
r^2	-	linear least squares correlation coefficient
s_{al}	-	alternating stress in fatigue cycle, MPa
s_e	-	effective alternating stress, MPa
s_m	-	mean stress in fatigue cycle, MPa
s_u	-	ultimate tensile strength, MPa
s_y	-	yield strength, MPa

INTRODUCTION

One form of Vertical Axis Wind Turbine (VAWT) blades uses large, hollow, internally ribbed extrusions made of aluminum alloy 6063-T5; such extrusions are typically produced up to 16 m long with a wall thickness of 6.4 mm. This alloy was selected primarily because of its ease of extrusion into large shapes. Its mechanical strength properties are moderate (1) and have not typically been important criteria for previous industrial applications, such as architectural trim. For this reason few earlier data have been generated to characterize the fatigue behavior of 6063 aluminum; the only published source found reports rotating bending-generated stress versus cycles to failure (S-n) data (2).

This paper reports results to date of an experimental testing program to establish a fatigue properties database for this alloy. Existing design methods can require either of two types of fatigue response data: 1) stress versus number of cycles to failure (S-n) and 2) fatigue crack growth rates. S-n testing measures total cyclic life as a function of applied alternating stress amplitude and mean stress level; multiple tests at a given condition are generally run to provide statistical significance.

Sandia National Laboratories has sponsored a series of beam bending fatigue tests to determine the S-n characteristics of extruded 6063-T5 aluminum. The majority of the testing has been performed under contract at Teledyne Engineering Services (3); the test matrix includes 5 alternating stress levels at each of 4 mean stress levels being cycled to a maximum of $5X10^8$ cycles. In addition, Southern University (4) has conducted beam bending fatigue experiments on the same extrusion material (sponsored by the Solar Energy Research Institute, Boulder, CO). This work has utilized the same specimens and testing setup as

*This work performed at Sandia National Laboratories supported by the U. S. Department of Energy under contract number DE-AC04-76DP00789.

the Teledyne work, so the data is compatible; a total of 20 experiments have been run at Southern to date.

Fatigue crack growth rate tests have been performed on extrusion material to measure the cyclic propagation rate (da/dn) as a function of applied cyclic stress intensity (ΔK) for different values of loading ratio R, where $R=K_{min}/K_{max}$. These data are required for a fracture mechanics-based design procedure where structural fatigue life is determined by a flaw growth criterion.

Aluminum alloy 6063 is an age hardenable alloy of nominal composition 0.4% Si, 0.7% Mg, with balance Al (all in weight percent) (1). Typical commercial strength levels for differing aging treatments are listed in Table 1. The extrusion material tested here was purchased to a -T5 aged minimum strength level specification. This condition is produced by rapidly air-quench cooling from the extrusion press followed by an aging treatment of 175°C for 6 h.

EXPERIMENTAL

Tensile test and fatigue specimens were sectioned from the outer skin (6.4 mm thick) of a VAWT blade extrusion that was manufactured by Spectrulite Consortium, Inc., Madison, IL. Their stress axes were parallel to the blade length so that cracking was in the transverse direction across the blade chord. Tensile specimens were rectangular in cross-section with gage dimensions 50 mm long X 13 mm wide X 5.1 mm thick. These were run at room temperature at a strain rate of $5X10^{-3}$ s^{-1}.

The S-n specimen was a tapered constant-stress cantelever bending design (Fig. 1). Sample machining and surface preparation were specified to minimize surface and sub-surface damage which could potentially affect initiation of fatigue cracks and to provide specimen to specimen uniformity. Final surface finishing was done using 600 grit SiC paper. Tests were performed using a Fatigue Dynamics, Inc. reversed bending fatigue test machine at cyclic rates up to 87 cy/s. An instrumented specimen grip was designed to dynamically monitor loads during cycling to minimize test setup variations on fatigue life.

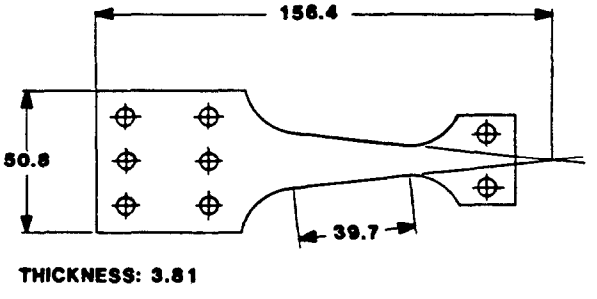

Fig. 1 Schematic S-n specimen design using tapered constant stress cantelever bending geometry; dimensions in mm.

Fatigue crack growth rate testing was conducted in accordance with ASTM specification E 647-86 using an MTS servohydraulic test frame at a frequency of 20 cy/s. The specimen was a standard compact tension design with a thickness of 3.8 mm and a width of 76.2 mm. Tests were cycled at constant load ranges, and crack lengths were monitored optically at 20X magnification. From measured pairs of crack length and cycle number taken at 0.5 mm intervals, crack growth rates were calculated using the 7-point incremental polynomial method outlined in the specification.

Several tensile and fatigue crack growth test specimens were heat treated to the commercial -T6 peak aged condition to compare properties with the -T5 extrusion. Starting from the extrusion material, these specimens were solutionized in air at 525°C, quenched in water, and subsequently aged at 175°C for 6 h.

RESULTS AND DISCUSSION

Measured tensile properties of the -T5 extrusion and peak aged -T6 conditions are listed in Table 1 along with nominal handbook values (1). Strengths of measured -T5 and -T6 are similar, with somewhat lower yield and higher ultimate strengths for the -T5 extrusion. Both these values are similar to the handbook level for -T6, which is much higher than the nominal -T5. These strength properties

Table 1. Tensile Properties of 6063 Aluminum

	s_y (MPa)	s_u (MPa)	% Elong
Nominal (1)			
-T4	90	170	22
-T5	145	185	12
-T6	215	240	12
Measured			
-T5	205	245	---
-T6	217	236	---

indicate that the rate of cooling from the extrusion temperature, estimated to be 3.5°C s^{-1} from 560°C, is rapid enough to maintain the alloying elements in solution during cooldown and allow a precipitation reaction to occur during subsequent aging. Extensive microstructural examinations of these and other heat treatments for this alloy are reported elsewhere (5).

S-n Data

Results of the S-n tests completed to date by the two laboratories out to lifetimes of $1X10^8$ cycles are shown in Fig. 2. The data are arranged into four tensile mean stress values between 0 and 103.5 MPa, and linear least squares curve fits through each mean stress data set are given to help show the trends in behavior. As expected, higher mean stresses promote shorter fatigue lives. At the highest cycles to failure the scatter increases somewhat and there is an indication that the slope of the data curves may decrease.

The S-n data has been fit with a number of proposed constitutive formulations (6). These included a Goodman fit using the yield strength of the material (s_y), a Goodman fit using the ultimate strength of the material (s_u), a Gerber fit, and a

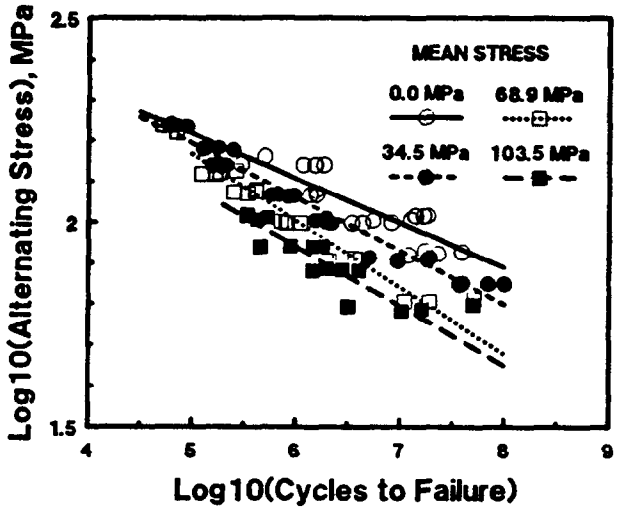

Fig. 2 Results of S-n testing of 6063-T5 aluminum

modified Gerber fit. For these fits, the standard deviations between the data and the fits were found to be 0.1332, 0.04290, 0.04752 and 0.03632, respectively (the modified Gerber fit optimized with the exponent equal to 1.28). From these calculations, Goodman's rule using s_u and the modified Gerber fit both yield small standard deviations, but Goodman's rule is simpler to apply, and it has one less adjustable parameter.

As used here, the Goodman rule states that the fatigue life at an alternating stress s_{al} and a mean stress s_m is equivalent to the fatigue life at an equivalent alternating stress s_e at zero mean stress by:

$$s_{al} = s_e \left(1 - s_m / s_u \right) . \qquad (1)$$

From the tensile tests, s_u = 245 MPa (35.4 ksi). The fatigue data gathered by Teledyne and Southern University are plotted in Fig. 3 using this formulation. Also shown in this figure is a least-squares curve fit to the data. The form chosen here is:

$$\log_{10}(s_e) = a + b \log_{10}(n_f) , \qquad (2)$$

where n_f is the number of cycles to failure. The data fit yields values of 2.93421 for a and -0.13256 for b, with a standard deviation of 0.04290 (units of stress are MPa). This curve fit is the solid line shown passing through the center of the data in Fig. 3. The dashed lines in the figure are the curves for two standard deviations above and below the norm (i.e., a = 2.93421 ± 2 [0.04290] and b = -0.13256 in Eq. 2).

This curve fit is not the optimum fit of the data. If s_u is taken to be 317 Mpa (46 ksi), the standard deviation can be reduced from 0.04290 to 0.03552. However, the 317 MPa is not a realistic value for s_u.

These data may be compared to fatigue data from rotational bending tests. In Fig. 4, the data are plotted with design data reported in Ref. 2 for the -T5 and the -T6 conditions. As seen in this figure, the flexural data reported here lie slightly above the -T6 design curve at relatively low cycles to failure. This is reasonable since the extrusion material is similar in strength to nominal -T6 levels. At the high cycles to failure, the design data show a change in slope (at approximately $5X10^6$ cycles to failure). As the data reported here do not extend past $1X10^8$ cycles, a slope change may or may not be present. Remaining tests out to lifetimes of approximately $5X10^8$ cycles may indicate whether there is a slope change.

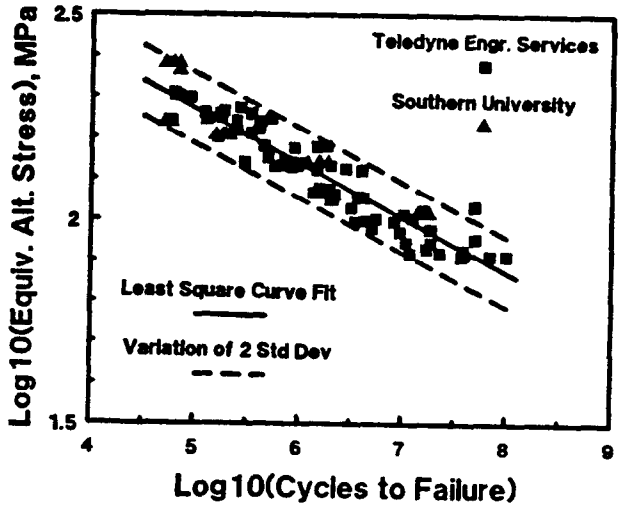

Fig. 3 S-n data of 6063-T5 aluminum plotted with Goodman fit using ultimate strength to calculate effective alternating stress

Crack Growth Rate Data

The fatigue crack growth behavior of 6063-T5 aluminum is shown in Fig. 5, plotting growth rate (da/dn) versus applied stress intensity factor range (ΔK) at loading ratio, R, levels of 0.09, 0.3, and 0.5. The curves at R = 0.09 and 0.5 are combined data from at least three separate tests, while the curve at R = 0.3 is a single test. The data are linear on this log-log scale, which indicates a power law dependence of the form:

$$da/dn = A \, \Delta K^{(m)} \qquad (3)$$

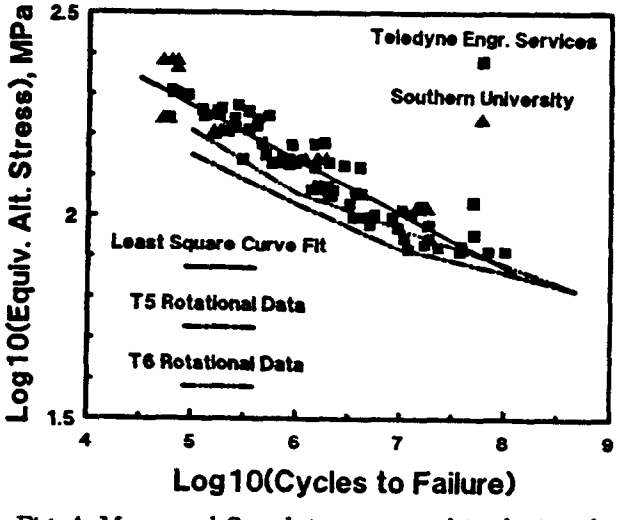

Fig. 4 Measured S-n data compared to design data for 6063-T5 and -T6 aluminum from Ref. 2

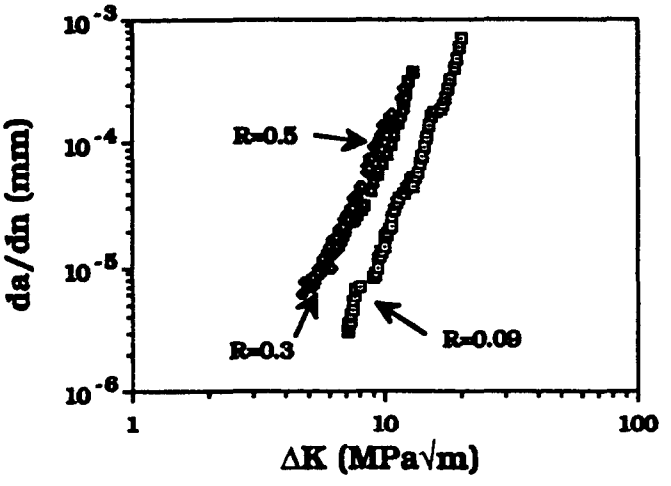

Fig. 5 Fatigue crack growth response of 6063-T5 aluminum

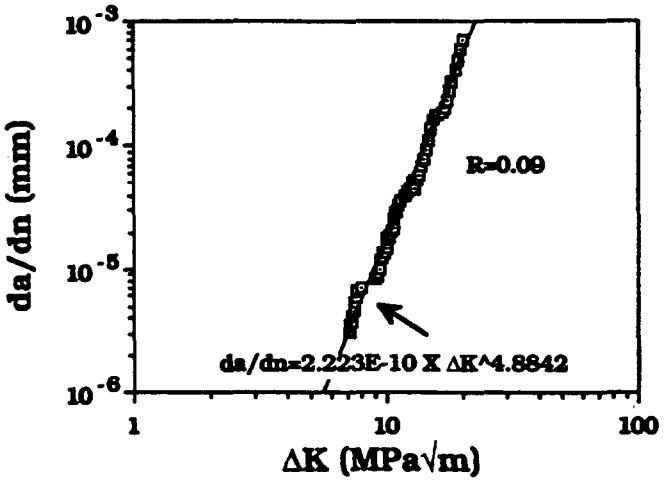

Fig. 6 Crack growth of 6063-T5 aluminum at R=0.09 with least-squares curve fit to data

A least-squares curve fit through the data for R = 0.09 is shown in Fig. 6; this is typical of the other fits. Values of the constants A and m in Eq. 3 for each R ratio are:

R	A	m	r^2
0.09	$2.223X10^{-10}$	4.8842	0.99
0.30	$1.037X10^{-8}$	3.9224	0.98
0.50	$1.100X10^{-8}$	4.0099	0.98

This power law dependence with m=4 is consistent with other data for aluminum and other alloys in the growth rate range 10^{-6} to 10^{-3} mm/cycle, which is above the fatigue crack growth threshold (7).

For a given ΔK the growth rates increase with increasing R ratio (Fig. 5). This R ratio effect is commonly observed and is attributed substantially to early crack closure (8). Crack closure occurs during the unloading portion of the fatigue cycle when separated crack surfaces touch before the applied load reaches its minimum level; during reloading, a finite load, termed the opening load, must be reached before the crack separates fully and opening stress is applied to the crack tip. Thus only a portion of the full loading cycle or applied ΔK is used to strain the crack tip to cause crack growth. At higher R ratios with higher tensile mean stress, a larger fraction of the applied ΔK acts to strain the crack tip, and growth rates are faster.

Rough crack surfaces tend to promote early closure because of interference between surface asperities (8). Examinations of fatigue specimen fracture surfaces visually and in the scanning electron microscope (SEM) show a very rough morphology where the crack primarily follows grain boundaries (Fig. 7). The fracture surface is mostly intergranular with small interconnecting transgranular regions;

Fig. 7 Rough intergranular fatigue fracture surface of 6063-T5 aluminum (scanning electron micrograph)

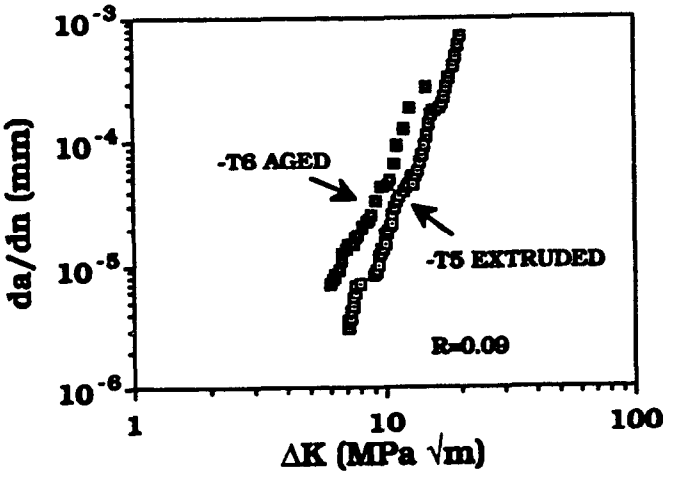

Fig. 8 Lower fatigue crack growth rates for 6063-T5 aluminum compared to -T6 at R=0.09

this mode is also seen in tensile overload fractures in the -T5 extruded and aged alloy. The grain size is large at approximately 200 μm, which contributes to the rough surfaces. The thermal treatment these extrusions experience produces a microstructure with large grain size and other grain boundary features which cause intergranular fracture (5).

Fig. 9 Smoother transgranular fatigue fracture surface of 6063-T6 aluminum (scanning electron micrograph)

To further study this effect, samples were heat treated to the -T6 aged condition, which has the same strength level and grain size as the as-received -T5 material (Table 1). Crack growth rates at R = 0.09 are higher for the -T6 specimen (Fig. 8). The fatigue fracture changed to a transgranular mode which features a much flatter surface (Fig. 9). Due to the smoother surfaces, the crack closure effect is less, and growth rates are higher.

Fatigue crack growth rates of the 6063-T5 extrusions are beneficially lowered due to microstructural features produced by the thermal history of the extrusion process. It is uncertain what effect this microstructure has on the process of crack initiation. Current research is investigating the mechanisms of crack initiation in this alloy (9).

CONCLUSIONS

1. Results of S-n fatigue testing of 6063-T5 aluminum alloy at five alternating stress levels and four mean stress levels can be correlated by a Goodman fit using the ultimate strength to calculate an equivalent alternating stress.

2. Fatigue crack growth rates follow a power law relationship with ΔK over the range of growth rates studied. Crack growth has been measured at three loading ratios (R).

3. Reduced growth rates are measured in 6063-T5 extrusions compared to 6063-T6 laboratory-aged to the same strength level. This is attributed to crack closure effects caused by rough intergranular fracture surfaces in 6063-T5.

ACKNOWLEDGEMENTS

The authors wish to acknowledge the contributions of Paul Hatch of the Mechanical Metallurgy Division at Sandia National Laboratories who performed fatigue crack growth measurements and Dave Johnson and Richard Greeno of Teledyne Engineering Services and Habib Mohamadian and Ira Graham of Southern University who performed S-n fatigue testing.

REFERENCES

1. Hatch, J. E., ed., 1984, Aluminum: Properties and Physical Metallurgy, American Society for Metals, Metals Park, OH, pp 362-368.

2. Military Handbook, 1966, MIL-HDBK-694A(MR), p 51.

3. Teledyne Engineering Services, 130 Second Avenue, Waltham, MA 02254

4. Mohamadian, H. P. and Graham, I. J., Southern University, Baton Rouge, LA, personal communication, July 1988.

5. Van Den Avyle, J. A. and Hills, C. R., "Effects of Precipitate Free Zones on Fatigue Crack Propagation in 6063-T5 Aluminum Extrusions", to be published.

6. Osgood, C. C.,1962, Fatigue Design, 2nd Edition, Permagon Press, Oxford, UK.

7. Paris, P. C., 1964, Fatigue--An Interdisciplinary Approach, Proceedings 10th Sagamore Conference, Syracuse University Press, Syracuse, NY, p107.

8. McEvily, A. J., 1988, "On Crack Closure in Fatigue Crack Growth", Mechanics of Fatigue Crack Closure, ASTM STP 982, American Society for Testing and Materials, Philiadelphia, pp 35-43.

9. Pelloux, R. M. and Warren, A. S., Dept. of Materials Science and Engineering, Massachusetts Institute of Technology, Cambridge, MA, personal communication, 1988.

Proceedings of the Eighth ASME Wind Energy Symposium
D. E. Berg and P. C. Klimas (ed.), SED-Vol. 7, ASME, January 1989

SIMPLIFIED FATIGUE DAMAGE AND CRACK GROWTH CALCULATIONS FOR WIND TURBINES

P. S. Veers
Member of the Technical Staff
Wind Energy Research Division
Sandia National Laboratories
Albuquerque, New Mexico

ABSTRACT

Estimating fatigue life of wind turbine components, where the loading and structural response are random, can be a difficult task. The life estimate is sensitive to rare large loads and can be influenced by the sequence of load applications. Sequence effects in fatigue crack initiation and crack growth are outlined. A simplified model for sequence effects in crack growth is presented along with model predictions of an American Society for Testing and Materials (ASTM) crack growth test series. The relative importance of including these effects in fatigue calculations is discussed. Analytical solutions for the time to crack initiation and crack growth provide quick estimates of fatigue life by approximating the loading as a narrow-band Gaussian process and by neglecting sequence effects. This approximation is both conservative and within the usual scatter in fatigue life estimates due to material variability. It is therefore a useful tool in estimating fatigue life, especially when turbine response data is limited.

INTRODUCTION

Fatigue of wind turbine blades has been shown to be an important factor in the economic viability of wind energy conversion systems. The design of the next generation of wind turbines must have fatigue life at the center of structural decision making. It is necessary, therefore to possess simple methods of quickly estimating component fatigue lives for several design alternatives, without detailed and costly fatigue analysis. While it may not be possible to conduct detailed fatigue analysis when the loads and structural dynamics are still poorly defined, even a crude life estimate would be very useful.

Wind turbine fatigue life estimation requires data on the component fatigue characteristics and loading. Fatigue characteristics are obtained from component testing or from materials tests and careful component stress analysis. Loading may be determined using either strain gage measurements from an operating wind turbine or numerical structural analysis. The emphasis of this paper is on useful approximations to fatigue life estimation that can be obtained with limited load information. The error due to these approximations is considered small as long as the life prediction remains within a factor of two of more sophisticated life predictions — an uncertainty in fatigue life estimates equal to that due to material variability [1,2].

There is also uncertainty about the validity of competing fatigue models, i.e., whether the sequence of load cycles must be considered in addition to cyclic amplitudes. Methods of estimating both fatigue damage (crack initiation) and crack growth are reviewed. Again, the emphasis is on striking a balance between a fatigue model that includes all the significant phenomena and one that provides an approximate result commensurate with the accuracy and uncertainty of the available loading and material data.

It is assumed that, for wind turbine applications, fatigue failure must be avoided during the economic lifetime of the component. Because a 30 year lifetime is on the order of 500 million cycles, even replacement parts are expected to survive for at least a million cycles. Only high cycle fatigue and linear elastic fracture mechanics are therefore considered. If conditions prove otherwise, the predicted life will be unacceptably short, and design revisions will be required.

FATIGUE MECHANISMS AND MODELS

Fatigue life calculations can be separated into three mechanistic divisions: 1) crack initiation, 2) growth and coalescence of micro-cracks, and 3) growth of a macroscopic crack. Ideally, a fatigue analysis would include each of these mechanisms in the total estimate of time to failure. Originally, all three were lumped into a single analysis based on the S-n curve (a plot of the number of cycles to failure versus constant amplitude cyclic stress level). The test specimens used for fatigue life (S-n) analysis were typically compact (round or rectangular cross sections) in which most of the time to failure is taken up in crack initiation. Crack growth analysis is now treated separately by

relating the rate of crack growth to the stress intensity factor range, a function of both crack geometry and loading. Recently, the growth of micro-cracks has been shown to be mechanistically unrelated to macroscopic crack growth and is considered a third phase. In most applications, however, micro-crack growth is still included in the crack initiation phase. Crack initiations will be treated here as the initiation and coalescence of micro-cracks until a macroscopic crack is formed.

Crack Initiation

The methods of estimating time to crack initiation are most closely tied to the historical method of estimating total life by a cumulative damage summation. The governing principle, known as Miner's rule, is that each stress cycle causes a fixed amount of damage, which accumulates until failure (crack initiation) [3]. Damage is a not a physical quantity that can be measured directly. Rather, it is an internal state variable that is a measure of the material's ability to withstand further cyclic loading. In equation form,

$$D = \sum_k \frac{n(S_k)}{N_f(S_k)} \tag{1}$$

in which D is the damage, $n(S_k)$ is the number of applied cycles at stress state S_k (depending on mean stress and stress amplitude), and $N_f(S_k)$ is the number of cycles to failure at constant stress state S_k. Failure is predicted when $D \geq 1$. When the S-n curve can be drawn as a straight line on a log-log plot as shown in Fig. 1, $N_f(S) = (cS^b)^{-1}$ (where c and b are material constants), and Eq. 1 can be written in terms of each stress cycle,

$$D = \sum_{i=1}^{N} cS_i^b \tag{2}$$

where N is the total number of applied cycles.

For a narrow-band Gaussian loading, the mean stress is constant and the stress amplitudes are described by the Rayleigh probability density function (pdf);

$$p_s(S) = \frac{S}{\sigma^2} \exp\left(\frac{-S^2}{2\sigma^2}\right) \qquad S \geq 0 \tag{3}$$

where σ^2 is the variance of the applied stress. After N cycles of narrow-band random loading, one expects $n(S) = Np_s(S)dS$ cycles with amplitudes between S and $S + dS$. The expected (or average) damage, $E[D]$, can therefore be calculated by replacing the summation in Eq. 2 with integration over the pdf of S.

$$E[D] = \int_0^\infty cNp_s(S)S^b dS \tag{4}$$

Substituting Eq. 3 into Eq. 4 and solving for N with $E[D] = 1$ gives a closed form solution for the average number of cycles to failure.

$$N = \left(c(\sqrt{2}\sigma)^b(b/2)!\right)^{-1} \tag{5}$$

(For noninteger values of $b/2$, the factorial can be determined using the Gamma function [4].) When N is large, as it must be in wind turbine applications, there is very little variation about the average due to the randomness in the loading [5].

The above equations are valid for narrow-band Gaussian loadings in applications where the loading sequence does not matter.

Sequence effects in crack initiation. When stress concentrations cause local yielding, the local stress and strain states differ from the bulk of the material, which remains elastic. For example, a tensile load peak could cause local yielding while the nominal stress remains elastic. After the tensile load is removed, the elastic material will seek to retain its initial shape, clamping the zone of material near the stress concentration, which has been plastically stretched, leaving a compressive residual stress. The cycle following the tensile overload therefore has a lower mean stress than it would have had if the tensile overload had not occurred. When yielding occurs frequently and in both tension and compression, the local stress state must be carefully tracked to determine the mean value of each stress cycle. The combination of instantaneous cycle amplitude and mean stress can then be used in conjunction with a Goodman diagram (relating cycles to failure to both stress amplitude and mean stress) to calculate the damage.

In the case of wind turbine rotors, any loading that exceeds the yield stress in both tension and compression, even locally, will be unacceptable. It is common, however, for the nominal mean stress in the blades during operation to be a significant fraction of the yield stress. It is therefore possible that stress concentrations in blade joints will cause local yielding, although it will not be in both tension and compression. If the material yields in tension, the local stress state, due to the clamping action of the bulk of the elastic material, will be lower (less tension) than without yielding. Compressive yielding is usually not of concern because the bulk of the material must also be in compression. Although cracks can form with a compressive mean stress, they can not grow.

If the sequence effects due to local yielding are neglected in wind turbine applications, the mean stress will be overestimated in fatigue sensitive regions of nominal tension. The resulting time to crack initiation will be underestimated. In the early design stages, when an approximate but conservative life estimate is desired, sequence effects due to local yielding can therefore be neglected.

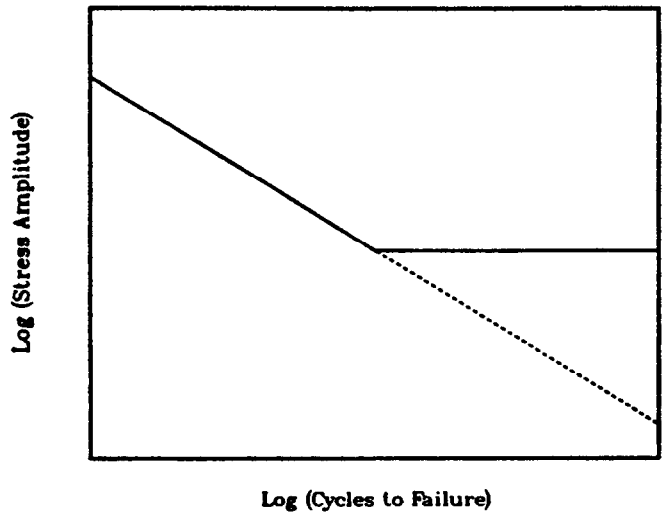

Figure 1: The S-n curve usually plots as a straight line in log-log space. The solid line shows a fatigue limit, while the dashed line has none.

One exception occurrs when a section of the blade is in nominal tension during operation (say, due to steady flatwise bending) but is exposed to occasional compressive overloads (say, due to emergency braking transients in edgewise bending). The compressive overloads induce tensile residual stresses at stress concentrations that can substantially reduce time to crack initiation.

Another phenomenon that could be considered a *sequence effect* is the existence and elimination of the fatigue limit in many metals. The fatigue limit is a stress level below which constant amplitude loading will not cause crack initiation. Figure 1 illustrates this behavior by the horizontal portion of the solid line. It has long been known, however, that failure can occur due to loading below the fatigue limit if the limit is occasionally exceeded [12]. This phenomenon has since been explained in terms of micro-mechanical locking mechanisms that restrict local plasticity and inhibit fatigue damage. The locking mechanism is removed whenever stress peaks above the fatigue limit are applied, eliminating the fatigue limit and resulting in finite life at stress levels below the fatigue limit. (See Ref. 6 for an explanation of the mechanism of *Cotrell atmospheres*, Ref. 7 for the effects of localized plasticity on fatigue damage, and Ref. 8 for a practical application of these effects to the fatigue limit.)

In a cumulative damage analysis, no damage is assigned to any stress cycles below the fatigue limit, because as long as the fatigue limit is never exceeded (e.g., constant amplitude loading) no damage is done. But if a small stress cycle is preceeded by a peak above the fatigue limit, the locking mechanism is removed and the stress cycle will cause local plasticity resulting in fatigue damage. The sequence of loading is important — a small cycle that is initially undamaging will cause damage if it is preceeded by a large cycle.

The suggested approach for irregular loading is to assume that the fatigue limit does not exist; i.e., the S-n curve has no flat portion as shown by the solid line in Fig. 1. The slope of the S-n curve should be assumed constant as shown by the dashed line in Fig. 1 [8]. This is equivalent to assuming that a large stress peak has eliminated the fatigue limit at the very start of the loading and that all small cycles are damaging, regardless of when they occur. A standard Miner's rule analysis, as outlined by the above equations, will then provide a conservative crack initiation estimate without further consideration of sequence effects.

In wind turbine applications, the loading at any time is random, and the intensity of the random loading changes as the mean wind speed rises and falls. The fatigue limit will therefore occasionally be exceeded at points of stress concentration. At the same time, most of the stress cycles will be much smaller, perhaps even less than the fatigue limit. If these cycles are assumed to be undamaging, the time to crack initiation can be substantially overestimated. The fatigue limit should therefore be eliminated in wind turbine fatigue analysis, using the dashed, rather than the solid, line in Fig. 1 to extrapolate S-n data.

Crack Growth

The rate of fatigue crack growth is related to linear elastic fracture mechanics by *Paris' law* [9];

$$\frac{da}{dN} = c\Delta K^b \tag{6}$$

where c and b are again material constants (but different than the crack initiation constants). The stress intensity factor range is defined to be $\Delta K = \sqrt{\pi a} Y(a) \Delta S$, where a is the crack length, $Y(a)$ is a geometric shape factor dependent on a (for a center crack in a large sheet, $Y(a) \approx 1$), and ΔS is the stress range. Improvements to Paris' law initially centered on adjustments for the stress ratio, $R = S_{min}/S_{max}$, of each cycle. More recently, emphasis has been on identifying an effective stress intensity range, $\Delta K_{eff} = \sqrt{\pi a} Y(a) \Delta S_{eff}$ [10,11]. The effective stress range, ΔS_{eff}, is defined in various ways, as discussed in the next section.

The crack growth can be determined directly by summing the increments in crack growth due to each cyclic stress range.

$$\Delta a = a_f - a_o = \sum_{i=1}^{N} c\left(\sqrt{\pi a_i} Y(a_i) \Delta S_{eff_i}\right)^b \tag{7}$$

Each increment in crack length depends on current crack length, a_i, as well as current effective stress range.

More efficient solutions for the number of cycles of narrow-band random loading needed to grow from initial to final crack lengths are possible as long as:

1. there are no sequence effects in the crack growth model.
2. the crack growth equation remains separable in crack length, a, and applied stress, S.

The seperable form allows the crack length dependent terms in Eq. 7 to be brought over to the left hand side. The lack of sequence effects makes the summation over ΔS_{eff_i} independent of the order of application, allowing the summation to be replaced by an integral over the pdf of stress amplitudes (just as was done in the crack initiation case, Eq. 4). The result is

$$\int_{a_o}^{a_f} \frac{da}{c\left(\sqrt{\pi a} Y(a)\right)^b} = N \int_0^\infty p_e(S) \Delta S_{eff}{}^b dS \tag{8}$$

where ΔS_{eff} is a function S.

Contrary to popular opinion, the nonlinear nature of the crack growth equation is not responsible for sequence effects in crack growth prediction — the order of application does not affect Eq. 8 [12,13]. Sequence effects will be included in the crack growth prediction if the model includes the influence of one stress cycle on subsequent effective stress ranges, as discussed in the next section.

Sequence effects in crack growth The theoretically infinite stress concentration at a crack tip demands that there be a crack-tip plastic zone, as shown schematically in Fig. 2. The inelastically stretched material at the crack tip is compressed upon unloading by the bulk of the material, which remains elastic. The residual strain of material that has been failed in the wake of the crack growth also acts as a wedge behind the crack tip resulting in additional compression. The larger the tensile load, the greater the extent of the plastic zone and the greater the clamping action on the crack tip when the load is removed. The nominal (tensile) stress at which compression at the crack tip is relieved and the crack begins to open is called the crack-opening stress, S_{op}. The effective stress range for crack growth is the difference between the maximum applied stress, S_{max}, and the crack-opening stress or the minimum stress, S_{min}, whichever

is higher.

$$\Delta S_{eff} = \begin{cases} S_{max} - S_{op} & S_{max} > S_{op} \geq S_{min} \\ S_{max} - S_{min} & S_{min} \geq S_{op} \\ 0 & S_{op} \geq S_{max} \end{cases} \quad (9)$$

Whether sequence effects are included in the crack growth model or not depends on how S_{op} is determined.

One simple model neglects load sequences by assuming that the crack-opening stress is a fraction, q, of the current load peak [14].

$$S_{op} = qS_{max} \quad (10)$$

where q is determined from constant amplitude testing. Here, q can be approximated as a constant, although it is usually treated as a function of stress ratio [15] and maximum stress [16,17].

This sequenceless model is a clearly inaccurate approximation to the crack-closure phenomenon; changes in S_{op} will endure long after the current cycle. Occasional tensile overloads will increase the crack-opening stress, reducing ΔS_{eff} and retarding the crack growth rate, while compressive overloads remove the crack tip compression, lowering the crack-opening stress and accelerating crack growth. But the sequenceless model can be a very useful tool when a simple, yet conservative, crack growth estimate is needed. For a narrow-band Gaussian loading with a mean stress level of m_s, the extremes of each cycle are $S_{max} = m_s + S$ and $S_{min} = m_s - S$. Equation 8 can be numerically integrated to estimate the number of cycles needed to grow from a_o to a_f, without the need to add up crack growth cycle-by-cycle. Over typical lives of millions of cycles, the computational savings is substantial.

Although the effect of a tensile overload on the subsequent crack-opening stress is fairly complex, a simplified crack-growth model that preserves the net sequence effect, without precise duplication of all the mechanisms, has been proposed [15]. The model defines the crack opening stress to be the same fraction q of a *reset stress*, S_r, which is the stress necessary to *reset* the maximum extent of crack-tip plasticity.

$$S_{op} = qS_r \quad (11)$$

Figure 2 schematically illustrates the plastic zone resulting from a tensile overload at a crack length of a_{ol}. Immediately following a tensile overload, the reset stress is equal to the overload because a stress peak of equal size would be required to produce a plastic zone of equal extent. As the crack grows into the plastic zone, as shown by the dashed line in Fig. 2, the reset stress decreases because the size of the crack-tip plastic zone required to reset the maximum extent has been reduced from d_{ol} to d_p. (See Ref. 15 for a more detailed description of the reset stress and the crack-growth model.)

This formulation no longer permits the use of Eq. 8 to calculate the number of cycles to grow from one crack length to another. Crack growth must be summed cycle-by-cycle, as in Eq. 7, while continuously updating d_p, S_r, and ΔS_{eff} as the crack grows through each crack-tip plastic zone.

The results of crack growth calculations using the above model are compared to American Society for Testing and Materials (ASTM) [18] test results in Fig. 3. The ASTM loadings consist of published tables of sequential peaks and valleys taken from typical fighter aircraft wing loadings during four types of missions:

- AA — Air-to-Air mission
- AG — Air-to Ground mission
- IN — Instrumentation and Navigation
- CF — Composite Fighter

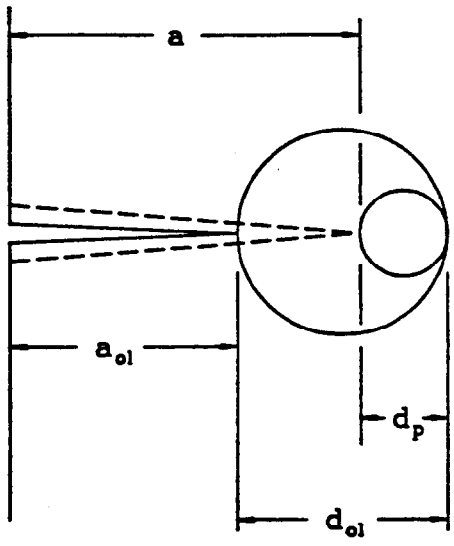

Figure 2: Schematic of the crack tip plastic zone caused by a tensile overload, S_{ol}, at a crack length of a_{ol}. After the crack has grown into the plastic zone (dashed lines) the *reset stress*, S_r, is the stress necessary to create a plastic zone larger than d_p.

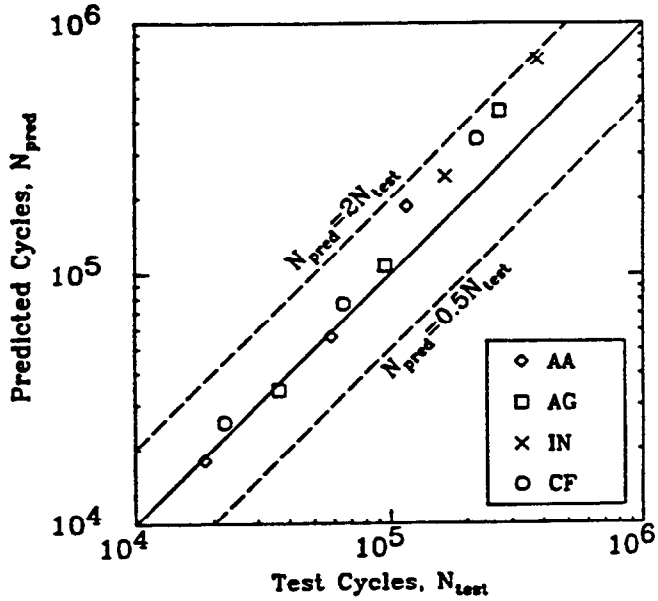

Figure 3: Predicted cycles to failure using the crack closure model vs test cycles to failure for the ASTM test series.

All of the loadings are slightly non-Gaussian and relatively wide band.

The predictions using the above reset stress model agree very well with the test results, especially at shorter lives. The longer test lives are slightly overestimated, a trend that has been attributed to a poor fit of crack growth data at low stress levels [18]. The test material is 2219-T851 aluminum, with estimated material properties: $b = 3.64$, $c = 3.1 \times 10^{-9}$, with stress in ksi and crack length in inches. Similar agreement with test results were also obtained (see Ref. [15]) in comparisons with test results published by the Society of Automotive Engineers [19] using ground vehicle load histories and steel specimens.

Predictions of the same ASTM test results were conducted using the sequenceless crack growth model (Eq. 10), both with the published tables of stress peaks and valleys and by using the Rayleigh distribution of amplitudes (Eq. 3) with successive peaks and valleys equal to $m_s \pm S$. The results are shown in Fig. 4. Two important observations should be made. First, the sequenceless predictions using the actual tabulated load histories are conservative and within a factor of two of the test results. Second, the Rayleigh results are conservative with respect to the actual loadings, but again by less than a factor of two.

More extensive simulation studies show that these observations are the usual case in stationary Gaussian loadings [15]. Crack growth predictions using the above sequenceless model will be conservative — usually by less than a factor of two — except when the mean stress is compressive. In wind turbine applications, a compressive mean stress in one location is usually accompanied by a location (on the other side of the blade) with equal stress ranges and a tensile mean stress, which is a much more damaging loading. The narrow-band Gaussian assumption therefore provides a quick estimate of crack growth (Eq. 8) that is conservative and within the usual scatter in material fatigue properties.

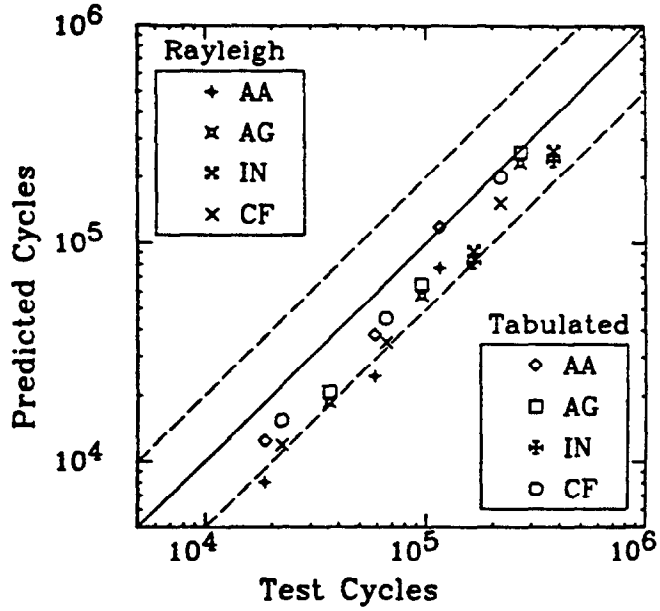

Figure 4: Predicted cycles to failure using the sequenceless crack growth model, with the actual "Tabulated" test loading and with the "Rayleigh" narrow-band approximation.

WIND TURBINE STRESSES

Horizontal Axis Wind Turbines (HAWTs) and Vertical Axis Wind Turbines (VAWTs) have different blade orientations and operating conditions. They do, however, share some common loading characteristics. Both tend to have harmonic response in the edgewise, or stiffer, blade bending direction — in HAWTs due to gravity loads and wind shear, and in VAWTs due to the cyclic orientation of the blades with respect to the wind. Both tend to have flatwise, or flapwise, loading that is more influenced by turbulence, resulting in significant response at the blade natural frequencies.

The fatigue life of wind turbine components can be estimated relatively quickly with the above methods if the stresses are well approximated as stationary, narrow-band, Gaussian processes. Each of these conditions is violated in some degree by the operating stresses in both HAWT and VAWT blades. The following sections describe the extent that these violations affect predictions using the simplified fatigue models in wind turbine applications.

Nonstationary Response

Just as the winds that drive the wind turbine are constantly changing, the level of wind turbine response will also be constantly changing. The stresses are clearly nonstationary; the RMS stress level fluctuates with the mean wind speed as averaged over the turbine rotor. If there are no sequence effects, the fatigue damage (or crack growth) can be estimated by simply summing the damage (or crack growth) at each RMS level, followed by a summation over the time spent at each RMS level [20]. Estimating fatigue damage by the sequenceless method (Miner's rule) is conservative as long as the fatigue limit is eliminated from the S-n curve (as shown by the dashed line in Fig. 1 and discussed earlier). For crack-growth predictions, however, the sequenceless approximation can deteriorate when the loading becomes significantly nonstationary [15].

The length of time over which the RMS level remains highly correlated (relatively constant) is called the RMS correlation time, which, for wind turbine applications, is the same as the wind speed correlation time. Rapidly changing RMS levels are associated with short correlation times, while slowly varying RMS levels have long correlation times. Simulations of nonstationary processes have been generated with the RMS changes ranging from very rapid to very slow. The simulated processes were used as stress histories to drive crack growth calculations with both the sequenceless crack growth model and the model that includes sequence effects. The ratios of the resulting number of cycles to grow the crack to the final crack length (cycles without sequence effects divided by cycles with sequence effects) are shown in Fig. 5. Both the average ratio and the average plus three standard deviations are plotted.

When the correlation time of RMS fluctuations is short, the average ratio can be very small, implying overly conservative sequenceless predictions. However, there can be substantial scatter about the mean, which tends to grow as the correlation time increases. When the correlation time is a large portion of the total crack growth time, the variation about the mean leads to small probabilities that the ratio will approach, or even exceed, unity (no conservatism), even though the average ratio is quite

small (high conservatism). Wind turbine RMS levels are correlated for the same amount of time as the average wind speed — on the order of an hour. The number of cycles depends on the operating speed and natural frequencies of the rotor, but an hour should be much less than the total crack-growth life. A sequenceless crack growth analysis is therefore an appropriate calculation to maintain a conservative crack growth estimate when there is limited data on wind turbine loads, or only an approximate crack growth estimate is needed.

Narrow-Band Approximation

The frequency content of wind turbine stresses will never have the classic narrow-band character of a single degree of freedom system. Several modes are likely to be present in addition to the harmonic content at integer multiples of the rotational frequency. However, most of the response is limited to a *relatively* narrow range between one and five per rev, and often between one and three per rev. Although this may sound like a wide band, genuinely *wide-band* response includes energy at much more diverse frequencies. The most wide-band response is expected in small HAWTs, which may have proportionately more flapwise response at very low frequencies due to quasi-static response to turbulence.

Wirshing and Light [21] and Lutes, et al. [22] have shown that the narrow-band approximation is conservative with respect to wider-band Gaussian loadings. They define the rate of cycles (average frequency) to be equal to the rate of mean level crossings with positive slope (up-crossings). The rate of up-crossings can be calculated from the power spectral density (PSD) by taking the square root of the second moment about zero frequency divided by the variance (see Ref. 5, pp. 44-53). Wide-band loadings actually have many more cycles than mean crossings, but the difference is more than made up for with the increased cycle amplitudes in the narrow-band approximation.

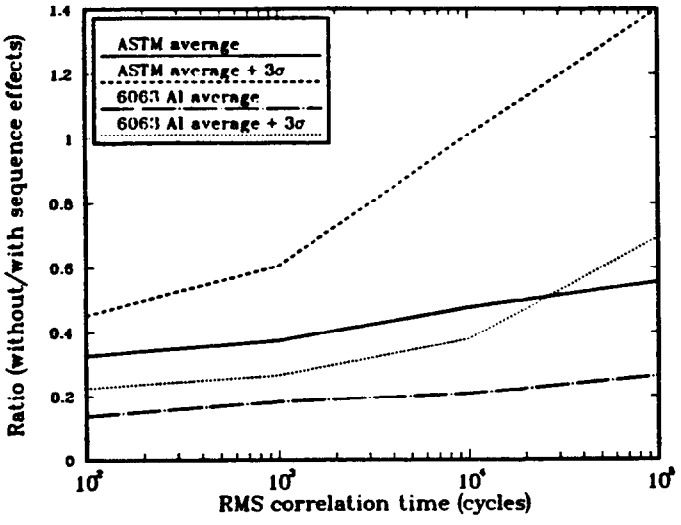

Figure 5: Ratio of predicted crack growth lives due to nonstationary loading. Predictions without sequence effects are divided by those with sequence effects for the ASTM material (2219-T851 Al) and a common VAWT blade material (6063-T6 Al). Both the average ratio and the average plus three standard deviations are plotted.

Wind turbine response deviates from ideally narrow band much less than the examples shown in the above references, which at worst resulted in narrow-band approximations for fatigue life a factor of 2 less than the exact calculations. The narrow-band approximation for most wind turbine applications would yield fatigue life predictions in the neighborhood of 10 to 30 percent too short. (For small HAWTS, the conservatism due to bandwidth could approach the maximum of a factor of 2.)

Non-Gaussian Behavior

A Gaussian process is the natural result of the response of a linear system to Gaussian loading. Even though incident wind speed is a Gaussian process [23], wind turbine loading is contaminated by harmonics of the turbine operating speed — in HAWTs by wind shear and yaw errors, and in VAWTs due to the inherent cyclic blade orientation. Holley and Madsen [2] studied harmonic additions in conjunction with band-width effects. They showed that the error produced by the combination of wide-band response and this non-Gaussian behavior is less than 40%. For narrow-band loadings, the addition of the the harmonic content never produced fatigue life prediction differences greater than 10%.

Deviations from Gaussian behavior are also possible when the loading or structural stiffness are asymmetric, both of which lead to non-Gaussian *skewness*. VAWTs are subject to skewed loading because the blades pass through the shadow of the upwind blade passage, making the loading slightly asymmetric. Fortunately, skewed loadings do not affect stress range distributions, which determine crack initiation. Crack growth is sensitive to peak distributions, which will be affected, but there is no literature specifically related to skewed non-Gaussian peak distributions.

Symmetric nonlinearities, which lead to non-Gaussian *kurtosis*, influence the range distributions as well as peak distributions. Lutes, et al. [22] have shown that loadings with non-Gaussian kurtosis, such as drag forces from ocean waves, can cause fatigue prediction errors as large as a factor of two (in either direction) for reasonable amounts of nonlinearity. VAWT flatwise blade stresses are almost surprisingly well approximated by the Rayleigh pdf [20,24]. Flapwise responses in large HAWTs are also likely to be approximately Gaussian, being dominated by linear modal response to broad band wind excitation.

SUMMARY

Wind turbine stress histories are inherently nonstationary, but can easily be divided into stationary segments over short periods of time. As the mean wind speed changes, the RMS stress level also changes. The rate of damage accumulation or crack growth during each stationary period can be estimated using Eqs. 5 or 8, respectively, providing three constraints are satisfied:

1. there are minimal loading sequence effects,
2. the stresses can be approximated as narrow-band Gaussian and
3. the crack growth equation is separable in crack length and stress amplitude.

Overall damage or crack growth is calculated with a second integration over the wind speed distribution [20].

Sequence effects can be eliminated from consideration in fatigue damage (crack initiation) analysis as long as the fatigue limit is also removed from the S-n curve, as shown in Fig. 1. The main exception is in the case of occasional compressive overloads in a region of nominal tensile operating stresses. The sequenceless crack growth model presented here is conservative, but usually within a factor of two of more complicated prediction methods. One notable exception for wind turbine crack growth is that variable RMS levels can cause the model to be excessively conservative on average, although there is a small probability that for any single loading the conservatism will be greatly reduced.

Wind turbine loadings will not be perfectly Gaussian or narrow band, but these effects are small when compared to the inherent variability in material fatigue properties. In most cases, the narrow-band Gaussian approximation is conservative and well within a factor of two of the damaging potential of the actual loading.

Although the calculation methods outlined here involve substantial approximations, they are useful tools for evaluating competing design alternatives, especially when there is limited data availible on turbine stresses. As the design becomes solidified and prototypes are built, more sophisticated fatigue analysis methods will likely replace these approximations. But these methods should enable the designer to bring fatigue analysis into the early-design decision-making process.

REFERENCES

1. ASCE, "Fatigue and Fracture Reliability: A State-of-the-Art Review," *J. Structural Div., ASCE,* Vol. 108, No. ST1, January, 1982.

2. Holley, W.E., and P.H. Madsen, "A Method for Estimating the Fatigue Damage Rates for Wind Turbine Structures," Proc., 4th *ASME Wind Energy Symposium,* Dallas, TX, 17-21 February 1985.

3. Miner, M.A., "Cumulative Damage in Fatigue," *J. Applied Mechanics, Trans. ASME,* Vol. 67, September, 1945.

4. Abramowitz, M., and I.A. Stegun, *Handbook of Mathematical Functions,* National Bureau of Standards, Applied Mathematics Series, No. 55, June, 1964.

5. Crandall, S.H., and W.D. Mark, *Random Vibration in Mechanical Systems,* Academic Press, New York, NY, 1963.

6. Cotrell, A.H., *Mechanical Properties of Matter,* John Wiley and Sons, New York, NY, 1969.

7. Brown, L.M., "Dislocations and the Fatigue Strength of Metals," *Dislocation Modeling of Physical Systems,* Pergamon Press, 1981.

8. Mitchell, M.R., "Fundamentals of Modern Fatigue Analysis for Design," *Fatigue and Microstructure,* ASM Material Science Seminar, St. Louis, MO, 14-15 October 1978, American Society for Metals, 1979.

9. Paris, P.C., and F. Erdogan, "A Critical Analysis of Crack Propagation Laws," *J. Basic Eng., Trans. ASME,* Vol. 85, 1963.

10. Elber, W., "The Significance of Fatigue Crack Closure," *Damage Tolerance in Aircraft Structures, ASTM STP 486,* American Society for Testing and Materials, 1971.

11. Jono, M., J. Song and A. Sugeta, "Prediction of Crack Growth and Crack Closure of Structural Materials under Random Loadings," *Advances in Fracture Research, ICF-6,* Vol. 3, Pergamon Press, Oxford, England, 1984.

12. Freudenthal, A.M. and E.J. Gumbel, "Physical and Statistical Aspects of Fatigue," *Advances in Applied Mechanics,* Vol. 4, 1956.

13. Orringer, O., "Rapid Estimation of Spectrum Crack-Growth Life Based on the Palmgren-Miner Rule," *Computers & Structures,* Vol. 19, No. 1-2, 1984.

14. Nelson, D.V., "Cumulative Fatigue Damage in Metals," Stanford University PhD Dissertation, March, 1978.

15. Veers, P.S., "Fatigue Crack Growth due to Random Loading," SAND87-2039, Sandia National Laboratories, Albuquerque, NM, November, 1987.

16. Schijve, J., "Some Formulas for the Crack Opening Stress Level," *Engineering Fracture Mechanics,* Vol. 14, 1981.

17. Newman, J.C. Jr., "A Crack Closure Model for Predicting Fatigue Crack Growth under Aircraft Spectrum Loading," *Methods and Models for Predicting Fatigue Crack Growth under Random Loading, ASTM STP 761,* American Society for Testing and Materials, 1981.

18. ASTM, *Methods and Models for Predicting Fatigue Crack Growth under Random Loading, ASTM STP 761,* Eds. J.B. Chang and C.M. Hudson, American Society for Testing and Materials, Philadelphia, PA, 1981.

19. SAE, *Fatigue Under Complex Loading: Analysis and Experiments, Advances in Engineering,* Vol. 6, Ed. R.M. Wetzel, Society of Automotive Engineers, Warrendale, PA, 1977.

20. Veers, P.S., "Blade Fatigue Life Assessment with Application to VAWTs," *J. Solar Energy Engr., Trans. ASME,* Vol. 104, May, 1982.

21. Wirsching, P.H. and M.C. Light, "Fatigue under Wide Band Random Stress," *J. Structural Div., ASCE,* Vol. 106, No. ST7, July, 1980.

22. Lutes, L.D., M. Corazao, S-l.J. Hu, and J. Zimmermann, "Stochastic Fatigue Damage Accumulation," *J. Structural Div., ASCE,* Vol. 110, No. 11, November, 1984.

23. Prenninger, P.H.W. and G.I. Schuëller, "Stochastic Properties of Wind Spectra," Proc., 5th *ASCE Specialty Conference on Probabilistic Methods in Civil Engineering,* Blacksburg, VA, 25-27 May 1988.

24. Veers, P.S., "A General Method for Fatigue Analysis of Vertical Axis Wind Turbine Blades," SAND82-2543, Sandia National Laboratories, Albuquerque, NM, 1983.

Proceedings of the Eighth ASME Wind Energy Symposium
D. E. Berg and P. C. Klimas (ed.), SED-Vol. 7, ASME, January 1989

CRACK PROPAGATION ANALYSIS OF WECS COMPONENTS USING THE LIFE2 COMPUTER CODE*

H. J. Sutherland and L. L. Schluter
Wind Energy Research Division
Sandia National Laboratories
Albuquerque, New Mexico

ABSTRACT

The LIFE2 code is a fatigue/fracture analysis code that is specialized to the analysis of wind energy conversion system components. The code was originally developed by Sutherland, Ashwill and Naassan (1987). It is a PC-compatible Fortran code that is written in a top-down, modular format. This paper discusses the additions to the code that permit WECS components to be analyzed using linear fracture mechanics. To illustrate the capabilities of the numerical techniques employed here, two example problems are presented.

INTRODUCTION

The LIFE2 code is a fatigue/fracture analysis code that is being developed to analyze the service lifetime of a component for a wind energy conversion system (WECS). The code was originally developed by Sutherland, Ashwill and Naassan (1987). It is a PC-compatible Fortran code that is written in a top-down, modular format. The code has five principal sections. The first section describes the wind resource; the second describes the constitutive properties of the material; the third describes the operational stresses encountered by the system; the fourth describes the operational parameters of the system; and the last uses input from the first four sections with a damage rule to compute the service lifetime of the component.

In the initial form, the LIFE2 code was limited to fatigue analysis based on Miner's rule for damage accumulation. This paper describes the modules that have been added to this code to permit a linear fracture mechanics analysis of crack propagation of a WECS component. To illustrate the use of the new features of the code, two example problems are presented.

*This work was supported by the U.S. Department of Energy at Sandia National Laboratories under contract DE-AC04-76DP00789.

CONSTITUTIVE FORMULATION

Many constitutive equations have been proposed for the description of crack propagation in metallic materials. One general form for the crack propagation rate da/dn that has been proposed by Forman et al. (1986) is given by:

$$\frac{da}{dn} = \frac{C\,(1 - R)^m\,\Delta K^n\,[\Delta K - \Delta K_{th}]^p}{[(1 - R)\,K_c - \Delta K]^q} \quad , \qquad (1)$$

where a is the current crack length; n is the number of stress cycles; R is the stress ratio; ΔK is the change in the stress intensity factor K at the crack tip for cycle n; and the exponents C, m, n, p, q, ΔK_{th} and K_c are material constants.

As noted by Forman (1986) this formulation may be reduced to other commonly used forms by setting the exponents m, p and q to the values listed in Table I.

Table I. Specialized Values for the Exponents in Eq. (1).

Proposed Constitutive Relation	Exponent		
	m	p	q
Paris	0	0	0
Forman	0	0	1
Walker	$(m_w-1)n$	0	0

In Table I, m_w is a material constant. The material constants for this formulation have been listed by Forman (1986) for a selected set of materials.

To illustrate the use of this formulation and to verify our implementation of it in the LIFE2 code, the material constants for 300M steel were input into the code. The resulting constitutive properties are shown in Fig. 1. Here we have chosen to plot the crack growth rate for constant values of R [Note: this plot is equivalent to the example plot provided by Forman (1986)].

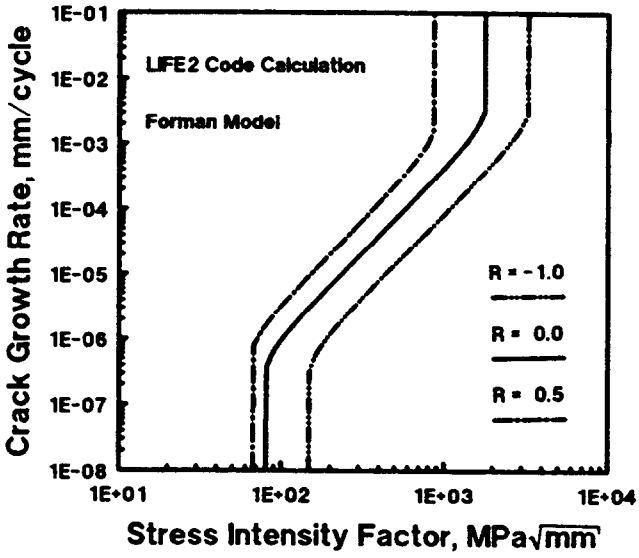

Fig. 1. Crack Growth Rate for 300M Steel.

SERVICE LIFETIME

To determine the service lifetime of a WECS component using linear fracture mechanics requires that the crack propagation rate da/dn be integrated over all stress cycles; namely,

$$a_f - a_o = \int_0^N (da/dn)\, dn \quad , \qquad (2)$$

where a_o is the initial crack size, a_f is the final crack size, and N is the total number of stress cycles. This formulation has been incorporated into the LIFE2 code as one of the "damage rules" for the determination of the service lifetime of a WECS component. The numerical technique employed here to implement this rule assumes the integral in Eq. 2 may be divided into a finite number of steps. Each step is evenly spaced, on a logarithmic scale, between a_f and a_o. For each step, or integration segment, the current crack length, a, is taken to be a constant that is centered in the segment. An average crack growth rate is determined for each segment by integrating (again using a finite sum) the constitutive formulation [e.g., Eq. (1)] over all stress cycles and over the wind spectrum. This average crack growth rate is then used to determine the time (number of stress cycles) required for the crack to grow across that integration segment. The sum over all of the integration segments yields the time for growth from a_o to a_f.

EXAMPLE PROBLEMS

The analysis and constitutive equations cited above have the ability to describe the propagation characteristics of a macro-crack. They do not describe the initiation of cracks and their initial propagation. This section presents two example problems. In both, we will assume that a macro-crack is contained in the structure when the analysis begins.

Welded Aluminum Joint: Sutherland and Ashwill (1987) presented a fracture analysis of a proposed joint for a 6063 aluminum VAWT blade that had been fatigue tested in a laboratory. Although this class of aluminum joints proved to be inadequate for this application, the data obtained from the fatigue experiments offer a unique data set for the verification of analytical techniques based on fracture mechanics. Here, we present the original analysis and an equivalent analysis using the LIFE2 code so that the two analyses may be compared to one another.

The basic design of the joint used a 6063 aluminum extruded airfoil section that was butt welded to a flange. Blade sections were then to be bolted together using the flange. To test this design, several prototype joints were fabricated and tested under cyclic loading (Mitchell and Murphy, 1986). As cracks developed in the joint, their length was monitored as a function of the number of applied stress cycles. Post-test inspections showed that the weld material had not penetrated the joint fully. Initial flaws were measured to be on the order of 2.5 mm (0.10 in). Final crack sizes of 10.2 mm (0.4 in) are reported here.

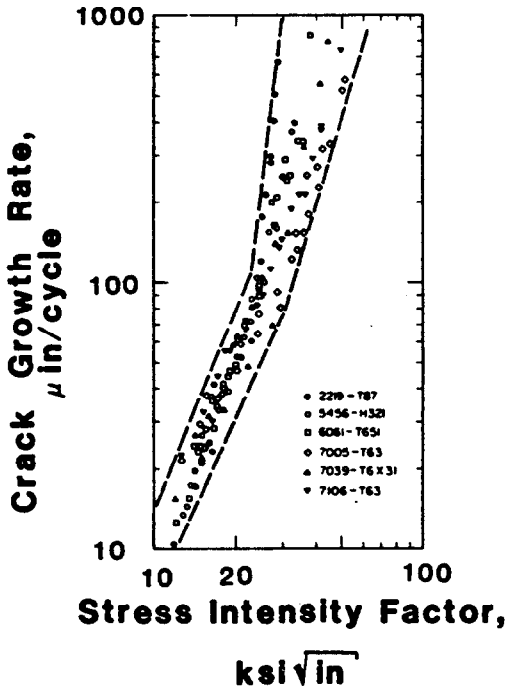

Fig. 2. Fracture Mechanics Characterization for Aluminum Alloys.

These data were analyzed by Sutherland and Ashwill (1987) using the generalized constitutive properties for aluminum shown in Fig. 2 (Rolfe, and Barsom, 1977). The stress intensity factor K chosen for their analysis of the joint is given by the relation (Hertzberg, 1977):

$$K = \sigma \sqrt{\pi a}\ C_W / C_Y \quad , \qquad (3)$$

where σ is the nominal stress in the joint, a is the crack length, and C_W and C_Y are correction terms for a finite width plate and the yield stress σ_Y, respectively. The correction terms are given by:

$$C_W = \sqrt{\sec(\pi a/W)} \quad , \qquad (4)$$

where W is the width of the plate, and,

$$C_Y = \sqrt{1 - 0.5\ (\sigma/\sigma_Y)} \quad . \qquad (5)$$

The results of Sutherland and Ashwill (1987) are plotted with the experimental results of Mitchell and Murphy (1986) in Fig. 3. In this figure, the upper and lower bounds from Fig. 2 have been used to calculate the number of cycles required to propagate the crack to its final length of 10.2 mm (0.4 in). The results are plotted for initial crack sizes of 2.5 mm (0.10 in) and 3.8 mm (0.15 in). As seen in Fig. 3, the upper and lower bounds converge to one another as the stress level decreases. This convergence is a result of the extrapolation of the constitutive relations shown in Fig. 2 to lower stress concentration factors. Namely, the upper and lower bounds cross each other at a stress intensity factor of approximately 12.5 Mpa$\sqrt{m}$ [0.361 ksi$\sqrt{in}$] and a crack growth rate of approximately 9.18E-8 mm/cycle (3.61E-3 μin/cycle).

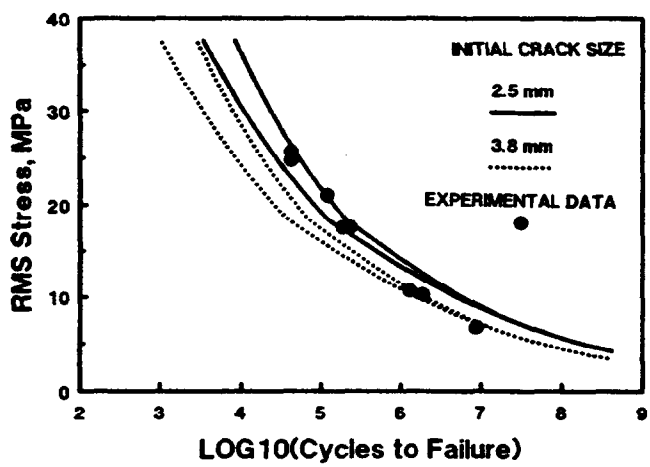

Fig. 3. Initial Crack Propagation Calculations for the Welded Aluminum Joint.

To permit a direct comparison of the results from these two analyses, these calculations were duplicated, as closely as possible, using the LIFE2 code. As seen in Fig. 4, the results are essentially identical. For the high stress values (above 30 MPa), there are some slight changes in the position of the curves. These changes reflect the differences in the numerical implementation of Eqs. (3), (4) and (5), the numerical integration used to evaluate Eq. (2).

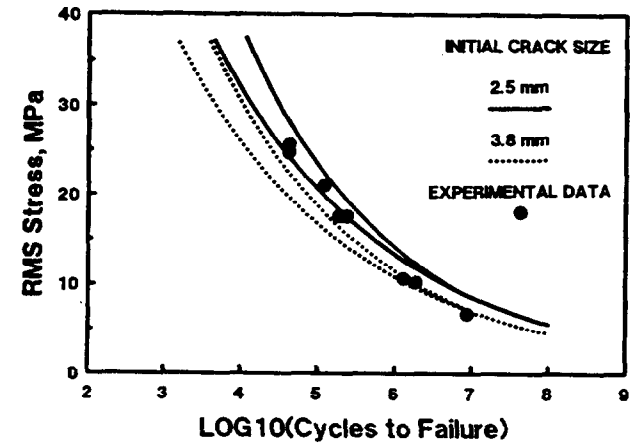

Fig. 4. LIFE2 Crack Propagation Calculations for the Welded Aluminum Joint.

17-m VAWT Blade Joint Analysis: To further illustrate the use of this code, consider the vertical axis wind turbine (VAWT) blade joint analysis performed by Sutherland, Ashwill and Naassan (1987). In this analysis, the lower blade joint on the DOE 100-kW Low Cost VAWT was analyzed using the fatigue analysis capabilities of the LIFE2 code. In the analysis, the mean stress on the joint was taken to be 48.3 MPa (7 ksi). The root mean square (RMS) of the vibratory stresses is described as a function of wind speed in Fig. 5 (Lobitz and Sullivan, 1984). A Rayleigh distribution was used to describe the distribution of the operating stresses at each wind speed for these RMS stress values (Veers, 1983). The stress concentration was taken to be 2.73. The wind regime was assumed to have a Rayleigh distribution with a mean velocity of 6.26 m/s (14 mph). The probability distribution function for the wind regime and the damage are plotted in Fig. 6 [Note: these functions were originally reported by Sutherland, Ashwill, and Naassan (1987)]. The code predicted a service lifetime of 13.9 years when the machine was operated between 4.47 m/s (10 mph) and 20.1 m/s (45 mph).

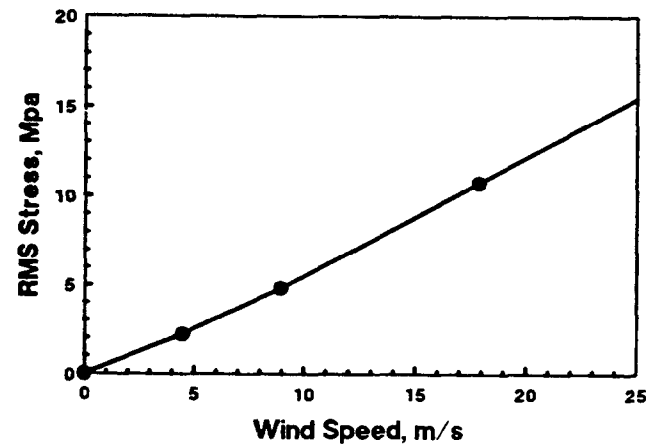

Fig. 5. Vibratory Stresses vs. Wind Speed for the DOE 100-kW Low Cost VAWT.

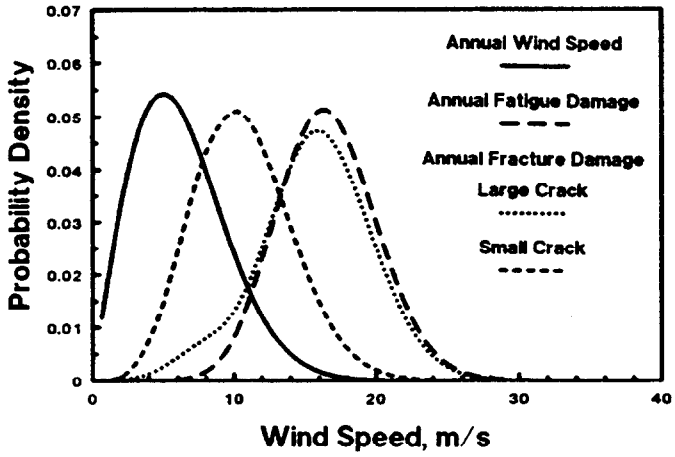

Fig. 6. Probability Density Functions for the DOE 100-kW Low Cost VAWT.

The same problem was analyzed with the fracture modules of the LIFE2 code. The initial analysis used the wind spectrum, operational stresses, and operational parameters from the fatigue analysis cited above. The upper bound for the constitutive equation cited in Fig. 2 was used to describe the fracture behavior of aluminum. The stress concentration at the crack tip was analyzed using Eq. (3). The correction terms C_W and C_Y were set equal to one for this analysis. Assuming that the joint contains a crack that was 0.0254 mm (0.001 in) in length and that the annual wind speed distribution was acting on the turbine, the analysis predicted that the crack length would increase with time as described in Fig. 7. As seen in this figure, this crack will reach catastrophic size in 66.8 days. If the size of the initial crack is assumed to be 0.254 mm (0.01 in), then the time to catastrophic failure is reduced to 34.7 days. As seen in Fig. 7, this time to failure is equal to the total time of failure for the 0.0254 mm (0.001 in) crack less the time required for the crack to grow from 0.0254 mm (0.001 in) to 0.0254 mm (0.01 in); i.e., 66.8 days minus 32.1 days. Because the upper bound of crack propagation rate was used in these calculations, the times presented here represent the minimum time to failure, as predicted by the constitutive relation described in Fig. 2.

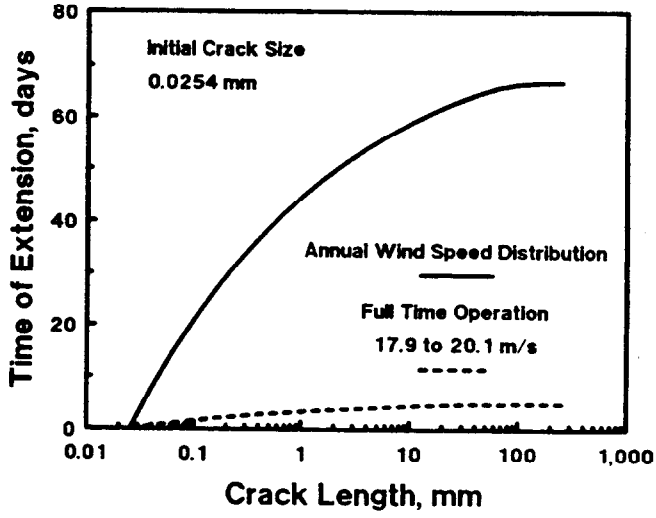

Fig. 7. Time of Extension for a Crack Propagating in the DOE 100-kW Low Cost VAWT.

As one would not expect the annual wind speed distribution to be applicable to such a short period of time, the growth of the crack was also investigated for a continuous wind whose speed varied uniformly from 17.9 m/s (40 mph) to 20.1 m/s (45 mph). This analysis yields a time of extension to catastrophic failure of 4.9 days for an initial crack of 0.0254 mm (0.001 in), see Fig. 7. For an initial crack of 0.254 mm (0.01 in), the time to failure is reduced to 2.4 days.

As discussed by Veers [1988], the service lifetime of a component can be divided into three phases: 1) crack initiation, 2) growth and coalescence of micro-cracks and 3) growth of a macro-crack. The test specimens used for fatigue life calculations (S-n analysis) usually describe the first two phases and fracture analyses the third phase. Thus, based on these calculations, the total service life of this blade component will be 13.9 years plus the time for the macro-crack to grow to catastrophic size; i.e., 66.8 days or 4.9 days, depending on the operational wind spectrum.

As seen in Fig. 7, the time of extension is a non-linear function. The non-linearity of this analysis also is observed in the rate at which damage is accumulated. As shown in Fig. 6, the damage accumulation rate for a fracture analysis has a similar form (shape) to that determined by the fatigue analysis. However, the size of the crack and the constitutive equation chosen for the aluminum influences the position of the distribution with respect to wind speed. As shown in Fig. 6, the damage distribution function for a small crack [for the calculations presented here, a small crack is one that is of the order of 0.254 mm (0.01 in)] has its maximum at approximately 10 m/s (23 mph). For a large crack [of the order of 250 mm (10 in)], the maximum of the distribution located at approximately 15.5 m/s (35 mph). These values compared closely to 16 m/s (36 mph) for the maximum of the damage density spectrum that was determined for the blade joint using the fatigue analysis capabilities of the LIFE2 code.

This result is not surprising. In the fatigue analysis of a VAWT blade component presented by Veers (1983), the position of the maximum of the damage distribution function is shown to be a function of the slope of the constitutive formulation. Thus, for the analysis presented here, the position of the maxima for a "small crack" is dominated by the slope of the da/dn curve at relatively low propagation rates [i.e., below 2.54E-3 mm/cycle (100 μin/cycle) in Fig. 2]. For a "large crack", its position is dominated by the slope at relatively high propagation rates [i.e., above 2.54E-3 mm/cycle (100 μin/cycle) in Fig. 2].

This fracture analysis suggests that the service lifetime of this WECS component is relatively short once a crack is present. If the turbine is being operated in relatively moderate winds, a monthly inspection program would permit the detection of a crack before catastrophic failure would occur. However, in relatively high wind conditions, the inspection program would have to be conducted daily to insure detections before catastrophic failure.

CONCLUDING REMARKS

The LIFE2 code is being written as a design tool for the wind turbine industry. With the addition of the fracture analysis modules described here, the code is capable of doing both fatigue and fracture mechanics analyses of WECS components. Two example problems, which examine a metallic material and VAWT components, are presented here. They were chosen to illustrate the current capabilities of the code. Also, the choice of these two examples was based on the availability of experimental data for the analysis. However, the LIFE2 code can also be used to analyze other WECS components and other materials. Input modules currently available in the code permit direct inputs of other constitutive formulations, stress histories, operating parameters and wind spectrum. And, with its modular format and inherent versatility, additional computational capabilities may be added to the code as they are identified, without changing the main body of code.

REFERENCES

Forman, R. G., 1986, Derivation of Crack Growth Properties of Materials for NASA/FLAGRO, NASA, Materials Branch Report 86-ES5-1.

Forman, R. G., et al., 1986, Fatigue Crack Growth Computer Program "NASA/FLAGRO," NASA, JSC-22267.

Hertzberg, R. W., 1977, Deformation and Fracture Mechanics of Engineering Materials, Wiley, New York.

Mitchell, M. R., and Murphy, A. R., 1986, Fatigue Behavior of Vertical Axis Wind Turbine Airfoils with Two Weld Configurations, Contract Report No. 47-4155, Sandia National Laboratories, Albuquerque, NM 87185.

Rolfe, S. T., and Barsom, J. M., 1977, Fracture and Fatigue Control in Structures, Applications of Fracture Mechanics, Prentice-Hall, New Jersey, p. 244.

Sutherland, H. J., and Ashwill, T. D., 1987, "Fatigue Life Prediction for VAWT Components Using the LIFE Codes," Proceedings of the Sixth ASME Wind Energy Symposium, R. W. Thresher (ed.), ASME, pp. 193-195.

Sutherland, H. J., Ashwill, T. D., and Naassan K. A., 1987, "Fatigue Analysis Codes for WECS Components," Proceedings of Wind Power '87, American Wind Energy Association, SERI/CP217-3315, pp. 298-308.

Veers, P. S., 1983, A General Method for Fatigue Analysis of Vertical Axis Wind Turbine Blades, SAND82-2543, Sandia National Laboratories, Albuquerque, NM 87185.

Veers, P. S., 1988, Simplified Fatigue Damage and Crack Growth Calculations for Wind Turbines, Proceeding of the 8th ASME Wind Energy Symposium, ASME, in publication.

Proceedings of the Eighth ASME Wind Energy Symposium
D. E. Berg and P. C. Klimas (ed.), SED-Vol. 7, ASME, January 1989

MODEL VALIDATION OF THE SANDIA 34-METER TEST BED TURBINE USING SUBSTRUCTURED MODAL-TESTING*

T. G. Carne, J. P. Lauffer, A. J. Gomez, and T. D. Ashwill
Sandia National Laboratories
Albuquerque, New Mexico

ABSTRACT

The Sandia 34-Meter Test Bed Turbine is a vertical-axis wind turbine, thirty-four meters in diameter, designed to provide a test-bed for research in aerodynamics, structures and control. In order to design a large wind turbine, knowledge of the modal frequencies and mode shapes is essential for predicting structural response. During the design, analytical or finite element models are utilized for estimates of these modal parameters. However, when hardware becomes available, modal testing can be used to verify or update the models. The concept of substructure modal testing was developed for the Sandia 34-Meter Test Bed in order to more fully evaluate the accuracy of the finite element model. Instead of performing only one test on the entire turbine, separate tests and analyses were performed on major substructures of the turbine, including three separate blade sections, the tower supported by the guy cables, and the entire turbine. The results were then compared to analytical predictions from the finite element models of the substructures and the entire turbine.

INTRODUCTION

In the design of a large flexible wind turbine, knowledge of the modal frequencies and mode shapes is essential for predicting structural response and fatigue life. During the design process, analytical models must be depended upon for estimates of the modal parameters. When the turbine hardware becomes available for testing, the actual modal parameters can be experimentally determined. These measured data can be used to update the analytical predictions or modify the model.

The analytical model is a critical design tool because it is used to predict fatigue life, evaluate operational constraints (wind speed and rotation speed), and guide redesign if needed. The model can also include the effects of a rotating coordinate system in the calculations [1]. Consequently, verification of the model with test data is very

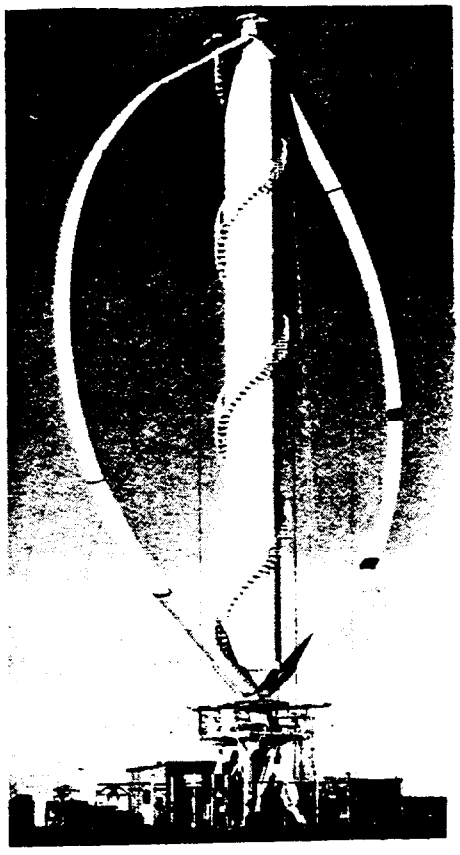

Figure 1. Sandia 34-Meter Test Bed

*This work was supported by the U.S. Department of Energy under Contract DE-AC04-76DP00789

important, and this is ordinarily performed after the turbine is assembled. Typically, results of a modal test on the entire turbine are compared with predictions from the model. If the agreement is acceptable, then the verified model can be used with assurance of reasonable accuracy. However, if there are some discrepancies between the test results and the analytical predictions, then determining where the model is inadequate and improving it can be a most difficult problem.

The concept of verification through substructure modal testing can be used to alleviate this problem. With this concept the structure is divided into substructures, usually major portions of the structure, and then each of these substructures are individually tested and their models verified. If possible, some substructures can be further assembled; these combined substructures tested; and their models verified. Using this technique, any inadequacies in the models are discovered at the substructure level. If all the substructures have verified models and if there still are any discrepancies between the test data and analytical results for the entire turbine, then the problem can be isolated to the modeling of the joints which connect the substructures.

The 34-Meter Test Bed is rated at 500 kW at 37.5 rpm and has a thirty-four meter diameter rotor and a total height of fifty meters. The entire rotor, including the central column and the two slender curved blades, rotates on bearings. The top of the rotor is supported by guy cables through a bearing.

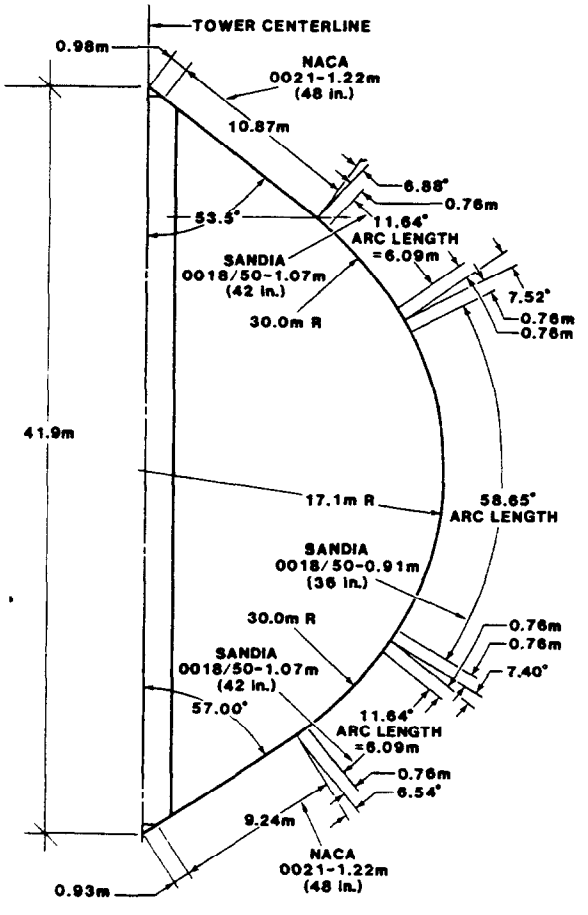

Figure 2. Diagram of Blade Sections

Figure 1 is a photograph of the completely assembled turbine. Each blade consists of five different blade sections with different chords and airfoils. These sections are constructed from extruded 6063-T6 aluminum, and cold bent to the appropriate radius of curvature. Figure 2 shows a diagram of the assembled blade with the five sections indicated. The center blade section has a seventeen meter radius and a 0.91 meter chord and is approximately 17.5 meters long. The center section is connected on both ends to intermediate sections which have a thirty meter radius and a 1.07 meter chord, and are approximately six meters in length. Lastly, there are top and bottom sections which are straight with a 1.22 meter chord and approximately eleven meters long. Reference [2] describes the design and fabrication of the turbine in more detail.

For the Test Bed Turbine we have tested three different blade substructures, the column substructure supported by the guy cables and base, and finally the entire turbine. The blade substructures include both the center section and an intermediate section. These two sections were then joined and tested as a unit, creating a combined blade section over twenty-five meters long with one joint between the sections. These tests are described in the following Experimental Techniques section. The Results section contains a discussion of the analytical predictions as compared to the experimental results.

EXPERIMENTAL TECHNIQUES

To measure the modal frequencies and mode shapes of the various substructures, we have used the frequency response function (FRF) approach. In this approach one first measures the response of the structure as a function of frequency due to a force input at a driving point. Using a set of these FRFs, which represent the responses at all the points of interest on the structure, one can estimate the modal frequencies and mode shapes of the modes within the frequency range of the measurements. The type of input force can be fairly general, that is, it can be sinusoidal, random, or transient in nature, as long as it has sufficient frequency content over the frequency range of interest. Given the force input to the structure, the FRF can be measured with good accuracy provided that proper experimental techniques are utilized [3,4]. Once the FRFs are measured, there are many techniques that can be used to estimate the modal parameters [3-5]. The specific experimental techniques used for the individual substructures will be described in this section.

Blade Section Tests

For any modal test in which one wants to compare the results with analytical calculations, a key element is matching the boundary conditions in the test with that in the model. For the tests on the blade sections, this was the principal difficulty. For all three of the blade tests the sections were supported very softly with elastic cords to simulate free boundary conditions. Free boundary conditions are used in the experiment because they could be approximated in the laboratory, and are quite easy to include in the finite element model. As a rule of thumb, to simulate the free boundary conditions one would like the frequencies of the rigid-body modes of the structure on its support system to be less than ten percent of the frequency of the first elastic mode. Ideally, if one had truly free boundary

condition, then the rigid-body modes would all be at zero Hz.

The blade sections basically have two different types of modes, flatwise bending and edgewise bending. The flatwise modes involve bending normal to the chord of the blade (the flatwise or the soft direction) and consequently are much lower in frequency than the edgewise modes which involve bending in the same direction as the chord (edgewise or the stiff direction). See Figures 1 and 2 for details of the blades. By hanging the blade sections in a pendulum fashion so that the flatwise direction was normal to the pendulum support, we created a very soft or low-frequency support in the flatwise direction. In the edgewise direction the softness of the elastic straps was sufficiently low so that the highest edgewise rigid-body mode was well below the elastic edgewise modes. For example in the case of the center section, the first flatwise mode was at 2.17 Hz while the highest pendulum-type rigid-body mode was at 0.30 Hz. While this is higher than suggested by our rule of thumb, the effect of the support was further minimized by supporting the blade at the nodes of the first mode, so that the support had a negligible effect on the elastic mode frequency.

To measure the FRFs for the blade a transient force was input with a rubber-tipped sledge hammer, instrumented with a force transducer. Two sets of FRFs were measured using flatwise and edgewise excitation to insure that all the modes of interest were excited. Tri-axial measurements were made along both the leading and trailing edges of the sections using high output accelerometers.

Tower Test

The tower test was different from the blade tests in that we wanted to include the uncertain boundary conditions which the turbine base provide for the tower. This test was performed in the field on the erected tower supported at the top by the guy cables and the bottom by the turbine base. Figure 3 shows a photograph of the tower alone without the blades attached. The tower was instrumented with accelerometers normal to its axis along its length.

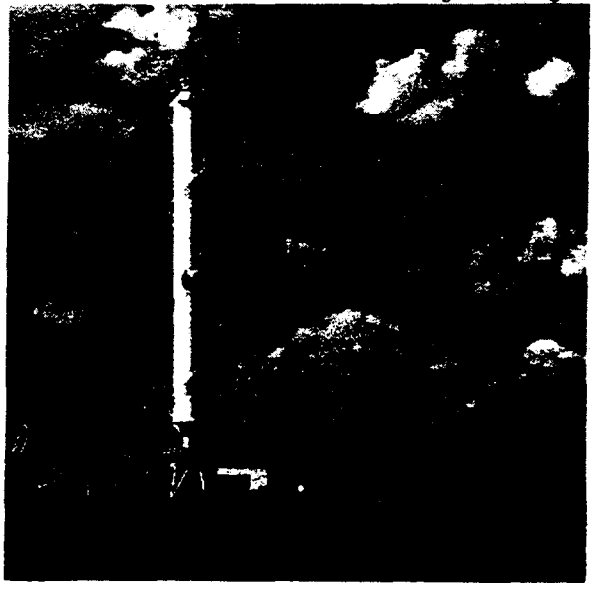

Figure 3. Tower Supported by Guy Cables

As in the blade test, a transient input force was used to excite the structure. However, in this case the transient was provided by suddenly cutting a steel cable tensioned to 45,000 N (10,000 lbs). The cable was attached near the middle of the tower, and then tensioned to the preload by a winch at the ground level. By suddenly cutting the cable, a step force is input to the structure. This force can be measured using a load cell in series with the cable. With this as the input, FRFs can be measured using techniques developed in [6]. This particular force input has a very desirable feature in that its frequency content is inversely proportional to frequency. This creates most of the energy at the very low frequencies and will excite the low frequency modes of the tower quite well.

Using this step force input (called step-relaxation), and the response accelerometers on the tower, a complete set of FRFs were measured. The mode shapes and frequencies for the tower were extracted from the FRF data, and these will be discussed in the Results section.

Turbine Test

Figure 4 displays front, top, and side views of the mode shapes for the entire turbine as computed using the finite element model. One can see that the mode shapes become fairly complex, although they typically involve only in-plane motion or out-of-plane motion, where the plane is defined by the undeformed blades and tower. These mode shapes are for the parked turbine; for the rotating turbine the shapes vary with the rotation speed and couple with each other, [2].

For the modal test of the entire turbine, we used two different excitation techniques, step-relaxation, as discussed above for the tower, and wind excitation. This results in two separate modal tests. The wind excitation technique [7] was developed because there is a difficulty in performing step-relaxation testing of a wind turbine. This is due to the fact that the vibratory response induced by the wind on the blades may be large when compared to the response from the step input. The vibratory response due to the wind is uncorrelated with the step-relaxation force and has the same effect as noise on the response signal. This results in noisy estimates of the FRFs. Because modal parameters can not be accurately extracted from noisy FRFs, and because windless days could not be guaranteed, we performed a modal test of the turbine using wind as the excitation force. However, there was sufficient time when the winds were low, so a normal step-relaxation test could also be conducted.

Performing a modal test with wind excitation is similar to performing a step-relaxation test with some important differences. One significant difference is that the forces acting on the structure are not measured. We assume that these forces are random, broadband, and have sufficient energy content over the entire frequency range of interest. Additionally, we assume the the wind forces acting on the turbine do not have any holes or peaks in the frequency domain. Because the force can not be directly measured, we cannot calculate FRFs as is normally done in a modal test; instead, we measure auto- and cross-spectra between the response acceleration signals. From these spectra, using techniques developed in [7,8], the modal parameters including the modal frequencies, mode shapes, and modal damping can be extracted.

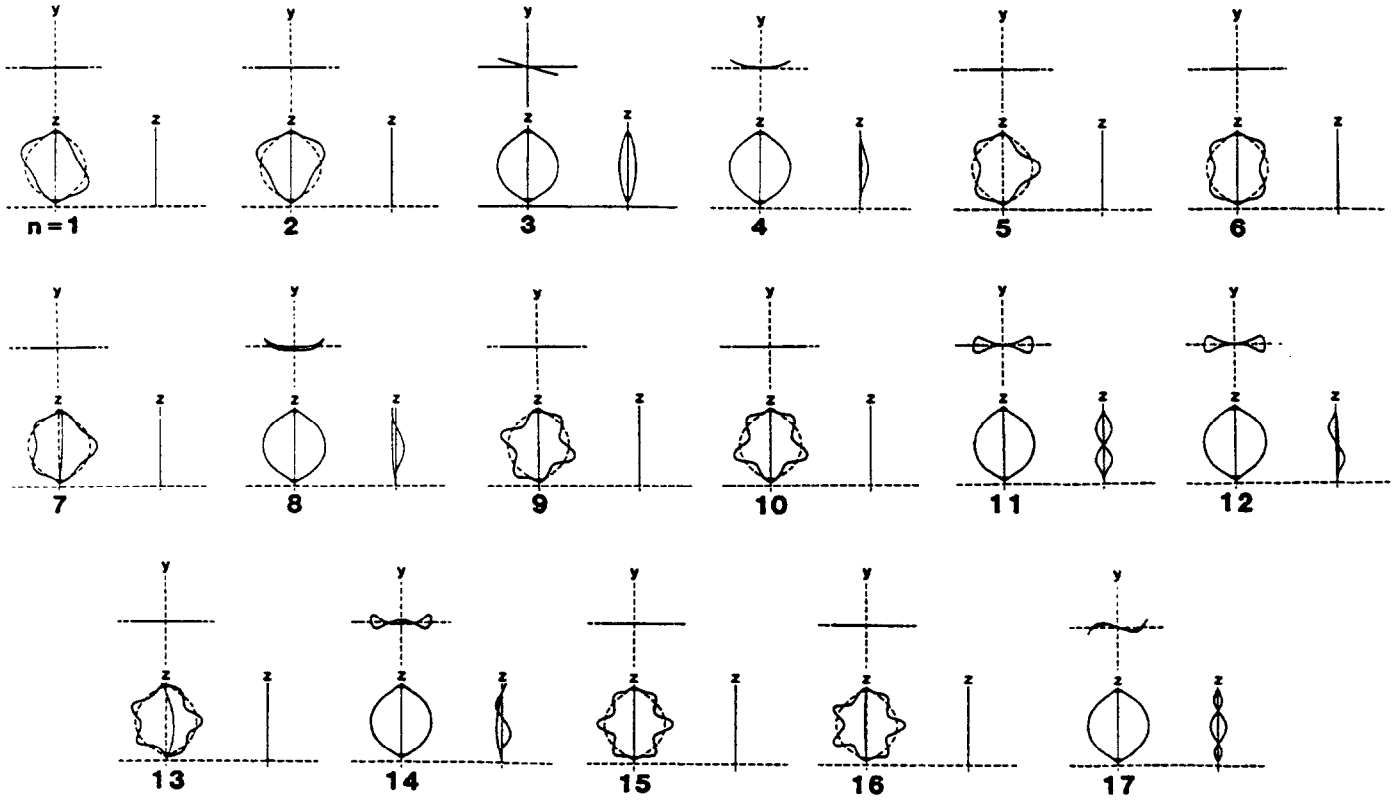

Figure 4. Mode Shapes of the Turbine from the Finite Element Model

Table 1 shows results from these two tests with both the modal frequencies and damping factors listed for the two excitation techniques. The mode numbers of the first column refer to the numbering of Figure 4. The modal parameters extracted using the wind or step-relaxation testing are virtually identical, except for the first rotor twist mode (1.51 Hz for wind and 1.35 Hz for step-relaxation). This difference can be attributed to the brakes which were applied during the tests. During the step-relaxation test, large torques were applied to the braking system when pulling on the blades. This excited a nonlinear response in the friction brakes which was not excited in the low torque wind excitation test. One can also observe that the damping in this mode is much higher for the step-relaxation test than for the wind test. This indicates that substantial energy has been dissipated through the sliding friction of the brakes. Further discussion and results of these tests can be found in Reference [8].

RESULTS

The principal results are comparisons of the modal frequencies between the tests and the analyses for each of the substructures and the entire turbine. If there is close agreement between the two results, then one can have high confidence in the accuracy of the model. Some qualitative comparisons of mode shapes are also presented, but in general, the mode shapes were quite similar between the tests and the analysis. For the substructure tests only a few modes were measured as compared to the turbine test, since the lowest modes of each substructures should capture the fundamental dynamics of that structural unit.

Table 1. Modal Frequency and Damping Ratios

Mode #	Wind Frequency (Hz)	Wind Damping (% critical)	Step-Relaxation Frequency (Hz)	Step-Relaxation Damping (% critical)	Description
1&2	1.06	2.0	1.04	1.8	1st Flatwise (Combined Mode)
3	1.51	1.1	1.35	10.0	1st Rotor Twist
4	1.81	0.2	1.81	0.2	1st Blade Edgewise
5	2.06	1.1	2.06	1.3	2nd Flatwise Anti-Symmetric
6	2.16	1.7	2.16	1.2	2nd Flatwise Symmetric
7	2.50	0.4	2.49	0.4	1st Tower In-Plane
8	2.61	0.3	2.60	0.2	1st Tower Out-of-Plane
9&10	3.49	0.7	3.45	0.9	3rd Flatwise (Combined Mode)
11	3.59	0.1	3.59	0.1	2nd Rotor Twist
12	4.06	0.2	-	-	2nd Blade Edgewise
13	4.69	0.4	-	-	2nd Tower In-Plane
14	5.28	0.4	-	-	3rd Blade Edgewise
15	5.08	0.5	-	-	4th Flatwise Symmetric
16	5.33	0.4	-	-	4th Flatwise Antisymmetric

Center Blade Section

Table 2 presents the results for the center blade section, see Figure 2. Three flatwise and two edgewise modes are included from both the test and the analysis. The differences are quite small for the lower modes, but increase somewhat for the higher modes. Overall, one would conclude that the model for the center section is quite accurate.

Table 2. Modal Frequencies for the Center Blade Section

Mode Shape	Analysis (Hz)	Test (Hz)	Difference (%)
1st Flatwise	2.22	2.17	2
2nd Flatwise	6.31	6.16	2
3rd Flatwise	12.7	12.3	3
1st Edgewise & Twist	15.6	16.4	5
2nd Edgewise	33.5	29.8	12

Intermediate Blade Section

Table 3 presents the results for the intermediate blade section. The correlation between the analysis and test results is not nearly as good as it was for the center blade section. Of the five modes, the three flatwise modes have excellent agreement while the edgewise mode is different by over one hundred percent and the twisting mode does not even appear in the analysis. Examining the mode shapes for both this test and the center section, one can see that the modes that include twisting are not well predicted by the model, as compared to the pure flatwise or pure edgewise modes. That is not unexpected since the model does not include any rotary inertia about the blade axis. Consequently, if a mode's primary kinetic energy comes from twist about the blade axis, that mode will not be modeled well. Clearly this substructure has a good model for flatwise deformation for all modes up to the third mode; however, it demonstrates the inadequacy of the model for twisting modes about the axis of the blades. As we will see later in the results for the entire turbine, this particular inadequacy does not affect the quality of the overall model, since this twisting deformation is not dominant for the low frequency modes of the entire turbine.

Table 3. Modal Frequencies for the Intermediate Section

Mode Shape	Analysis (Hz)	Test (Hz)	Difference (%)
1st Flatwise	15.6	15.4	1
2nd Flatwise	44.5	44.4	0
Twisting	-	62.9	-
1st Edgewise with Twisting	146.	71.7	103
3rd Flatwise	89.2	87.6	2

Combined Blade Section

For the substructure consisting of a combination of the center and intermediate sections (over twenty-five meters long), the modal frequencies are quite low, starting at about one Hz. These results are shown in Table 4. Here, as with the center section, the agreement is outstanding with very small differences in the frequencies including four flatwise modes and two edgewise modes. This fine agreement also establishes the adequacy of the model of the joint between the blade sections. Figure 5 shows test and analysis results for the three flatwise and the first edgewise modes for this substructure. One can see the shapes are very similar. The edgewise mode does include some twisting, but it does not contribute significantly to the kinetic energy of the mode. Note also that the first edgewise mode has three nodes along its length rather than two as we see for the flatwise modes; this is a result of the curvature in the blade.

Table 4. Modal Frequencies for the Combined Section

Mode Shape	Analysis (Hz)	Test (Hz)	Difference (%)
1st Flatwise	1.11	1.09	2
2nd Flatwise	3.32	3.14	6
3rd Flatwise	6.83	6.54	4
1st Edgewise	6.88	7.07	3
4th Flatwise	11.4	11.0	4
2nd Edgewise	18.2	18.1	1

Tower Substructure

Table 5 shows the modal frequency results for the tower supported by the guy cables and the turbine base. Just a few modes were measured as it was felt that they represented the basic dynamics of this structural unit. The first modal frequency has been predicted quite well with only a two percent difference, and the mode shapes agree as depicted in Figure 6. In contrast, there appear to be two second bending modes in the test data, while only one is predicted by the analysis. Both of these modes are higher than the analysis by eight and fifteen percent. The difference between the analysis and the test is apparently due to the dynamics of the guy cables. In the model the cables are treated as massless axial springs, but in fact, they possess mass and have lateral modes in the frequency range of this test. These two "second bending modes" which are measured in the test are actually coupled modes including both the tower and the guy cables. This effect has not been included in the model. The differences are further illustrated by the mode shapes shown in Figure 6. The node points for the two test modes are shifted relative to each other, showing that they are distinct modes.

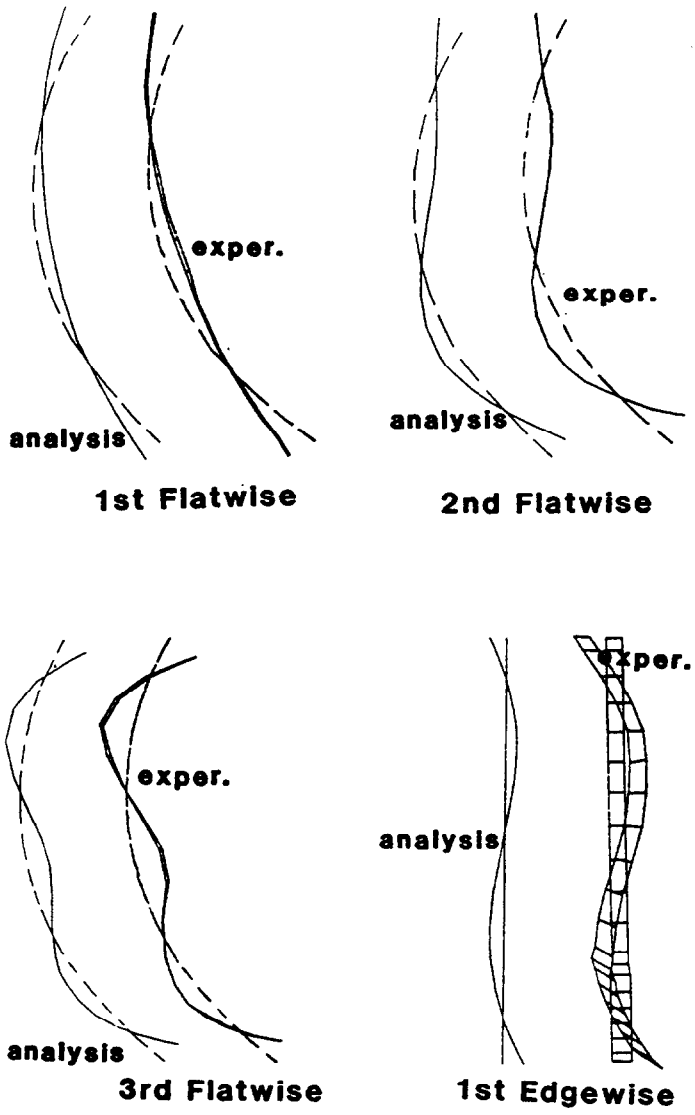

Figure 5. Comparison of Mode Shapes, Analysis and Test, for Combined Blade Section

Table 5. Modal Frequencies of the Tower with Guys

Mode Shape	Analysis (Hz)	Test (Hz)	Difference (%)
1st Bending	2.60	2.64	2
2nd Bending	4.43	4.81	8
		5.19	15

Entire Turbine

Finally, Table 6 shows the results of the analysis and test for the entire turbine. The test results are the average of the step-relaxation and the wind data, except for the first rotor twist mode where the wind result is used. The agreement is excellent for the ten modes listed, most having less than two percent difference. Only the first blade edgewise mode has a difference greater than three percent.

Refer to Figure 4 for a diagram of these mode shapes. Interestingly, the agreement for the entire turbine is as good as that for any of the substructures, apparently showing a forgiveness of the small modelling inadequacies or a cancelling of errors. In any case, the results for the entire turbine do show that it is not absolutely necessary that every substructure be perfectly modeled in order to have an adequate model for the entire structure. This is due to the fact that certain deformations, which may not be modeled adequately, will be exercised in a substructure test, but are not involved in the low frequency modes of the entire turbine.

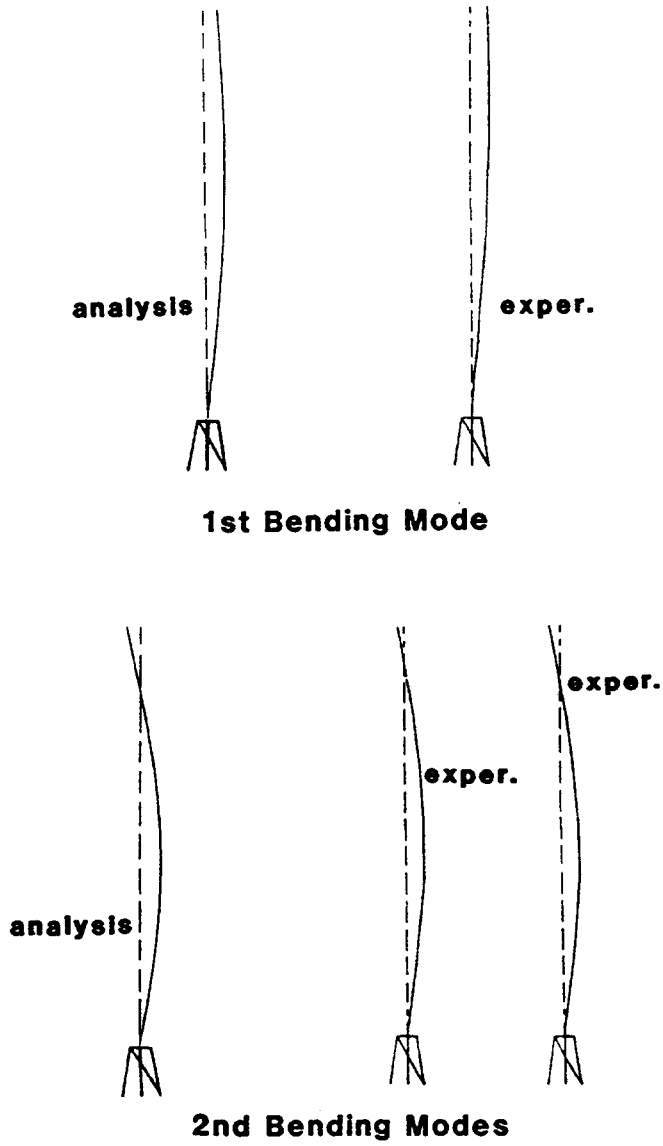

Figure 6. Comparison of Tower Mode Shapes, Analysis and Test

Table 6. Modal Frequencies for the Entire Turbine

Mode Shape	Analysis (Hz)	Test (Hz)	Difference (%)
1st Blade Flatwise	1.05	1.05	0
1st Rotor Twist	1.56	1.51	3
1st Blade Edgewise	1.72	1.81	5
2nd Blade Flat, Anti	2.07	2.06	0
2nd Blade Flat, Symm	2.14	2.16	1
1st Tower In-Plane	2.46	2.50	2
1st Tower Out-of-Plane	2.58	2.61	1
3rd Blade Flat, Anti	3.49	3.47	1
3rd Blade Flat, Symm	3.51	3.47	1
2nd Rotor Twist	3.52	3.59	2

CONCLUSIONS

The finite element model of the 34-Meter Test Bed Turbine has been validated with modal tests of four substructures (three blade sections and the tower) and the entire turbine. In general, the correlation between tests and analyses were excellent for both the substructures and the turbine. The excellent correlation between model and test for the substructures helped ensure a similar result for the entire turbine. However, the substructure model testing approach did reveal areas of the substructure models which were inadequate. The models were not accurate for certain deformations exercised in the substructure tests. These inadequacies did not affect the accuracy of the overall turbine model as these deformations were not important for the low frequency turbine modes.

A variety of modal testing techniques were employed to test the different structures, including excitation with transient impacts, step-relaxation, and wind excitation. Free boundary condition were well approximated on the very flexible blade sections by using a combination of a pendulum support with soft elastic straps.

REFERENCES

1. Carne, T. G., Lobitz, D. W., Nord, A. R., Watson, R. A., "Finite Element Analysis and Modal Testing of a Rotating Wind Turbine," The International Journal of Analytical and Experimental Modal Analysis, Vol. 3, No. 1, January 1988, pp. 32-41.

2. Ashwill, T. D., "Structural Design and Fabrication of the Sandia 34-Meter Vertical Axis Wind Turbine," Proceedings of the 1987 ASME-JSME Solar Energy Conference, Honolulu, HA, March 1987.

3. Ewins, D. J., Modal Theory: Theory and Practice, John Wiley & Sons Inc., New York, 1985.

4. Allemang, R. J. and Brown, D. L., "Experimental Modal Analysis," Handbook on Experimental Mechanics, Prentice-Hall, Inc., Englewood Cliffs, NJ, 1987, pp. 659-738.

5. MODAL-PLUS Reference Manual, Version 9, The SDRC Corporation, Milford, Ohio.

6. Lauffer, J. P., Carne, T. G., and Ashwill, T. D., "Modal Testing in the Design Evaluation of Wind Turbines," Proceedings WindPower '87, SERI/CP-217-3315, 1987, pp. 79-87.

7. Carne, T. G., Lauffer, J. P., Gomez, A. J., and Benjannet, H., "Modal testing the EOLE," Seventh ASME Wind Energy Symposium, ASME, New York, 1988, pp. 61-68.

8. Lauffer, J. P., Carne, T. G., and Gomez, A. J., "Modal Survey of the 34-m Test Bed Turbine," Sandia Technical Memo, June 7, 1988.

Proceedings of the Eighth ASME Wind Energy Symposium
D. E. Berg and P. C. Klimas (ed.), SED-Vol. 7, ASME, January 1989

INITIAL STRUCTURAL RESPONSE MEASUREMENTS FOR THE SANDIA 34-METER VAWT TEST BED*

T. D. Ashwill
Wind Energy Research Division
Sandia National Laboratories
Albuquerque, New Mexico

ABSTRACT

Sandia National Laboratories has designed and constructed a 34-meter diameter vertical axis wind turbine (VAWT) Test Bed. The machine will be used to advance research in aerodynamics and structural dynamics, improve fatigue life prediction capabilities, and investigate control algorithms and system concepts. The Test Bed has extensive instrumentation including 70 strain gauges to measure blade and tower response. Immediately after the blades were mounted, blade gravity stresses were measured and a modal analysis on the stationary rotor was performed to determine zero rpm modal frequencies. Assembly and start-up tests have been completed, and testing is in the machine characterization phase. Resonance surveys are underway to fully characterize the modal frequencies and mode shapes of the rotor, drive train and support cables. Measured gravity stresses, centrifugal stresses, and modal frequencies are compared to predicted values.

INTRODUCTION

The 34-m VAWT Test Bed is a variable-speed, research turbine recently designed and constructed by Sandia National Labs. The design of this 500 kW machine incorporates the results of recent VAWT research in aerodynamics and structural dynamics. The turbine will be used to evaluate the advances in these areas and to contribute to developments in other areas such as fatigue life predictive techniques, stochastic wind modeling, variable-speed control algorithms, and system design concepts. The construction of the Test Bed, which is located at the U.S.D.A. Agricultural Research Service facility, 15 miles west of Amarillo, Texas, is now complete, and testing is underway. The blades were mounted on the tower in November, 1987, and the first rotation occurred on February 4, 1988.

Assembly and start-up tests, Phase I of the Test Plan (1), are complete. Phase I included testing of the power system and controller, verification of the blade strain gauges, testing of the transmission and drive train for vibrations and power losses, set-up and checkout of the brake system and implementation of the data acquisition system. Immediately after the blades were mounted, blade gravity stresses were measured and a modal analysis performed on the stationary rotor. The modal analysis measured stationary modal frequencies, which were compared to predicted frequencies. This comparison allows the predicted fanplot (a plot of modal frequencies versus rotation rate) to be used more accurately as a guide for identifying resonance frequencies during rotation and provides some validation of the finite element analysis used to obtain the predictions.

The turbine testing has progressed into the machine characterization phase - Phase II of the Test Plan. This testing will determine the structural response and aerodynamic performance over the entire operating range. It will include further evaluation of the variable speed controller, understanding its capabilities, and upgrading the control algorithm to reflect knowledge gained during the characterization. Before running for long periods of time at different rotation rates and wind speeds, a resonance survey is being performed. The resonance survey is conducted by operating for short periods at several rotation rates from 6 through 40 rpm in low, medium, and high wind conditions. This will fully characterize the modal frequencies in the rotor, drive train, and support cables and allow for the determination of mean stress levels and approximate cyclic stress levels. The evaluation of structural response and turbine performance during these short periods is currently underway and will be followed by operation for longer periods of time to collect enough time series data to create statistically valid, averaged data (2).

This paper reports on the measured structural response obtained during the partially completed resonance surveys. (The turbine has rotated from 6 to 40 rpm in winds up to 11.5 mps). After a general description of the Test Bed structure and the finite

element model used in the structural design, measurements of gravity stresses, centrifugal stresses, and modal frequencies are shown and compared to predicted values.

GENERAL DESCRIPTION OF THE TEST BED

The 34-meter Test Bed is rated at 500 kW at 37.5 rpm in a 12.8 mps (28 mph) wind. Figure 1 shows a photograph of the turbine in its completed form. The rotor is 34 meters (110 feet) in diameter and has a height-to-diameter ratio of 1.25. The turbine, which has a total height of 50 meters (165 ft), is supported at the top by three sets of double guy cables each of which is 63.5 mm (2 1/2 in.) in diameter. Each cable pair is tensioned to 826 kN (186,000 lb) and is anchored at ground level to a reinforced concrete tiedown block measuring 4.3x4.3x6.1 m^3 (14x14x20 ft^3). The tower, or column, is an aluminum cylinder, 3 meters (10 ft) in diameter, constructed of 13 mm (0.5 in.) rolled plates, butt-welded together. Two blade mounts attached to the tower at each end are box-like structures that provide blade attachment surfaces and transition the tower diameter down to bearing shaft diameters.

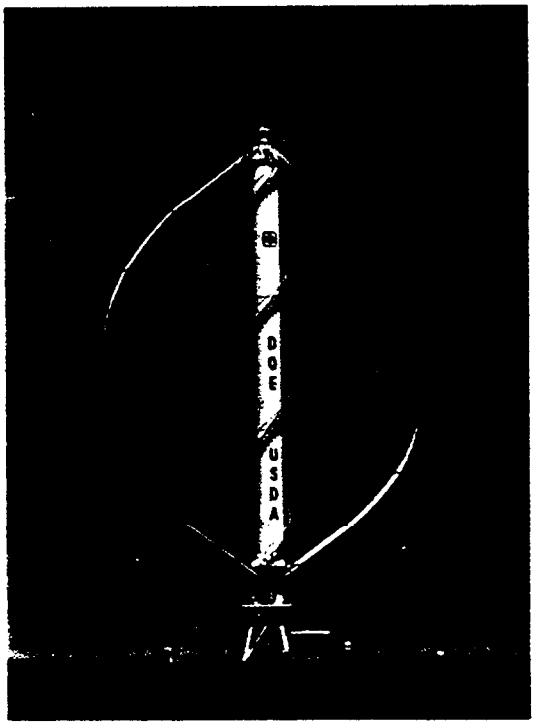

Fig. 1. 34-Meter Test Bed

Each blade is step-tapered with five sections constructed of extruded 6063-T6 aluminum. The root sections are straight with a 1.22 meter (48 in.) chord using a NACA 0021 profile. The equatorial section, with a 17.1 meter (675 in.) radius of curvature, has a 0.91 meter (36 in.) chord with an SNLA 0018/50 profile. The intermediate sections, with a 30.0 meter (1180 in.) radius of curvature, have a 1.07 meter (42 in.) chord with an SNLA 0018/50 profile. The SNLA 0018/50 airfoils are part of a series of natural laminar flow airfoils developed at Sandia specifically for use on VAWT's (3). Because all three chords are too large to be fabricated from a single extrusion, each blade section is made of two or three single extrusions bolted together in the spanwise direction. The 36-inch and 42-inch chord sections were then bent to the proper radius around dies designed specifically for the Test Bed. The extrusion-to-extrusion bolts were retorqued to specification after the blade bending.

The blade shape approximates a 37.5 rpm troposkien and contains "kinks", or slope discontinuities, of 6-7 degrees at the blade-to-blade joints as shown in Figure 2, a schematic of the blade shape geometry. Because of the multi-sectioned, step-tapered characteristics of the Test Bed blades, the normally-used straight/single-curve/straight approximation to a troposkien was not employed. A better approximation resulted by implementing the different radii of curvature along the blade and the slope discontinuities at the blade joints where mass is concentrated. Design calculations (4) show that these implementations reduce peak mean flatwise stresses approximately fifty percent. This mean stress reduction extends the estimated fatigue life by a factor of two to four.

THE FINITE ELEMENT MODEL

The structural design (5) of the Test Bed used the finite element code NASTRAN to determine the turbine dynamic response. Gravity stresses were also predicted with NASTRAN using a static solution (Rigid Format 24). Predicted modal frequencies were computed with NASTRAN using an eigenvalue solution methodology (FEVD) developed at Sandia (6). In this methodology the stiffness matrix of the finite element model, when subjected to centrifugal and gravitational loading, is determined by running a series of geometric nonlinear analyses (Solution 64). This stiffness matrix is then input to the complex eigenvalue analysis (Solution 67) along with a damping matrix that incorporates centrifugal softening and Coriolis effects. The mean stresses due to gravitational and centrifugal loading at a particular rpm are output by Solution 64. The complex mode shapes and their respective frequencies of vibration are determined by Solution 67.

A similar methodology called FFEVD (7) is used to determine the operating stresses. In FFEVD the stiffness matrix computed by Solution 64 and the damping matrix that incorporates centrifugal softening and Coriolis effects are input to the complex frequency response analysis (Solution 68) along with the wind loads determined by the double streamtube code CARDAA (8). Solution 68 then computes the structural response in the frequency domain.

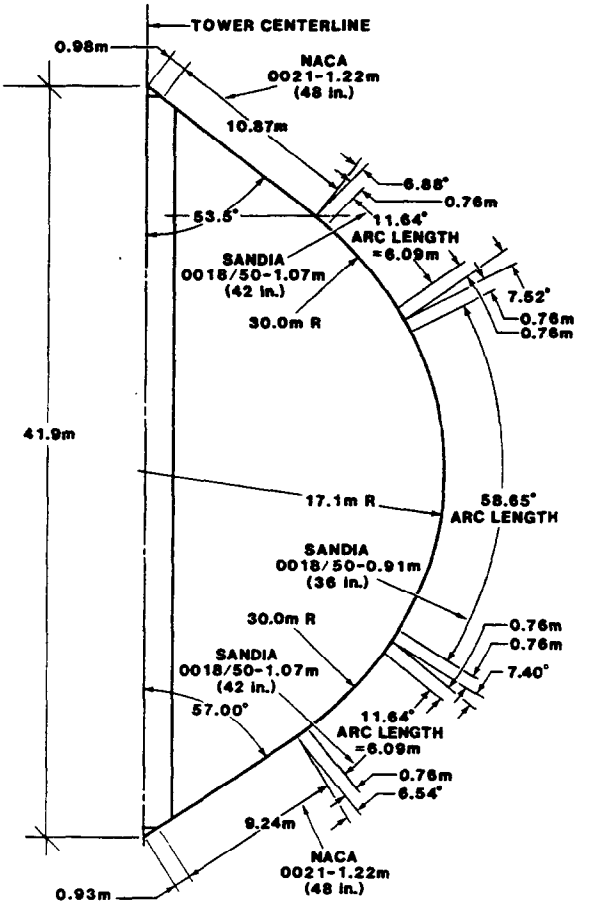

Fig. 2. Blade Shape Geometry

Figure 3 shows the finite element grid for the 34-m Test Bed. It consists of 42 CBEAM elements for each blade, 25 CBEAM elements for the tower, and 2 CBEAM's for each of the four "mini-struts." (The NASTRAN beam element, CBEAM, has properties that include two-dimensional bending, extension, and torsion.) These ministruts are used as a way to model the large blade mounts. The cables that restrict motion at the top of the turbine are represented by two orthogonal, horizontal springs, a torsional spring, and a vertical load acting down through the tower. At the bottom of the rotor at grid point 1 the restriction of motion by the support stand is represented by two orthogonal, horizontal springs. A torsional spring at grid point 1 represents the torsional stiffness of the drive train. Concentrated masses are added at several grid points along the tower to account for the entire tower mass. The mass of the blade joints is distributed evenly along the relatively short joint elements. As the turbine was constructed, each component was measured and weighed. (This meant weighing about 150 items). The concentrated masses and properties of the finite elements were then updated in the model to reflect these "as-built" conditions.

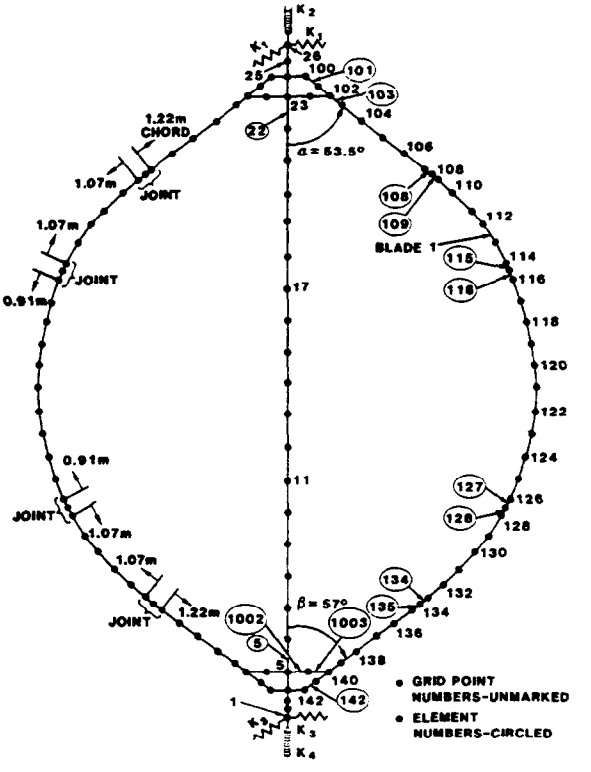

Fig. 3. Finite Element Grid

For blade one, elements 101-108 and 135-142 represent the blade root sections, elements 109-115 and 128-134 the intermediate sections, and elements 116-127 the equatorial section. Blade two is identical in structure to blade one. For the modal analysis, an additional boundary condition was added to the model at grid point 2 to represent the brakes in the engaged condition. This condition was modelled as two orthogonal, horizontal springs and a torsional spring (torsion about the vertical axis) equal to the appropriate stiffnesses of the support stand.

GRAVITY STRESSES

The Test Bed has been instrumented with 70 strain gauges that measure axial, lead-lag, and flatwise response in the blades and torque and bending in the tower (9). Brake paddle strain gauges and damage gauges that measure crack growth of a pre-cracked aluminum coupon also are installed. When the blades were first instrumented, the flatwise gauges were validated by hanging known weights from each blade section, recording the strains and comparing them to the calculated. The entire set of gauges functioned correctly, and the measured strains agreed with predictions to within 2 percent. Following the gauge validation tests, the blade sections were transported to the turbine site and bolted together while at the same time pulling instrumentation cabling through two blade cavities. The blade cavities containing the cabling were then foamed to prevent cable movement. Before the blades were mounted, the gauges were rechecked to verify their working condition and then

recalibrated. Immediately after the blades were mounted, the gauges were monitored to measure gravity strains.

Figure 4 compares the measured flatwise gravity stresses to the predicted. Stresses along the blade from the top to the bottom are plotted left to right on the x-axis, and positive stress corresponds to tension on the outside of the blade. The location of the different blade sections that make up the blade are noted along the x-axis. The patterns of stress distribution for the measured and predicted are very similar and the values agree well at the ends of the blades. Discontinuities in the stress distribution occur at the joints because of the change of blade stiffness at those locations. The analytical values show an offset along the middle portion, however, indicating an underprediction at the tension side and an overprediction at the compression side of up to 10 MPa (1440 psi). This is also the area where the only significant differences between blades one and two occur. This discrepancy may be due to small errors in the blade shape geometry in the model. Gravity stresses are sensitive to small angle changes at the blade-to-tower connection. The blade section lengths were carefully measured in the field, and the blade sections (including the instrumentation cabling, paint and aerodynamic smoothing compound) were weighed several times. A survey of the turbine structure will be performed to attempt to determine the exact "as-mounted" blade attachment angles.

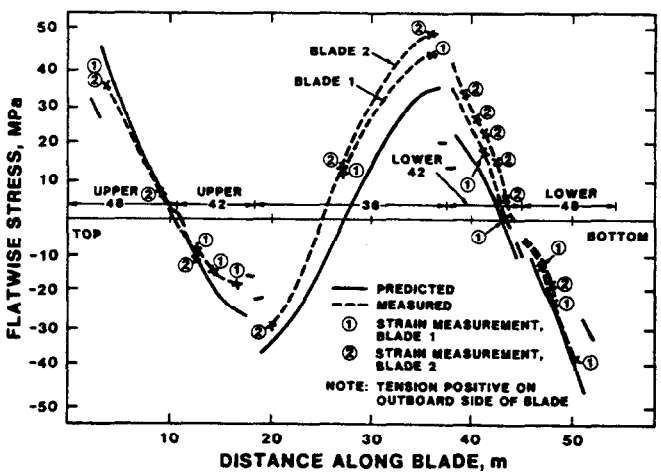

Fig. 4. Flatwise Gravity Stress Distribution

MODAL FREQUENCIES

After the blades were mounted on the tower, a modal analysis was performed on the stationary rotor by Sandia's Modal and Structural Mechanics Division (7544). During this test, frequency response functions due to both wind and step function (snap releasing) excitation were measured with accelerometers temporarily attached to the blades, tower and cables. These measurements were used to determine the mode shapes, their frequencies of vibration, and modal damping values. Reference 10 describes the details of the Test Bed modal analysis.

Table I compares the measured modal frequencies with those determined analytically. The mode number and name are listed in the first two columns. (Figure 5 shows the shapes of these modes when viewed from three orthogonal directions.) Columns three and four show the modal frequencies for a stationary rotor measured by the modal analysis after a snap release and during wind excitation, respectively. Column five lists the predicted values, and column six lists measured frequencies obtained from amplitude spectra plots of strain gauge data taken during the the wind-excited modal analysis. There is excellent agreement between the measured and predicted frequencies for the first eleven modes. At the higher modes the predicted modal frequencies do not agree as well with the measured. The two dimensional finite element model appears to have a limit on its ability to predict these higher modes. However, in general, the higher modes have lower deformation and less energy associated with them.

Mode Number	Mode Shape	Modal Analysis: Snap Release	Modal Analysis: Wind Excitation	Predicted	Strain Gauge Spectra
1	1FA-First Flatwise Antisymmetric	1.04	1.06	1.05	> 1.06
2	1FS-First Flatwise Symmetric	1.04	1.06	1.05	
3	1Pr First Propeller (Rotor Twist)	1.35	1.52	1.56	1.50
4	1B-First Blade Edgewise	1.81	1.81	1.72	1.82
5	2FA-Second Flatwise Antisymmetric	2.06	2.06	2.07	> 2.14
6	2FS-Second Flatwise Symmetric	2.16	2.16	2.14	
7	1TI-First Tower In-Plane	2.49	2.50	2.46	2.50
8	1TO-First Tower Out-of-Plane	2.60	2.61	2.58	2.61
9	3FA-Third Flatwise Antisymmetric	3.45	3.50	3.49	> 3.51
10	3FS-Third Flatwise Symmetric	3.45	3.50	3.51	
11	2Pr Second Propeller	3.59	3.59	3.52	3.59
12	2B-Second Blade Edgewise	-	4.06	3.90	4.05
13	2TI-Second Tower In-Plane	-	4.69	4.33	-
14	2TO-Second Tower Out-of-Plane	-	-	4.57	-
15	4FS-Fourth Flatwise Symmetric	-	5.09	5.25	-
16	4FA-Fourth Flatwise Antisymmetric	-	5.30	5.37	-
17	3Pr Third Propeller	-	-	5.71	-

Table I. Stationary Modal Frequencies-Brakes Engaged

The first propeller mode vibrates at 1.5 Hz with the brakes engaged and 0.2 Hz with the brakes released. The capability to change this modal frequency was designed into the drive train. By adding or changing elastomeric pads (known as hockey pucks because of their size and shape), the drive train stiffness can be adjusted. The first three flatwise modes (both antisymmetric and symmetric), the first tower in-plane and out-of-plane modes, and the second propeller mode were all predicted to within two percent of the measured. The first blade edgewise mode (1B) is underpredicted by 0.09 Hz (approximately 5 percent) indicating that the blades are actually slightly stiffer in the lead-lag direction. The close agreement between predicted and measured frequencies for the first eleven modes is an indication that the finite element model does an excellent job in representing the Test Bed - a complicated three-dimensional structure.

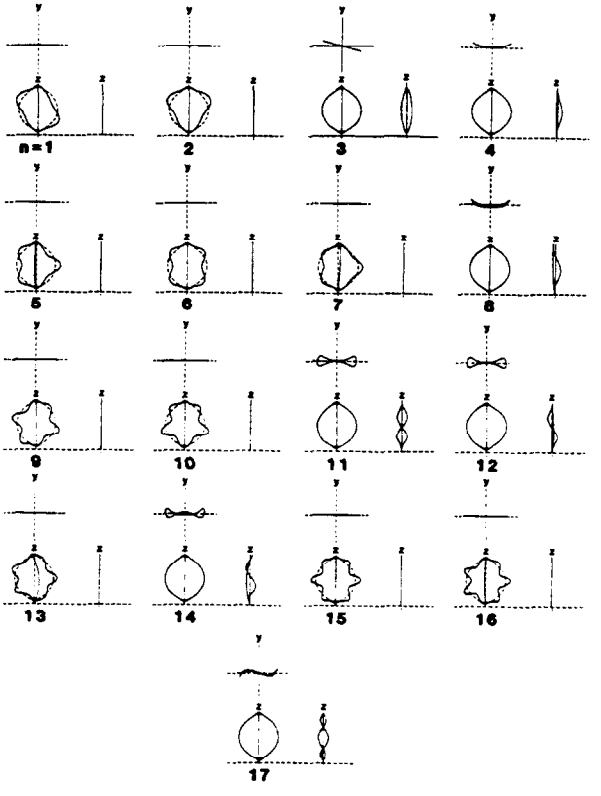

Fig. 5. Mode Shapes

The measured frequencies resulting from the two methods of excitation - snap releasing and wind excitation - are very close. Only the first propeller mode (1Pr) shows any significant difference in frequency between the two methods. The reason for this difference is not clear. However, the snap release inputs more energy into the system and possibly alters the brake boundary condition slightly. As shown in column six, the peak frequencies from the strain amplitude spectra agree closely with those measured by the modal analysis.

The first three cable frequencies were measured at 0.78, 1.22, and 1.59 Hertz. The cable n=1 and n=2 modes were designed to vibrate at 0.81 Hz and 1.62 Hz, respectively, at a nominal cable tension of 826 kN (186,000 lb). These design modes compare closely with the first and third measured modes. The measured intermediate cable mode, however, is unexpected and is probably due to an interaction between the cables and heavy cable attachment hardware at the lower cable connection. Before the blades were mounted, tower rotation tests were performed at various cable tensions and rotation rates. The n=1 cable mode was excited, but neither the new intermediate mode nor the n=2 mode was observed. During the resonance survey, however, a two node cable excitation was observed at 37 rpm. There is much less motion associated with this mode than the n=1 mode. As the cable fanplot (Figure 6) indicates, this resonance is probably the intermediate mode crossing the 2P (two "per rev") line.

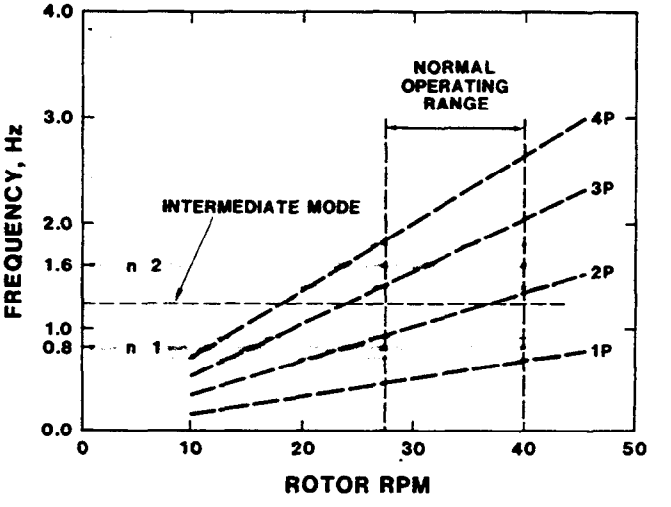

Fig. 6. Cable Fanplot

The predicted fanplot for the "as-built" finite element model with the brakes released is shown is Figure 7. Because the brake boundary condition is eliminated, some of the zero rpm tower modal frequencies, as expected, are lower than the modal frequencies shown in Table I. The blade modal frequencies are not affected by this boundary condition. Because potential resonances are possible wherever a modal frequency crosses a "per-rev" line, both this rotor fanplot and the cable fanplot have been employed extensively during the resonance surveys.

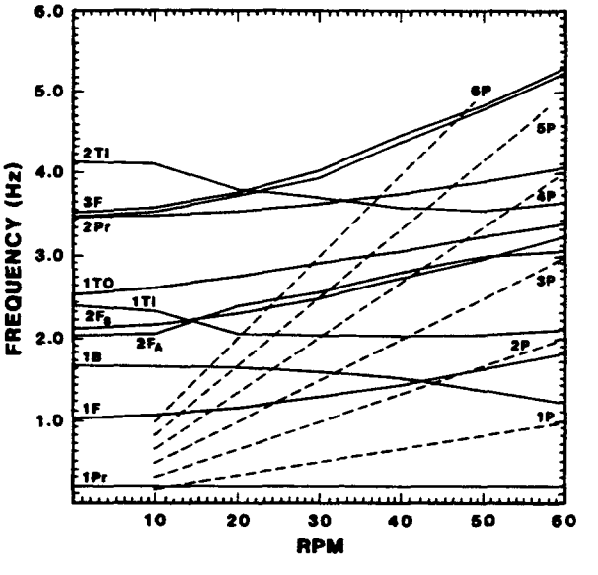

Fig. 7. Rotor Fanplot - Brakes Disengaged

The turbine has operated at rotation rates from 6 to 40 rpm in winds up to 11.5 mps. The collected time series have been analyzed with the aid of the data acquisition and analysis (DAAS) software (11). This software can plot any segment of a time series,

compute the statistical properties of a segment, statistically reduce the data, and perform spectral analyses. A plot of a strain amplitude spectrum for a flatwise gauge at the upper root at 10 rpm is shown in Figure 8. The first five per-rev peaks and several excited modal frequencies are evident. By plotting these measured modal frequencies at several rotation rates on the predicted fanplot, as shown in Figure 9, one can track several modes with rpm. The lower frequency modes (below 3 Hz) including the first and second flatwise, the first blade edgewise, the first tower in-plane and the second propeller, all track along the same predicted mode lines very well. The two measured first flatwise modal frequencies are either the antisymmetric and symmetric modes, which normally vibrate at the same frequency, or the two blades vibrating at slightly different frequencies. The first tower out-of-plane (1TO) does not show up in any of the many spectral plots examined thus far. The first blade edgewise mode (1B) was underpredicted by 5% at zero rpm, but above 25 rpm the observed and predicted frequencies coincide. The first blade edgewise crossing of the 3P (three "per rev") line shows up as a larger spike in the spectra of lead-lag gauges at 32 rpm. However, the stresses are not high in this region, at least for the range of windspeeds presently experienced. The first tower in-plane mode (1TI) tracks well except in the region where it crosses the second flatwise modes. An excitation of this tower in-plane mode begins at 39.5 rpm, and the response is still increasing at 40 rpm. This is due to the 3P crossing predicted at 40.5 rpm. The tower-in-plane excitation couples with blade-edgewise motion causing large lead-lag cyclic stresses (standard deviations about the mean) at the blade roots approaching 6 MPa in an 11.5 mps wind at 40 rpm.

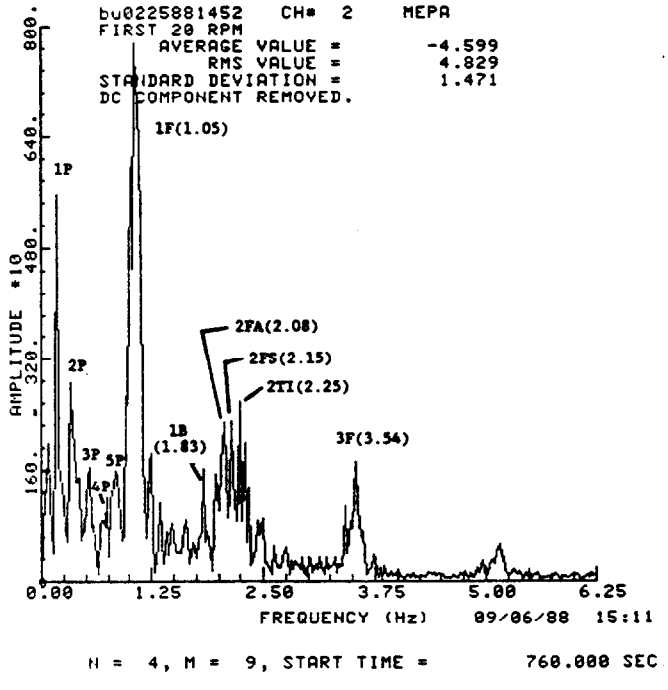

Fig. 8. Strain Amplitude Spectrum At 10 RPM

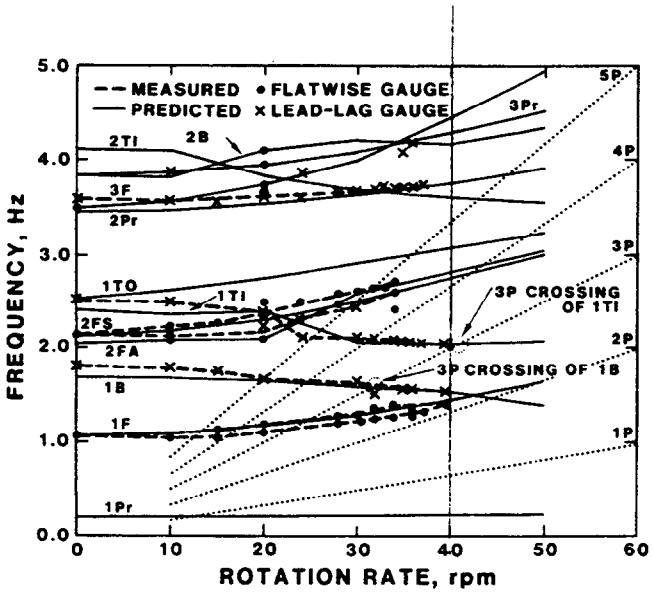

Fig. 9. Rotating Modal Frequencies - Measured Vs. Predicted

CENTRIFUGAL STRESSES

Figure 10 shows a time series record of an upper root, flatwise-bending strain gauge and turbine rotation speed. Since the gauges are zeroed out before testing, the mean stresses are centrifugal only. As the rpm is increased from 0 to 40 rpm, there is an increase in blade bending stresses due to growing centrifugal loading. By averaging each flatwise strain gauge for 40 seconds at each rpm, centrifugal stresses are determined which may be compared to analytical results. The increase of centrifugal stresses with higher rpm continues to offset the bending stresses due to gravity until the mean stresses are minimized at 37.5 rpm (the troposkien rpm). Figures 11 and 12 show a comparison of the measured flatwise centrifugal bending stresses at 28 and 40 rpm to those determined analytically. The stresses along the blade from top to bottom are plotted left to right on the x-axis. There is excellent agreement between the measured and predicted values. Comparisons have also been made at 10,15,20,32,and 36 rpm, and similar agreement was observed.

CYCLIC STRESSES

Standard deviations of stress time histories for all recorded channels have been computed for segments of data. This information has been used during the resonance survey in determining the presence and severity of resonances. Sufficient data are not yet available for comparisons to predictions. Hours of time series records at each rpm of interest are required for the Method of Bins to obtain cyclic response and turbine performance as a function of wind speed up to the cutout of 20.5 mps.

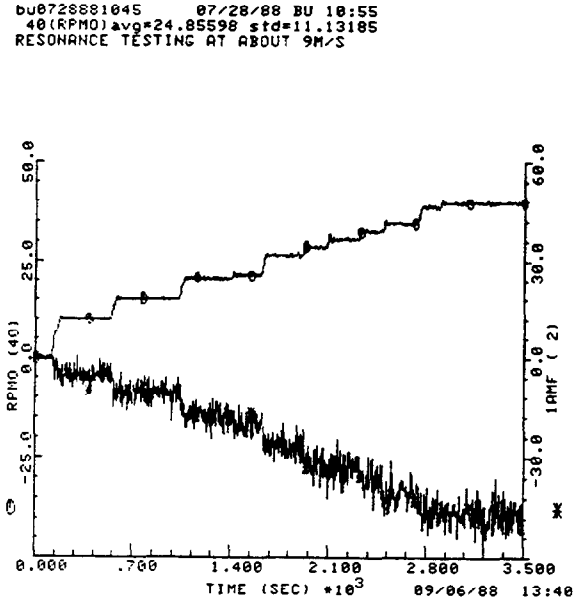

Fig. 10. Upper Root Flatwise Stress Vs. RPM

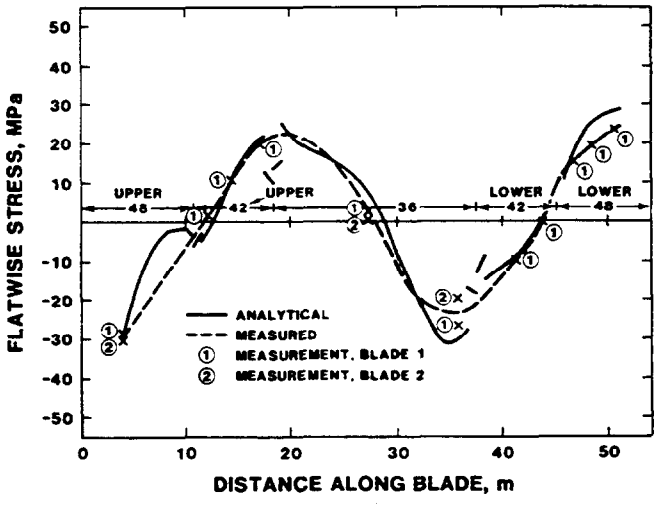

Fig. 11. Centrifugal Stress Distribution At 28 RPM

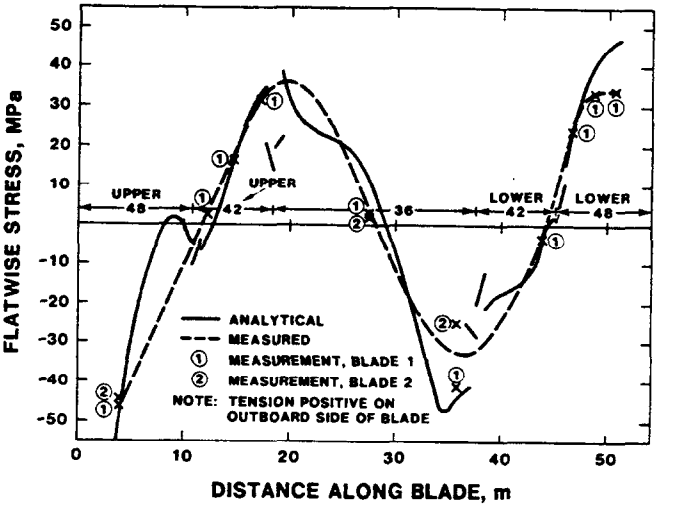

Fig. 12. Centrifugal Stress Distribution At 40 RPM

SUMMARY

At this early stage of testing the turbine is responding structurally as expected. Predicted gravity stresses compare very well over most of the blade. Small adjustments to the model's blade attachment angles, if justified, may result in even better agreement.

The first two cable frequencies were measured and shown to compare closely with the design frequencies. An additional cable mode between these two was discovered and appears to become excited at two "per rev" at 37 rpm.

A modal analysis was performed on the stationary rotor. The measured modal frequencies were compared to analytical predictions with excellent results. Rotating modal frequencies obtained from strain amplitude spectra also agree closely with predicted values (Figure 9).

Measured centrifugal stresses have been compared to analytical predictions at several rotation rates, and again, results have been excellent.

The close agreement between measured and predicted modal frequencies and mean stresses indicates that the finite element model accurately represents the 34-m Test Bed structure.

REFERENCES

1. Stephenson, W. A., "Test Plan for the 34 Meter Vertical Axis Wind Turbine Test Bed Located at Bushland, Texas," SAND86-1623, Sandia National Laboratories, Albuquerque, NM, December, 1986.

2. Akins, R. A., "Performance Evaluation of Wind Energy Conversion Systems Using the Method of Bins - Current Status," SAND77-1375, Sandia National Laboratories, Albuquerque, NM, March, 1978.

3. Klimas, P. C., "Tailored Airfoils for Vertical Axis Wind Turbines," SAND84-1062, Sandia National Laboratories, Albuquerque, NM, November, 1984.

4. Ashwill, T. D. and Leonard, T. M., "Developments in Blade Shape Design for a Darrieus Vertical Axis Wind Turbine," SAND86-1085, Sandia National Laboratories, Albuquerque, NM, September, 1986.

5. Ashwill, T. D., "Structural Design and Fabrication of the Sandia 34-Meter Vertical Axis Wind Turbine," Proceedings of the 1987 ASME-JSME Solar Energy Conference, Honolulu, HA, March, 1987.

6. Carne, T. G., Lobitz, D. W., Nord, A. R., Watson, R. A., "Finite Element Analysis and Modal Testing of a Rotating Wind Turbine," SAND82-0345, Sandia National Laboratories, Albuquerque, NM, October, 1982.

7. Lobitz, D. W., and Sullivan, W. N., "Comparison of Finite Element Predictions and Experimental Data for the Forced Response of the DOE 100 kW Vertical Axis Wind Turbine," SAND82-2534. Sandia National Laboratories, Albuquerque, NM, February, 1984.

8. Paraschivoiu, I., "Aerodynamic Loads and Performance of the Darrieus Rotor," AIAA Journal of Energy, Volume 6, No. 6, pp 406-412, December, 1982.

9. Sutherland, H. J. and Stephenson, W. A., "Rotor Instrumentation Circuits for the Sandia 34-Meter Vertical Axis Wind Turbine," SAND88-1144, Sandia National Laboratories, Albuquerque, NM, July, 1988.

10. Lauffer, J. P., Carne, T. G., and Gomez, A. J., "Modal Survey of the 34-m Test Bed Turbine," Sandia Technical Memorandum, March, 1988.

11. Berg, D. E., Rumsey, M. A., Gallo, L. L., and Burwinkle, D. P., "Data Acquisition and Analysis System for the Sandia 34-Meter Vertical Axis Wind Turbine, Proceedings of the Seventh ASME Wind Symposium, New Orleans, La., January, 1988.

Proceedings of the European Wind Energy Conference (EWEC '89)
10-13 July, 1989

DAMAGE PREDICTIONS FOR WIND TURBINE COMPONENTS USING THE LIFE2 COMPUTER CODE

Herbert J. Sutherland

Sandia National Laboratories, USA

INTRODUCTION

The LIFE2 computer code is a fatigue/fracture analysis code that is specialized to the analysis of wind turbine components. It is a PC-compatible FORTRAN code that is written in a top-down modular format. The code was originally written by Sutherland, Ashwill and Naassan (1), and it was subsequently modified by Sutherland and Schluter (2). The User's manuals for the code are cited in References (3) and (4).

The service lifetime of a component can be divided into three phases: (1) crack initiation, (2) growth and coalescence of micro-cracks and (3) growth of a macro-crack. In the LIFE2 formulation, an "S-n fatigue" analysis is used to describe the first two phases, and a linear, "da/dn" fracture analysis is used to describe the third phase.

The code is divided into five main sections. The first four describe the wind resource, constitutive properties of the turbine material, stress state in which the turbine operates and operational parameters for the turbine system. The fifth uses the data generated by the first four sections to calculate the service lifetime of a turbine component. Auxiliary sections are included to permit the storage and plotting of data and code calculations.

The fifth section of the code contains two analysis techniques for determining the service lifetime of a turbine component. The first uses an S-n fatigue analysis, based on Miner's Rule, to determine the initial portion of the service lifetime of a turbine component. In this formulation, the damage rule is integrated over all stress cycles to determine the rate at which damage is being accumulated. The lifetime of the component is inversely proportional to this damage accumulation rate.

In the second analysis technique, the crack propagation characteristics of a pre-existing crack are analyzed using a da/dn constitutive rule. In this formulation, the crack growth rate, da/dn, for a crack of current length a, is integrated over all stress cycles, n. As da/dn is a function of a, the calculation is divided into a finite number of steps. For each step, the current crack length is taken to be a constant, an average growth rate is determined, and the time required for the crack to grow across that integration segment is calculated. The sum over all of the integration segments yields the time of growth for the crack from its initial size to its final size.

This report describes the computational framework used in the LIFE2 code to evaluate the damage rules cited above. An example problem is presented here to illustrate the capabilities of the code.

NUMERICAL PHILOSOPHY

From its inception, the LIFE2 code has been designed to run on an IBM personal microcomputer (PC) or compatible, to insure that it could be used by the maximum number of wind turbine designers. Implementing this analysis on a small computer required special formulations and techniques.

First, its relatively small operational memory placed rather severe limitations on the program. Programming compromises included the extensive use of data and program overlays and judicious limits on the size of the matrices used in the code.

The relatively slow PC processor makes for excessively long computational times when all computations are performed at one time. This problem was addressed using extensive "library" functions (i.e., data storage to permanent files). Calculations are based on data read from these files, rather than requiring the code to recalculate them each time the code is run. The major problem with this scheme is that the program uses tables (matrices) to transfer computations between subroutines. Thus, the computations must use interpolation schemes, which decrease their accuracy.

The "open architecture" created by this memory management scheme has major benefits. Data files, generated elsewhere, may be incorporated into the code simply by adding them to the code's library. Parameter studies may be conducted relatively quickly because a large portion of the computations do not have to be duplicated. And, all computations may be archived for future reference. This architecture also permits the addition of subroutines to the code without re-validating the entire code. Rather, only the new module (subroutine) must be validated.

NUMERICAL FRAMEWORK

Fatigue Analysis

The LIFE2 computer code has been developed to compute the fatigue lifetime of a turbine component. It uses either Miner's Rule or linear fracture mechanics to analyze the behavior of the component. In the case of the former, the damage law used in the computations is given by the relation:

$$D(\Delta t) = \int_{V_{ci}}^{V_{co}} p_V \int_{-\infty}^{\infty} \int_{-\infty}^{\infty} \frac{n(S_m, S_a, V, \Delta t)}{N(S_m, S_a)} \, dS_m \, dS_a \, dV, \qquad (1)$$

where p_V is the probability density function for the annual wind speed distribution, S_m is the mean stress, S_a is the alternating

stress, $N(\cdot)$ is the total number of cycles required to fail the materials at the stress state (S_m,S_a), and $n(\cdot)$ is the number of stress cycles at stress state (S_m,S_a) imposed on the turbine component in time Δt with a wind velocity V. V_{ci} and V_{co} are the cut-in and cut-out wind speeds, respectively. When the damage D equals one, the component is expected to fail. As this formulation is linear, the service lifetime T_f of the component is given by:

$$1 = \int_0^{T_f} D(\Delta t)\, dt = D(\Delta t)\, T_f \quad . \qquad (2)$$

In this form, we have assumed apriori that the stress cycles are a function of the velocity of the wind impinging on the turbine and that the annual wind speed distribution may be described by a probability density function. Equation 1 has been discretized to the following finite summation:

$$D(\Delta t) = \sum_{q=1}^{Q} \sum_{r=1}^{R} \sum_{s=1}^{S} (P_V)_q \frac{n[(S_m)_r,(S_a)_s,V_q,\Delta t]}{N[(S_m)_r,(S_a)_s]} \quad . \qquad (3)$$

The exact formulation of each term in this sum will be defined later in this report.

Fracture Mechanics Analysis

The propagation of a pre-existing, finite length crack is determined here by integrating the crack growth rate da/dn over all stress cycles. As the growth rate is a function of the current crack length $a(\Delta t)$, this integration is typically divided into a finite number of integration steps of the form:

$$a(\Delta t) = a_i + \sum_{w=1}^{W} \Delta a_w \quad . \qquad (4)$$

where a_i is the initial length of the crack. Heuristically, the growth rate at each step is determined by integrating the average growth rate over all stress cycles N; namely:

$$\Delta a_w = \int_0^{N} avg[(da/dn)_w]\, dn = avg[(da/dn)_w]\, N \quad . \qquad (5)$$

Expanding this integral to illustrate its functional dependence,

$$\Delta a_w = \int_{V_{ci}}^{V_{co}} p_V \int_{-\infty}^{\infty} \int_{-\infty}^{\infty} \frac{da(\kappa_m,\kappa_a)}{dn}\, n(S_m,S_a,V,\Delta t)\, dS_m dS_a dV \quad . (6)$$

(Note: This form of the crack growth equation is parallel in construction to the damage accumulation integral for fatigue shown in Eq. 1.)

As seen in this formulation, the crack growth rate da/dn is a function of the stress intensity state κ and the cycle count n is a function of the stress state. The stress state is mapped into the stress intensity state using the current crack length, a_w. Thus, Eq. 4 may be written as:

$$a(\Delta t) = a_i + \sum_{w=1}^{W} \int_{V_{ci}}^{V_{co}} p_V \int_{-\infty}^{\infty} \int_{-\infty}^{\infty} \left[\frac{da(\kappa_m,\kappa_a)}{dn} \right] \cdot \left[n[(\kappa_m)_w,(\kappa_a)_w,V,\Delta t)] \right] d\kappa_m d\kappa_a dV \quad . \qquad (7)$$

Discretizing Eq. 7 for numerical evaluation yields:

$$a(\Delta t) = \sum_{w=1}^{W} \sum_{q=1}^{Q} \sum_{r=1}^{R} \sum_{s=1}^{S} (P_V)_q \left[\frac{da[(\kappa_m)_{wr},(\kappa_a)_{ws}]}{dn} \right] \cdot \left[n[(\kappa_m)_{wr},(\kappa_a)_{ws},V_q,\Delta t)] \right] + a_i \quad . \qquad (8)$$

And, again, each term will be defined in detail later in this report.

WIND REGIME

The annual wind speed distribution can be described by a probability density function p_V. This function may take the form of a table or it may be described by Rayleigh or Weibull distributions (5). The Weibull family of distributions is given by:

$$p_V = \left[\frac{\alpha}{\beta} \right] \left[\frac{V}{\beta} \right]^{\alpha-1} \exp\left\{ - \left[\frac{V}{\beta} \right]^{\alpha} \right\} \quad . \qquad (9)$$

where p_V is the probability density function, α and β are the shape factor and amplitude factor of the distribution, respectively. The Rayleigh distribution is a special case of the Weibull distribution when $\alpha = 2$.

CONSTITUTIVE FORMULATION

Two sets of constitutive properties are required by the code. The first is used for the fatigue analysis, and the second is used for the linear fracture mechanics analysis.

Fatigue Analysis

For the fatigue analysis, a classical "S-n" fatigue characterization is required. In this formulation, the number of stress cycles required to fail the component is described as a function of applied stress state (6). The stress state is characterized by both its mean stress level and its alternating stress level. This relation may be entered in tabular form into the code. In addition, the code can accept a number of constitutive descriptions for this relationship.

Four constitutive relationships for determining the S-n fatigue characterization matrix are supported at this time. They are Goodman's rule using the yield stress, Goodman's rule using the ultimate stress, Gerber's rule and the modified Gerber rule (6). The general formulation for these rules is given by:

$$S_a = \sigma_e \left\{ 1 - \left[\frac{S_m}{\sigma_{ref}} \right]^{\gamma} \right\} \quad . \qquad (10)$$

where, σ_e is the effective cyclic stress amplitude at zero mean stress, and the

TABLE I - Constitutive parameters for the S-n formulations.

Constitutive Relations	Constitutive Parameter	
	σ_{ref}	γ
Goodman (Yield)	σ_y	1
Goodman (Ultimate)	σ_u	1
Gerber	σ_u	2
Modified Gerber	σ_u	material constant

reference stress σ_{ref} and the exponent γ are constitutive parameters that are listed in Table I for the four different formulations. In this table, σ_y and σ_u are the yield stress and the ultimate stress of the material, respectively.

Fracture Mechanics Analysis

The second set of constitutive properties describes the rate of crack growth as a function of the cyclic change in the stress intensity factor. The growth rate is assumed to depend on the mean stress intensity factor and the alternating stress intensity factor. Again, the relationship between these variables may be entered into the code in tabular form. A Forman constitutive model is also included in the code (7).

Classical da/dn fracture mechanics describes the crack growth rate of a macro-crack as a function of the stress intensity factor κ. The relationship between the stress state and the crack length is discussed below. Here, the stress intensity factor is taken to have two components, a mean and an alternating stress intensity factor, κ_m and κ_a, respectively.

Many constitutive equations have been proposed for the description of crack propagation in metallic materials. One general form proposed by Forman (7) is supported by the LIFE2 code at this time. The governing equation for this formulation is given by:

$$\frac{da}{dn} = \frac{C\,(1 - R)^{\mu}\,\Delta\kappa^{\nu}\,[\Delta\kappa - \Delta\kappa_{th}]^{\eta}}{[(1 - R)\,\kappa_c - \Delta\kappa]^{\psi}} \quad . \tag{11}$$

where a is the current crack length; n is the number of stress cycles; R is the stress ratio (6); $\Delta\kappa$ is the change in the stress intensity factor κ at the crack tip for cycle n; and C, μ, ν, η, ψ, $\Delta\kappa_{th}$ and κ_c are material parameters (constants).

STRESS STATES

The third section of the code describes the cyclic content of the stress state imposed on the turbine component. Classes of stress states include operational stresses, parked stresses (i.e., the stresses due to the wind buffeting a parked blade) and start-stop stresses. The first two are taken to be functions of the annual wind speed distribution and the last as specific events. For each of these stress states, the code accepts a cycle count matrix in which the number of stress cycles (for a specified time period) are characterized as a function of the mean stress and the alternating stress. These matrices, commonly called "rain-flow" matrices, are three dimensional (3D) matrices of the form n_{qrs}. In this form, each stress cycle is characterized as a function of its mean stress $(S_m)_r$ and its alternating stress $(S_a)_s$ and the input wind speed or the class of start-stop cycles that produced it (the q index).

The matrices are accepted in tabular form. A narrow-band Gaussian model for operational stresses in vertical axis wind turbines (VAWTs), developed by Veers (8), is supported in the code. The technique is based on the assumption that the amplitude of the vibrational stresses at any wind speed follows the distribution of peak values of a narrow-band Gaussian process; i.e., a Rayleigh distribution. The conditional probability density function $p_{S|V}$ of the vibratory stress S_a occurring at a particular wind speed V may be written as:

$$p_{S|V} = \left[\frac{S_a}{\sigma_V^2}\right] \exp\left[\frac{-S_a^2}{2\,\sigma_V^2}\right] \quad . \tag{12}$$

where σ_V is the standard deviation of the vibratory stresses. Here, we assume that σ_V is only a function of the wind speed V and that the mean stress is constant.

To determine the cyclic count matrix from this formulation, the probability density function in Eq. 12 is integrated over a series of S cyclic count intervals, at each wind speed V_q. Namely,

$$(P_{S|V})_s = \int_{(S_a)_{s-1}}^{(S_a)_s} \left[\frac{S_a}{\sigma_V^2}\right] \exp\left[\frac{-S_a^2}{2\,\sigma_V^2}\right] dS_a \quad . \tag{13}$$

This integration evaluates σ_V at the center of the wind speed interval $[V_q, V_{q-1}]$.

Thus, a probability matrix has been determined for the stress cycles at each wind speed interval V_q. Each one of these matrices is composed of one column of S elements. The s^{th} element is the probability of occurrence of a stress cycle with a mean stress of S_m and an alternating stress in the range between $(S_a)_{s-1}$ and $(S_a)_s$.

To convert these probabilities into cycle count matrices, the rate at which the stress cycles occur must be known. Veers (8) assumes that the stress cycle rate is, on the average, equal to the dominant frequency of blade vibration f_o (this frequency is an input parameter for the model). Thus, the time Δt for the average stress cycle is given by:

$$\Delta t = \frac{1}{f_o} \quad . \tag{14}$$

The probability matrices become cycle count matrices by setting their count period Δt_q to Δt.

OPERATIONAL PARAMETERS

The fourth section of the code describes the operational parameters for the turbine. This section records the miscellaneous parameters required for the calculations. Typical inputs include such parameters as the cut-in wind speed, the cut-out wind speed and stress concentration factor(s).

DAMAGE CALCULATION

The fifth section of the code uses the data files written by the other four sections to determine the service lifetime of the turbine component. At this time, two analysis techniques are supported by the code. The first is Miner's rule (6), see Eq. 1, and the second is based on linear fracture mechanics, see Eq. 6.

The computations for each technique proceed along similar lines. First, the code reads into current memory the files generated by the wind, constitutive and parameters sections of the code. Next, the code reads in each cycle count matrix $(n_{rs})_q$ and adjusts it to an equivalent annual cycle count, using the time parameter Δt_q, the fraction of the time at which the turbine operates in the wind velocity interval V_{q-1} to V_q, and the estimated number of annual start-stop cycles. The nominal stress levels in each matrix are then adjusted to the component stress levels using the appropriate stress concentration factor. The constitutive relation is then interpolated to determine the damage rate per cycle at each adjusted stress (or stress intensity) state. This damage rate is then used with the cycle count matrix to determine the annual average damage rate for that stress state. The damage rates are then summed for all stress states in that cycle count matrix, to determine the damage rate for that cycle count matrix. The calculation is then repeated for each cycle count matrix. Finally, each damage rate is summed over the wind velocity intervals from V_{ci} to V_{co} for the operational stress; over all velocities greater than V_{co} for the parked stresses; and over all classes of start-stop. For the fatigue calculation, this total annual average damage rate is directly related to the service lifetime of the component, see Eq. 2. For the fracture analysis, this rate defines the average crack growth rate for the current crack length, and this defines the time for the crack to grow from a_{w-1} to a_w. The entire process is then repeated for the next interval of crack growth. The time for the crack to grow across each interval is then summed to determine the time required for the crack to grow from its initial length a_o to its final length a_f.

Thus, the code computes the triple sum described in Eq. 3 for the fatigue analysis and the quadruple sum in Eq. 8 for the fracture analysis.

17-M VAWT BLADE JOINT ANALYSIS

To illustrate the use of this code, consider the analyses, performed in References (1) and (2), on the lower blade joint on the DOE 100-kW Low Cost VAWT. This joint was analyzed using the fatigue and fracture analysis capabilities of the LIFE2 code. They are repeated here for illustration purposes.

The wind regime was assumed to have a Rayleigh distribution with a mean velocity of 6.26 m/s (14 mph). The probability density function for this relation is shown in Figure 1.

The blade joint was made of 6063 aluminum. An S-n curve and a da/dn curve for this material are shown in References (1) and (2), respectively.

The stress state for the joint was determined using Veers' narrow band Gaussian model and the distribution of the vibratory stresses, as a function of wind speed, cited in Reference (1). The mean stress component was taken to be a constant 48.3 MPa (7 ksi), and the stress concentration factor was taken to be 2.73 (1).

The turbine was assumed to operate between 4.47 m/s (10 mph) and 20.1 m/s (45 mph).

This turbine joint was analyzed first using an S-n fatigue analysis. These results are summarized in Figure 1 as the probability distribution function for the damage accumulated in the joint as a function of wind speed. The distribution functions shown in this figure have been expanded to cover a wide range of wind speeds for purposes of illustration. For the operating range of the turbine cited above, this analysis predicts a service lifetime of 13.9 years.

The same configuration and stress state was analyzed with the fracture modules. Assuming that the joint contains a crack that was 0.0254 mm (0.001 in) in length, the analysis predicted that the crack length would increase with time as described in Figure 2.

As seen in this figure, this crack will reach catastrophic size in 66.8 days. If the size of the initial crack is assumed to be 0.254 mm (0.01 in), then the time to catastrophic failure is reduced to 34.7 days. As seen in Figure 2, the 34.7-day period is equal to the total time to failure for the 0.0254 mm (0.001 in) crack less the time required for the crack to grow from 0.0254 mm (0.001 in) to 0.0254 mm (0.01 in); i.e., 66.8 days minus 32.1 days.

As one would not expect the annual wind speed distribution to be applicable to such a short period of time, the growth of the crack was also investigated for a continuous wind whose speed varied uniformly from 17.9 m/s (40 mph) to 20.1 m/s (45 mph). This analysis yields a time of extension to catastrophic failure of 4.9 days for an initial crack of 0.0254 mm (0.001 in), see Figure 2. For an initial crack of 0.254 mm (0.01 in), the time to failure is reduced to 2.4 days.

As seen in Figure 2, the time of extension is a non-linear function. The non-linearity of

this analysis also is observed in the rate at which damage is accumulated, see Figure 1. The damage accumulation rate for a fracture analysis has a similar form (shape) to that determined by the fatigue analysis. However, the size of the crack influences the position of the distribution with respect to wind speed. As shown in Figure 1, the damage distribution function for the initial phase of crack growth ("small crack") has its maximum at approximately 10 m/s (23 mph). For the final phase of growth ("large crack"), the maximum of the distribution located at approximately 15.5 m/s (35 mph). The latter value compares closely to 16 m/s (36 mph) for the maximum determined for the blade joint using the fatigue analysis capabilities of the LIFE2 code. (A "large crack" and a "small crack" distribution are observed in these calculations because a bi-linear, log-log formulation was chosen for the da/dn constitutive formulation of the aluminum).

The dependence of the maximum of this distribution on the constitutive formulation (manifested here as a function of crack size) has been predicted by Veers (9).

As discussed by Veers (9), the service lifetime of a component can be divided into three phases: (1) crack initiation, (2) growth and coalescence of micro-cracks, and (3) growth of a macro-crack. The S-n fatigue life analysis usually describes the first two phases and fracture analyses the third phase. Thus, based on these calculations, the total service life of this blade component will be 13.9 years plus the time for the macro-crack to grow to catastrophic size; i.e., 66.8 days or 4.9 days, depending on the operational wind spectrum.

SUMMARY

The LIFE2 computer code is a fatigue/fracture analysis code that is specialized to the analysis of wind turbine components. The numerical formulations that have been implemented in the code and example problems to illustrate its capabilities are presented here.

ACKNOWLEDGMENTS

This work is supported by the U.S. Department of Energy at Sandia National Laboratories under contract DE-AC04-76DP00789.

REFERENCES

1. Sutherland, H., Ashwill, T., and Naassan, K., 1987, "Fatigue Analysis Codes for WECS Components," Proceedings of WindPower '87, SERI, Golden, U.S.A., 74-78.

2. Sutherland, H., and Schluter, L., 1989, "Crack Propagation Analysis of WECS Components Using the LIFE2 Computer Code," Proceedings of the Eighth ASME Wind Energy Symposium, ASME, New York, U.S.A., 141-145.

3. Schluter, L., and Sutherland, H., 1989, "User's Manual for the LIFE2 Computer Code," Sandia, Albuquerque, U.S.A.

4. Sutherland, H., 1989, "Numerical Formulation of the LIFE2 Computer Code," Sandia, Albuquerque, U.S.A.

5. Amstadter, B., 1971, "Reliability Mathematics," McGraw-Hill, New York, U.S.A.

6. Osgood, C., 1982, "Fatigue Design, 2nd Edition," Pergamon Press, Oxford, England.

7. Forman, R., 1986, "Derivation of Crack Growth Properties of Materials for NASA/FLAGRO," NASA, U.S.A.

8. Veers, P., 1983, "A General Method for Fatigue Analysis of Vertical Axis Wind Turbine Blades," Sandia, Albuquerque, U.S.A.

9. Veers, P., 1989, "Simplified Fatigue Damage and Crack Growth Calculations for Wind Turbines," Proceeding of the 8th ASME Wind Energy Symposium, ASME, New York, U.S.A., pp. 133-140.

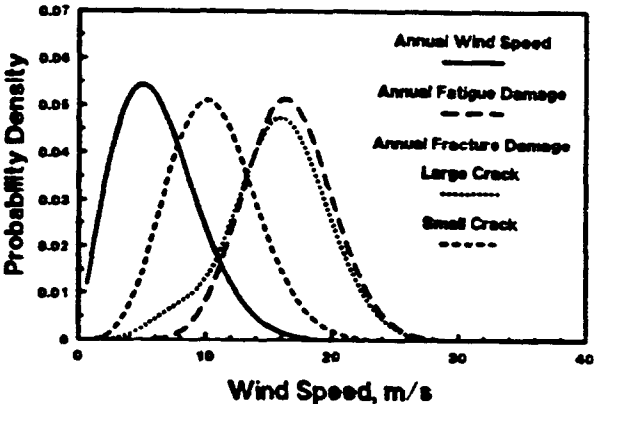

Figure 1 Probability density functions for the DOE 100-kW low cost VAWT.

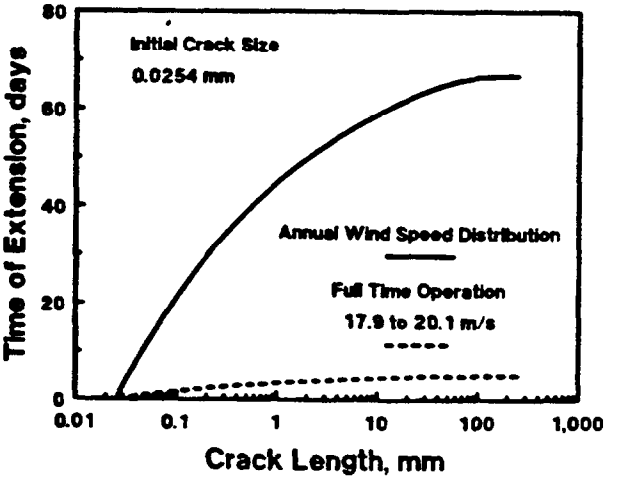

Figure 2 Time of extension for a crack propagating in the DOE 100-kW low cost VAWT.

For presentation at Windpower '89, September 25-27, 1989, San Francisco, CA

CONTROL OF THE VARIABLE SPEED GENERATOR ON THE SANDIA 34-METRE VERTICAL AXIS WIND TURBINE *

Mark E. Ralph
Wind Energy Research Division, 6225
Sandia National Laboratories
Albuquerque, New Mexico 87185-5800

ABSTRACT

The DOE/Sandia 34-metre VAWT Test Bed is a 500kW variable-speed wind turbine. The turbine is operated between 25 and 38 rpm and has been characterized from a structural and aerodynamic stand point. A preliminary variable speed control algorithm has been implemented on the Test Bed. This paper describes the initial variable-speed control algorithm developed for the Test Bed and the performance of that algorithm to date. Initial performance comparisons between variable-speed and fixed-speed operation are made as well as some thoughts on the expansion of the operating envelope of the Test Bed.

INTRODUCTION

The 34-metre vertical axis wind turbine (VAWT) Test Bed has a nominal power rating of 500 kW electric with a peak power rating of 625 kW electric. The generator's torque, and thus speed, is controlled by a load-commutated-inverter (LCI) variable speed motor drive.[1] The LCI connects the turbine to the utility system by converting the variable voltage and frequency of the generator to the constant voltage and frequency of the utility system. The turbine is operated over a speed range from 25 to 38 rpm.

---

* This work was supported by the U.S. Department of Energy under contract DE-AC04-76DP00789.

The control algorithm for the turbine is implemented on a programmable logic controller (PLC).[2] The PLC implements the variable speed control algorithm as well as monitoring and safety features for the turbine.

Initial testing of the test bed at fixed operating speeds is nearing completion. This testing has verified the aerodynamic and structural response of the turbine. Performance surfaces at fixed operating speeds have been developed from the data collected. From this control surface, an operation scheme was determined which maximizes the power output of the turbine by operating the turbine at the speed which produces the maximum power for the available mean wind. In higher winds, where the turbine can produce more power than the generator is rated for, the algorithm operates the turbine in a fixed speed mode.

Mechanical resonances which must be avoided are present within the desired operating range. The control algorithm is programmed to limit the amount of time that the turbine is operated on the mechanical resonances.

This paper will discuss the variable speed control algorithm that is being developed and implemented on the test bed. Preliminary results of the turbine's operation and its effect on system performance will be presented. Conclusions about the algorithm's performance will include possible improvements.

TEST BED DESCRIPTION

The 34-metre VAWT Test Bed is a Darrieus wind turbine with a nominal power rating of 500 kW and a peak power rating of 625 kW.[1] The Test Bed was designed to facilitate various testing programs. Electrical power produced by the turbine is fed into the local utility company's distribution system. The turbine's rotational speed is controlled by a variable-speed motor drive which produces constant 60 Hz output power in synchronism with the local utility distribution system. The generator's speed can be controlled from 288 rpm to 1900 rpm. A fixed ratio transmission decreases the speed of the generator's shaft down to the rotor's shaft speed, which can vary from 6 to 40 rpm. Mechanical spring applied brakes are used to stop and park the turbine.

The turbine is controlled by a programmable logic controller (PLC).[2] In addition to controlling the speed and power output of the turbine, the PLC monitors the status of the turbine and will shut it down when an abnormal condition arises. The software on the PLC is written in a high-level "ladder relay logic" language. Modifications to the operation of the system are easily implemented by changing the program.

OPERATION PARAMETERS

Extensive performance and response data have been taken on the turbine.[3] The turbine was operated at various fixed speeds under varying wind conditions. One of the results of this testing was the development of an operating surface showing the turbine's power production at different wind speeds as a function of turbine rotational speed. Figure 1 shows the calculated shaft power produced as a function of wind speed and

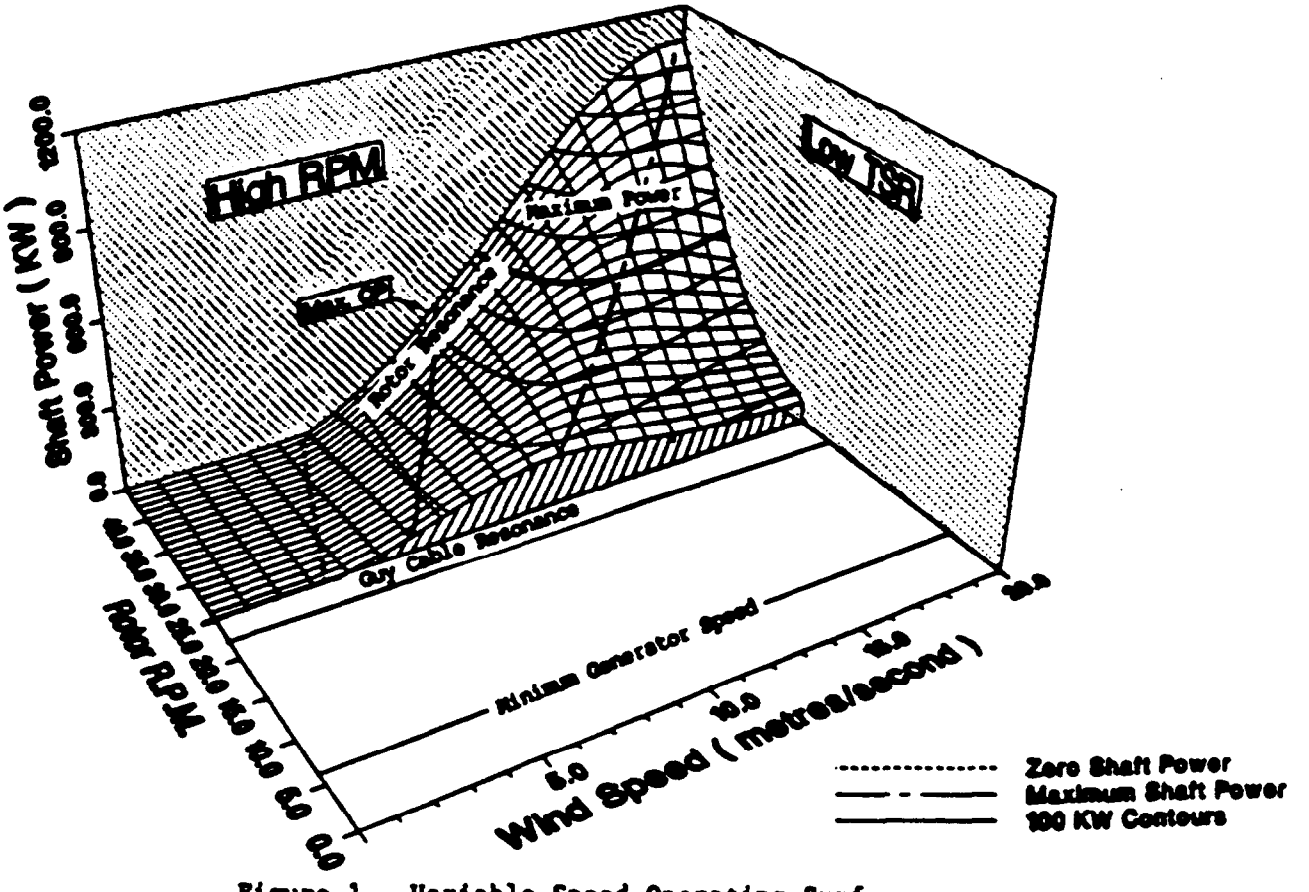

Figure 1 - Variable Speed Operating Surface

turbine rotational speed. From this surface, the optimal operating speed for maximum power production can be selected. In the wind speed range from 6 to 9.5 mps, the optimum rotor speed varies with the wind speed. Between 9.5 and 15 mps, the generator's maximum rotational speed limits turbine operation to 38 rpm. And, at wind velocities above 15 mps, the turbine can produce more mechanical power than the generator can convert to electrical power. At these high wind velocities, the turbine's rotational speed is reduced to below 38 rpm to limit the power produced by the turbine.

Turbine structural resonances have further limited turbine operation in three regions.[4,5] First, a guy cable resonance has prevented operation in the range from 23 to 25 rpm. Since the turbine does not develop very much power below 25 rpm, this is not a very significant operation limitation. The second resonance is located above 40 rpm, but this resonance starts to couple when the turbine is operated above 39 rpm. To prevent this resonance from being excited, turbine operation is restricted to below 38 rpm. A third resonance is located around 36 rpm. This resonance will soon be moved out of the operating range by modifying the guy cables, but for now, the resonance has to be avoided.

The variable speed generator can vary the turbine's speed by up to 1.9 rpm/sec. Large acceleration and deceleration rates require large power transfers between the utility system and the turbine and increase the stresses on the turbine. To minimize the impact on the turbine and on the utility system, the acceleration and deceleration rate of the turbine are kept small, 0.1 rpm/sec, under normal conditions.

Figure 2 shows the rotational speed for the turbine as a function of wind velocity for producing maximum power. For wind speed between cut-in, 4 mps and 6 mps, the turbine is operated in a fixed speed mode at 25 rpm. Operating the turbine at 25 rpm avoids coupling with the guy cable resonance at 24 rpm. Between 6 mps and 8.5 mps, the turbine's rotational speed is increased linearly with wind speed from 25 rpm to 35 rpm. To reduce the operating time of the turbine in the speed range around 36 rpm, a hysteresis loop was built into the control algorithm.

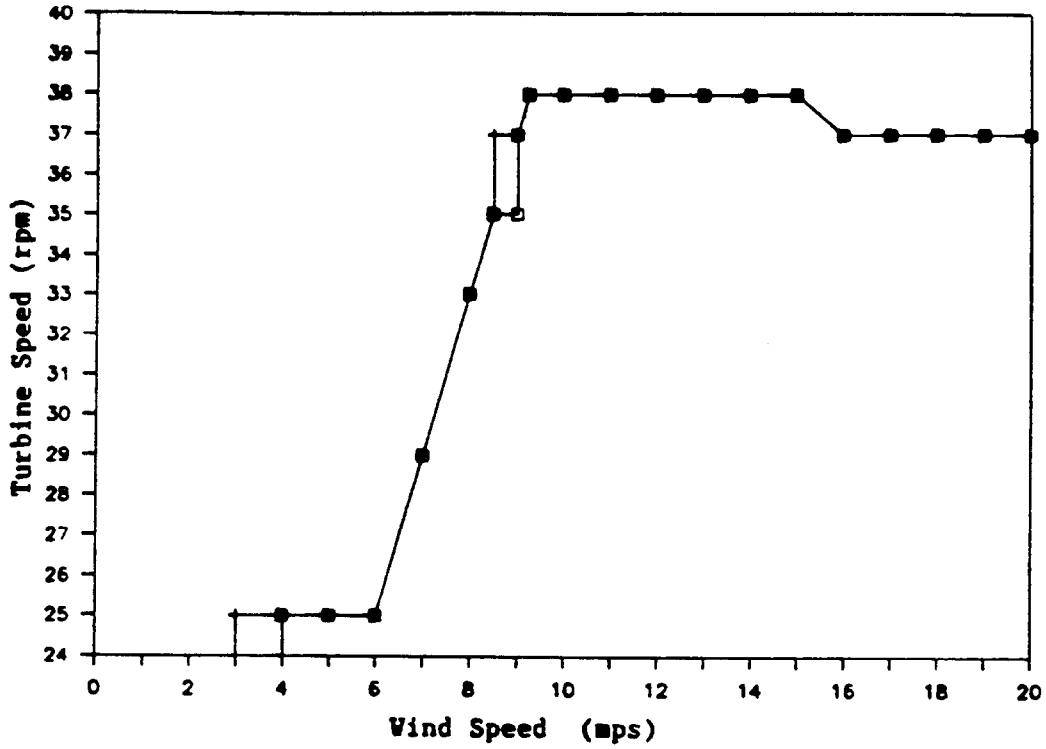

Figure 2 - Variable Speed Operating Speed

When the turbine is operating at rotational speeds below 35 rpm, the turbine speed set point will not be increased above 35 rpm until the average wind speed has remained above 9 mps for 2 minutes. And conversely when the turbine has been operating above 37 rpm, the set point will not be reduced to below 35 rpm until the wind speed has remained below 8.5 mps for 2 minutes. Above 9 mps, the operating speed is increased until 38 rpm is reached at 9.25 mps. The turbine is operated as a constant speed turbine for winds between 9.25 and 15 mps. Above 15 mps, the operating speed is reduced to 37 rpm to limit the power output of the turbine. For winds above 20 mps, the turbine is shut down.

In the variable speed range, the desired operating speed is very sensitive to wind speed. The desired operating speed varies from 25 to 38 rpm with a corresponding wind speed range of 6 to 9.25 mps. This equates to a 4 rpm change in rotational speed for a one mps change in wind speed. With this steep slope, a variable speed algorithm must be highly damped to avoid speed fluctuations in operating speed. To increase the turbine's speed, kinetic energy must be added to the turbine's rotor. If the speed change takes place faster than the wind accelerates the turbine, electrical energy will be extracted from the

utility system. On the other hand, if speed changes are not made fast enough, the potential increased energy capture from variable speed operation will be lost. Here, we have chosen the acceleration/deceleration rate to be 0.1 rpm/sec, as the best compromise.

CONTROL ALGORITHM

The speed control algorithm is implemented on the PLC using wind speed measurements from two anemometers. The control anemometers are located approximately 5 rotor diameters from the turbine at 10 and 30 metres above the ground. The anemometers are located far enough away from the turbine to minimize shadowing effects. The control algorithm uses the highest measured wind speed from the two anemometers to compute a moving 200 second wind speed average. The moving average is updated every 20 seconds with a wind speed average taken over the previous 20 seconds. The 200 second wind speed average is converted into a table location. From the table, a desired rotational speed set point is selected (every 20 seconds). This desired rotational speed is a table equivalent to the operating speed curve shown in Figure 2. If the desired speed would cause the turbine to cross the guy cable resonance at 36 rpm, the desired speed set point is not updated until a timer records that the wind speed has been in the proper range for 2 minutes.

The turbine's rotational speed is then incremented at a rate of 0.1 rpm/second towards the new desired set point. If the set point is very far from the current operational speed, the turbine does not reach the new set point before the next set point is selected.

TEST RESULTS

Figures 3 and 4 illustrate the effects of variable speed operation on energy output and power quality. In Figure 3, the turbine was operated in a fixed speed mode at 31 rpm with winds averaging 8.5 mps. In Figure 4, the turbine was operated in a variable speed mode with approximately

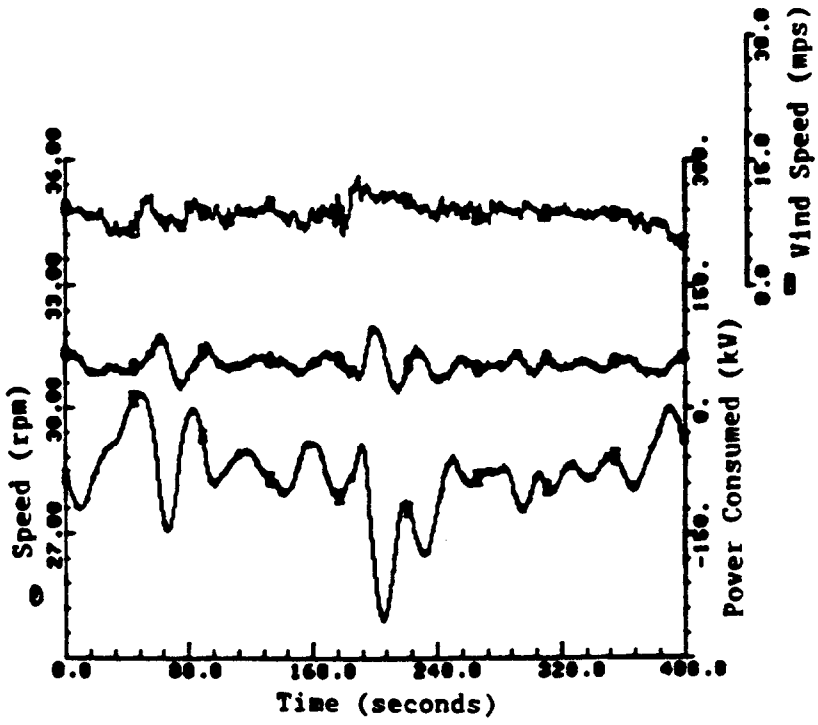

Figure 3 - Fixed-Speed Operation

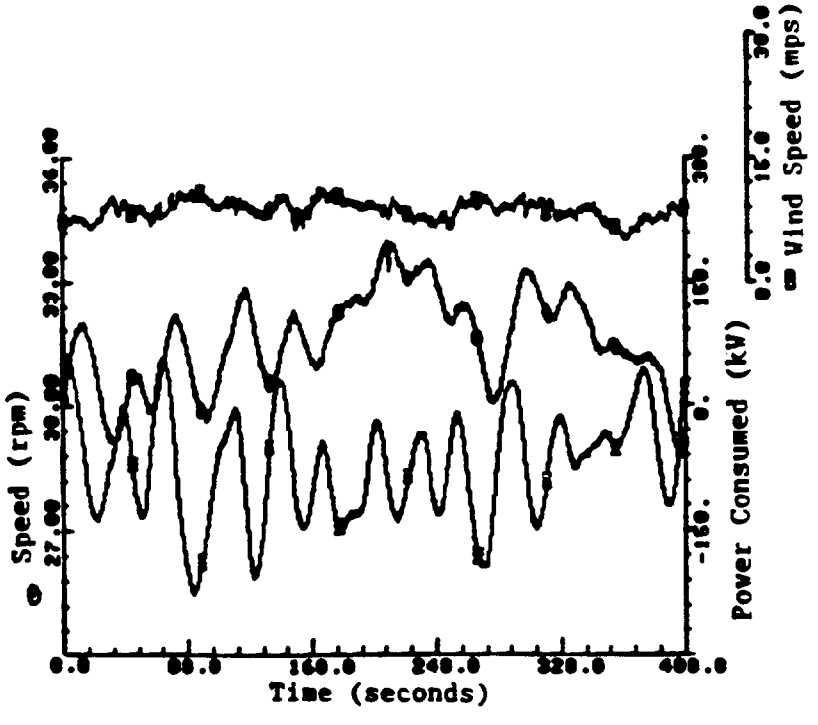

Figure 4 - Variable-Speed Operation

the same wind speed average. Both graphs display the same three variables. The top line on the graphs is the wind speed as measured two rotor diameters upstream from the turbine at equator height. In both test runs, the wind speed averaged about 8.5 mps. The middle line is the turbine's rotational speed in rpm. The bottom line is the electrical power from the utility system. In these figures, negative power is power generated by the wind turbine, and positive power is power consumed by the turbine.

Evident on Figure 3 is the under-damped speed regulator in the variable speed generator system. This speed regulator controls the turbine's rotational speed to +/- 5% of the selected speed. Since the speed regulator is under-damped, the turbine's speed oscillates after a change in wind speed. Both at around 65 seconds and again around 190 seconds, small changes in wind speed cause the turbine speed to oscillate, and then slowly re-approach steady state operation. While the speed variations are relatively small, they result in fairly large power flow swings as the LCI corrects for the speed error. These large power swings could become significant with a high penetration of variable speed wind turbines on a utility system. Similar results have been reported by others.[6] Methods for reducing fixed speed power swings are being investigated.[7]

The variable speed algorithm as implemented changed the turbine's rotational speed by 0.1 rpm/sec. In the 20 second period between set point up-dates, the turbine's speed could have been changed by two rpm. A two rpm change would have been driven by a change in average wind speed of only 0.5 mps. The under-damped speed regulator exacerbates this problem by continuing the speed oscillations after the turbine has reached a new operating speed.

CONCLUSIONS

Experimentation with operation of the turbine in variable speed mode has shown the dependance of power output on the various parameters. So far the following parameters appear to be significant with respect to energy output and power quality:

Speed regulation of the generator
Wind speed averaging period
Rate of change of the turbine's speed
Slope of the desired operational speed
vs wind speed

The under-damped nature of the Test Bed's speed regulator can cause power swings of up to 200 kW over a 20 second period. This power swing could have a significant effect on the electrical utility system.

The wind speed averaging period and the rate of change of the turbine's rotational speed together control how fast the turbine's operating speed is changed for a given wind turbulence level. With the implementation of the present algorithm, the rate of change of the turbine's speed was too large. The control system was constantly speeding up or slowing down the turbine, which consumed a significant amount of power. The next step in the algorithm's development will be to reduce the rate of change of the turbine's speed.

The slope of the desired operating speed vs wind speed, as shown in Figure 2, has a significant effect on the performance of the control algorithm. Small changes in wind speed will produce significant changes in desired operating speeds. This step slope makes the control algorithm sensitive to small wind speed changes.

SUMMARY

The operating performance of the Test Bed has been defined over several fixed speeds. This data was used to developed an operating strategy for variable speed operation which maximizes the power output of the turbine for the given wind. An initial implementation of the control strategy has been completed and evaluated. From this evaluation, the control algorithm will be modified and re-tested.

This first variable-speed algorithm has suggested that successful variable-speed control will require careful attention to wind speed averaging windows and the rate that the turbine's rotational speed will be changed.

ACKNOWLEDGEMENTS

The work reported in this paper has been supported by several personal, especially Thomas D. Ashwill and William A. Stephenson who participated in many discussions on how to proceed with variable speed operation.

REFERENCES

1. Ashwill, T.D., Berg, D.E., Gallo, L.R., Grover, R.D., Klimas, P.C., Ralph, M.E., Rumsey, M.A., Stephenson, W.A., Sutherland, H.J., "The Sandia 34-Meter VAWT Test Bed," Proceedings of Windpower '87, October 5-8, 1987, San Francisco, California, pp 298-306.

2. Ralph, M.E., "Design and Control of a Variable-Speed Generator System for a WECS," Proceedings of Windpower '87, October 5-8, 1987, San Francisco, California, pp 55-59.

3. Berg, D.E. and Klimas, P.C., "Initial Aerodynamic Performance Measurements for the Sandia 34-Metre Diameter Vertical-Axis Wind Turbine," to be published in Proceedings of the Ninth ASME Wind Energy Symposium, January 14-18, 1990, New Orleans, Louisiana.

4. Ashwill, T.D. and Veers, P.S., "Current Structural Response Measurements for the Sandia 34-meter VAWT Test Bed," to be published in Proceedings of the Ninth ASME Wind Energy Symposium, January 14-18, 1990, New Orleans, Louisiana.

5. Vachon, W.A., "The Effect of Controls on Life and Energy Production of the 34-m VAWT Test Bed," Proceedings of the Eighth ASME Wind Energy Symposium, January 22-25, 1989, Houston, Texas.

6. Herrera, J.I., Reddoch, T.W., Lawler, J.S., "Experimental Investigation of a Variable Speed Constant Frequency Electric Generating System form a Utility Perspective," DOE/NASA/4105-1, NASA CR-174950, NASA Lewis Research Center, Cleveland, Ohio, May 1985.

7. Ralph, M.E., "A Model of the 34-metre VAWT Variable-Speed Control System," to be presented at The Ninth ASME Wind Energy Symposium, January 14-18, 1990, New Orleans, Louisiana.

Proceedings of the Canadian Wind Energy Association Conference
18-21 September, 1989

TEST RESULTS AND STATUS OF THE DOE/SANDIA 34-M VAWT TEST BED

H. M. Dodd, T. D. Ashwill, D. E. Berg,
M. E. Ralph, W. A. Stephenson and P. S. Veers
Wind Energy Research Division
Sandia National Laboratories
Albuquerque, New Mexico

ABSTRACT

The DOE/Sandia 34-m VAWT Test Bed has been fully operational for over a year. During that time extensive performance data have been gathered. This paper first briefly discusses the background and evolution of this research turbine and its testing philosophy. Next, specific results are presented in the areas of aerodynamics, structural dynamics, and operation and control. The aerodynamics section primarily discusses measured versus predicted output power. In the structural dynamics section turbine response is presented with results shown for rotating natural frequencies and stresses at critical (blade) locations. Finally, operation and control results are presented, which include normal start/stop, speed variation, emergency handling and power quality issues.

INTRODUCTION

The DOE/Sandia 34-m VAWT (Vertical Axis Wind Turbine) Test Bed is a unique research machine whose design and operation include the latest innovations in Darrieus technology[1]. Of particular note are the blades, the structural design, the variable speed/dynamic control operations and the turbine's extensive instrumentation. The blades incorporate variable chord and variable section profiles, including the first VAWT-specific, natural laminar flow (NLF) airfoil sections. The structural design includes unique stress-reducing features as well as a modular configuration to allow flexibility in testing various configurations. The variable-speed-constant-frequency (VSCF) generator and programmable controller permit a range of operating strategies for studying not only the performance of the machine, but also its impact on the utility grid. In order to accurately establish machine performance, very extensive instrumentation and data acquisition/analysis subsystems are incorporated into the VAWT Test Bed that have advanced the state of the art in wind turbine performance analysis.

This paper discusses Test Bed performance to date in three major areas: aerodynamics, structural dynamics and variable speed/control strategy. In addition, the paper will begin with an overview of the testing program, with special emphasis on the problems encountered and how they have been

resolved. In general, the Test Bed program has been extremely successful; it has been completed within original budget estimates and on schedule. As this report will show, performance has been very promising; but more data are needed to complete the initial characterization phase.

TESTING OVERVIEW

Current Status

At the present time (August 1989) the machine has operated for approximately 300 hours (230 with the blades on the turbine). Because the occurrence of winds is unpredictable, several parts of the test plan[2] are often pursued simultaneously. However, a major limitation is that the turbine must be tested cautiously in each higher wind regime and then the structural data must be analyzed before proceeding with continuous operation at that wind speed. Tests cannot be conducted at a wind speed until it has been determined that complete control can be maintained without unacceptable levels of strain and vibration. Both control and strain/vibration levels are directly related to braking, which is being tested at the same time.

Resonance surveys have been completed for rotor speeds up to the design maximum of 40 rpm at wind speeds up to 18 m/s. Data on winds above this level are yet to be collected. Approximately 63 hours of data have been collected at 28, 34, and 38 rpm at average wind speeds up to 16.4 m/s for basic aerodynamic and structural characterization. Work on braking techniques has been done simultaneously as various caliper sequences and variable hydraulic orifices have been incorporated. Braking experiments at wind speeds of 17.7 m/s and 38 rpm have been performed.

Up to the present time, testing has concentrated in four areas, depending on wind speed windows and the results of structural analyses. They are:

1. Start-up drag tests to determine the effect of temperature on tare torque (zero wind condition required).

2. Coefficient of drag at zero angle of attack tests to determine the amount of aerodynamic drag of the blades (also zero wind condition required).

3. Vibration/resonance tests to confirm structural response predictions and ensure a safe operating envelope.

4. Aerodynamic characterization tests to verify performance predictions and allow accurate projections of performance for the next generation of VAWTs.

Operational History

Drive Train. Problems were encountered with the high speed shaft torque sensor early in the test program as a result of excessive transmission

vibration. Therefore, the transmission and generator were instrumented with three vibration monitors, and the high speed shaft torque sensor has been replaced with two commercial couplings and a dummy shaft. Data from the monitors show that the axial vibration of the high speed shaft will exceed 25.4 mm/s (1.0 in/s) RMS when the turbine is driven by the motor/generator in little or no wind and rotor acceleration is about 7 rpm/min (the vibrational amplitude is proportional to the acceleration rate). This vibration level is in excess of that recommended for long term operation. The vibration instrumentation is also utilized to monitor rpm, stand/column vibration and brake disc temperature. The control program has been modified to use these sensors to ensure safe operation of the turbine. As a result of early test data, the drive train torsional stiffness has been increased from 10k lb-in/radian to 20k lb-in/radian.

Brakes. Brake tests have included measurements of the coefficient of friction, stopping capability, strains, timing, heating, and water effects (to determine braking efficiency in adverse weather). Numerous hardware problems were addressed: hydraulic valves were changed to pneumatic operation; hydraulic cylinders were rebuilt to eliminate leakage; a warped brake disc made adjustments less precise; the hydraulic reservoir was enlarged; fittings have failed with large losses of fluid; and a mechanical shock required the addition of mechanical reinforcements and the addition of orifice valves. Brake timing was adjusted to ensure the pump/reservoir system can supply the required volumes of oil in a timely manner. As a result of these modifications, the current brake performance is very good.

Control. The fully programmable turbine control system has undergone continuous development throughout the testing program. The turbine may now be started, run at various rpms, and stopped on a routine basis. Additional instrumentation has been incorporated to measure vibration, temperature, and rpm. Control programs have been modified to accommodate independent brake caliper pair operation, start-up timing to accommodate the hydraulics, and stopping sequences to minimize strain and handle high winds. Preliminary tests of automatic operation have been conducted, and software to permit fully automatic operation is under development.

Seals. The initial column grease seals failed and new seals have been designed, fabricated and installed. Thus far they are functioning properly. Some modifications to the test plan were required to accommodate this activity (i.e., aerodynamic characteristic tests were held up until the new seals could be fabricated).

Software. The Data Acquisition and Analysis System (DAAS) was designed to perform basic data acquisition and analysis. It has been extensively enhanced to provide additional capabilities and improve "user friendliness." For example, the system can now bins[3] data on a real time basis and automatically zero strain gauges, a great aid to data collection.

Instrumentation. Most of the 34 strain gauge circuits that have been monitored by the DAAS have performed well, of particular importance since they provide critical data for proceeding through the early stages of the test plan. Three gauges failed recently, after heavy rains. The four gauge circuits placed on the brake paddles had to be moved from a relatively low

strain location to a higher strain location in order to provide meaningful signals.

Daily Operations. A turbine operating procedure has been written, as has an inspection and maintenance procedure, complete with check lists. During one inspection of the turbine blades, peeling paint that had a detrimental effect on the aerodynamic performance of the turbine was discovered (see the Aerodynamics section below). This problem has been corrected and a new set of aerodynamic data has been collected.

Thus far, the turbine has operated over its entire rpm range in transient winds up to 20 m/s. Normal, alarm, and emergency stops have been recorded, including an emergency stop at 42 rpm in 17.7 m/s winds when the generator power rating was exceeded. Major cable resonances have been observed at 22-23 rpm and 36 rpm. The beginning of a predicted machine resonance has been observed at 40 rpm (see the Structural Dynamics section below). Temperature effects on cable resonances have also been observed. Cable snubbers (called node drivers) have been designed and installed to change the effective guy cable lengths at low temperatures in order to avoid these cable resonance conditions.

AERODYNAMICS

The Test Bed blades are step-tapered with five sections each. They are constructed of extruded 6063-T6 aluminum. The root sections (those nearest the tower) are straight with a 1.22-m (48-in) chord NACA 0021 profile. The equatorial sections, with a 17.1-m (675-in) radius of curvature, have a 0.91-m (36-in) chord SAND 0018/50[4] NLF profile. The intermediate sections (between the root sections and the equatorial section) have a 30.0-m (1180-in) radius of curvature and a 1.07-m (42-in) chord SAND 0018/50 NLF profile.

Turbine performance predictions have been made with the double-multiple streamtube computer code known as SLICEIT. This code is based on the CARDAA code developed by Paraschivoiu[5] and uses the Gormont dynamic stall model[6] as modified by Masse[7]. It accounts for local Reynolds number effects, and is capable of analyzing the performance of rotors with multiple section profiles and step changes in chord length. No attempt was made to model the effects of the discontinuities in chord size and the hardware at the blade-to-blade joints. The airfoil data used in predicting the turbine performance came from two sources: The NACA 0021 data is from reference 8, and the SAND 0018/50 is a combination of data obtained in a Texas A&M University test in 1983, an Ohio State University test in 1985, and predictions from the Eppler code[9].

The initial performance measurements are shown in Figure 1, along with the predicted performance of the machine. The performance was very disappointing, falling well below the predicted values over the entire wind-speed range. Inspection of the blades revealed extensive regions on the SAND 0018/50 profiles where the paint had flaked from the leading edge. The resulting series of forward facing steps with a height of approximately 0.25 mm (0.010 in) were a very effective boundary layer trip. Figure 2, a photograph of a typical section of the blade leading edge, shows the extent

of paint failure. There was no evidence of paint failure on the leading edge of the NACA 0021 blade sections. We elected to remove the remaining paint from the problem areas rather than repair them. All of the paint was removed from an area extending at least 1 cm (0.4 in) back from the leading edge. If flaking had occurred further aft, we removed additional paint until we reached an area where the paint adhered well to the metal. After scraping the paint off, we used fine grit emery cloth to fair the remaining paint smoothly into the bare metal. The resulting transition was smooth enough that it could not be detected by touch. Although this repair altered the blade profile somewhat, we feel that the effect on performance is negligible.

Turbine performance following the cleanup of the leading edge is shown in Figure 3. Although the measured performance agrees fairly well with the predictions, significant differences exist at both low and high wind speeds. We feel that the differences at high wind speeds are due to the use of the simplistic Gormont model to estimate dynamic effects. We are currently analyzing wind-tunnel dynamic stall data in an effort to improve the stall model. We attribute the differences at low wind speeds to two causes: 1) the blade-to-blade joints are extremely 'dirty' from an aerodynamic point of view, resulting in high drag and poor blade performance at low angles of attack; and 2) performance predictions at low wind speeds are notoriously inaccurate, partly because the assumptions on which the models are based are violated at low wind speeds.

Current plans call for the installation of streamlined fairings over the blade-to-blade joints in the near future. This will address the impact of the first of the two factors mentioned above that are assumed to impact low speed operation. This is important because commercial designs would almost certainly not use the "dirty" kinks (which were partially chosen for their ability to allow future changes in the Test Bed blade configuration).

STRUCTURAL DYNAMICS

The structural dynamics of a VAWT are complex. Not only is the structure rotating, which modifies its blade stiffness due to centrifugal effects, but the blade loads are also dynamic due to constantly changing angle of attack and wind that is never steady. For the Test Bed, additional complications in the structural loads are created by its variable speed capability and multiply-sectioned blades composed of different chord length segments. In addition to normal operation (rotation rates to 40 rpm and winds to 20 mps), the machine is designed for severe loading conditions including parked survival in winds up to 68 mps (150 mph), large variations in guy cable tension, and emergency stopping loads.

In the recent past, the structural dynamic analyses of VAWTs have been accomplished with the use of the NASTRAN-based structural codes FEVD[10] and FFEVD[11], which determine natural frequencies and forced responses. These codes, and other design tools developed by Sandia, were used in the Test Bed design procedure. Now that the turbine is operational and providing large amounts of data, comparisons with design predictions are being made to evaluate and improve the design/analysis tools.

Resonance surveys were conducted by operating the turbine for short periods of time at several rotation rates from 6 through 40 rpm in low, medium, and high wind conditions. These surveys characterized the natural frequencies of the rotor, drive train, and guy cables and enabled us to determine the mean and approximate operating stress levels. Time series records were collected for longer periods during operation to create statistically averaged data using a "binsing" methodology.[3]

Comparisons between predicted and measured data are covered below in the areas of deterministic stresses, operating stresses, and the natural frequencies of the rotor and guy cables.

Deterministic Stresses

Deterministic stresses consist of stresses caused by gravity and steady centrifugal forces. In VAWT blade shape design, the deterministic flatwise stresses are usually minimized by employing a straight/single-curve/straight approximation to a troposkien (the shape required to eliminate all flatwise bending stresses). A better approximation of this shape results by implementing different radii of curvature along each blade section with slope discontinuities at the blade joints where mass is concentrated. For the Test Bed, the blade shape is designed to approximate a 37.5 rpm troposkien and contains slope discontinuities or "kinks", of 6-7 degrees at the blade-to-blade joints. Design calculations[12] show that these implementations reduce peak mean flatwise stresses approximately fifty percent below the straight curve/straight stresses, increasing blade fatigue life by a factor of 2 to 4.

Gravity stresses (due to the blade weights) were measured as the blades were mounted to the turbine. It is important that this measurement be performed quickly because strain gauges will drift and the stresses due to gravity will no longer be retrievable. Comparisons of predicted and measured gravity stresses have yielded good results[13].

Centrifugal stresses were obtained during the resonance surveys. Figure 4 is a plot of both the measured and predicted flatwise centrifugal bending stresses at 40 rpm. There is excellent agreement between the measured and predicted values. Comparisons have also been made at 10, 15, 20, 28, 32,and 36 rpm; similar agreement is observed.

Natural Frequencies

Before operating the turbine, a modal test was performed on the stationary rotor by Sandia's Modal Test Group[14]. Accelerometers were temporarily attached to the blades, tower and cables to measure turbine response. Two types of input excitation were used: step relaxation (snap releasing) and ambient wind excitation. The measurements were used to estimate mode shapes, their frequencies of vibration, and modal damping coefficients.

In Table I the first eight natural frequencies obtained by modal testing are compared with frequencies obtained analytically using FEVD. The mode

number and shape designator are listed in the first two columns. The third column shows the natural frequencies for the stationary rotor measured by the modal test during wind excitation. Column four lists the predicted values from FEVD, and column five lists the relative deviation between the results presented in columns three and four. The last column lists measured frequencies obtained from amplitude spectrum plots of strains taken during the the wind-excited modal test. There is excellent agreement between the measured and predicted frequencies for the first eight modes. All predicted modal frequencies agreed to within 2.5% of the measured values except for the first blade edgewise mode (5.2%). As shown in column five, the peak frequencies from the strain amplitude spectra of the stationary rotor also agree closely with those measured by the modal test.

Spectral plots, obtained from the data collected during the resonance surveys, permitted the determination of modal frequencies, see Figure 5. From these data, one can estimate the accuracy of predicted rotor modes as a function of rpm. The lower frequency modes (below 3 Hz) all track along their predicted mode lines very well. The two measured first flatwise modal frequencies are the antisymmetric and symmetric modes, which are predicted to vibrate at nearly the same frequency. The first blade edgewise mode (1BE) was underpredicted by 5% at zero rpm, but above 25 rpm the observed and predicted frequencies coincide. Overall the prediction of natural frequencies agree well with measurements over the entire range of turbine operating speeds.

The first tower in-plane mode (1TI) crossing of the 3P (three "per rev") excitation occurs at 40.5 rpm. This resonance is observed, as an increased rotor vibration, at turbine speeds more than one rpm slower than the crossing. Figure 6 is a plot of the upper root lead-lag stress and rpm at the edge of the resonance. The turbine controller was set to run the machine at a nominal 39.5 rpm, but the rotation rate was oscillating between 39 and 40 rpm. As the rpm increases, the response begins growing and continues increasing through 40 rpm. When the rpm slows to almost 39, the response dies out considerably. The tower-in-plane mode at these rotation rates has coupled with blade-edgewise motion to create large lead-lag cyclic stresses at the blade roots. Operation has been restricted to 38 rpm and below to avoid this resonance.

The turbine is supported at the top by three pairs of guy cables, each 2.5 inches in diameter. The lowest two guy cable frequencies, modes n=1 and n=2, were designed to vibrate at 0.81 Hz and 1.62 Hz, respectively, at a nominal cable tension of 826 kN (186,000 lb). Design calculations were made assuming a uniform cross-sectional area for the entire cable length. This places the first cable mode below 2P and the second mode between 2P and 4P for the entire operating range, as shown in the cable fanplot, Figure 7. Cable frequencies were measured during the modal testing and are also shown in Figure 7. The measured natural frequencies of all but the first mode are lower than predicted due to the heavy cable attachment hardware at the lower cable connection. This hardware violates the uniform cable assumption. A new analytical tool that includes the ability to model variation in guy cable mass distribution has been developed and predicts the first four cable modes to be 0.76, 1.23, 2.05, and 2.95 Hz, very close to the measured values.

The 2P crossing of the second cable mode at 37 rpm is in the middle of the operating range, and will interfere with the turbine operation in the variable speed mode. Cable snubbers were installed at thirty-five feet from the bottom of the cable to force a node in the cables at that location. These snubbers, coupled with an adjustment to the main guy cable tension, move the second cable mode above the operating range of the turbine and keep the first cable mode below it.

Operating Stresses

Following completion of initial resonance surveys, many hours of data have been collected at 28, 34, and 38 rpm at average winds up to 16.4 mps (36 mph). Binsing of this data allows for comparison of measured and predicted operating stresses.

Figures 8 and 9 show the lead-lag and flatwise RMS stresses in the blade near the lower tower attachment as a function of windspeed at 28 rpm. Analytical stress level estimates (triangles) generated by FFEVD are included in the plots at four wind speeds. The FFEVD calculations included zero turbulence and no damping. For both locations, FFEVD predictions compare well with data at winds below 12 mps. Above 12 mps FFEVD tends to overpredict the lead-lag stresses and significantly underpredict the flatwise stresses. Predictions from a second analytical code, TRES4[15] are included (squares). TRES4 is a NASTRAN-based code that includes wind turbulence and damping. The two TRES4-generated analytical points shown on each curve included 10% turbulence intensity in the incident wind and 2% modal damping (flatwise only) plus 2% structural damping. At high winds, these analytical results are closer to the measured values than the FFEVD predictions are. Further data comparisons are made in reference 16.

VARIABLE SPEED/CONTROLS

The Test Bed incorporates a Variable Speed Constant Frequency (VSCF) generator and a Programmable Logic Controller (PLC). These two subsystems allow considerable flexibility in conducting tests on the turbine. The turbine can be operated as a fixed speed machine, or continuously variable or distinct multiple speed control strategies can be investigated. This section of the paper will discuss the salient features of the VSCF generator and the PLC. Operating strategies that utilize the VSCF generator will be described and actual operating data will be presented. Finally, some of the power quality issues of the Test Bed will be presented.

The VSCF generator system (VSGS) converts the variable speed mechanical power into constant frequency electrical power that is synchronized to the utility system. The VSCF generator system is a variable speed Load Commutated Inverter (LCI) motor drive with a synchronous generator. The speed of the turbine is controlled by the LCI by regulating the current from the generator. The rated power output of the generator is 650 kW. The VSGS has a utilizable operating range from 275 to 1900 rpm, which corresponds to a rotor speed range of 5.8 to 40 rpm.

The Test Bed's control system is implemented on the PLC, which is responsible for monitoring the turbine, generator system, wind, and utility system and implementing constant and variable speed control algorithms. The PLC is programmed in a high level language allowing changes to the control algorithm to be made quickly.

Turbine Operation

The VSGS allows the turbine to be operated at discrete speeds as well as over selected variable speed ranges. The variable speed capability is also used in starting and stopping the turbine. The advantage of the variable speed capability during starting and stopping includes reduced stresses on the turbine blades, since the torque transients are reduced. In addition, there is a reduced current demand on the utility system because high starting current is not drawn.

During startup, the VSGS accelerates the turbine at a very low rate up to its operating speed. This rate of the speed change is controlled by the PLC and can be varied.

Normal stopping is accomplished by reducing the speed of the turbine down to 6 rpm, at which time the mechanical brakes are applied. The deceleration rate of the turbine is controlled by the PLC and also can be varied. By reducing the speed of the turbine with the generator, we can extract the kinetic energy in the spinning turbine and convert it into electrical energy. As well as recovering energy, the blade stresses due to braking are reduced. Figure 10 illustrates a normal stop from 15 rpm. The top line in the figure shows the speed of the turbine gradually being reduced from 15 to 6 rpm where the mechanical brakes are applied. The lower line in Figure 10 shows the response of a strain gauge installed on the lower root of one of the blades. As the brakes are applied, the blade root sees a stress swing of approximately 15 MPa. An equivalent stop from 15 rpm using only the brakes results in the same strain gauge recording a stress swing of over 40 MPa.

A VSGS offers a lot of flexibility in testing a research turbine and should also increase energy production. However, there are several factors tending to increase costs that may offset this increase in energy capture. These include: increased maintenance cost, reactive power demand, speed regulation requirements and quality of output power.

During normal operation, the VSCF generator system controls the turbine speed. The VSCF generator system is not as stiff as an induction generator, so as turbulence in the wind perturbs the turbine, the turbine's speed can vary up to 5%. Figure 11 shows a typical rotational speed plot for the turbine. The top line in the Figure is the wind speed as measured up-wind from the turbine. The bottom line shows the turbine speed varying about the set speed of 38 rpm. This speed variation increases the rpm window around structural resonances which must be avoided.

Power Quality

Since the VSCF generator switches the current to the generator during each cycle, harmonics of 60Hz are produced. The generator is connected to the utility system through a delta connected transformer, which prevents undesirable harmonics from entering the utility system. Qualitatively, the power produced by the turbine has not had a noticeable effect on the computer or instrumentation at the site. However, detailed measurements of power quality have not yet been completed.

REFERENCES

1. Klimas, P. C., Dodd, H. M. and Clark, R. N., "An Overview of the DOE/Sandia/USDA Vertical Axis Wind Turbine Test Bed Project," Proceedings of Windpower '87, October 5-8, 1987, San Francisco, California, pp 35-40.

2. Stephenson, W. A., "Test Plan for the 34 Meter Vertical Axis Wind Turbine Test Bed Located at Bushland, Texas," Sandia National Laboratories Report, SAND86-1623, December 1986.

3. Akins, R. E., "Performance Evaluation of Wind Energy Conversion Systems Using the Method of Bins - Current Status," SAND 77-1379, Sandia National Laboratories, Albuquerque, New Mexico, March 1978.

4. Klimas, P.C., "Tailored Airfoils for Vertical Axis Wind Turbines," SAND84-1062, Sandia National Laboratories, Albuquerque, New Mexico, November 1984.

5. Paraschivoiu, I., "Aerodynamic Loads and Performance of the Darrieus Rotor," Journal of Energy, 6(6):406 (1982)

6. Gormont, R.E., "A Mathematical Model of Unsteady Aerodynamics and Radial Flow for Application to Helicopter Rotors," US Army Air Mobility R&D Laboratory, Vertol Division, Philadelphia, Pennsylvania, Report on Boeing-Vertol Contract DAAJ02-71-C-0045, May 1973.

7. Masse, B., "Description de Deux Programmes d'Ordinateur pour le Calcul des Performances et des Charges Aerodynamiques pour des Eoliennes A'Axe Vertical," Institut de Recherche de L'Hydro-Quebec, Report IREQ 2379, Varennes, Quebec, July 1981.

8. Sheldahl, R.E., and Klimas, P.C., "Aerodynamic Characteristics of Seven Symmetrical Airfoil Sections Through 180-Degree Angle of Attack for Use in Aerodynamic Analysis of Vertical Axis Wind Turbines," SAND80-2114, Sandia National Laboratories, Albuquerque, New Mexico, March 1981.

9. Eppler, R., and Somers, D.M., "A Computer Program for the Design and Analysis of Low-Speed Airfoils," NASA TM-80210, 1980.

10. Carne, T.G., Lobitz, D.W., Nord, A.R., Watson, R.A., "Finite Element Analysis and Modal Testing of a Rotating Wind Turbine," SAND82-0345, Sandia National Laboratories, Albuquerque, New Mexico, October 1982.

11. Lobitz, D.W., and Sullivan, W.N., "Comparison of Finite Element Predictions and Experimental Data for the Forced Response of the DOE 100 kW Vertical Axis Wind Turbine," SAND82-2534, Sandia National Laboratories, Albuquerque, New Mexico, February 1984.

12. Ashwill, T.D. and Leonard, T.M., "Developments in Blade Shape Design for a Darrieus Vertical Axis Wind Turbine," SAND86-1085, Sandia National Laboratories, Albuquerque, New Mexico, September 1986.

13. Ashwill, T.D., "Initial Structural Response Measurements for the Sandia 34-Meter VAWT Test Bed," Proceedings of the Eighth ASME Wind Energy Symposium, Houston, Texas, January 1989.

14. Carne, T.G., Lauffer, J.P., Gomez, A.J., and Ashwill, T.D., "Model Validation of the Sandia 34-Meter Test Bed Turbine Using Substructured Modal-Testing," Proceedings of the Eighth ASME Wind Energy Symposium, Houston, Texas, January 1989.

15. Malcolm, D.R., "A Model for the Response of Vertical Axis Wind Turbines to Turbulent Flow Parts 1 and 2," Contractor Report, SAND88-7021, Sandia National Laboratories, Albuquerque, NM, July 1988.

16. Ashwill, T.D. and Veers, P.S., "Current Structural Response Measurements for the Sandia 34-meter Test Bed," to be published in Proceedings of the Ninth Wind Energy Symposium, New Orleans, Louisiana.

This research was sponsored by the U.S. Department of Energy, Wind/Ocean Technologies Division, under contract DE-AC04-76DP00789.

TABLE I. STATIONARY MODAL FREQUENCIES (Hz): MEASURED VS. ANALYTICAL

MODE NUMBER	MODE SHAPE*	MODAL ANALYSIS (WIND EXCITATION)	ANALYTICAL	ANALYTICAL/ MODAL DEVIATION	STRAIN GAUGE SPECTRA
1, 2	1FA/1FS	1.06	1.05	1.0%	1.06
3	1Pr	1.52	1.56	2.6%	1.50
4	1BE	1.81	1.72	5.2%	1.82
5	2FA	2.06	2.07	0.5%	2.14
6	2FS	2.16	2.14	1.0%	2.14
7	1TI	2.50	2.46	1.6%	2.50
8	1TO	2.61	2.58	1.2%	2.61

*Shape Key:

1FA = First flatwise - antisymmetric
1FS = First flatwise - symmetric
1Pr = First propeller
1BE = First blade edgewise
2FA = Second flatwise - antisymmetric
2FS = Second flatwise - symmetric
1TI = First tower in-plane
1TO = First tower out-of-plane

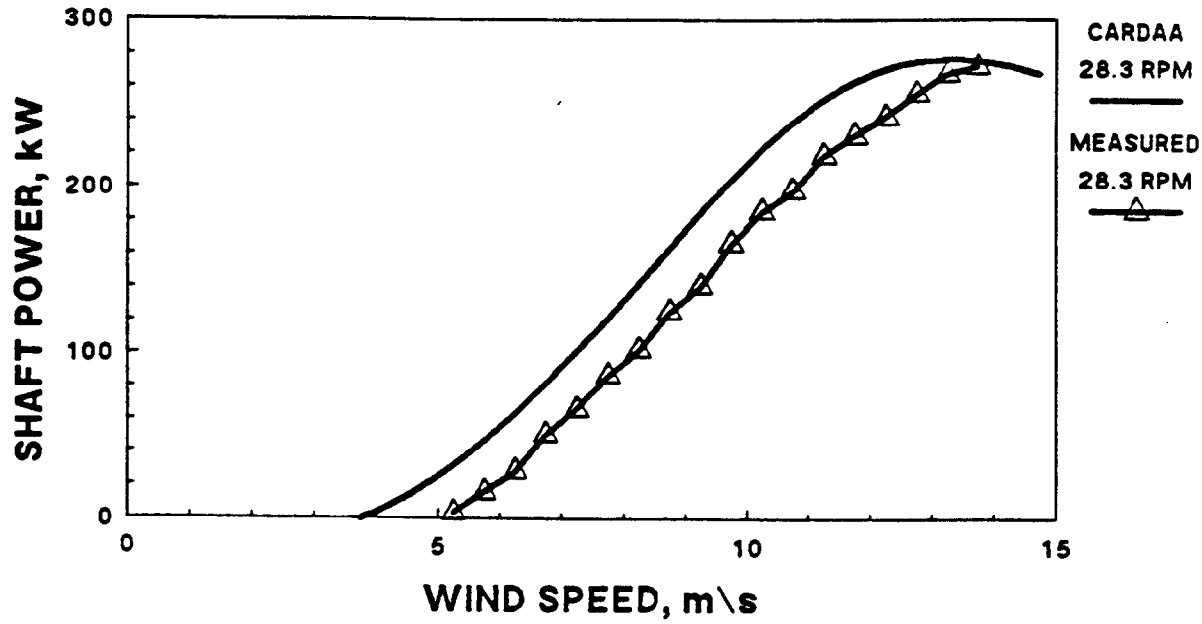

FIGURE 1A. PERFORMANCE RESULTS
PRIOR TO JANUARY 1, 1989
28.3 RPM

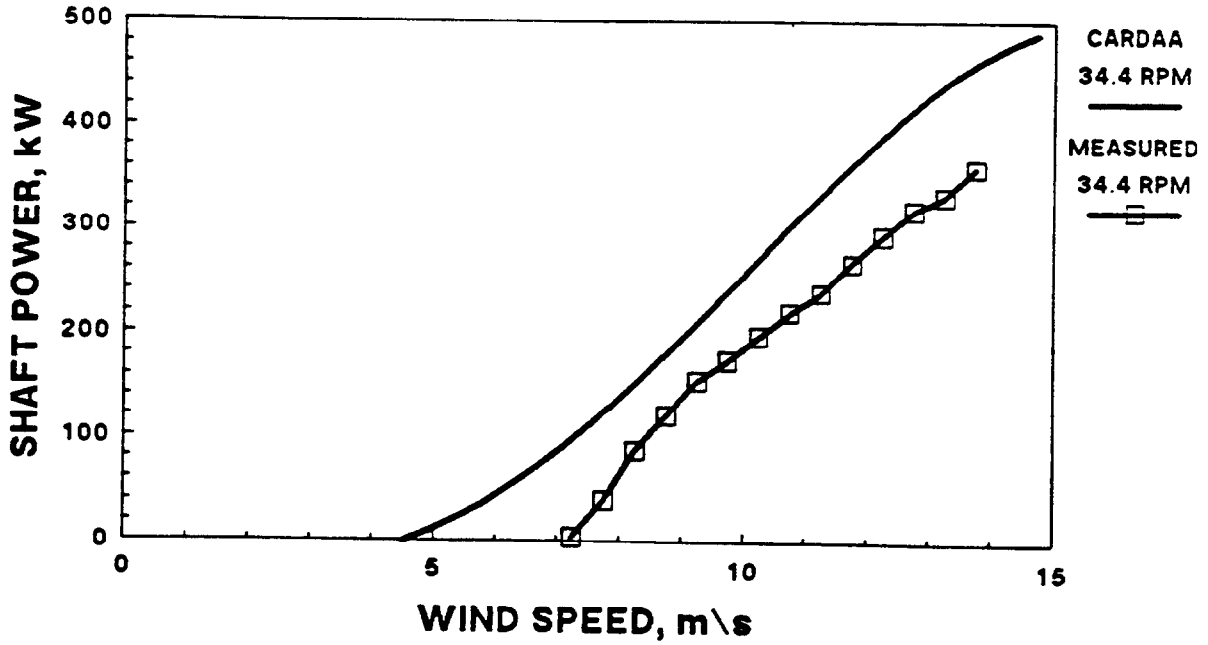

FIGURE 1B. PERFORMANCE RESULTS
PRIOR TO JANUARY 1, 1989
34.4 RPM

FIGURE 2. TYPICAL BLADE PAINT FLAKING

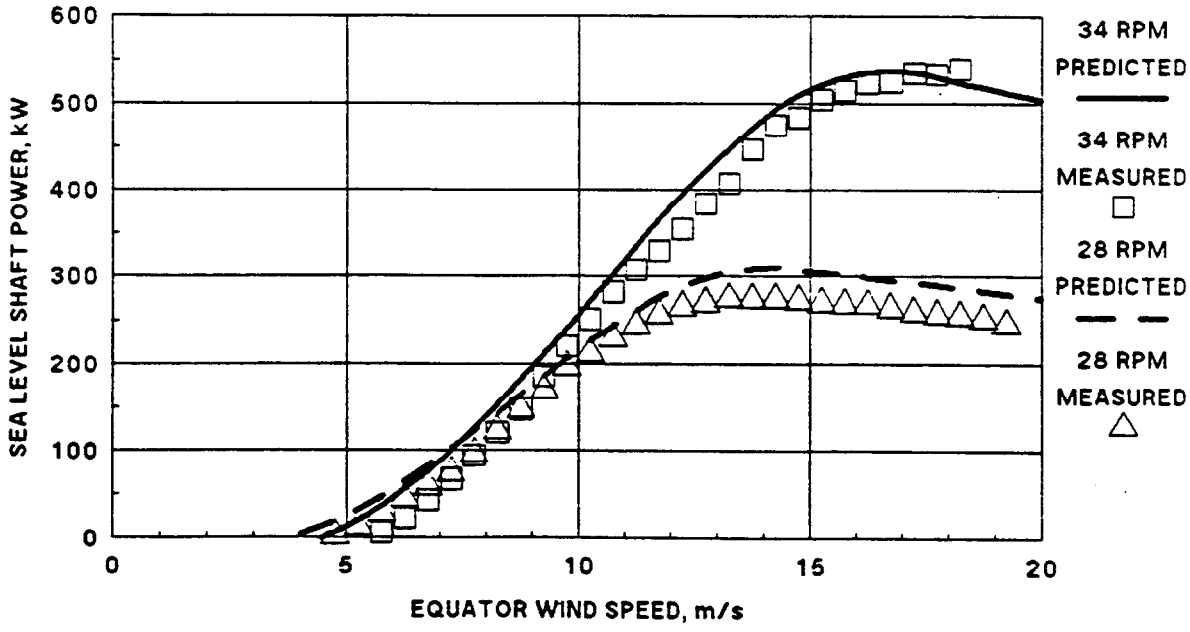

FIGURE 3. DOE/SANDIA 34-M TEST BED
RESULTS AFTER SANDING
(FEB-MAR, 1989)

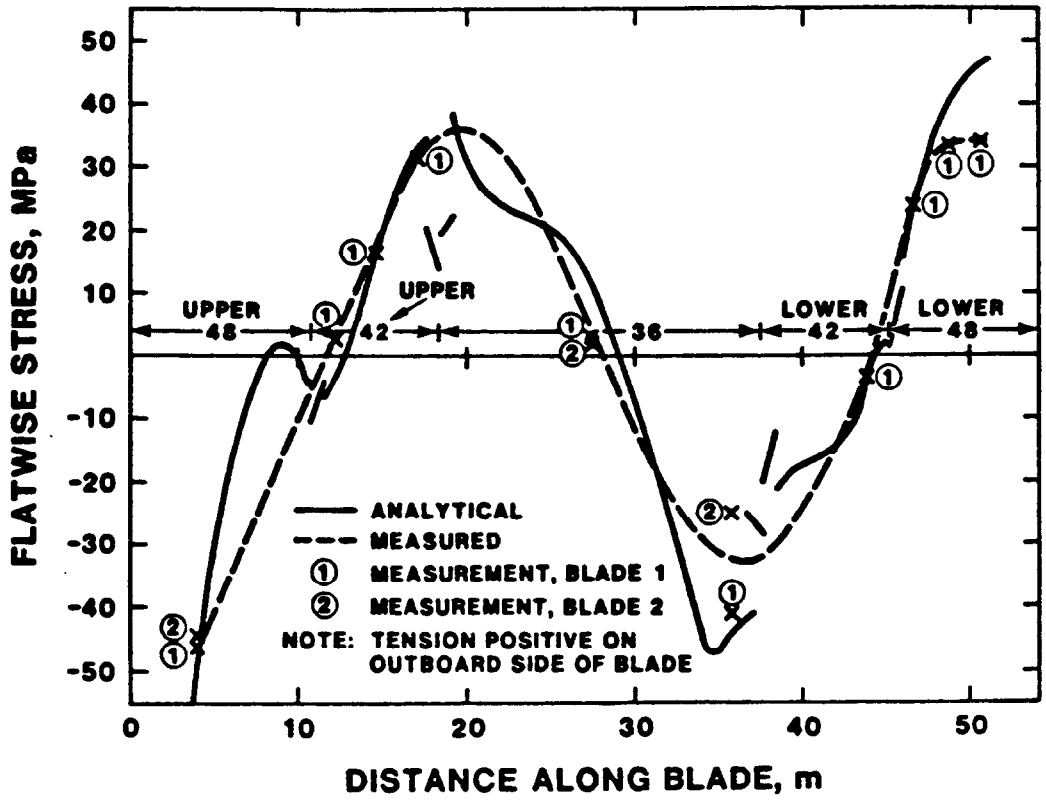

FIGURE 4. CENTRIFUGAL STRESS DISTRIBUTION AT 40 RPM

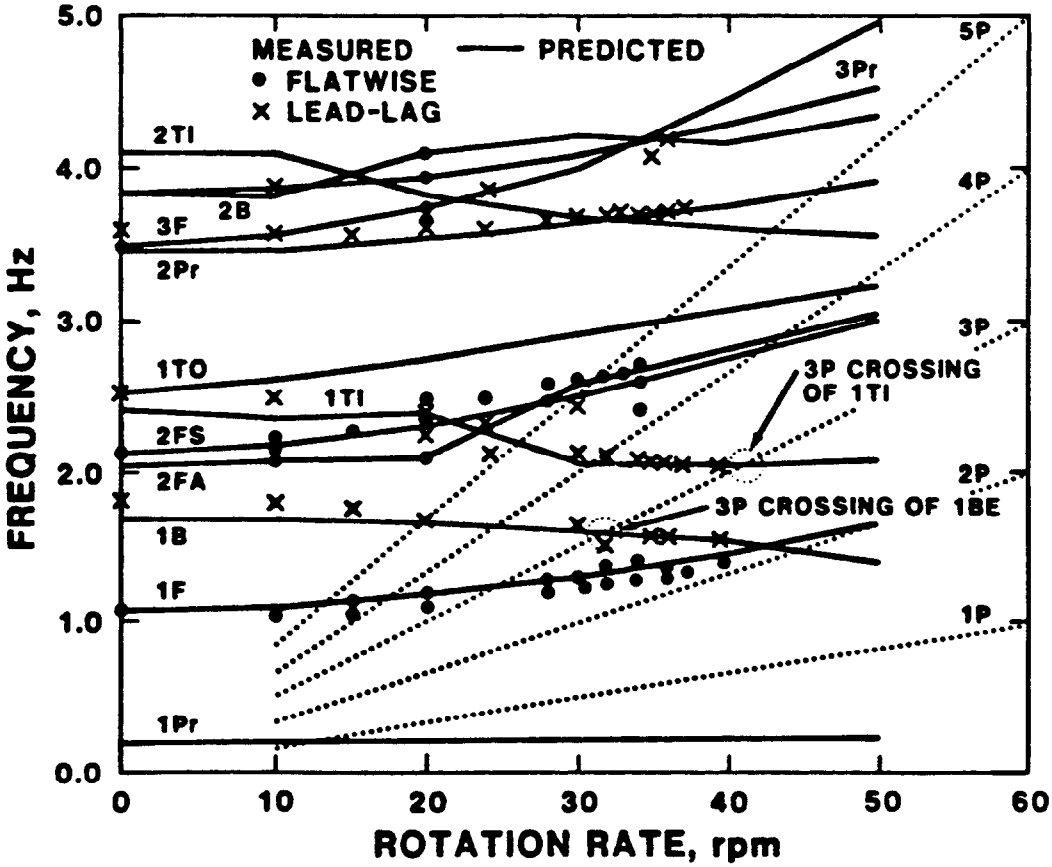

FIGURE 5. COMPARISON OF MEASURED AND ANALYTICAL MODAL FREQUENCIES

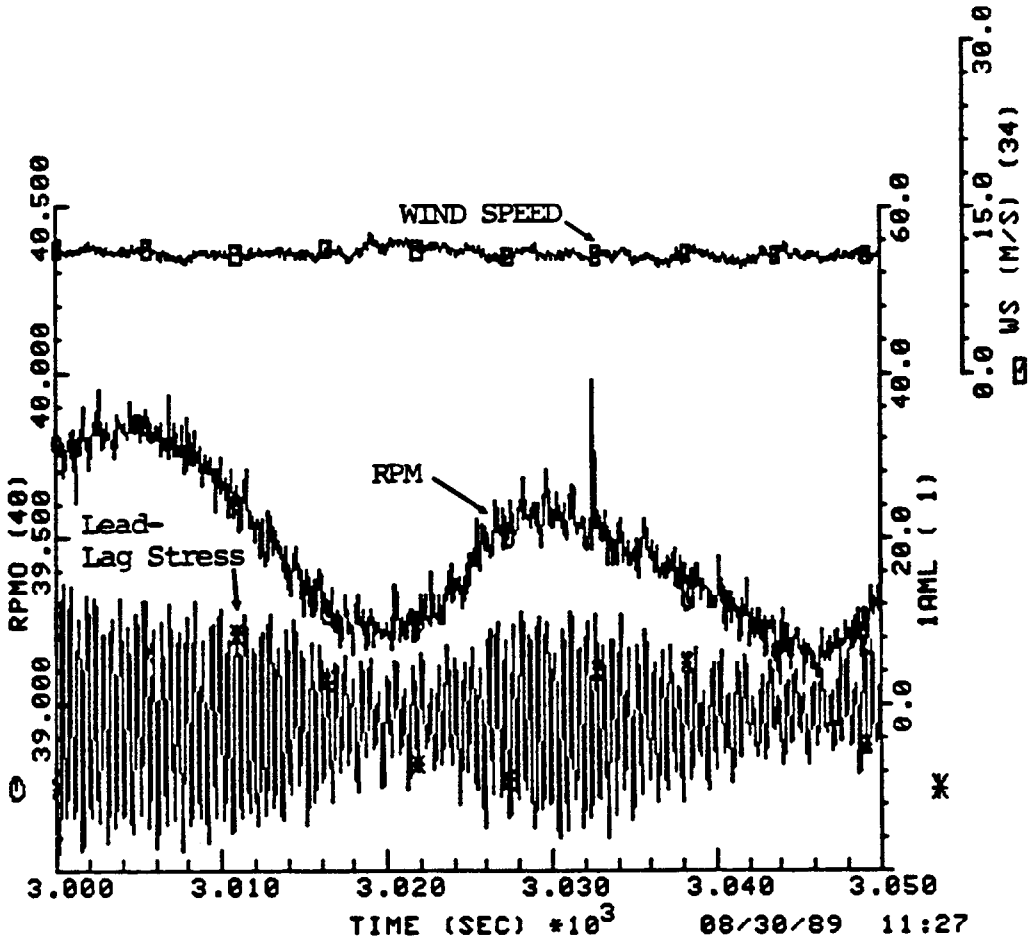

FIGURE 6. EFFECT OF 3P EXCITATION ON FIRST TOWER IN-PLANE MODE

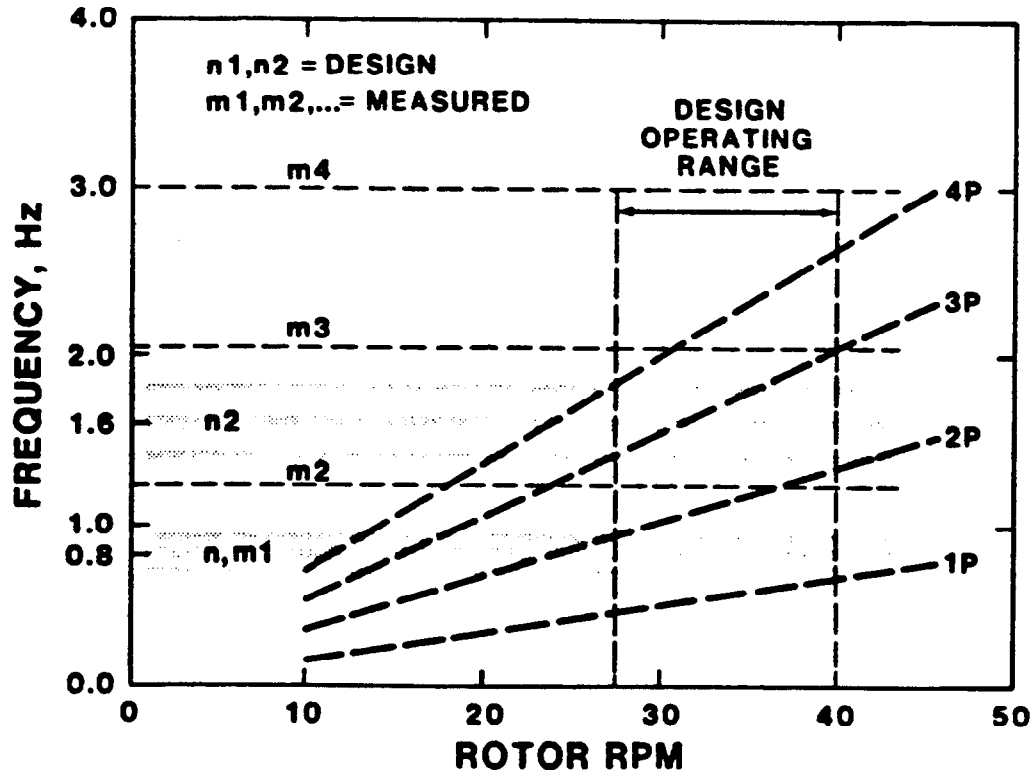

FIGURE 7. CABLE FANPLOT

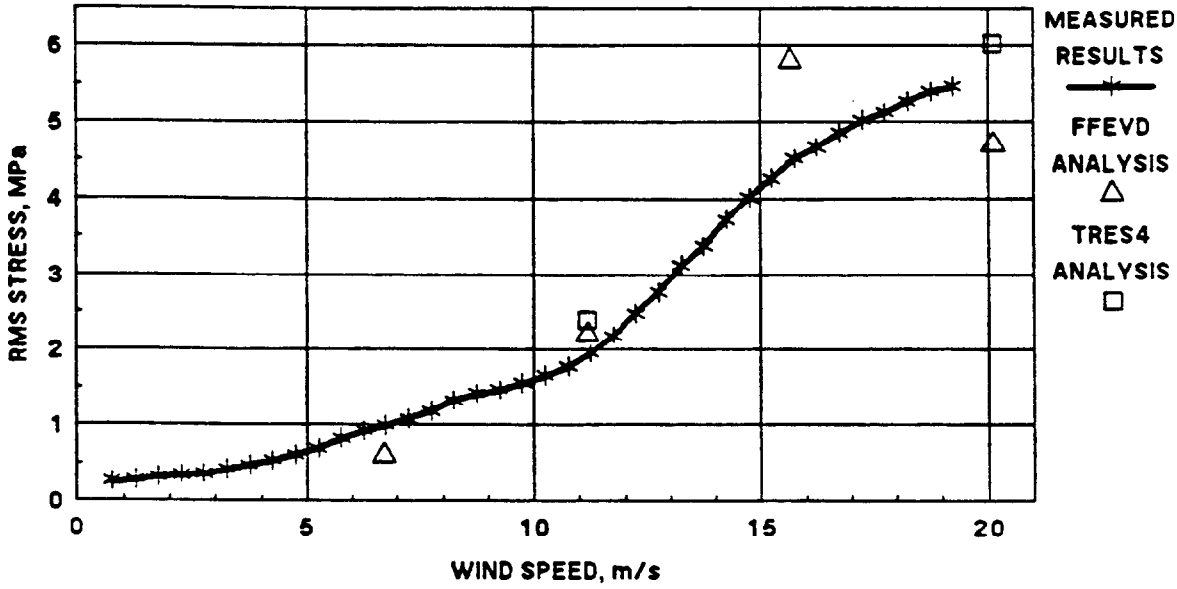

FIGURE 8. TEST BED LEAD-LAG STRESSES (28 RPM)

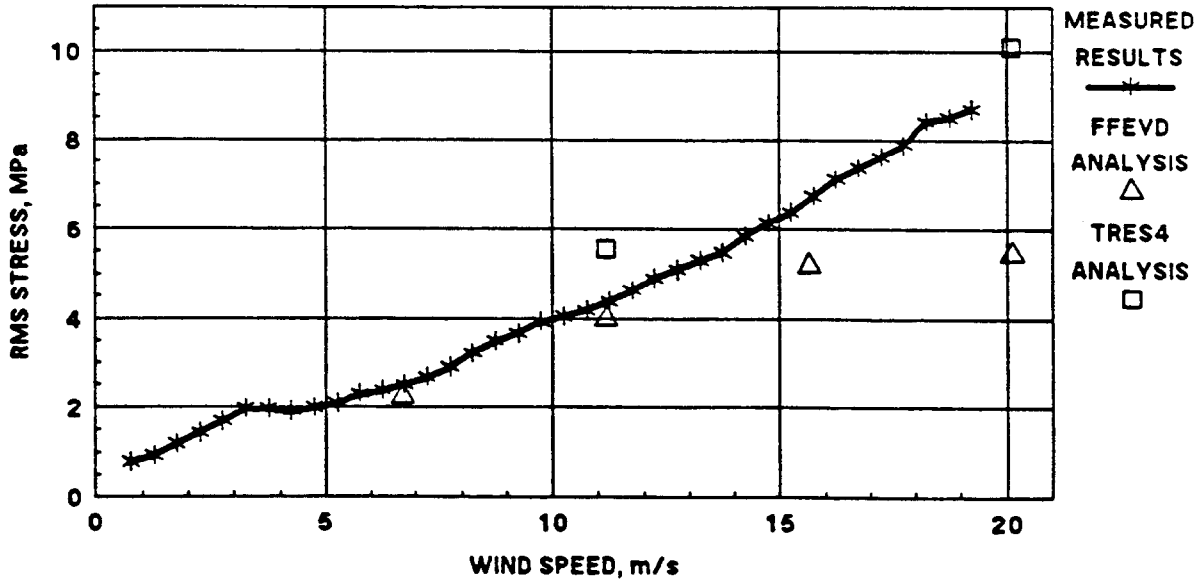

FIGURE 9. TEST BED FLATWISE STRESSES (28 RPM)

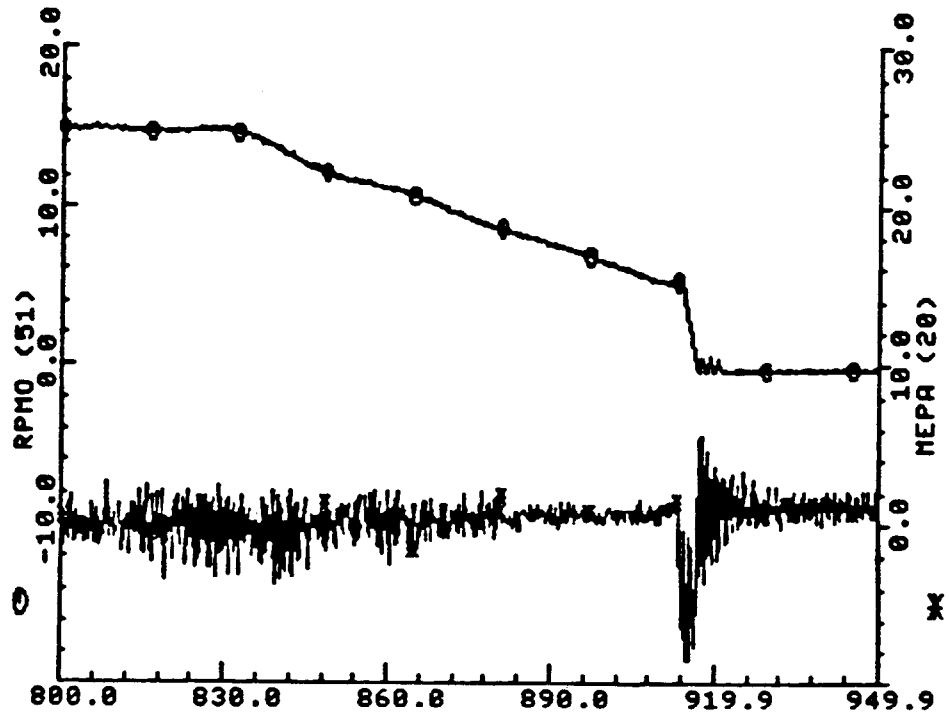

FIGURE 10. CONTROL AND POWER SYSTEMS
NORMAL STOP WITHOUT DELAY

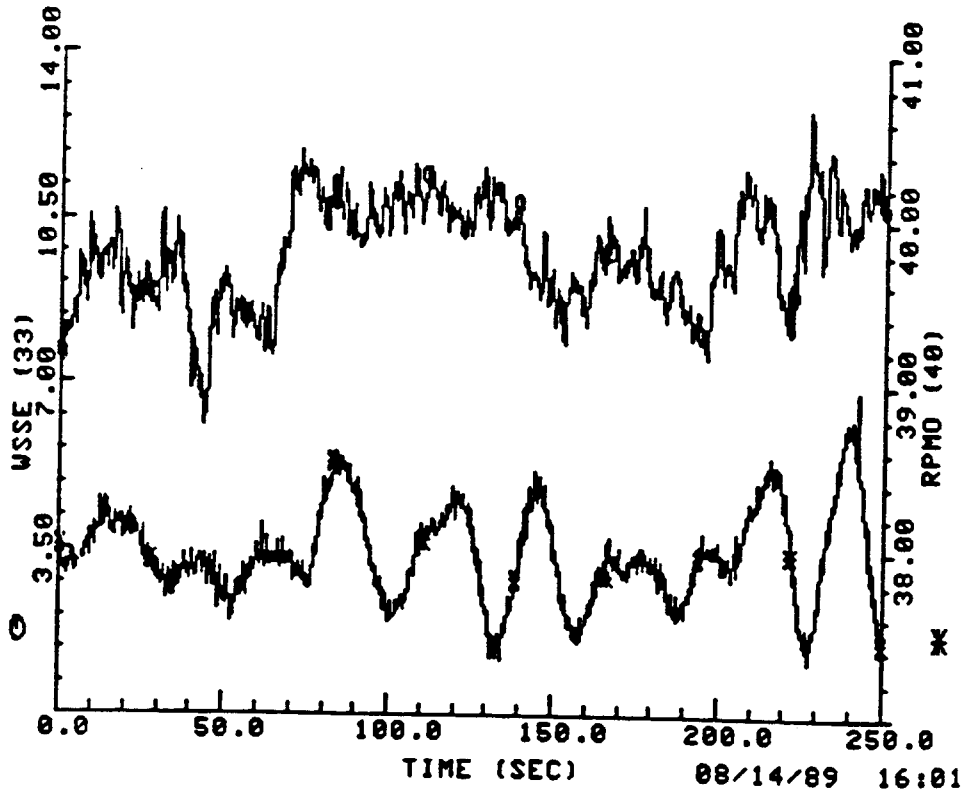

FIGURE 11. EFFECT OF WIND VARIATIONS ON
TEST BED ROTATIONAL SPEED

Proceedings of the Ninth ASME Wind Energy Symposium
D. E. Berg (ed.), SED-Vol. 9, ASME, January 1990

AERODYNAMIC DESIGN AND INITIAL PERFORMANCE MEASUREMENTS FOR THE SANDIA 34-m DIAMETER VERTICAL-AXIS WIND TURBINE*

D. E. Berg, P. C. Klimas, and W. A. Stephenson
Sandia National Laboratories
Albuquerque, New Mexico

ABSTRACT

The DOE/Sandia 34-m diameter Vertical-Axis Wind Turbine (VAWT) utilizes a step-tapered, multiple-airfoil section blade. One of the airfoil sections is a natural laminar flow profile, the SAND 0018/50, designed specifically for use on VAWTs. The turbine has now been fully operational for more than a year, and extensive turbine aerodynamic performance data have been obtained. This paper reviews the design and fabrication of the rotor blade, with emphasis on the SAND 0018/50 airfoil, and compares the performance measurements to date with the performance predictions. Possible sources of the discrepancies between measured and predicted performance are identified, and plans for additional aerodynamic testing on the turbine are briefly discussed.

INTRODUCTION

Sandia National Laboratories, as the DOE-designated lead laboratory for the development of VAWT technology in the United States, has built a 34-m diameter, research-oriented VAWT Test Bed on the Great Plains near Amarillo, Texas. This variable-speed turbine, designed and constructed by Sandia, is rated at 500 kW in a 12.5 mps (28 mph) wind (at 37.5 rpm), and incorporates aerodynamic, structural dynamic, and control improvements with respect to earlier VAWTs. The Test Bed turbine has been and will continue to be used to evaluate our current analytical capabilities and guide future developments in the areas of structural dynamics and aerodynamics. In addition, it will be used to aid in the development of variable-speed control algorithms, fatigue-life predictive techniques, unsteady viscous airflow modelling, and system design concepts.

*This work is supported by the U.S. Department of Energy at Sandia National Laboratories under contract DE-AC04-76DP00789.

BLADE DESIGN

The Test Bed, shown in Figure 1, features blade cross sections which have been specifically developed to operate in the VAWT environment. The operating regime of VAWT blade elements is very different from that experienced by airfoils used in aviation applications. VAWT blade elements function under unsteady conditions, passing through zero angle-of-attack twice per revolution on their way between relative maxima and minima often exceeding ± 90°, respectively. Aviation airfoils usually function under nearly steady conditions at near-zero angles-of-attack. VAWT blade elements utilize stall in high winds to regulate the rotor's power output. Aviation airfoils avoid stall. VAWT blades operate at Reynolds numbers (Re) between a few hundred thousand and a few million. Most aviation airfoils operate at Reynolds numbers between three and thirty million. Moreover, the blade-element Reynolds number near the equator of a rotor is much larger than that near the blade root-tower junction.

The general approach followed by Sandia in defining its advanced VAWT began with identifying aerodynamic criteria which would contribute to lowering VAWT system cost of energy (COE). Some of the more important of these were: high power coefficient (energy conversion efficiency), high annual energy production per unit of rotor swept area, and low cut-in windspeeds. Using SLICEIT, a momentum-based, double-multiple streamtube (DMST) aerodynamic performance code based on the CARDAA code[1], the performance of various combinations of blade elements, some with real and some with assumed lift and drag characteristics, was calculated. SLICEIT uses the Gormont dynamic stall model[2], as modified by Masse[3], accounts for local Reynolds number effects, and is capable of analyzing the performance of rotors with multiple section profiles and step changes in chord length. Using these performance predictions, the COE for each blade element combination was calculated with the ECON16[4] code. This study revealed that the COE is reduced when blade element lift and drag characteristics exhibit the following features.

Elements located near the rotor equator should exhibit:

1. modest values of maximum lift coefficient,
2. low drag at low angles-of-attack, α, and high drag at high α,
3. sharp stall, and
4. low thickness/chord ratio.

Elements located near the tower should have:

1. high maximum lift coefficients,
2. gentle stall, and
3. high thickness/chord ratio.

VAWT rotors built of blade elements exhibiting these features offer significantly improved energy production without proportionate increases in system cost when compared to current-generation commercial machines.

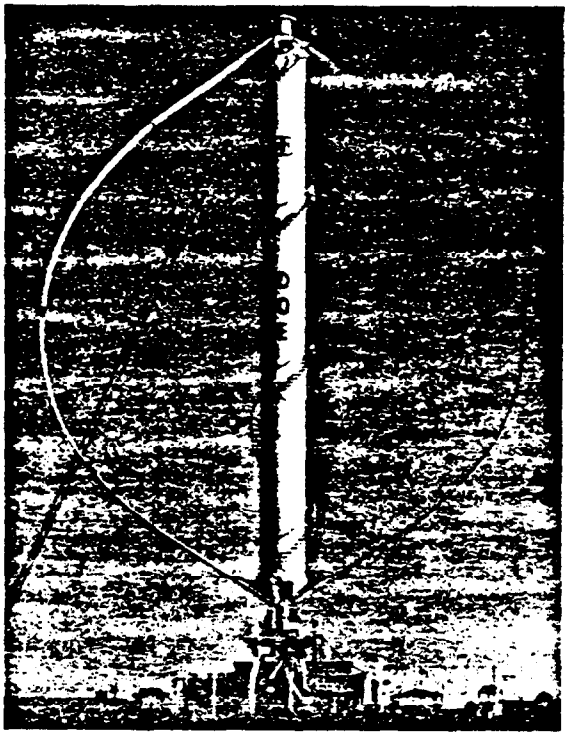

Figure 1. DOE/Sandia 34-m Diameter Vertical Axis Wind Turbine

The NASA-supported airfoil design code PROFILE[5], written by Richard Eppler, was used to design airfoil geometries which would exhibit the characteristics listed above. For the blade elements near the tower, the resultant airfoils closely resembled the NACA 00XX airfoil series with thickness-to-chord ratios of 18-25%. For the blade elements in the equatorial region, the resultant airfoils featured large extents of natural laminar flow (NLF) and thickness-to-chord ratios in the 15-21% range. These profiles resembled uncambered members of the NACA 6-series family.

Early attempts to utilize the NACA 6-series airfoils on airplanes were unsuccessful because airframe fabrication techniques of that era were incapable of producing airfoil surfaces that could maintain significant extents of laminar flow -- surface waviness and rivet heads quickly caused transition to turbulent flow. However, recent work on laminar flow wings had revealed that current manufacturing techniques were capable of producing surfaces that would support laminar flow. In addition, we intended to extrude the blades from aluminum, using the same technique used before to produce NACA 0015 profile blades. Our experiences with the NACA 0015 blades provided confidence that the blade profile could be held close enough to design specifications to generate sustained extents of laminar flow and that the blade surface finish would be sufficiently smooth to delay premature transition to turbulent flow.

Another area of concern was the possible extent of performance degradation caused by temporary roughening of the blade surfaces by dust, rain or the residue from insect impacts. This situation was examined analytically by predicting the performance of two turbines - one with NACA 00XX blades and the other with laminar flow blades. The boundary layer on each turbine blade was artificially tripped near the leading edge by introducing an analytical surface roughness. While the performance of the laminar flow blade was degraded by the surface roughness, it was still superior to the performance of the roughened NACA 00XX blade.

The complete design of the Test Bed NLF blades required iterations on the airfoil profiles incorporating results from static and dynamic wind tunnel tests and field tests on two research VAWTS[6,7]. These tests substantiated our predictions that airfoils fabricated from aluminum extrusions could generate and sustain significant chordwise extents of natural laminar flow. They also confirmed the predicted relative performance differences between the roughened NLF and NACA 00XX geometries.

Studies by Kadlec[8], Klimas[9], and Malcolm[10] provide additional detail on the systems and aerodynamic design processes briefly described in the preceding paragraphs. These studies have shown a significant potential for decreasing the VAWT-generated COE by using VAWT-specific blade element designs in place of those borrowed from aviation circles. Malcolm, in the most recent study, predicts a 25 percent decrease in the cost-of-energy for a turbine using a new NLF section near the equator in place of conventional NACA 0018 profiles. Variations of this same NLF section are being flown on the Test Bed.

The blades on the Test Bed are constructed with two distinct airfoil sections and three chord lengths. The curved equatorial section (17.6 m or 58 ft long) features the SAND 0018/50 NLF profile with a 0.91-m (36-in) chord. This 18 percent thick symmetrical section was developed by G. Gregorek, of The Ohio State University, under contract to Sandia, and is described by Klimas[9]. Its low drag at small angles-of-attack contributes to high rotor power coefficients in modest winds, and its sharp stall provides excellent stall regulation at higher winds. The curved transition sections (6 m or 20 ft long) which adjoin the equatorial portion also feature the SAND 0018/50 profile, but with a 1.07-m (42-in) chord and a slightly modified shape in the trailing edge region. The aluminum extrusion process requires a finite trailing edge radius, resulting in airfoils that have low angle-of-attack drag values somewhat higher than those of a similar airfoil with a sharp trailing edge. We maintained the same finite trailing edge thickness for both chord lengths, so the 1.07-m (42-in) chord section should have slightly less drag and therefore greater efficiency than the 0.91-m (36-in) chord section. Both NLF airfoils will be operating at Reynolds numbers between $1X10^6$ and $4X10^6$.

The straight root sections of the blade which join to the central column feature the NACA 0021 profile with a 1.22-m (48-inch) chord. This profile was chosen for its gradual and gentle stall characteristics, as these blade elements operate over the widest range of angle-of-attack. It will be operating at Reynolds numbers ranging from a few hundred thousand to about a million. Extensive design efforts failed to produce a geometry which showed a significant improvement over the NACA 0021 in this operating regime.

The increasing chord values from the equator to the root were chosen to maintain a nearly constant Reynolds number over the curved section of the blade and to keep blade material stresses within reasonable bounds.

BLADE FABRICATION

Like the rotor blades for most previous VAWTs in the Sandia program, the Test Bed rotor blades were fabricated from aluminum extrusions. These blade chords, however, were too large for a section to be made by a single extrusion. Each blade section, therefore, is made up of either two or three extrusions which are bolted together in the spanwise direction using nut strips. The extrusions are of 6063 T6 aluminum and were produced by Spectrulite, Inc., of Madison, Illinois. Figure 2 illustrates how the multiple extrusions mate to make up the three blade profiles. The 0.91- and 1.07-m (36- and 42-inch) chord sections (with the NLF profiles) were cold-bent into the proper shape after assembly by Flow, Incorporated of Kent, Washington.

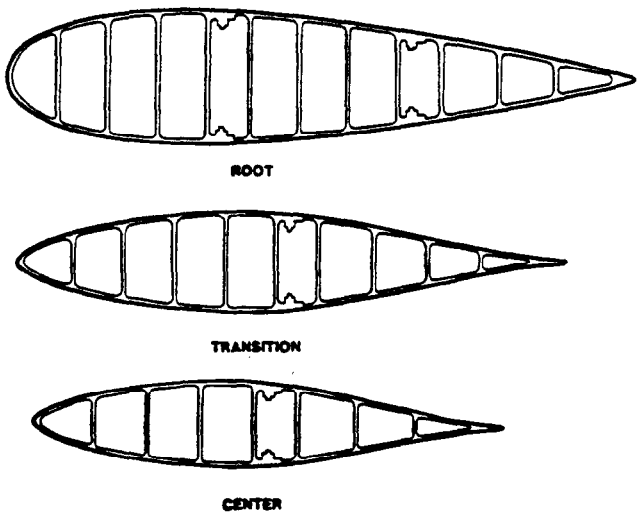

Figure 2. Blade Section Assembiles

The five individual sections in each blade were then joined together using the external joints illustrated in Figure 3. This design facilitates joint assembly and disassembly, inspection, and alteration. As Figure 3 also illustrates, the blade sections are joined with slope discontinuities or "kinks" at these blade-to-blade joints. Berg and Ashwill[11] discuss the use of these kinks in the blade and show that their use lowers the predicted mean blade bending stress by a factor of two.

Although the external joint configuration offers several structural advantages, its sharp edges and exposed nuts and bolts make it a relatively large source of parasitic drag which could contribute to degraded turbine performance. Since the Test Bed is a research machine, pressure lines and electrical cables are mounted within the blades to enable us to mount additional instrumentation such as pressure sensors on the blade at a later date. These pressure lines and electrical cables are brought to the surface in the vicinity of the joints and are terminated with connectors that extend above the blade surface, creating additional parasitic drag sources. The blade-to-tower joints are also external, but their contribution to drag losses is probably small because of the relatively low airspeeds seen by these elements.

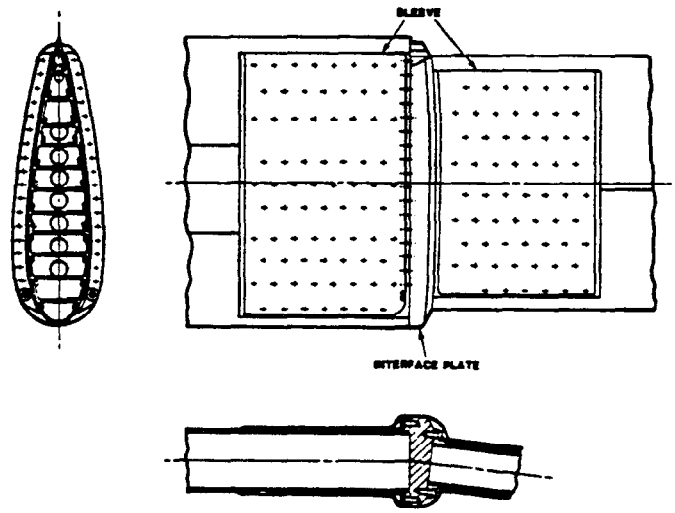

Figure 3. Blade-to-Blade Joint Detail

Prior to assembly, the blade extrusions were carefully measured and the surface finish examined. The basic contours of the extrusions were found to be generally within 0.1 percent of the specified nominal. These small deviations should cause very little degradation in aerodynamic performance. Surface finish was judged to be between 16 and 32 microns. Based upon our earlier test experiences with similar extruded blade shapes, we concluded that the surface was smooth enough to support laminar flow.

Once the blade sections were fully assembled, aerodynamic smoothing compound was used to cover recessed bolt heads, to fair portions of the external blade-to-blade joints into the blades, and to protect surface mounted transducers, their associated wiring and completion units. The compound used, with a trade name of Hysol, was chosen for its superior strength and minimal shrinkage characteristics. The Hysol was carefully sanded after application to remove as much excess as possible without damaging the transducers and their wiring.

We then painted the blades, both to mask the areas where the Hysol had been applied (its dark red color was a stark contrast to the silver of the aluminum extrusions), and to provide a hard, smooth surface to improve blade performance. The painting took place in two phases. Early in the assembly process, two test segments were painted with an epoxy enamel after a 400-grit hand-sanded cleaning and application of an acid-etch primer. After about two months (but before the blades were mounted on the tower), we noticed that the primer was separating from the blade surface at several locations. We repaired those sections of the paint and sand-blasted the remaining eight blade sections over

most of their surfaces to provide an improved surface anchor for the primer. Those sand-blasted blades were then painted using the same acid-etch primer and epoxy enamel. The surface areas which were not sand-blasted were the first 2-3 inches (5-8 cm) back from the leading edge on the curved segments. We felt that the impact of insects, dirt, and rain would eventually erode the paint from this area of the blade, regardless of how firmly anchored that paint was. If the eroding paint were to uncover an excessively roughened surface on a natural laminar flow section, premature transition from laminar to turbulent flow might occur, causing performance degradations. However, if the leading edge were not sandblasted, the eroding paint would reveal a 16-32 micron surface -- adequate for maintaining a laminar boundary layer.

AERODYNAMIC PERFORMANCE

The variable-speed capability of the Test Bed permits operation in a variable-speed mode or in a fixed-speed mode at any rpm we desire. In the fixed rpm mode, the controller does allow some variation of rotational speed, occasionally as much as plus or minus one rpm. However, the effect of this variation on the aerodynamic performance of the machine should be minor.

In order to characterize the performance of the machine, we tested it at three basic rotational speeds that span the operating range: 28, 34, and 38 rpm. 28 rpm is the lower end of the design operating range, and is fixed by the existence of a turbine resonance mode at 25 rpm. 38 rpm is the safe upper limit of the operating range, as a very severe resonance exists at 40 rpm. Another, relatively minor, resonance exists at 32.5 rpm, and 34 rpm was selected as the third and final test speed to avoid that resonance.

Initial measurements of the aerodynamic performance of the Test Bed were obtained during the period of August through October, 1988. The results of those measurements are plotted in Figure 4, together with the predicted performance curves for the turbine. We were very concerned with the large discrepancies between the predicted and measured performance. After careful review of our data acquisition and reduction programs, we concluded that the data were correct -- the turbine simply wasn't producing the predicted power.

Visual inspection of the turbine blades from the ground revealed nothing that might be causing the problem, but a close-up inspection of the blade from a crane-positioned man bucket did -- paint had flaked from extensive regions of the leading edge of the NLF sections of the blade, especially on the first two sections to be painted, where we had earlier observed the primer separation. Figure 5 is a photograph of the paint flaking on that portion of the blade. The other NLF sections had experienced some flaking, but it was far less severe. Virtually no flaking had occured on the NACA 0021 sections of the blade. The flaking had created forward facing steps near the leading edge with a height of approximately 0.25 mm (0.010 in), a very effective boundary layer trip which could be expected to destroy the laminar flow over the blade. Loss of laminar flow would cause the blade to produce higher drag and lower lift than it was designed to produce, resulting in a significant degradation of turbine performance.

The paint flaking was confined to the leading edge area, extending no more than 1.0 cm (0.4 in) aft in most cases. In general, the bare metal of the blade was revealed wherever the paint had flaked off - the acid-etch primer had failed to adhere to the bare aluminum. The major contributors to the paint failure were the sharp leading edges of the NLF sections and inadequate surface preparation. Rather than attempt to repair the existing paint, we removed all the paint from the leading edges of the NLF airfoils for a distance of at least 1 cm (0.4 in) aft of the leading edge. If the flaking extended further aft, we removed additional paint until we reached an area where the paint adhered well to the metal. After the paint had been scraped off (using care to avoid scratching the underlying metal), we used fine grit emery cloth to remove the last traces of paint from the leading edge and to fair the remaining paint smoothly into the bare metal near the leading edge. The final transition from the bare metal to the painted blade was smooth enough that it could not be detected by touch. Although this paint removal altered the blade profile slightly, its effect on performance should be negligible.

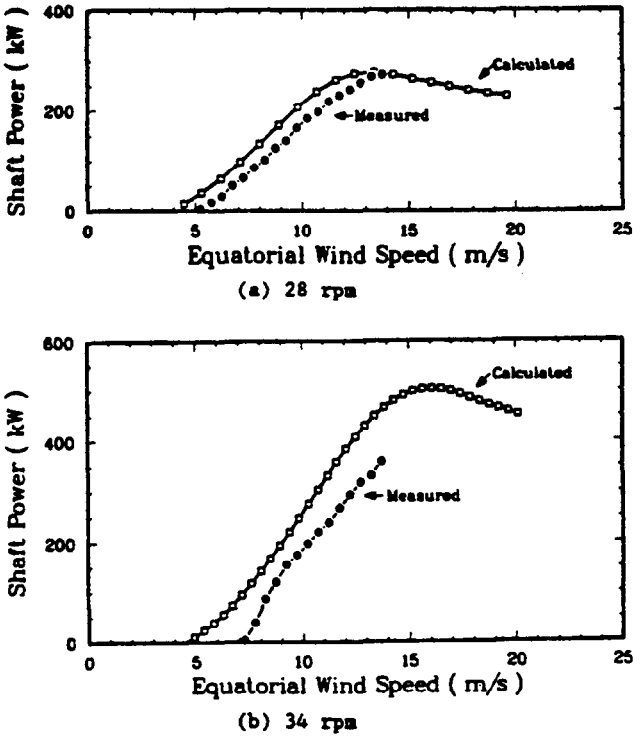

Figure 4. Initial Turbine Performance

After the blade leading edge had been thoroughly cleaned, we again measured turbine aerodynamic performance, starting in January, 1989. The aerodynamic data obtained from January through April, 1989 are compared with the predicted performance in Figures 6-8, and the agreement between measurement and prediction is far better than for the initial data. However, sizeable differences still exist at both low-wind wind and high-wind conditions. The data presented in Figure 8 should be regarded as very preliminary data, as we have not acquired a sufficient number of points at all wind speeds to accurately define the power curve. The approximate power curve presented here will undoubtedly change as we acquire additional data.

Note the behavior of the measured power curves in the high-wind speed area in Figures 6-8. Although the data do not agree exactly with predictions in this area, the power curve does level off as predicted for the 28 and 34 rpm cases. The 38 rpm power curve is terminated at 15 mps, below the rpm at which a roll-off is predicted. (15 mps is our high wind limit for operation at 37 rpm or above, to avoid exceeding the maximum generator capacity.) This leveling off or regulation of the power output is due to the stall characteristics of the blades, and its achievement was one of the key objectives of the Test Bed blade design effort.

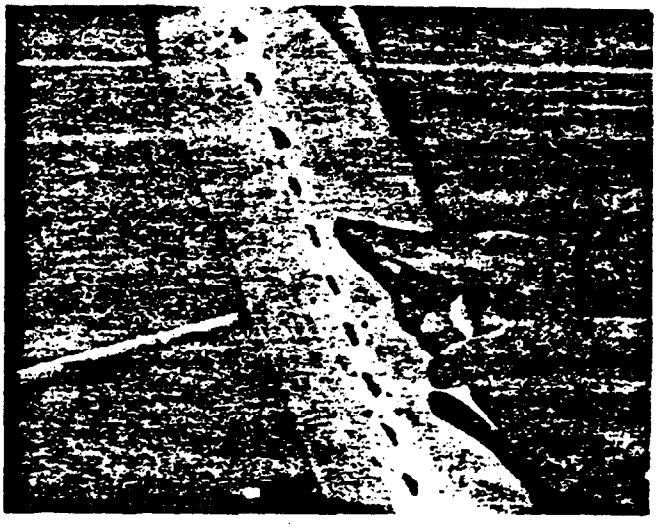

Figure 5. Paint Flaking on the NLF Section Leading Edge

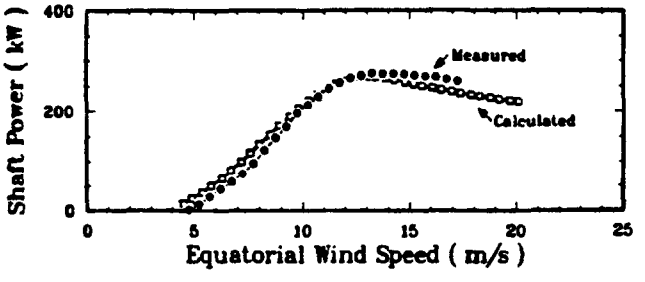

Figure 6. Turbine Performance at 28 rpm

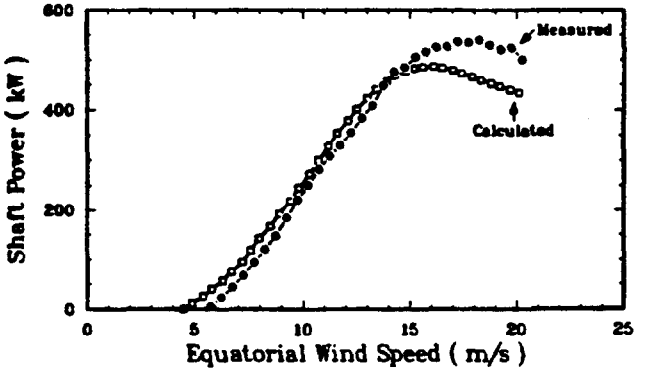

Figure 7. Turbine Performance at 34 rpm

The disagreement between predicted and measured performance at high wind speeds exhibits a distinct trend with increasing rotational speed -- the measured performance increases with respect to the predicted values. This leads us to suspect the disagreement may be the result of inaccurate modelling of dynamic stall phenomena, which are known to depend on the rate of change of angle of attack. The Gormont model used in the SLICEIT code does include a dependence on this parameter, but the model is a simplistic semi-empirical correlation developed for thin airfoils (thickness-to-chord ratios less than 12%) undergoing small oscillations about the static stall angle. The current airfoils are thicker (thickness-to-chord ratios of 18 - 21%) and are undergoing large oscillations (>20°) about 0° angle of attack. Efforts to improve the dynamic stall model are currently underway.

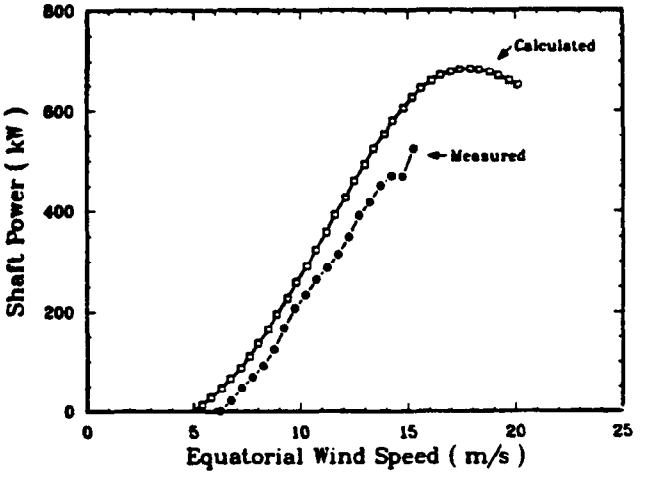

Figure 8. Turbine Performance at 38 rpm

We have identified two distinct probable causes for the observed disagreement between measured and predicted performance at low wind speeds. First, as mentioned earlier, the blade-to-blade joint areas are extremely 'dirty' from an aerodynamics point of view, with exposed bolt heads, blunt shapes, sharp leading edges, capped tubing unions, and capped electrical connectors perturbing the airflow. These features will create excessive drag, particularly at low angles of attack, and will result in degradation of the turbine performance. The performance predictions presented in Figures 6-8 made no attempt to model the effect of these features.

In order to check the veracity of this argument, we crudely simulated the increased drag in these areas. Lift was taken to be the same as that on a clean airfoil, but the drag was increased at low angles of attack -- the airfoil drag at 0° α was increased by a factor of 5, fairing into the unaltered airfoil drag at 12° α. The joint simulation predictions are compared with the measured data at 34 rpm in Figure 9. The excellent agreement must be regarded as fortuitous, but it does lend some weight to our argument.

The second contribution to the observed discrepancy in performance is an inherent inaccuracy of the prediction model itself. As mentioned earlier, SLICEIT is a DMST code, based on the CARDAA code developed by Paraschivoiu[1]. In his original paper, Paraschivoiu found that DMST models, as a whole, overpredict the performance of wind turbines at low wind speeds. CARDAA and the other DMST codes that Paraschivoiu examined do not account for streamtube spreading, which would be expected to be quite extensive at very low

wind speed where much of the available energy is extracted from the wind, and this may be the major reason for the optimistic predictions.

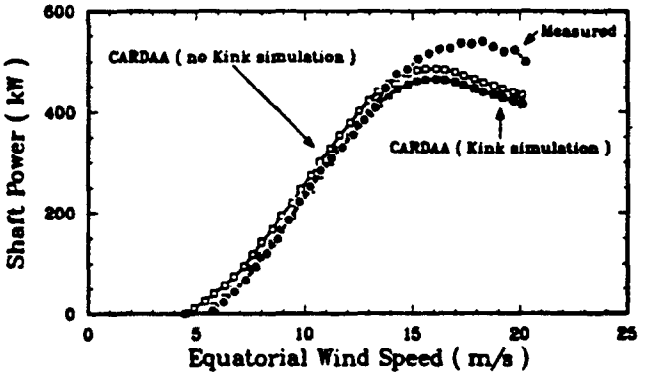

Figure 9. Blade-to-blade Joint Simulation Results

We are aware of another possible cause for the disagreement between the predicted and measured performance is the accuracy (or lack of accuracy) of the lift and drag data used by the codes. All of the predictions presented in this paper utilize SAND 0018/50 data that we acquired in a wind-tunnel test at Texas A&M University in 1983 for Reynolds numbers up to $1.8X10^6$, together with PROFILE code predictions for airfoil characteristics at Reynolds numbers in excess of $1.8X10^6$. We also have some preliminary data from Ohio State University wind-tunnel tests on that airfoil at a Reynolds number of $1.5X10^6$ which indicate that the drag coefficients obtained at Texas A&M are too high. If the Ohio State data are used to predict the performance, we observe no change in the performance at low wind speeds, but significant increases in the performance at high wind speeds, leading to better agreement between measured and predicted performance at post stall conditions. Efforts to resolve this discrepancy in our airfoil data are underway.

Figure 10 presents the performance data in normalized form, as performance coefficient versus tip-speed ratio. No low tip-speed ratio data is plotted for 38 rpm, as high-wind data at that operating condition have not been taken. Although the data collapse quite well for both high and low tip-speed ratios, they exhibit considerable scatter at tip-speed ratios between 5.5 and 7. No satisfactory explanation for this scatter has been found at this time.

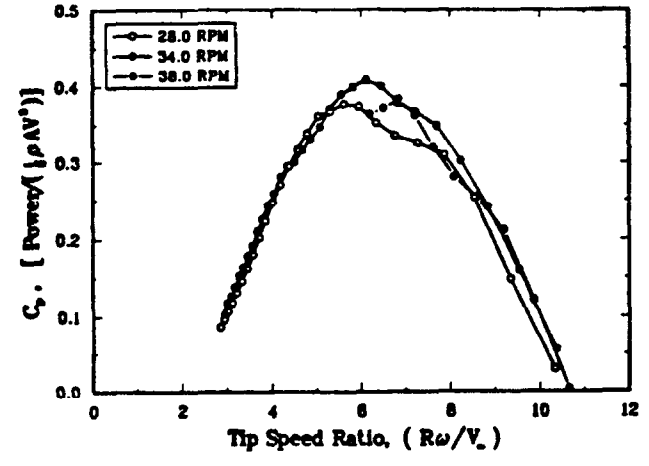

Figure 10. Measured Turbine Performance Coefficient

The peak measured performance coefficient is 42% at a rotational speed of 34 rpm. This compares to a predicted performance coefficient, at all rotational speeds, of 47%. The joint simulation discussed above yielded a predicted peak performance coefficient of 42%, suggesting that much of the 5% difference between predicted and measured values may be due to the unfaired blade-to-blade joints.

FUTURE PLANS

Additional aerodynamic performance data will be acquired at 38 rpm for all wind speeds, and at 28 and 34 rpm at high wind speeds to give us a statistically reliable data set.

Once adequate performance data for the current blade configuration is taken, we will install aerodynamic fairings on the blade-to-blade joints to decrease the drag generated in those areas. The aerodynamic and structural performance of the turbine will again be characterized and those results compared to the current measurements to determine the effect of the fairings. The performance of the turbine with the fairings installed will establish the optimum performance possible with the current blade set.

Future plans call for the modification of the root sections of the current blades by installing vortex generators (VGs). Analytical studies, based on previous tests of vortex generators on VAWTs[12] indicate that appropriately placed VGs could yield performance improvements of approximately 5% at moderate wind speed sites. Future blades for the Test Bed will incorporate improvements on the current SAND 0018/50 and NACA 0021 airfoils, and will likely feature composite construction with continuously varying airfoil section and chord.

SUMMARY

The rotor blades for the 34-m diameter VAWT Test Bed utilize two distinct airfoil section profiles -- a NACA 0021 profile near the tower, and a VAWT-specific SAND 0018/50 profile for the remainder of the blade -- and three different chord lengths. The SAND 0018/50 design resulted from iterative system economic and airfoil design studies, followed by wind tunnel and field testing. The blades are constructed of multiple aluminum extrusions, and the blade sections are attached to one another with external joints that incorporate slope discontinuities from one section to the next.

Initial performance data for the 34-m diameter VAWT Test Bed agree reasonably well with that predicted by the SLICEIT computer code. Differences at high wind speeds are attributed to the use of a simplistic dynamic stall model that does not adequately model the effects of rate-of-change of angle of attack on the airfoil sections. Differences at low wind speeds are attributed to excessive drag generated by the external blade-to-blade joints which were not modelled in the performance predictions and to inaccuracies in the double-multiple streamtube class of codes.

Additional aerodynamic performance data will be acquired for the current blade configuration in order to fill out the data sets in the high wind, high rotational speed portion of the operating envelope. Aerodynamic fairings will then be installed on the

blade-to-blade joints and the turbine performance will be recharacterized to determine the effects of the fairings.

REFERENCES

1. Paraschivoiu, I., "Double-Multiple Streamtube Model for Darrieus Wind Turbines," Proceedings of the Second DOE/NASA Wind Turbine Dynamics Workshop, February 24-26, 1981, Cleveland, OH

2. Gormont, R. E., "A Mathematical Model of Unsteady Aerodynamics and Radial Flow for Application to Helicopter Rotors," U.S. Army Air Mobility R&D Laboratory, Vertol Division, Philadelphia, PA, Report on Boeing-Vertol Contract DAAJ02-71-C-0045, May 1973.

3. Masse, B., "Description de Deux Programmes d'Ordinateur pour le Calcul des Performances et des Charges Aerodynamiques pour des Eoliennes A'Axe Vertical," Institut de Recherche de L'Hydro-Quebec, Report IREQ 2379, Varennes, Quebec, July 1981.

4. Sullivan, W.N., "Economic Analysis of Darrieus Vertical Axis Wind Turbine Systems for the Generation of Utility Grid Electrical Power, Vol. 2: The Economic Optimization Model," SAND78-0962, Sandia National Laboratories, Albuquerque, NM, 1979.

5. Eppler, R. and Somers, D. M., "A Computer Program for the Design and Analysis of Low-Speed Airfoils," NASA TM-80210, 1980.

6. Klimas, P. C. and Berg, D. E., "Aerodynamic Design of a Midsized Vertical Axis Wind Turbine Using Natural Laminar Flow Blade Elements," Sixth Biennial Wind Energy Conference, Minneapolis, MN, June 1-3, 1983.

7. Klimas, P. C. and Worstell, M. H., "Performance Testing of the Sandia National Laboratories 17-m Diameter Research Turbine with Natural Laminar Flow Blade Elements." Fifth ASME Wind Energy Symposium, New Orleans, LA, February 23-26, 1986.

8. Kadlec, E. G., "The Potential of Advanced Darrieus Wind Turbines," Sixth Biennial Wind Energy Conference, Minneapolis, MN, June 1-3, 1983.

9. Klimas, P. C., "Tailored Airfoils for Vertical Axis Wind Turbines," SAND84-1062, Sandia National Laboratories, Albuquerque, NM, November 1984.

10. Malcolm, D. J., "Increased Output From Darrieus Rotors," presented at the European Wind Energy Association Conference and Exhibition, Rome, Italy, October 7-9, 1986.

11. Berg, D. E., and Ashwill, T. D., "An Update on the Structural Design of the Sandia 34-m Vertical Axis Wind Turbine," Fifth ASME Wind Energy Symposium, New Orleans, LA, February 23-26, 1986.

12. Klimas, P. C., "Airfoil Treatments for Vertical Axis Wind Turbines." Windpower '85, San Francisco, CA, August 27-30, 1985.

Proceedings of the Ninth ASME Wind Energy Symposium
D. E. Berg (ed.), SED-Vol. 9, ASME, January 1990

STRUCTURAL RESPONSE MEASUREMENTS AND PREDICTIONS FOR THE SANDIA 34-METER TEST BED[1]

T. D. Ashwill and P. S. Veers
Wind Energy Research Division
Sandia National Laboratories
Albuquerque, New Mexico

ABSTRACT

Measurements of structural response during operation of the 34-Meter Test Bed vertical axis wind turbine are compared with analytical predictions. Measured structural data include stationary and rotating modal frequencies, cable natural frequencies, and operating stresses. These data are compared to analytical results obtained with the use of NASTRAN-based structural codes. In the case of operating stresses, analytical results with and without turbulence are compared to measured stresses. Data taken during two significant events, a high wind over-speed condition with an emergency stop and a cable resonance that couples with a tower natural frequency, are shown.

INTRODUCTION

The testing of the Sandia 34-Meter Test Bed, a new research, variable speed vertical axis wind turbine (VAWT), has been ongoing for over a year. This paper presents a variety of measured structural data: stationary and rotating modal frequencies, cable frequencies, and operating stresses. These data are compared to analytical results obtained during the design process with the use of the NASTRAN-based structural analysis codes, FEVD (1) and FFEVD (2), which predict natural frequencies and forced response without turbulence. More recent calculations which include turbulence were obtained using a newly developed structural analysis code, TRES4 (3), and are included in the operating stress comparisons.

The test plan for the 34-Meter Test Bed (4) is divided into several phases. Phase I testing, which is now complete, was primarily concerned with assembly and start-up tests. During this phase, parked modal frequencies and blade gravity stresses were measured. In addition, the turbine's extensive instrumentation was validated.

Phase II testing, which is currently 75% complete, is intended to characterize the turbine both aerodynamically and structurally. For structural characterization, two distinct sets of tests are being performed; the first set is a resonance survey and the second determines structural performance. Resonance surveys are performed by operating the turbine for short periods of time at rotation rates that are stepped in several increments from 6 to 40 rpm (revolutions per minute). These surveys are run in increasingly higher winds after it is determined that no problems exist in the lower wind data. The ability of the brakes to execute an emergency stop with acceptable blade and tower stresses is also checked as part of the resonance surveys. The distribution of centrifugal stresses along the blade and estimates of the rotor natural frequencies are extracted from the resonance survey data. Ashwill (5) has presented comparisons between analytical and measured gravity stresses, centrifugal stresses, stationary modal frequencies and rotating modal frequencies. Agreement was very good and provided confidence that the finite element model accurately describes the turbine structurally.

Phase II structural characterization testing also included what are called structural performance tests. During this mode of testing, the turbine is operated for several hours at each of three pre-selected rotation rates — 28, 34, and 38 rpm. Time series data are collected for 30 selected strain gauge channels and other sensors including wind speed and direction, generator electrical output and rotor torque. The variances of stress levels are later computed for each turbine revolution and sorted into half meter per second (mps) wind speed bins. The resulting root mean square (RMS) stresses as a function of wind speed are carefully observed, as these stresses are an integral part of the turbine component fatigue life.

During testing, two significant events occurred that caused special study. In the first, while operating in high winds at 38 rpm during a resonance survey test, the turbine produced power well above the generator rating, which caused the turbine to speed up, go through a resonance at 40 rpm, and finally

[1]This work was supported by the U.S. Department of Energy under contract DE-AC04-76DP00789.

shut down at 42 rpm with an emergency stop. In the second, a known cable natural frequency moved higher in frequency because of cold temperatures and was excited by the inherent harmonic loading of the turbine. A tower natural frequency then coupled with the resulting cable motion causing both large cable displacements and high blade lead-lag stresses.

NATURAL FREQUENCIES

After the turbine was fully assembled and before it was operated, a modal test was performed on the parked rotor by Sandia's Modal Test Group (6). Accelerometers were temporarily attached to the blades, tower and guy-cables to measure turbine motion. Two types of input excitation were used: step relaxation (snap releasing) and ambient wind. The measurements were used to estimate the mode shapes, their frequencies of vibration, and modal damping values.

The first eight natural frequencies obtained from the modal test are compared with analytical predictions from an FEVD normal modes and frequencies analysis in Table I. The mode number and name are listed in the first two columns. The third column shows the natural frequencies for the stationary rotor measured by the modal test during wind excitation. Column four lists the predicted values from FEVD. There is excellent agreement between the measured and predicted frequencies for these eight modes. All predicted modal frequencies are within 2.6% of the measurements (see column 5) except for the first blade edgewise mode (5.2%). More extensive coverage of these comparisons is provided in Ref. 5.

Amplitude spectra were obtained from the strain gauge data collected during the resonance surveys. An example of an amplitude spectrum of one block (40 seconds) of strain gauge measurements during operation at 20 rpm is shown in Fig. 1. Modal frequencies and harmonic excitations (per revs) appear as peaks in the amplitude spectra. By plotting these measured natural frequencies at several rotation rates on the predicted fan-plot, as shown in Fig. 2, one can estimate the accuracy of predicted rotor modes as a function of rpm. The two measured first flatwise modes plotted in Fig. 2 are the antisymmetric and symmetric, which are predicted to vibrate at nearly the same frequency. The first blade edgewise mode (1BE) was under-predicted by 5% at zero rpm, but above 25 rpm the observed and predicted frequencies coincide. Overall, all of the modes below 3 Hz closely match the predicted natural frequencies over the entire range of operating speeds.

We have recently developed a new spectral analysis capability for averaging several blocks of data. While the spectrum of Fig. 1 was computed from one block of 40 seconds of data, Fig. 3 shows a spectral estimate from the same time history produced with the new spectral analysis program that averages 9

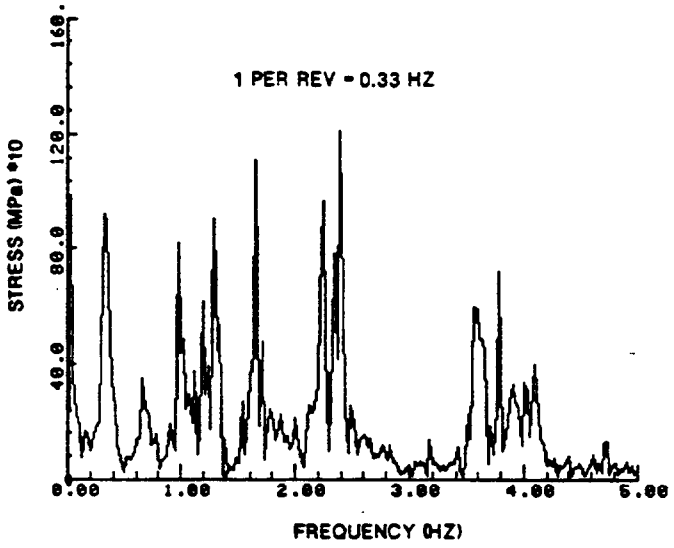

Fig. 1. Amplitude spectrum of upper root lead-lag response at 20 rpm — one block of data

MODE NUMBER	MODE SHAPE*	MODAL TEST	ANALYTICAL	DEVIATION
1,2	1FA/1FS	1.06	1.05	1.0%
3	1Pr	1.52	1.56	2.6%
4	1BE	1.81	1.72	5.2%
5	2FA	2.06	2.07	0.5%
6	2FS	2.16	2.14	1.0%
7	1TI	2.50	2.46	1.6%
8	1TO	2.61	2.58	1.2%

* Mode Shape Abbreviation Key:
1FA = First Flatwise Antisymmetric
1FS = First Flatwise Symmetric
1Pr = First Propeller
1BE = First Blade Edgewise
2FA = Second Flatwise Antisymmetric
2FS = Second Flatwise Symmetric
1TI = First Tower In-Plane
1TO = First Tower Out-of-Plane

Table 1: Parked Modal Frequencies (Hz) — Test and Analysis.

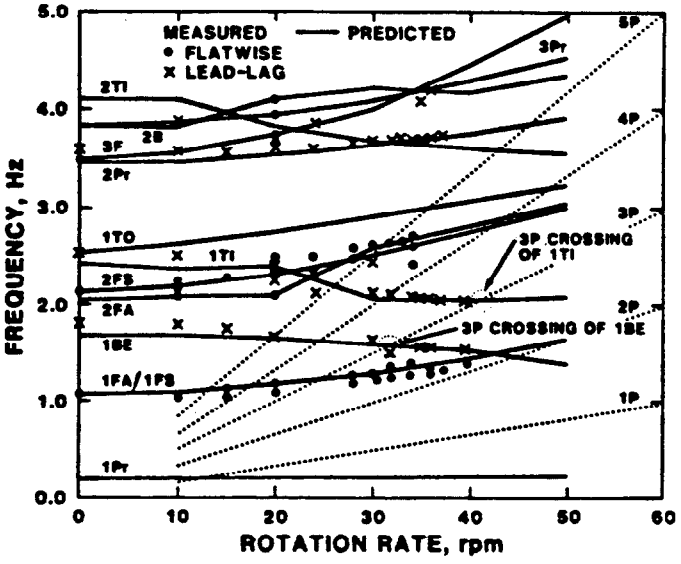

Fig. 2. Rotating modal frequencies — measured vs. predicted

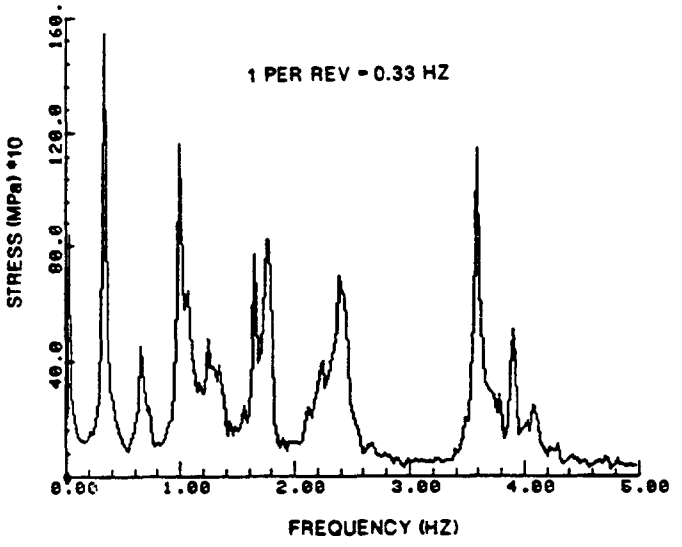

Fig. 3. Amplitude spectrum of upper root lead-lag response at 20 rpm — nine blocks of data averaged

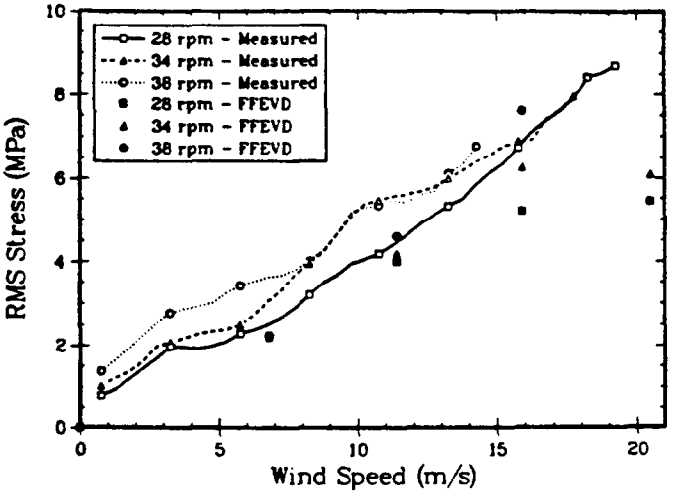

Fig. 4. Lower blade root flatwise RMS stress vs. wind speed — measured and analytical (FFEVD) without turbulence

blocks of data each 40 seconds long. The averaging reduces the error of the spectral estimate, smooths the plot and provides higher confidence that the remaining peaks correspond to natural frequencies or harmonic (per rev) excitations. With only one block of data, Fig. 1, the extra peaks due to inherent uncertainty (noise) in the spectral estimate could be mistaken for a modal response.

OPERATING STRESSES

Many hours of data have been collected at 28, 34, and 38 rpm at average wind speeds up to 16.4 mps (36 mph). Collection of the RMS stress levels into wind speed bins allows for easy characterization of the effect of wind speed on operating stress levels. Figures 4-5 show measured RMS stresses at the lower blade root due to flatwise and lead-lag (trailing edge) bending.

Predicted operating stresses from two analytical tools can be compared to measured values. Steady wind predictions are obtained with FFEVD calculations that assume no turbulence and include no structural damping. The steady wind assumption limits the loads, and therefore the response, to integer multiples of the operating speed (the per rev harmonics). When turbulence is included, as in TRES4, random loads, while strongly harmonic, include excitation at all frequencies. (The program TRES4 calculates spectral densities of modal loads and drives a modal random-vibration frequency-response calculation.) Both FFEVD and TRES4 are based on the general purpose finite element code MSC/NASTRAN. Figures 4-5 show the FFEVD predictions for steady winds superimposed on the measured data. Figures 6-7 replot the measured flatwise and lead-lag bending stresses with the TRES4 predictions superimposed. A 10% atmospheric turbulence intensity was used to match the 34-Meter Test Bed site at Bushland, Texas.

Measured Stresses

Each measured data point is the result of at least 100 samples (each sample is one turbine revolution). The number of samples obtained for each wind speed bin is plotted in Fig. 8 for all three

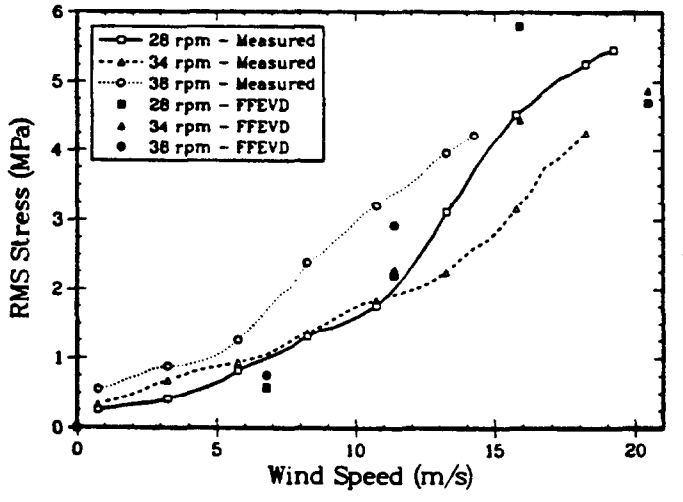

Fig. 5. Lower blade root trailing edge RMS stress vs. wind speed — measured and analytical (FFEVD) without turbulence

operating speeds. Most bins have over 1000 samples; a few have over 2000 samples. The generator rating prohibits operation at 38 rpm in winds above 15 mps.

The measured RMS stress vs wind speed plots illustrate that the response is not a simple reflection of the magnitude of the input loads. In neither the lead-lag nor the flatwise cases do the stress levels increase uniformly with increasing rotor speed, as might be expected because the aerodynamic loads get larger as the blade speed increases. For example, the trailing edge stresses at 28 rpm are almost 50% higher than at 34 rpm in winds around 15 mps (see Fig. 5). Also, the flatwise stresses at 34 and 38 rpm are almost equal over a wide range of wind speeds (see Fig. 4). While the flatwise stresses increase nearly linearly with wind speed, the lead-lag stresses show a marked change in slope, but at different wind speeds for each rpm.

Steady Wind Comparisons (FFEVD)

FFEVD uses input loads that are harmonics of the operating speed. Because the harmonics are usually not near a structural resonance (an important design goal), damping has a minor effect on the results and was not included in the calculations. In FFEVD the RMS stresses are calculated by summing the variances of the sinusoidal components of the stress response. A few trends can be identified by comparing the FFEVD predictions with the measured data, as shown in Figs. 4-5.

1. FFEVD under-estimates the flatwise stresses at all rpm's and all wind speeds for which data are available.

2. The lead-lag stresses are under-estimated by FFEVD in very low and very high winds.

3. The lead-lag stresses are greatly over-estimated in moderately high winds, around 15 mps (35 mph).

The tendency to over-estimate harmonic loading has been shown to exist when turbulence is neglected (7,8). When turbulence is included, the per rev excitation is reduced, but the loading is shown to include significant energy between the harmonics. FFEVD does not model this off-harmonic loading and therefore misses some of the turbine response, but, generally over-estimates the harmonic response because the harmonic loads are too high. The net result is two errors that could result in high or low predictions depending on which error dominates. Overall, the predictions follow the trends in the measured data fairly well, except in high winds.

Comparisons Including Turbulence (TRES4)

Structural response of the 34 Meter was predicted by David Malcolm using TRES4 (3), a VAWT structural analysis code that uses simulated atmospheric turbulence to estimate the random aerodynamic loading. Predictions were computed at 28 and 38 rpm using 2% modal damping (flatwise modes only) plus 2% structural damping, but no aeroelastic damping. The flatwise modal damping partially accounts for the predicted high aeroelastic damping in those modes (9). Estimates at 34 rpm and 38 rpm were also produced that include aeroelastic damping and 2% structural damping (10). The aeroelastic damping model is based on linear aerodynamics, which is violated when the blades stall.

In Fig. 6, the flatwise predictions with no aeroelastic damping (28 and 38 rpm) slightly over-predict the measured flatwise response, while the 34 and 38 rpm predictions with aeroelastic damping (over 8%) slightly under-predict flatwise response.

The lead-lag stress predictions with no aeroelastic damping, shown in Fig. 7, are in agreement with the measured data at both 11 and 20 mps for 28 rpm operation, while the 38 rpm result slightly under-estimates the stresses. The lead-lag predictions with aeroelastic damping are mixed - the 34 rpm result at 16 mps greatly over-estimates the stresses and the 38 rpm result at 11 mps greatly under-estimates the stresses. This over-estimate at 34 rpm is due in large part to the high predicted response of the first blade edgewise mode (1BE) at 1.6 Hz, which is near 3 per rev (1.7 Hz).

The RMS stress levels do not tell the entire story; structural response has contributions from a wide range of frequencies.

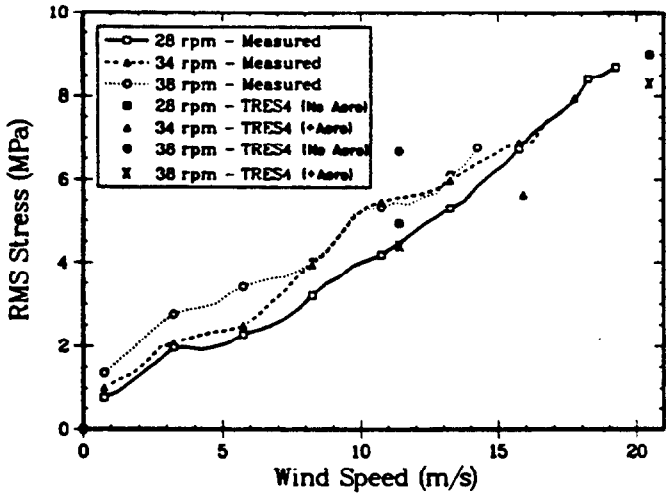

Fig. 6. Lower blade root flatwise RMS stress vs. wind speed — measured and analytical (TRES4) with turbulence

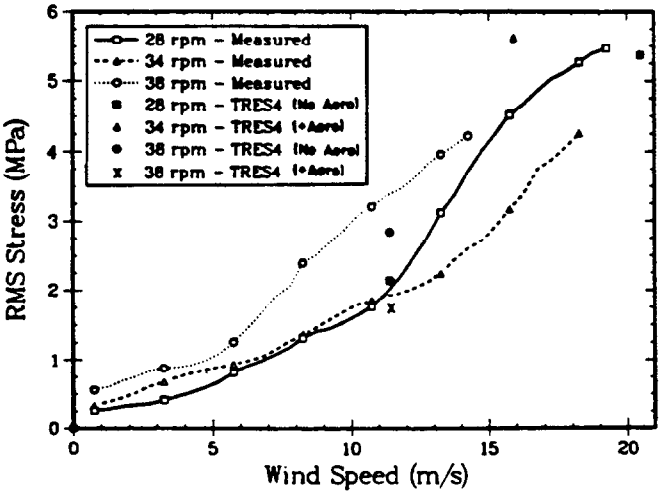

Fig. 7. Lower blade root trailing edge RMS stress vs. wind speed — measured and analytical (TRES4) with turbulence

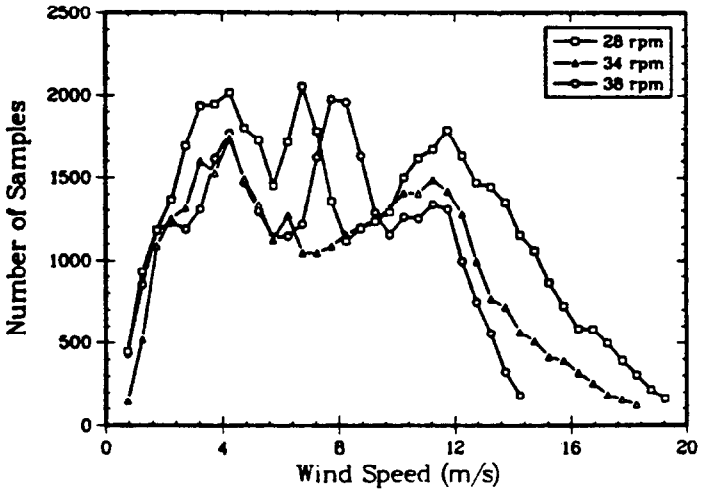

Fig. 8. Distribution of stress data samples at 28, 34, and 38 rpm

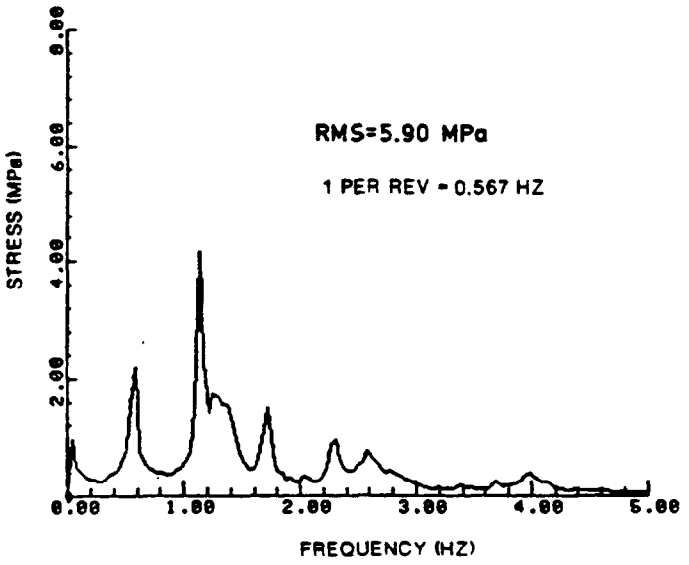

Fig. 9. Amplitude spectrum of upper root flatwise response at 34 rpm in 15 mps winds — measured, 50 blocks of 25 s each

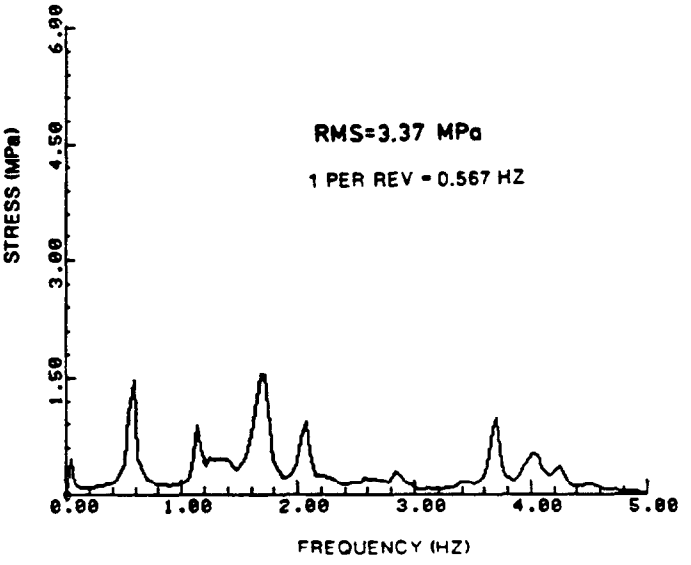

Fig. 11. Amplitude spectrum of upper root lead-lag response at 34 rpm in 15 mps winds — measured, 50 blocks of 25 s each

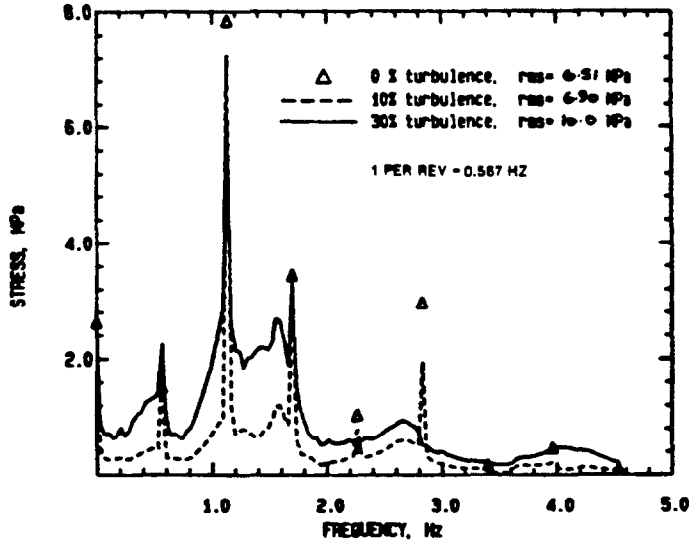

Fig. 10. Amplitude spectrum of upper root flatwise response at 34 rpm in 16 mps winds — analytical (TRES4) at sea level

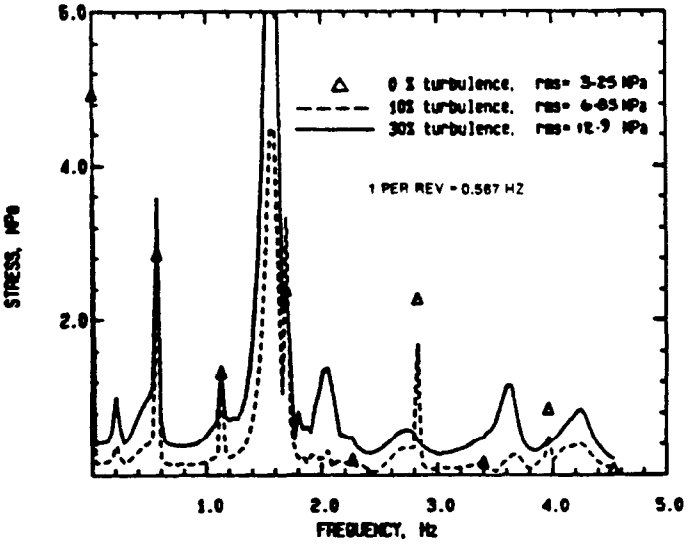

Fig. 12. Amplitude spectrum of upper root lead-lag response at 34 rpm in 16 mps winds — analytical (TRES4) at sea level

Measured and predicted amplitude spectra in both the flatwise and lead-lag directions at 34 rpm for 15-16 mps winds are shown in Figs. 9-12. The predictions include responses due to zero, 10%, and 30% turbulence intensity. The predicted spectra here were computed with a sea level air density which is 12% greater than the density at the test site. Also, the frequency spacing of the measured spectrum is slightly smaller than that of the predictions, which, while not influencing the per rev peaks, will make the off-harmonic measurements appear smaller than if they had the same resolution as the predictions (an artifact of using amplitude spectra rather than spectral density).

The lead-lag peak at 1.6 Hz below 3 per rev (1.7 Hz) predicted by TRES4 (Fig. 12) clearly is not as dominant in the measurements (Fig. 11). This large peak, which causes the overestimate of RMS stresses by TRES4 at 34 rpm mentioned earlier, is due to the the close proximity of the 1BE mode to 3 per rev. In addition, the predicted aeroelastic damping in the 1BE mode is very low (less than 1%) (9). Interestingly, the aerodynamic loading near the 3 per rev is quite sensitive to the treatment of dynamic stall (11).

The measured and predicted amplitude spectra are similar in distribution of energy over frequencies. The major difference, besides at the 1BE mode, is the tendency to over-predict the magnitude of the per rev components in the lead-lag direction. The difference, however, may be due to the measurements because the turbine never operates at an exactly fixed speed; the 5% variation in set speed could lead to some frequency spreading around the per rev frequencies. The structural response

estimates are only as good as the double-multiple streamtube aerodynamic codes used to calculate the input loads. More analyses exercising the latest TRES4 version will be required to sort out the combination of aeroelastic and aerodynamic assumptions that combine to limit the accuracy of the predictive codes.

Operating Near Resonance

The predicted first tower in-plane mode crossing of the 3 per rev excitation occurs at 40.5 rpm. Its effects on increased rotor vibration can be seen even while operating at somewhat slower speeds. Figure 13 is a plot of the upper root lead-lag stress response and turbine rpm at the edge of the resonance. The turbine was operating at a nominal 39.5 rpm with the rotation rate varying between 39 and 40 rpm. Each time the speed increased, the response began growing and continued to increase as the turbine approached 40 rpm. When the speed slowed to almost 39 rpm, the response decreased considerably. Operation has been restricted to 38 rpm and below to avoid the effects of this resonance.

SIGNIFICANT EVENTS

High Wind Over-speed and Blade Resonances

Near the end of the resonance survey testing (March of 1989), the turbine was operated at several speeds in winds that averaged 17 mps with gusts to 20 mps. Figure 14 shows a plot of rpm, wind speed, and blade lead-lag response during this period. At 32 rpm the response grew dramatically as the turbine passed through the first blade edgewise mode crossing of the 3 per rev excitation. (Peak-to-peak stress excursions as high as 50 MPa were noted.) At lower winds (less than 13 mps) the response at 32 rpm was not much greater than surrounding rotation rates.

Subsequent operation at 38 rpm in high winds (greater than 17 mps) caused power production to exceed the rating of the generator (625 kW), whereupon the turbine began slowly speeding up. At 40 rpm the tower-in-plane resonance was excited and caused very high lead-lag blade stresses. As illustrated in Fig. 15, the peak-to-peak stresses during this period were as high as 100 MPa. At 42 rpm the stresses decreased dramatically as this resonance was passed through. A few seconds later, at 42 rpm, an emergency stopped was invoked and the turbine came to a complete stop in 13 seconds with peak-to-peak lead-lag stopping stresses of only 20 MPa in the blade roots. This episode demonstrated the reliability of the controller and brakes. The brakes worked properly with no damage although some bluing of the brake disc due to high temperatures did take place. Operation of the turbine is now restricted to winds below 13 mps at 32 and 38 rpm.

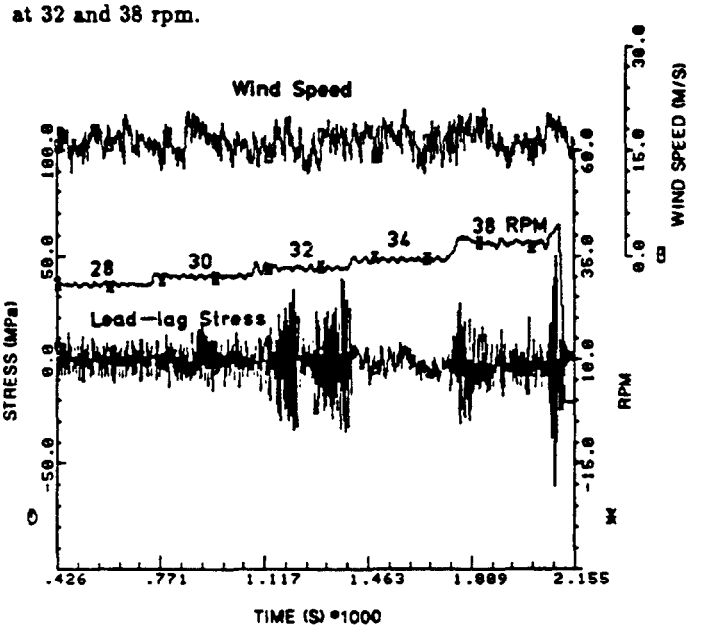

Fig. 14. Lead-lag response in 17 mps winds at 28 through 42 rpm

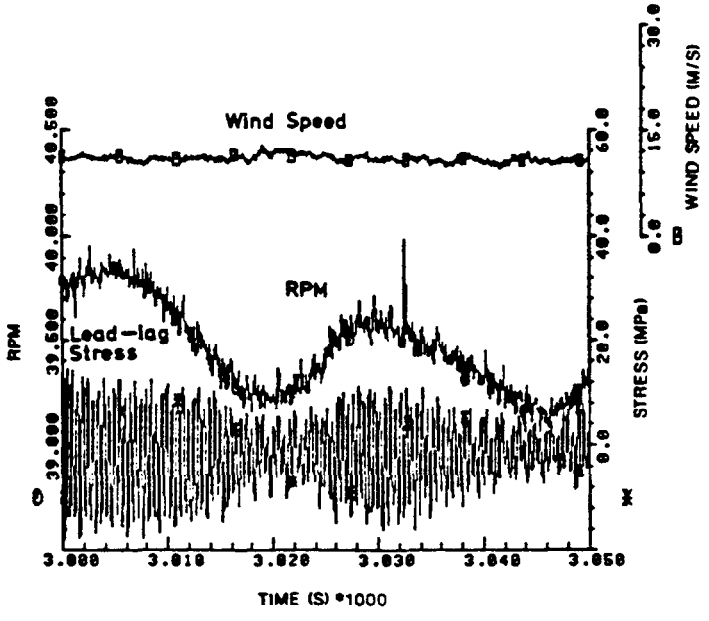

Fig. 13. Lead-lag response at nominal 39.5 rpm

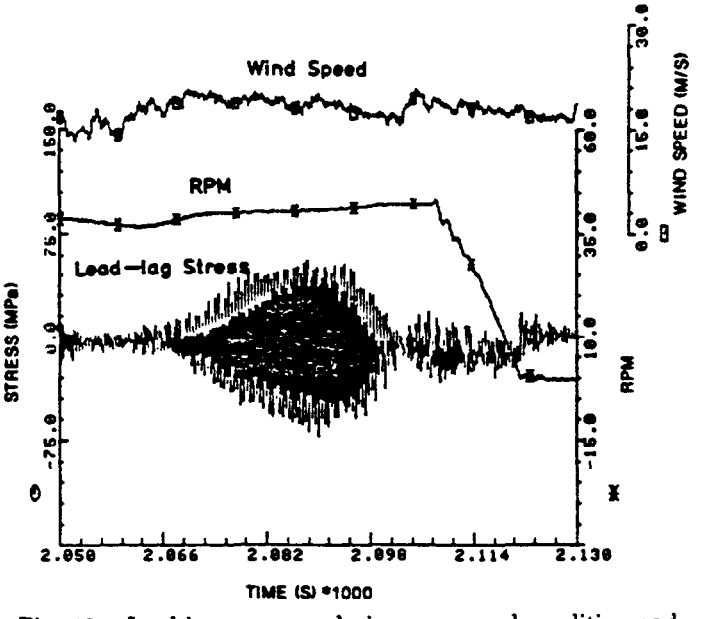

Fig. 15. Lead-lag response during over-speed condition and emergency stop (approximately last 80 s from Fig. 14)

Cable-Rotor Interaction

The turbine is supported at the top by three pairs of guy-cables, each of which is 63.5 mm (2.5 inches) in diameter. The lowest guy-cable frequencies, modes 1 and 2, were designed to vibrate at 0.81 Hz and 1.62 Hz, respectively, at a nominal cable tension of 826 kN (186,000 lb). The design assumed a uniform cross-sectional area the entire cable length. This design places the first cable mode below 2 per rev and the second mode between 2 and 4 per rev for the entire operating range, as shown in the cable fan-plot, Fig. 16. Cable frequencies were measured during the modal testing and are also shown in this figure. The measured natural frequencies of all but the first mode are lower than predicted because the heavy cable attachment hardware at the lower cable connection violates the uniform cable assumption. A new analytical tool that includes the ability to model non-uniform guy-cable mass distribution has been developed and predicts the first four cable modes to be 0.76, 1.23, 2.05, and 2.95 Hz, very close to the measured values.

The importance of avoiding guy-cable natural frequencies was demonstrated while operating at 38 rpm in moderate winds of 10 mps (22 mph) and cold temperatures. The time history shown in Fig. 17 illustrates the blade root lead-lag stress during operation at 38 rpm. At 210 seconds into the data record, the lead-lag stresses increased to almost 40 MPa peak-to-peak. The controller shut down the turbine when it sensed excessive cable tension. The operator noticed large cable vibrations during and after the shutdown.

Detailed study of this event indicated that the second cable mode resonance at 2 per rev, nominally at 37 rpm, moved to 38 rpm because of cold temperatures (cable tension increases in cold temperatures causing the natural frequencies to increase). The motion of the guy cables then coupled with the 1TI mode creating large lead-lag stresses. Figure 18 shows time histories of the lower root lead-lag stress and the guy cable tension before the excitation occurred. The cable tension contains 2 and 4 per rev components, while the lead-lag response is primarily 1, 2, and 3 per rev. Figure 19 shows the same measurements three minutes later during the tower-cable coupling. Here the cables are even more strongly 2 and 4 per rev, but the root lead lag gauge is overwhelmingly 3 per rev (3 per rev on the rotating frame is 2 and 4 per rev in the fixed reference frame).

Apparently, the tower-in-plane mode dropped in frequency from 2.05 Hz to 1.9 Hz, which is at 3 per rev at 38 rpm. One possible mechanism for this drop is for cable lateral motions at 2 per rev in the fixed frame to lock in phase with 3 per rev tower motion in the rotating frame (and 120 degrees out of phase with each other), resulting in a coupled cable-rotor mode at a lower frequency. Finite element models including both the guy-cables and the tower have shown similar coupling for a parked rotor when cable and rotor natural frequencies are within 10% of each other.

Auxilary cables have been added to the attachment hardware to move the second cable mode resonance at 2 per rev higher in frequency and out of the operating range.

SUMMARY

Comparisons of analytical and measured gravity stresses, centrifugal stresses, stationary modal frequencies and rotating modal frequencies show good agreement and increase confidence that the finite element model accurately describes the turbine structurally (5).

Measured RMS stresses, both lead-lag and flatwise, do not uniformly increase as the rotation rate increases from 28 to 34 to 38 rpm. Flatwise stresses increase nearly linearly with wind speed. Lead-lag stresses increase with wind speed, but not in a uniformly linear fashion.

The steady wind predictions, which include no damping, under-estimate the flatwise stresses at all rpm's and wind speeds — significantly so in high winds, but only slightly so in low to moderate winds. Lead-lag stresses are under-estimated in very low and very high winds and are greatly over-estimated in moderately high winds (around 15 mps).

In general, predictions including turbulence and structural damping are closer to measured values in high winds than those

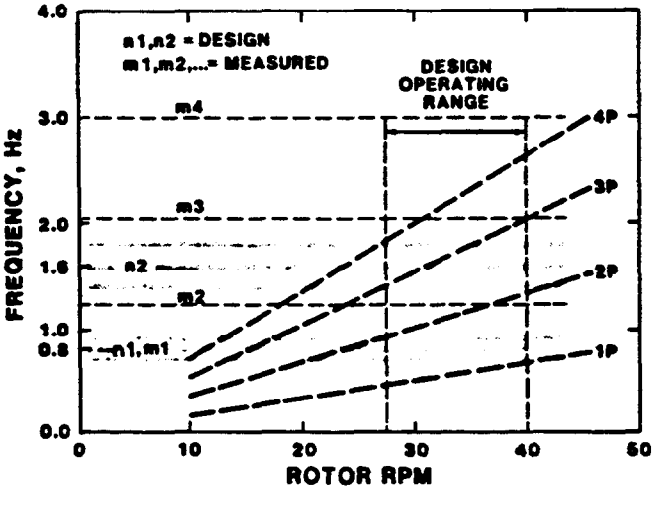

Fig. 16. Cable fanplot

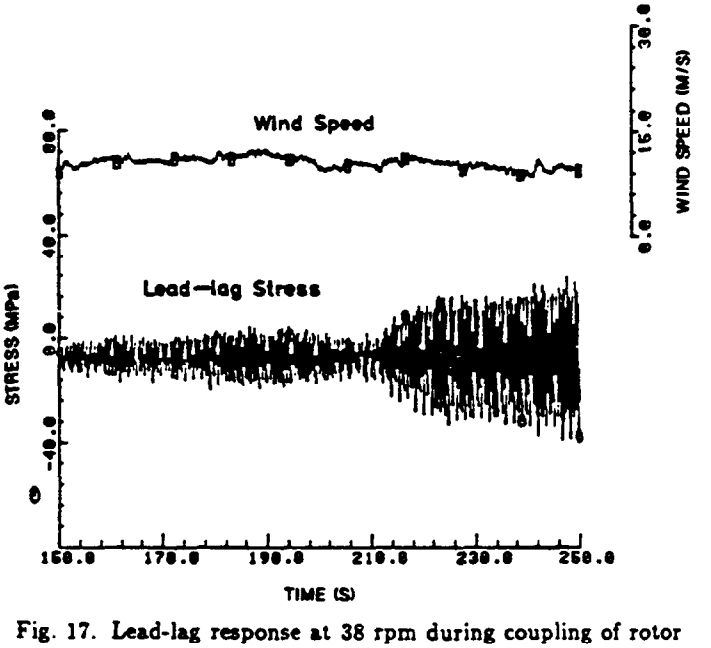

Fig. 17. Lead-lag response at 38 rpm during coupling of rotor and cable natural frequencies

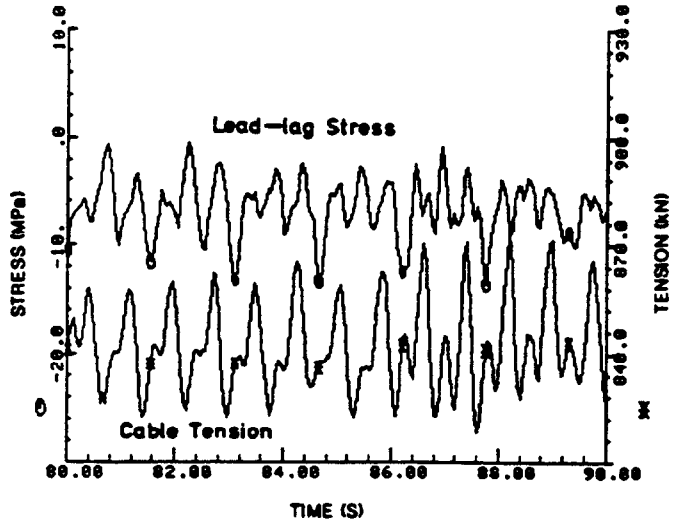

Fig. 18. Lead-lag and guy cable response before coupling

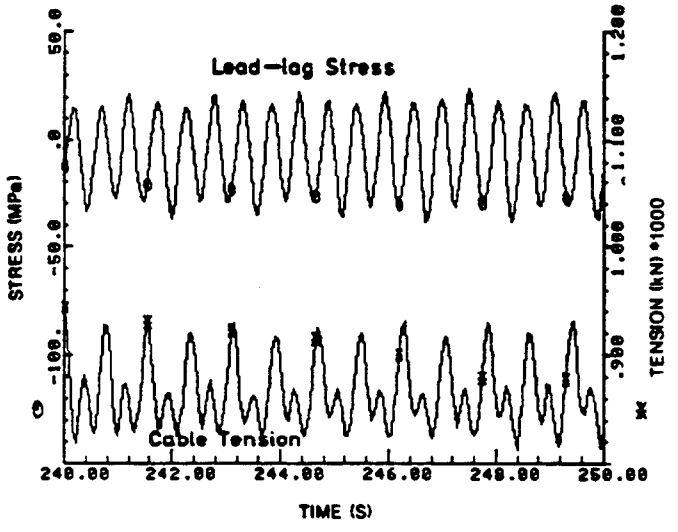

Fig. 19. Lead-lag and guy cable response during coupling

that assume a steady wind. The TRES4-generated amplitude spectra that include 10% turbulence intensity and aeroelastic damping have higher than measured amplitudes at the harmonics, but under-predict the off-harmonics. Flatwise stresses, which are mostly modal response to turbulence, are over-estimated with 2% modal damping and under-estimated with the full (8%) aeroelastic damping. Lead-lag stresses, which are highly harmonic and therefore most highly dependent on the character of the calculated loading, differ from measurements in both directions (high and low), although predictions are very good at 28 rpm. The aeroelastic model, therefore, appears to over-predict the flatwise damping and under-predict the lead-lag damping. More analyses with TRES4 will be required to sort out the combination of aeroelastic and aerodynamic assumptions that limit the accuracy of the predictive codes.

Two significant events showed the following: (1) The controller and brakes operated reliably in an over-speed condition. (2) Operation at a rotation rate near both cable and rotor natural frequencies can cause coupling between the modes, resulting in a resonance condition with high blade stresses.

ACKNOWLEDGMENTS

The authors would like to recognize the substantial contribution made by David Malcolm of Indal Technologies Inc. in developing TRES4 and providing the predictions that include turbulence. Clark Dohrmann of Sandia National Laboratories developed the new cable analytical tool that correctly models non-uniform mass distributions and conducted the parked-rotor, cable-vibration analysis. The spectral-averaging program was written by Dan Burwinkle of the New Mexico Engineering Research Institute.

REFERENCES

1. Carne, T.G., Lobitz, D.W., Nord, A.R., Watson, R.A., "Finite Element Analysis and Modal Testing of a Rotating Wind Turbine," SAND82-0345, Sandia National Laboratories, Albuquerque, NM, October, 1982.

2. Lobitz, D.W., and Sullivan, W.N., "Comparison of Finite Element Predictions and Experimental Data for the Forced Response of the DOE 100 kW Vertical Axis Wind Turbine," SAND82-2534, Sandia National Laboratories, Albuquerque, NM, February, 1984.

3. Malcolm, D.J., "A Model for the Response of Vertical Axis Wind Turbines to Turbulent Flow Parts 1 and 2," SAND88-7021, Indal Technologies, Mississauga, Ontario, Canada, for Sandia National Laboratories, Albuquerque, NM, July, 1988.

4. Stephenson, W.A., Test Plan for the 34 Meter Vertical Axis Wind Turbine Test Bed Located at Bushland, Texas, SAND86-1623, Sandia National Laboratories, Albuquerque, NM, December, 1986.

5. Ashwill, T.D., "Initial Structural Response Measurements for the Sandia 34-Meter VAWT Test Bed," *Proceedings of the Eighth ASME Wind Energy Symposium*, Houston, Texas, January, 1989.

6. Carne, T.G., Lauffer, J.P., Gomez, A.J., and Ashwill, T.D., "Model Validation of the Sandia 34-Meter Test Bed Turbine Using Substructured Modal-Testing," *Proceedings of the Eighth ASME Wind Energy Symposium*, Houston, Texas, January, 1989.

7. Homicz, G.F., "VAWT Stochastic Loads Produced by Atmospheric Turbulence," *Proceeding of the 7th ASME Wind Energy Symposium*, New Orleans, La., January 10-13, 1988.

8. Veers, P.S., "Modeling Stochastic Wind Loads on Vertical Axis Wind Turbine Blades," SAND83-1901, Sandia National Laboratories, Albuquerque, NM, September, 1984.

9. Lobitz, D.W. and Ashwill, T.D., "Aeroelastic Effects in the Structural Analysis of Vertical Axis Wind Turbines," SAND85-0957, Sandia National Laboratories, Albuquerque, NM, April, 1986.

10. Malcolm, D.J., "Vertical Axis Wind Turbine Turbulent Response Model Part 2 - Response of the SNL 34 with Aeroelastic Effects," Final Report by Indal Technologies, Mississauga, Ontario, Canada, for Sandia National Laboratories, Albuquerque, New Mexico, November, 1988.

11. Malcolm, D.J., Private correspondence, September, 9, 1989.

Proceedings of the Ninth ASME Wind Energy Symposium
D. E. Berg (ed.), SED-Vol. 9, ASME, January 1990

FATIGUE ANALYSIS OF THE SANDIA 34-METER VERTICAL AXIS WIND TURBINE*

T. D. Ashwill, H. J. Sutherland, and P. S. Veers
Wind Energy Research Division
Sandia National Laboratories
Albuquerque, New Mexico

ABSTRACT

Miner's Rule is used to estimate the service lifetime of a blade of the Sandia 34-meter wind turbine. The effects on the life estimates due to changes in wind regimes, constitutive properties, stress states and operational algorithms were determined in a parametric study. The results illustrate the sensitivity level of the estimates to such changes and are presented in both graphical and tabular form.

INTRODUCTION

Sandia National Laboratories has erected a research oriented, 34-meter diameter, Darrieus, vertical axis wind turbine (VAWT) near Bushland, Texas (1). This variable speed turbine has been operated at fixed speeds throughout its operating range of 28 to 38 rpm and in a true variable speed mode. The turbine and its site have been equipped with a large array of sensors that permit the characterization of the turbine under field conditions. Structural response measurements such as stationary and rotating natural frequencies, mean stresses and operating stresses have been compared to analytical predictions (2,3) with good results.

One important aspect of the comparison between measured and predicted (design) operating stresses is the effect of their differences on the fatigue life of the turbine blade. To this end, the LIFE2 fatigue analysis code for wind turbines (4,5) is used to predict blade life using both measured and predicted operating stresses. In particular, the highest stressed region of the blade (at the upper blade-to-tower joint) is analyzed in both the flatwise and lead-lag directions using Miner's rule (5). Several parameters are varied, including the characterization of the site's wind regime, the S-n curve for the extruded aluminum blades, and the turbine operational mode.

A description of each study parameter is presented, followed by a set of baseline service lifetime estimates for both predicted (design) and measured conditions. From this set, the variable-speed mode of operation is chosen for studying the influence of each parameter on the service lifetime of the blade by varying one parameter at a time. The results are presented in both graphical and tabular form.

WIND REGIME

The design of the Test Bed assumed that the turbine would be sited in a wind regime whose yearly wind speed distribution is described by a Rayleigh distribution with a 6.2 mps (14 mph) average, see Fig. 1. Two additional wind distributions for the turbine site have been included here. The first is data taken at the Amarillo Airport (6). These data, see Fig. 1, span 17 years and have an average wind speed of approximately 6.6 mps (15 mph). Wind distribution data have also been obtained for the past 6 years (1983-1988) at the Bushland site (6). These data, see Fig. 1, have a 5.8 mps (13 mph) average and are based on 1-hour averages obtained at a height of 10 m (30.5 ft).

There are three major differences between these wind speed distributions that affect the service lifetime predictions. The first is that the Rayleigh distribution has a long tail that extends out to very high winds, whereas the Bushland and Amarillo distributions contain little occurrence of winds above 20 mps. The second is that the Amarillo distribution has a hump in moderate winds which is not seen in the Bushland data. The third difference is that the Amarillo site has the highest frequency of moderate to high winds and the Bushland site the lowest. Thus for turbine operation between 6 and 20 mps, the Amarillo site is the most energetic and the Bushland site is the most benign.

*This work is supported by the U.S. Department of Energy at Sandia National Laboratories under contract DE-AC04-76DP00789.

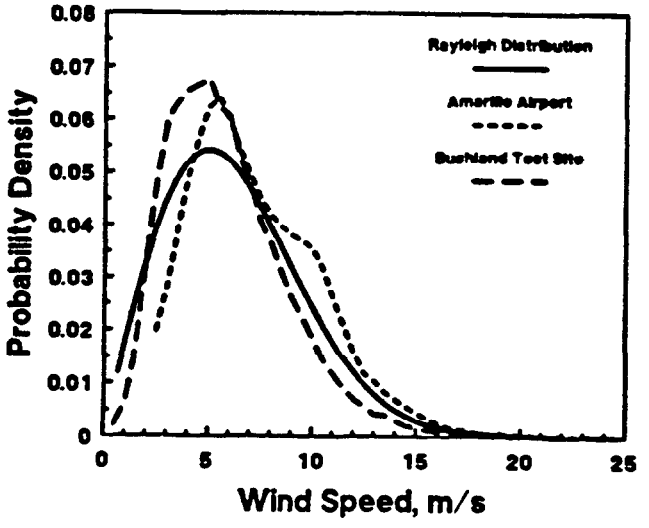

Fig. 1 The wind regimes

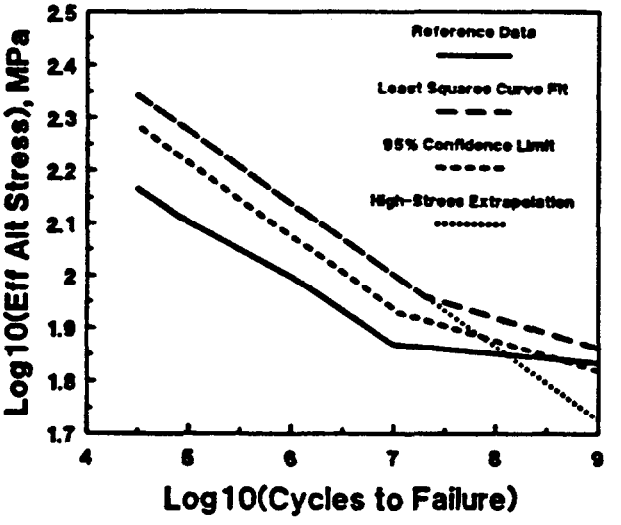

Fig. 2 The constitutive properties of 6063 aluminum

CONSTITUTIVE PROPERTIES

The blades of the Test Bed are constructed from extruded 6063 aluminum. Limited fatigue data were available for this material in the literature. Design fatigue estimates for the Test Bed were based on the extrapolation of a limited set of S-n data and knowledge of the properties of other aluminum alloys (7). The extrapolation was based on Goodman's rule (5) and assumed that the ultimate stress for the aluminum was 241 MPa (35 ksi). These data, see Fig. 2, will be described here as the "Reference" constitutive data.

Subsequent tests have determined the S-n properties for the extruded aluminum blade material (8). The data from these tests at various mean and alternating stress levels have been converted to "effective" stress levels using a Goodman rule, based on the ultimate stress (5). In this formulation, the effective stress is equal to the cyclic stress amplitude at zero mean stress. The ultimate stress for the extruded aluminum was measured to be 244 MPa (35.4 ksi).

Three formulations of the material S-n behavior are derived from the experimentally-measured data set. The first is the mean or least squares curve (LSC) fit to the data, which approximates a 50% confidence limit. The second, based on a statistical analysis of the data, is the 95% confidence limit for the data set (i.e., in a sample of 100 specimens, 5 are expected to fail and 95 are not). A third eliminates the change in slope at about 10 million cycles in the LSC data and linearly extends the curve out to the high cycle region. These constitutive formulations, which are included in Fig. 2, will be called the "least squares" (LSC), the "95%" and the "high cycle extrapolation" fits, respectively.

Fig. 2 shows that the reference S-n curve is significantly lower than the others (the reference S-n curve allows less cycles to failure for a given effective stress). The LSC fit to the test data provides the most durable properties of any of the formulations.

The change in slope in the curves at low stresses is similar to what many call the endurance or fatigue limit. The high-cycle extrapolation S-n curve eliminates this limit. This technique has been proposed for estimating the effects of the random nature of the stresses imposed on a wind turbine (9).

OPERATIONAL STRESSES

Structural responses of the Test Bed have been measured and compared to analytical predictions with good results (2,3). The highest stressed region of the blade both in the flatwise and lead-lag directions was found to be at the upper blade-to-tower joint (upper root). The upper root is where the 48 inch chord blade section attaches to the tower (1).

Measured and Predicted Operational Stresses

The stress states at many locations along the blades were predicted using FFEVD (10), the Sandia written frequency response finite element code. The FFEVD code assumes steady winds only, and the calculations incorporated no damping.

The stress states for the upper root were measured using strain gauges located 36 inches from the blade root (11). The measured stress data were increased by an analytically-derived factor (1.08 for lead-lag and 1.23 for flatwise) to adjust them to the true root location.

Operating stresses are characterized by the root-mean-square (RMS) of the oscillating stress after the mean stress is removed. These operating stresses are mapped into stress amplitudes using a narrow-band Gaussian approximation (5,9). The equivalent stress states are obtained in the LIFE2 code from the stress amplitudes and by using a Goodman rule (5). The measured and predicted flatwise RMS stresses, for fixed speed operation at 28, 34 and 38 rpm, are shown in Figs. 3 and 4, respectively. Comparison of the measured and predicted RMS stresses for constant 38 rpm operation is shown in Fig. 5. The lead-lag stresses are not shown here, but are reproduced in Ref. 3.

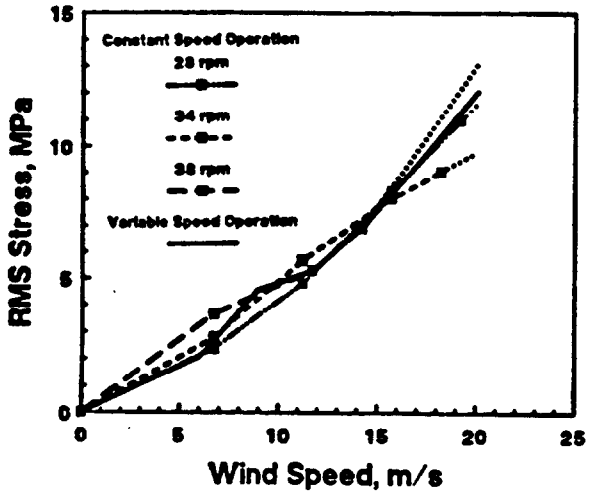

Fig. 3 Measured flatwise RMS stresses at the upper root

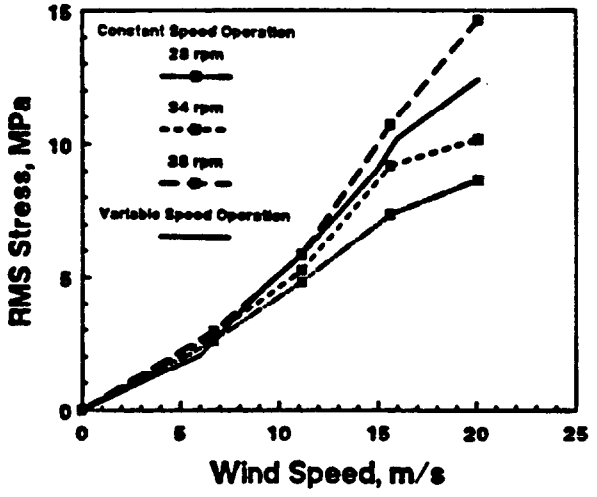

Fig. 4 Predicted flatwise RMS stresses at the upper root

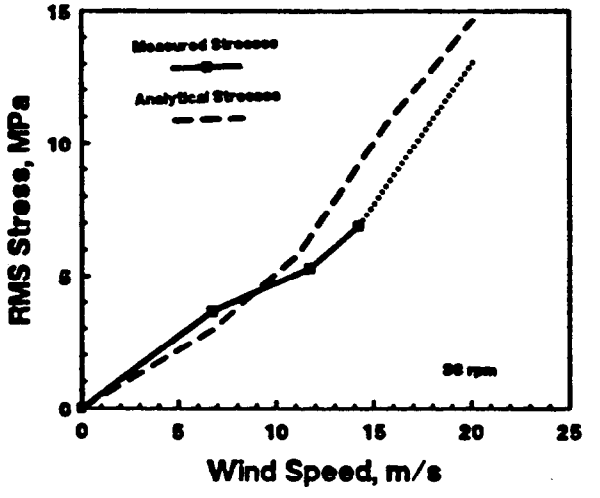

Fig. 5 Comparison of the measured and predicted RMS flatwise stresses for the Test Bed at 38 rpm

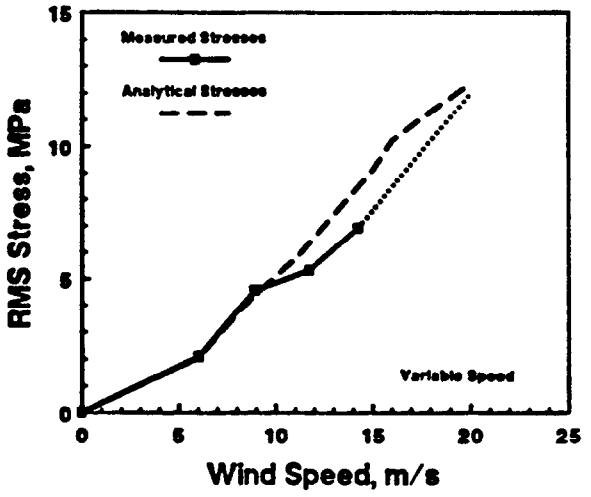

Fig. 6 Comparison of the measured and predicted RMS flatwise stresses for the Test Bed with variable speed

The constant rpm data was used to synthesize the operating stresses for variable speed operation. Using linear interpolation of the fixed speed data, the variable speed algorithm, discussed below, was mapped directly into the stress states. The results of the mapping of the measured and predicted flatwise stresses are shown in Figs. 3 and 4, respectively, and are compared to one another in Fig. 6.

Oscillation Rate

A necessary parameter for the determination of service lifetime of the blade is the rate at which stress cycles are accumulated. For the predictions, this rate was chosen to be 3 times the rotational rate of the turbine for the lead-lag stress cycles and 2 times for flatwise stress cycles. For the measurements, this rate was determined using the average "mean-crossing" rate (12). The rates used for constant speed operation of the turbine are shown in Table I. Abbreviations used in this and successive tables are explained in Appendix A. The cycle rate used for the variable speed control algorithm used a linear interpolation of these values.

Table I Average stress cycle rates for the Test Bed

Control Algorithm	Cycle Rate, Hz			
	Flat		L-L	
	Ana	Mea	Ana	Mea
28 rpm	0.93	1.43	1.4	1.92
34 rpm	1.13	1.52	1.7	1.86
38 rpm	1.27	1.5	1.91	1.96

Stress Concentration Factor

A stress concentration factor of 3.0 was used for most of the calculations cited here. This factor increases the nominal stress states to account for stress risers in the bolted, root joint.

Table II Service lifetime for various operating algorithms (in years)

Wnd	Fat	OPS	Flatwise Stress States				Lead-Lag Stress States			
			28 rpm	34 rpm	38 rpm	Var	28 rpm	34 rpm	38 rpm	Var
R	Ref	Ana	1360.	33.1	2.21	11.9	61.1	205000.	0.91	19.40
B	LSC	Mea	966.	504.	286.	391.	296000.	9470000.	73.9	494.

OPERATING PARAMETERS

Turbine Operation

For all calculations the cut-in wind speed was taken to be 5.8 mps (13 mph) and the cut-out wind speed was taken to be 20 mps (45 mph). The life predictions assume that the turbine is operating 100% of the time when the wind speed is between cut-in and cut-out. Effects of the control algorithm, such as the elimination or addition of turbine operation near the cut-in and cut-out wind speeds and operation at non-optimum rpm, are not considered here. Also, the stress cycles introduced by starting and stopping the turbine are not considered.

Variable Speed

To obtain maximum power production without exceeding the capacity of the generator system, the Test Bed is operated with the variable speed algorithm shown in Fig. 7 (13). As illustrated by this figure, the rotor speed of the turbine at the cut-in wind velocity of 5.8 mps (13 mph) is 25 rpm. Above a wind speed of 6 mps (13.6 mph), the rotor speed is increased at a rate of 4 rpm for a 1 mps increase in wind speed. At a wind speed of 9.5 mps (21.5 mph), the rotor reaches its maximum speed of 38 rpm. Between 9.5 mps (21.5 mph) and 15 mps (34 mph), the speed of the turbine is held constant at 38 rpm. For speeds above 15 mps (34 mph), the rotor speed is reduced to 37 rpm to prevent over loading the generator system.

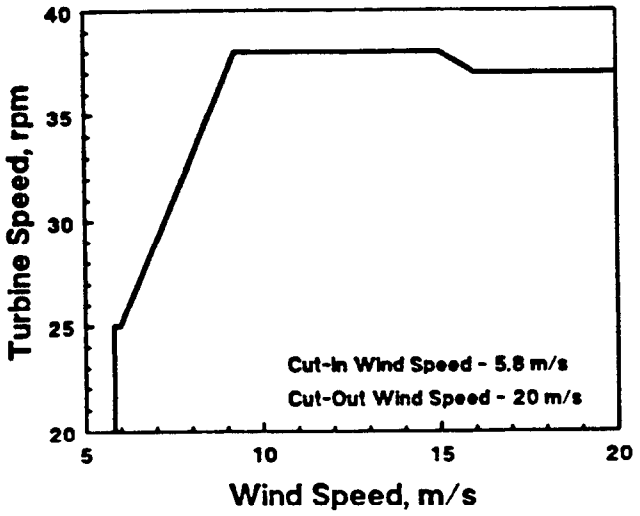

Fig. 7 Variable speed control algorithm for maximum power production

RESULTS

Baseline Data Set

To obtain a reference frame for the study parameters, a set of baseline service-lifetime calculations was performed. The baseline data, summarized in Table II, compare service lifetimes (all lifetimes are in years of service) of the blade at the critical upper blade root location. The flatwise and lead-lag stress states from all four operating conditions cited above are used. As seen in this table, the shortest lifetime for the turbine blade occurs for constant speed operation at 38 rpm. Because the Test Bed will not be operated in this mode in high winds (above 15 mps wind speeds, the capacity of the generator would be exceeded), the most critical, realistic case is for variable speed operation. Thus, variable speed operation was chosen for the parameter studies cited below.

Wind Regime

Table III lists the estimated fatigue lives in the lead-lag and flatwise direction for both the analytical and measured operating stresses for each of the three wind regimes. In the analytical case the "reference" S-n curve is used, and the LSC curve is used for the measured case. For both the analytical and measured cases the order of fatigue life estimates from lowest to highest is Amarillo, Rayleigh, and Bushland. This pattern is clearly illustrated by examining the distribution of fatigue damage as a function of wind speed. These flatwise "damage density distributions", for the three wind regimes, are shown in Fig. 8. The overall lowest life estimates occur in the flatwise analytical case and vary from 7.9 to 29.4 years depending on the wind regime.

Table III Effect of the wind regime on lifetime (in years)

Wnd	Fat	OPS	Flat	L-L
R	Ref	Ana	11.9	19.4
A	Ref	Ana	7.86	10.1
B	Ref	Ana	29.4	109.
R	LSC	Mea	150.	125.
A	LSC	Mea	100.	71.0
B	LSC	Mea	391.	494.

Constitutive Formulation

Table IV lists the estimated fatigue lives at the critical root location for both the analytical and measured cases as a function of the four S-n curves

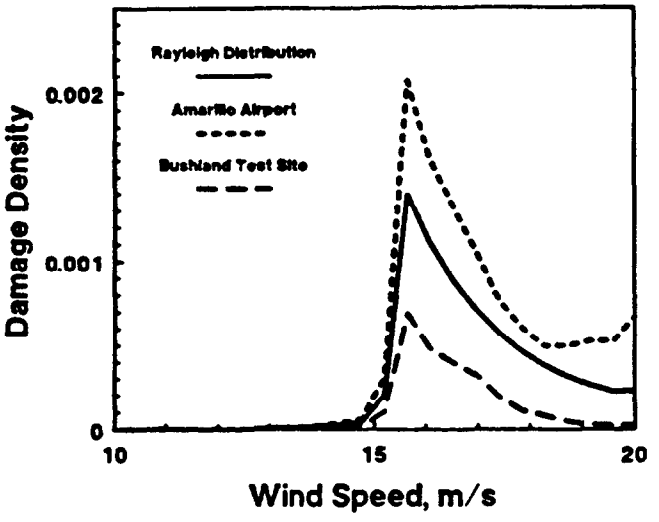

Fig. 8 Effect of the wind regime on damage density

cited above. The "reference" S-n curve is the most conservative as it predicts lifetimes that are much lower than the measured formulations. The "LSC" S-n curve is the least conservative. These trends again can be seen in the flatwise damage density distribution of Fig. 9.

Table IV Effect of the constitutive formulation on lifetime (in years)

Wnd	Fat	OPS	Flat	L-L
R	Ref	Ana	11.9	19.4
R	LSC	Ana	59.7	149.
R	95%	Ana	35.7	70.3
R	Hgh	Ana	52.8	135.
B	Ref	Mea	104.	83.7
B	LSC	Mea	391.	494.
B	95%	Mea	243.	249.
B	Hgh	Mea	307.	430.

The high cycle S-n extrapolation results in fatigue life estimates only slightly less than the least squares S-n curve. The 95% curve results in estimates approximately half those of the least squares curve.

Table V Effect of the operational stresses on lifetime (in years)

Wnd	Fat	OPS	Flat	L-L
R	Ref	Ana	11.9	19.4
R	Ref	Mea	33.5	15.7
B	LSC	Ana	121.	602.
B	LSC	Mea	391.	494.

Stress States

Table V lists the estimated fatigue lives for the analytical and measured stresses for two conditions. For either the LSC S-n curve with the Bushland wind case or the Reference S-n curve with the Rayleigh wind case, the analytical data provides lower estimates in the flatwise direction, but slightly higher estimates in the lead-lag direction. Figure 10 shows the flatwise damage density distribution. As seen in these data, the relatively small difference in RMS stress levels, shown in Fig. 6, yields a relatively large difference in the predicted service lifetimes.

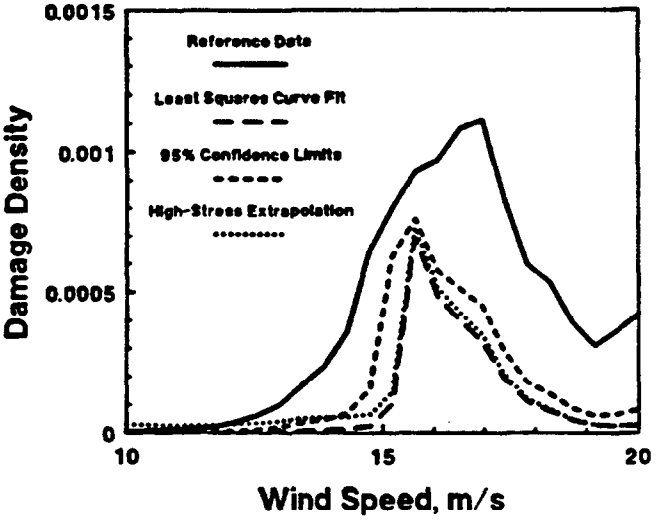

Fig. 9 Effect of the constitutive formulation on damage density

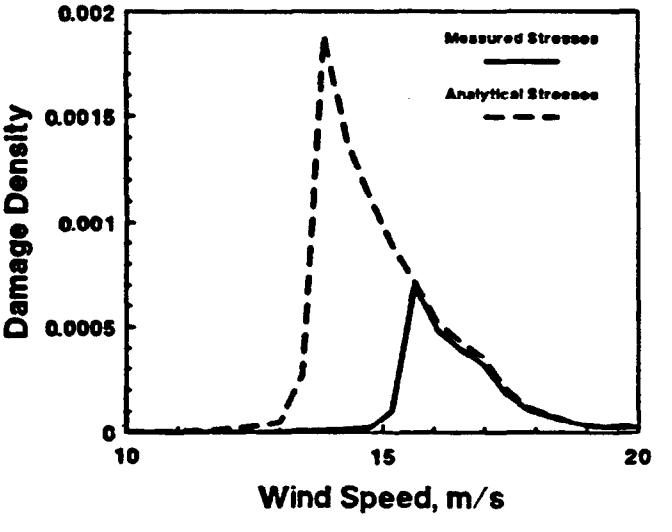

Fig 10 Effect of the operational stresses on damage density

Stress Concentration Factor

Stress concentrations are difficult to measure or estimate accurately and are different for each joint design. Unfortunately, fatigue life is very sensitive to the stress concentration as seen in Table VI and Fig. 11. When the reference stress concentration is raised from 3.0 to 3.5, the fatigue life estimates can decrease an order of magnitude.

Table VI Effect of the stress concentration factor on lifetime (in years)

Wnd	Fat	OPS	SCF	Flat	L-L
R	Ref	Ana	3.0	11.9	19.4
R	Ref	Ana	3.5	1.53	0.52
B	LSC	Mea	3.0	391.	494.
B	LSC	Mea	3.5	108.	37.6

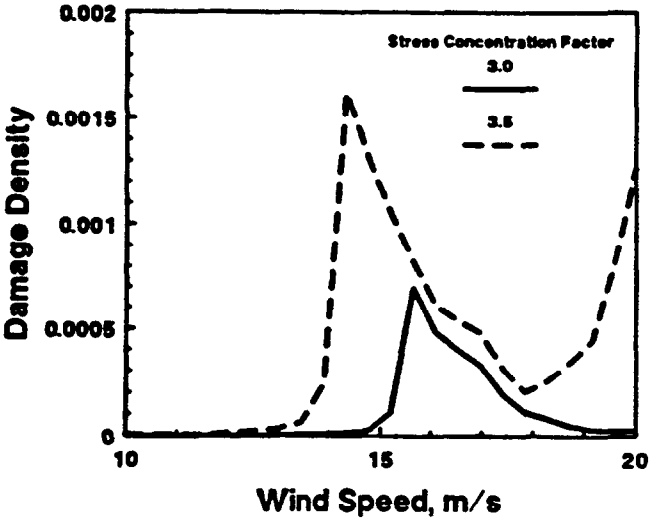

Fig 11 Effect of the stress concentration factor on lifetime

CONCLUSIONS

Fatigue life estimates have been calculated for the Test Bed blade at the highest stressed location using the LIFE2 code. Baseline calculations, which compare design-condition estimates to measured-condition estimates, indicate that the design condition consistently underestimates service lives for all of the operating modes investigated here. Thus, lifetime predictions based on design-conditions are consistently conservative.

Further calculations varied the wind speed distribution, the S-n curve, operating stresses, and the stress concentration. Significant differences in estimates occurred for each parameter studied - small changes in a single parameter can have large changes in lifetimes. The largest lifetime change was obtained when the stress concentration factor was increased from 3.0 to 3.5, decreasing the service lifetime of the blade by more than an order of magnitude.

Because the prediction of service lives is very sensitive to the various parameters, turbine designers must be especially careful in their determination of the wind regime for the each wind site of interest, the S-n curve for the blade material and the operating stresses, including stress concentrations, for their blade. If these parameters are not known accurately, the turbine design must be very conservative to obtain high confidence that components will not fail over the desired service lifetime of the turbine.

REFERENCES

1. Ashwill, T. D., et al, 1987, "The Sandia 34-Meter VAWT Test Bed", *Proceedings of Wind Power '87*, American Wind Energy Association, SERI/CP-217-3315, pp. 298-308.

2. Ashwill, T.D., 1989, "Initial Structural Response Measurements for the Sandia 34-Meter VAWT Test Bed," *Proceedings of the Eighth ASME Wind Energy Symposium*, D. E. Berg and P. C. Klimas (eds), SED-Vol. 7, ASME, pp. 285-292.

3. Ashwill, T.D. and Veers, P.S., 1990, "Structural Response Measurements and Predictions for the Sandia 34-Meter Test Bed," *Proceedings of the Ninth ASME Wind Energy Symposium*.

4. Schluter, L. L., and Sutherland, H. J., 1989, "Reference Manual for the LIFE2 Computer Code," SAND89-1396, Sandia National Laboratories, Albuquerque, NM.

5. Sutherland, H. J., 1989, "Analytical Framework for the LIFE2 Computer Code," SAND89-1397, Sandia National Laboratories, Albuquerque, NM.

6. Clark, N., 1989, USDA Agricultural Research Center, Bushland, Texas, personal communication.

7. Sutherland, H. J., Ashwill, T. D., and Slack, N., 1987, "The LIFE Computer Code: Fatigue Life Prediction for Vertical Axis Wind Turbine Components," SAND87-0792, Sandia National Laboratories, Albuquerque, NM.

8. VanDenAvyle, J. A., and Sutherland, H. J., 1989, "Fatigue Characterization of a VAWT Blade Material", *Proceedings of the Eight ASME Wind Energy Symposium*, D. E. Berg and P. C. Klimas (eds), SED-Vol. 7, ASME, pp. 125-129.

9. Veers, P. S., "Simplified Fatigue Damage and Crack Growth Calculations for Wind Turbines," *Proceedings of the Eighth ASME Wind Energy Symposium*, D. E. Berg and P. C. Klimas (eds), SED-Vol. 7, ASME, pp. 133-140.

10. Lobitz, D.W., and Sullivan, W.N., 1984, "Comparison of Finite Element Predictions and Experimental Data for the Forced Response of the DOE 100 kW Vertical Axis Wind Turbine," SAND82-2534, Sandia National Laboratories, Albuquerque, NM.

11. Sutherland, H. J., and Stephenson, W. A., 1988, "Rotor Instrumentation Circuits for the Sandia 34-Meter Vertical Axis Wind Turbine," SAND88-1144, Sandia National Laboratories, Albuquerque, NM.

12. Crandall, S. H., and Mark, W. D., 1963, *Random Vibration in Mechanical Systems*, Academic Press, New York, NY.

13. Ralph, M. E., 1989, "Control of the Variable Speed Generator on the Sandia 34-Metre Vertical Axis Wind Turbine," *Proceeding of Windpower '89*, in publication.

APPENDIX A. KEY FOR THE TABLES

Notes:

Wnd - Yearly Wind Regime
- R - Rayleigh Distribution with 14 mph Average
- A - Distribution for the Amarillo Airport, 17 years of Data
- B - Distribution at the Bushland Test Site

Fat - S-n Fatigue Data for Extruded 6063 Aluminum
- Ref - Reference Data
- LSC - Least Square Curve Fit to Experimental Data
- 95% - Curve Fit of Experimental Data with 95% Confidence Limits
- Hgh - Extrapolation of the High-Stress Data to All Stress Levels

OPS - Operation Stress States Obtained Using a Narrow Band Gaussian Model
- Ana - Analytical Predictions for the Stress States
- Mea - Measured Stress States
- Flat - Flatwise Stresses
- L-L - Lead-Lag Stresses

SCF - Stress Concentration Factor

Proceedings of the Ninth ASME Wind Energy Symposium
D. E. Berg (ed.), SED-Vol. 9, ASME, January 1990

RAINFLOW COUNTING ALGORITHM FOR THE LIFE2 FATIGUE ANALYSIS CODE*

L. L. Schluter and H. J. Sutherland
Wind Energy Research Division
Sandia National Laboratories
Albuquerque, New Mexico

ABSTRACT

The LIFE2 computer code is a fatigue/fracture analysis code that is specialized to the analysis of wind turbine components. The numerical formulation of the code uses a series of cycle count matrices to describe the cyclic stress states imposed upon the turbine. In this formulation, each stress cycle is counted or "binsed" according to the magnitude of its mean stress and alternating stress components and by the operating condition of the turbine. This paper describes a set of numerical algorithms that have been incorporated into the LIFE2 code. These algorithms determine the cycle count matrices for a turbine component using stress-time histories of the imposed stress states. Example problems are used to illustrate the use of these algorithms.

INTRODUCTION

The LIFE2 computer code is a fatigue/fracture analysis code specifically designed for the analysis of wind turbine components (1,2). It is a PC-compatible Fortran code that is written in a top-down modular format with a "user friendly" interactive interface. In this numerical formulation, an "S-n" fatigue analysis is used to describe the initiation, growth and coalescence of micro-cracks into macro-cracks. A linear, "da/dn" fracture analysis is used to describe the growth of a macro-crack.

In the LIFE2 formulation, the cyclic stresses imposed on the turbine component are characterized by the magnitude of their mean stress and alternating stress components and by the operating condition of the turbine. This paper describes a set of numerical algorithms that permit the code to analyze stress-time histories of component stress states. These "rainflow" counting algorithms are described in this paper and example problems are used to illustrate their use.

*This work is supported by the U.S. Department of Energy at Sandia National Laboratories under contract DE-AC04-76DP00789.

RAIN FLOW COUNTING ALGORITHM

The prime algorithm used here is a rainflow counting algorithm (3). This algorithm defines a stress cycle to be a closed stress/strain hysteresis loop. It determines the mean and alternating stress level for each stress cycle in the histogram. To illustrate the use this algorithm consider the typical stress-time history for a turbine component shown in Fig. 1. As this history is being used for illustrative purposes only, the stresses have been normalized.

Pre-Count Algorithms

Several auxiliary algorithms are used to support the rain-flow counting. The initial set of algorithms prepares the full time series data for counting by selecting peaks and valleys and discarding "small"

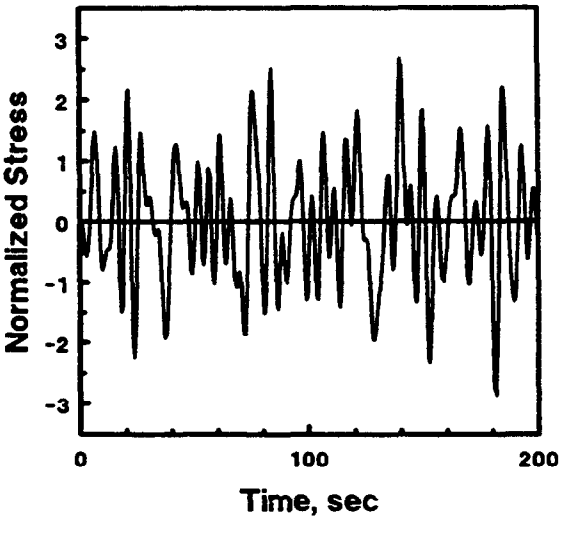

Fig 1 Typical stress-time history data

stress cycles. After counting, other algorithms record and store the cycle count data in an appropriate format for the LIFE2 analysis.

Peak-Valley Selection. The first algorithm identifies peaks and valleys in the data record by scanning for changes in the slope sign.

Typically, the data contained in this class of stress records are taken at uniform time intervals. This constant-time-interval sampling technique may or may not record actual maxima in the data, because the maxima may by "squared off", e.g., see the peak at approximately 185 seconds in Fig. 2. To obtain a better estimate of the actual maxima at a change in the slope sign, a parabola is fit to the three data points nearest that change. The maxima determined using this curve fitting technique are shown as triangles in Figs. 2 and 3.

As shown in Figs. 2 and 3, this technique for choosing the maxima may or may not significantly change the maxima recorded in the data. In particular, the maxima chosen for the peaks at approximately 140, 150, 165 and 180 seconds in Fig. 2 are very close to the maxima recorded in the data record, because the sampling technique has not squared off their maxima. However, when the maxima has been squared off, as with the peak at approximately 185 seconds in Fig. 2, the maxima is significantly increased by this curve fitting technique.

Filter. A "race track" filtering algorithm has been incorporated into the pre-processing algorithms to eliminate "small" stress cycles (4). In the technique used here, the operator sets a "threshold" value for the algorithm. When the absolute value of the difference between the maximum and minimum values of a stress cycle is greater than the threshold, the algorithm retains that cycle. When the difference is less than the threshold, the cycle is discarded. Fig. 4 illustrates the peak and valleys retained for the sample data record when the threshold is set to a value of 2.

The pre-count algorithms reduce the data record to a sequential list of peaks and valleys. This list is stored in a temporary file for processing by the count algorithm.

Count Algorithm

The rainflow counting algorithm used here (3) counts the number of closed stress/strain hysteresis loops in the data. It determines the mean and the peak-to-peak alternating stress level for each stress cycle in the histogram. These stress levels are stored in a temporary file for post processing. To speed operation, the algorithm uses "one-pass" through the data to count the stress cycles; i.e., the peak-valley data are read only once during processing by the count algorithm.

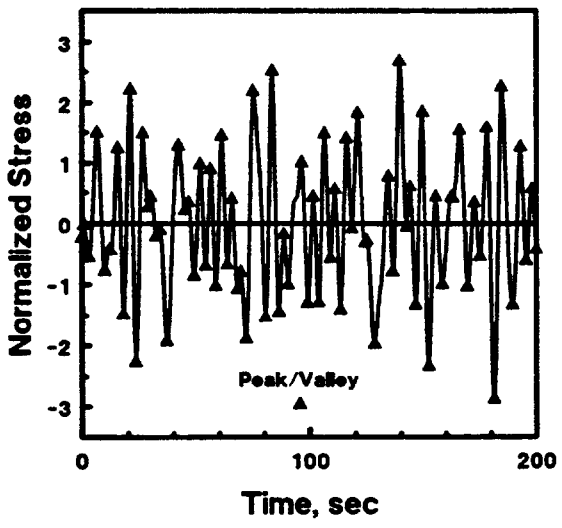

Fig 3 Selected peaks and valleys (no filter)

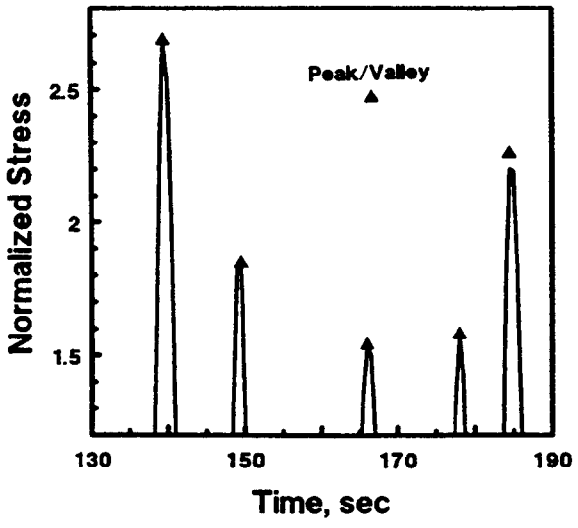

Fig 2 Estimation of peaks and valleys

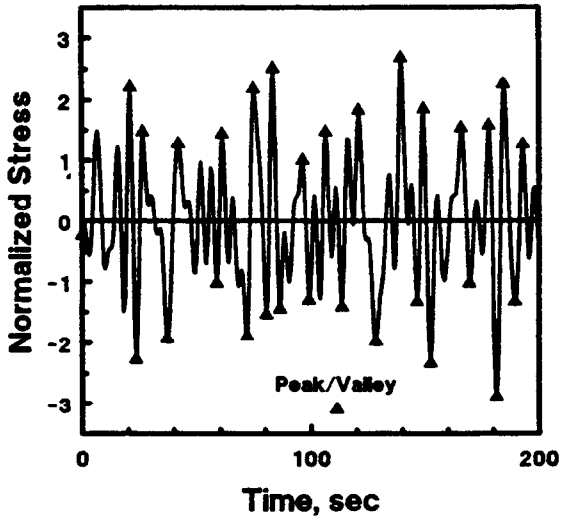

Fig 4 Selected peaks and valleys with a threshold of 2

Post-Count Algorithm

The final algorithm maps each stress cycle into a cycle count matrix that can be processed by the LIFE2 code. The algorithm sorts the stress cycle data into bins that are functions of mean stress and alternating stress levels.

The cycle counts from a data record may be used to create a new cycle count matrix, or they may be added to an existing cycle count matrix, at the discretion of the operator.

LIFE2 CODE MODIFICATIONS

These algorithms have been incorporated into the LIFE2 code in the stress states module. The operator may input operational stresses, buffeting stresses, or start/stop stresses. The rainflow counting algorithms have been added as Option 4 under these respective menus (see Ref. 1 for a complete description of the menuing system used by the LIFE2 code).

EXAMPLE PROBLEMS

Data records from the Sandia 34-m Test Bed will be used in this presentation to illustrate the use of these algorithms for the analysis of the service lifetime of a turbine blade.

SUMMARY

A set of algorithms that permit the analysis of time-series stress data have been incorporated into the LIFE2 fatigue/fracture analysis code. The algorithms are built around a rainflow counting algorithm. A normalized stress-time history and data from the Sandia 34-m Test Bed vertical axis wind turbine are used to illustrate the features of the algorithms.

ACKNOWLEDGEMENTS

The authors wish to thank P. S. Veers and D. P. Burwinkle for their help in implementing and checking these algorithms.

REFERENCES

1. Schluter, L. L. and Sutherland, H. J., "Reference Manual for the LIFE2 Computer Code," SAND89-1396, Sandia National Laboratories, Albuquerque, NM, September 1989, 170 p.

2. Sutherland, H. J., "Analytical Framework for the LIFE2 Computer Code," SAND89-1397, Sandia National Laboratories, Albuquerque, NM, September 1989, 42 p.

3. Downing, S. D., and Socie, D. F., "Simple Rainflow Counting Algorithms", *International Journal of Fatigue*, Vol. 4, N. 1, 1982, pp. 31-40.

4. Veers, P.S., Winterstein, S. R., Nelson, D. V. and Cornell, C. A., "Variable Amplitude Load Models for Fatigue Damage and Crack Growth," *Development of Fatigue Loading Spectra*, ASTM STP 1006, J. M. Potter and R. T. Watanabe, eds., 1989, pp. 172-197.

Proceedings of the Ninth ASME Wind Energy Symposium
D. E. Berg (ed.), SED-Vol. 9, ASME, January 1990

SMART CONTROL ALGORITHMS FOR OPERATION OF VARIABLE-SPEED WIND TURBINES

W. A. Vachon
W. A. Vachon and Associates, Inc.
Manchester, Massachusetts

ABSTRACT

The use of variable - speed, constant - frequency (VSCF) wind turbines (WTs) permits the use of mechanical design simplicities, while enabling WTs to capture energy more efficiently than constant-speed units. A key risk with such a design approach is that the WT rotor speed can coincide with one of the many mechanical resonant vibrational frequencies of the WT, and lead to severe material fatigue damage. To study the use of VSCF generators, a time-domain, dynamic control algorithm simulation has been developed. It takes into account most control parameters that are useful for governing WT cut-in and cut-out operation, while incorporating rotor speed control approaches that enable the WT to avoid or accelerate through critical rotor speed ranges that can lead to accelerated structural damage. Passage through such ranges are governed by the actual rotor rpm and trends in the wind speed. The code sums structural fatigue damage that occurs over the WT operating envelope, and sums energy production and motoring energy from both normal operation and from rotor speed changes arising from generator-controlled braking (rpm reductions) or generator-augmented accelerations.

This paper discusses the control approaches studied, and their overall effect on WT life and energy production. The various schemes for (1) modelling structural damage at all rotor speeds, and (2) controlling rotor speed and machine output power in the vicinity of critical structural resonances are outlined. The results of simulations of the performance of the Sandia National Laboratory's (SNL's) 34-m Test Bed WT are presented to illustrate key findings.

INTRODUCTION

Over the past decade, developments in power electronics devices and high-power, rapid switching circuits have made possible the economic use of variable - speed constant - frequency (VSCF) wind turbines [1]. The use of such WTs permits the designers to simplify the mechanical design of the machine, while placing a heavier burden on the electronic devices that regulate the frequency and quality of power being delivered by the WT. For example, drivetrain components may be made lighter and smaller if gust-induced transient loads can be inertially absorbed by a rotor speed change rather than reacting against a constant-speed rotor and being reflected as power swings. A VSCF WT also enables the designer to limit the maximum output power of a fixed-pitch machine to a predetermined level - thus permitting overall cost savings in the mechanical structure. There are also associated increases in energy gathering efficiency due to the fact that varying the rotor speed in response to varying wind speeds allows the WT rotor airfoils to operate more efficiently, while providing the opportunity for the rotor to dynamically respond to wind gusts, and gather a small amount of additional kinetic energy.

Historical Development of Control Studies

Several of the publicly available analytical studies of WT supervisory controls have been formally supported by SNL's wind energy research program funded by the U. S. Department of Energy (DOE). The original SNL studies estimated the sensitivity of WT life

and energy production to choices of control parameters and operational conditions for constant-speed vertical-axis wind turbines (VAWTs) [McNerney, 1980, 1981; McNerney and Veers, 1985; and Vachon, 1987 and 1988]. The parameters studied included:

(1) high and low wind speed cut-in and cut-out averaging methods and levels,
(2) post-shutdown wait times,
(3) WT sensitivity to cyclic stress loading, and
(4) site average wind speed and turbulence.

Basis of Analytical Procedures

The analytical procedures discussed in this paper, and those presented in the past, rely on a computer code entitled ASYM that simulates the stochastic nature of wind on an hourly basis using Markov chains [McNerney and Veers, 1985]. It subsequently employs the dynamic characteristics of the wind that are describable in the frequency domain by the Kaimal spectrum [Kaimal et al, 1972 and 1980]. The wind characteristics, summarized by Frost et al [1979], are used in ASYM to define the high frequency turbulence in the wind. The turbulence is then converted to the time domain by employing Veers' application of the Shinozuka method to develop second-by-second wind speeds that drive ASYM, and enable the time-domain simulation of WT fatigue and energy production [Veers, 1984 and Shinozuka, 1957].

WT fatigue damage is evaluated by computing a damage rate per cycle and an annual damage density function [Veers, 1983]. These computations employ measured lab data on fully reversing cyclic stresses versus the number of cycles to failure (i.e., S-N curves). These fatigue data for specific materials are employed in conjunction with Miner's linear cumulative damage rule [Miner, 1945] to estimate cumulative fatigue damage of specific, critically stressed components such as rotor blade joints. The fatigue calculation procedure is incorporated into a LIFE model developed by SNL [Sutherland and Schluter, 1989], and included as a subroutine in ASYM.

Recent applications of ASYM have addressed the control of the SNL VSCF Test Bed WT located in Bushland, Texas [Vachon, 1989]. The effort is an element of the long-term strategy for defining a control approach for the Test Bed unit under varying wind conditions, dynamic inputs, and material fatigue characteristics [Ralph, 1989]. This paper provides an update on the the current state of ASYM developments, aimed at controlling rotor speed while operating near and within critical rotor speed ranges that may lead to high fatigue damage due to modal response of the WT mechanical structure [Carne et al, 1989]. Ideally, wind turbine designers seek to avoid the presence of any critical structural resonance frequency that coincides with an integer multiple of the drive frequency. Because this is not always possible, the control system for the VSCF unit must seek to avoid prolonged operation within critical speed ranges (CSRs) that would excite structural resonances.

WIND TURBINE OPERATING ENVELOPE

Because rotor speed is an additional operating parameter for a VSCF WT, in addition to wind speed and power output, it is useful to define the machine's operating envelope in terms of all three parameters. The revised three-dimensional operating envelope of the SNL Test Bed WT is shown as the solid line in Figure 1. At present the WT is allowed to rotate over a range of rotor speeds from 6 to 38 rpm, where originally it was planned to operate up to 40 rpm. As discussed later in this paper, SNL tests have identified a rotor critical structural resonance that will receive excitation in the rotor speed range of 39.5 to 42.0 rpm, and must be avoided to minimize fatigue damage.

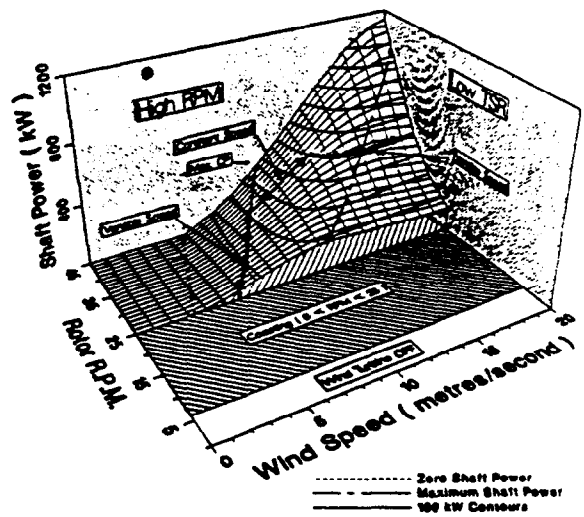

Figure 1. Operating Envelope of SNL 34-m Test Bed WT

Controller Ranges

The WT begins to put out positive power for rotor speeds greater than approximately 25 rpm at wind speeds of greater than 6 m/s. For rotor speeds between 6 and 25 rpm, the controller allows the machine to coast - neither generating power to nor taking power from the network. The benefit of the coasting control approach is that when the wind speed is sufficient to generate useful power, the rotor may already have some kinetic energy, and not require as much energy from the network to motor up to operating rpm. A VAWT such as the Test Bed is generally not self-starting, and therefore needs some power from the network in order to speed up to operating speed. Thus, coasting may efficiently assist in this speed-up process.

For wind speeds from 6 to 10 m/s the WT

will operate in a variable-speed control mode that strives to operate at the point of maximum energy gathering efficiency (i.e., power coefficient) at all times. Rapid variations in wind speed due to large gusts and turbulence, may cause brief rotor speed deviations that move the operating point away from from that of maximum efficiency. However, the rotor speed controller will soon correct for such excursions.

For wind speeds in the range of approximately 10 to 17 m/s, the Test Bed is expected to operate at a constant rpm similar to a conventional, constant-speed WT. For wind speeds greater than 17 m/s, the machine output reaches its current power limit of 625 kW, and again controls as a VSCF unit. Therefore, in this speed range, as rotor torque increases with wind speed, the rotor rpm is reduced to spill power as shown in Figure 1. This region of operation illustrates another significant benefit of VSCF units - that they can be made to limit their power similar to a pitchable WT.

For wind speeds above a predetermined high cutout level, the WT shuts down to protect the components from high cyclic structural loads and associated material fatigue. ASYM includes two high wind speed shutdown algorithms, either of which could trigger a shutdown. The majority of shutdowns are triggered when the measured wind speed, averaged over a period of several seconds, exceeds a nominal level of approximately 20 m/s. However, if the wind speed should suddenly increase rapidly such that severe fatigue damage could occur before a normal shutdown is triggered, a second algorithm will shut the machine down based on a higher wind speed trigger level that employs a substantially shorter averaging period. The variation of machine life and energy production to various cutout levels and averaging periods have been discussed in prior literature [Vachon, 1987 and 1988].

Due to scaling differences between the WT and wind sensors historically employed, the WT is expected to react more sluggishly to unsteady wind speeds (gusts and turbulence) than would be predicted by the application of typical wind spectra measured by wind sesnors. Therefore, to simulate a wind turbine's lower-bandwidth response to wind speed changes, the simulated wind speeds are filtered with a moving average filter with an adjustable time constant. For most results to be discussed later in this paper, a 10-second time constant filter is employed. When sufficient measured data are available from SNL, the true equivalent time constant will be determined.

Regenerative Braking

There are two conditions under which the generator may apply added torques to the drivetrain to slow it down while generating additional energy. The first instance is when the generator acts as a speed modulating device to keep the rotor speed at an appropriate level to follow the operating envelope. Such control can occur anywhere within the WT operating envelope, but will generally occur during variable-speed operation. The second instance is when the generator acts as a brake to bring the rotor to a stop. Unless the generator torque is dramatically raised to stop the rotor under emergency conditions, or the WT is undergoing a high wind speed stop, there is expected to be little regenerative braking during stops. For low wind speed stops, the parasitic drag applied to the drivetrain from the column bearings and the gearbox will slow the rotor down at approximately the maximum-permitted rate under normal stop conditions. Therefore, there is expected to be little useful regenerative braking energy developed during stops.

DESCRIPTION OF ASYM CONTROL SEQUENCES FOR RPMs NEAR ROTOR CRITICAL SPEED RANGES

Damage Density and Rotor Speed Control

The damage rate function (DRF) is the distribution of fatigue damage rate per cycle as either a function of wind speed or rotor rpm. Past studies, related to constant-speed WTs, have employed the DRF as a function of wind speed. The wind probability distribution function is convolved with the DRF to produce the damage distribution function (DDF) that is a bell-shaped curve with a maximum value that may occur for wind speeds above 22 m/s. The DDF is a useful function to aid in defining the high cutout wind speed for shutting down the machine to protect it from fatigue damage [Vachon, 1988].

For a VSCF WT, the equivalent damage density distribution as a function of rpm (based on the desire to have the controller follow the operating envelope) is useful in evaluating the role of operation at various rotor speeds in consuming fatigue life. The basis of such a curve is the damage rate per cycle for operation at each rotor speed. Figure 2 is a plot of (1) typical damage rate values for the case of a wind stress function (WSF) of 40 RMS(psi)/m/s, and (2) the projection of the operating envelope on the power-rpm plane. Integer values of wind speed are labelled on the power curve. The WSF is the sensitivity of the rotor cyclic stress components (RMS value) at critically stressed joints to the input wind speed [Vachon, 1988]. A WSF value of 40 RMS(psi)/m/s has been employed because it represents a reasonable maximum design goal for critically stressed 6063-T6 aluminum rotor components that are expected to achieve a useful fatigue operating life of several years.

Figure 2 indicates that there are three critical speed ranges (CSRs) that may excite structural resonances. The lowest CSR, associated with a cable resonance, is

centered at 23 rpm, and is modelled as having a "bandwidth" of plus or minus 1 rpm. The actual location of the mode will change slightly with temperature as the cable length and tension vary. This CSR for modal vibration is expected to lead to accelerated fatigue in components associated with the cable mount at the top of the rotor. The second CSR, for a "butterfly" or 1st edgewise mode, is generally centered at approximately 32 rpms. SNL tests have indicated that this mode will not be excited as long as the wind speed is less than 14 m/s when the rotor is at this speed. Based on the curves shown in Figures 1 and 2, the Test Bed should be operating at constant speed at 38 rpm for wind speeds of 14 m/s - and thus not excite this mode. The first edgewise mode will, however, receive brief excitation when the machine undergoes high wind speed shutdowns. During such periods, the machine is expected to be reducing speed at approximately 0.15 rpm/sec, and will pass through the CSR in approximately 7 to 10 seconds.

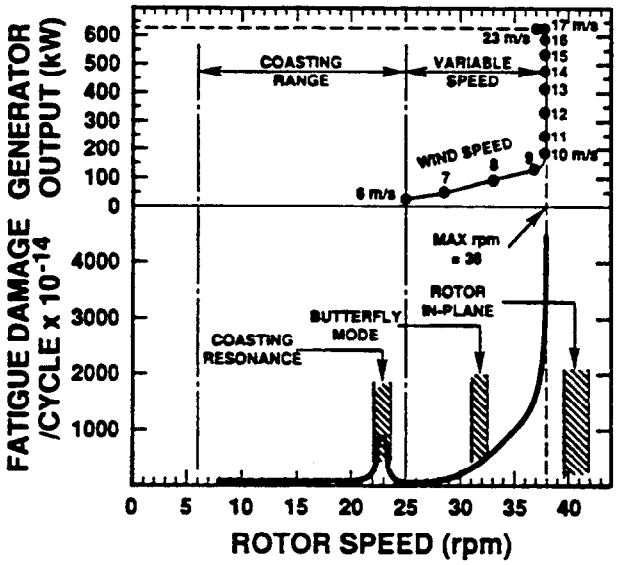

Figure 2. Variation of Test Bed Power Output and fatigue Damage/Cycle vs. Rotor rpm

The third CSR is the tower in-plane mode located at rotor speeds of between 39.5 and 42.0 rpm. Excitation of this mode must be avoided because of the potential of severe fatigue damage accumulation. Through the use of regenerative braking, the controller is expected to always keep the rotor rpm at values below approximately 38.5 rpm - even in the presence of gusts.

Speed Control Near Cable Resonance

ASYM has been modified to control rotor speeds and minimize fatigue damage while operating near rotor speeds of 23 rpm. Figure 3, which is an expanded representation of the fatigue damage rate for speeds near 23 rpm, indicates that the fatigue damage rate is a relatively narrow-band phenomenon that has a "bandwidth", BW, that is half the total CSR of concern. A simple mathematical representation of the fatigue damage rate has been developed for operation in the CSR. The cable is assumed to respond in a manner similar to a lightly damped, second order dynamic system with a response amplitude described by the equation:

$$G(\ ) = A\left\{\frac{1}{\left[1-\left(\frac{\Omega_R}{\Omega_n}\right)^2\right]^2+\left[2\xi\frac{\Omega_R}{\Omega_n}\right]^2}\right\}^{1/2} \quad (1)$$

where Ω_R is the rotor speed, Ω_n is the critical speed (23 rpm), ξ is the damping coefficient, and A is an attenuation coefficient employed in ASYM to provide flexibility in adjusting the amplitude of the damage response. For rotor speeds between 22 and 24 rpm, equation (1) is employed by ASYM to describe the damage rate function. The effect of fatigue damage from operation within the CSR is linearly added to the fatigue damage that results from normal operation and increases with wind speed.

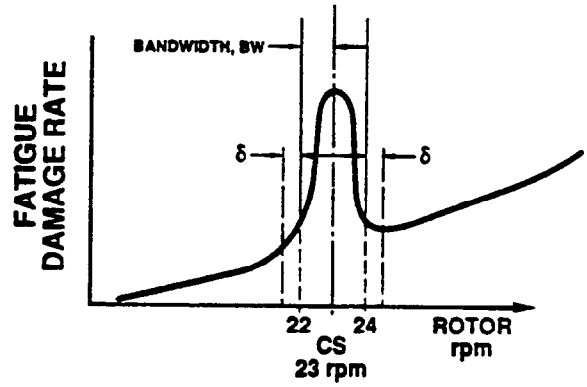

Figure 3. Representation of Fatigue Damage Rate in the Vicinity of a Critical Speed Range

Although the true values for A and ξ are at present uncertain, for this writing their values have been assumed to be 0.5 and 0.001 respectively. This results in a relatively high response amplitude ratio of 250 (and associated fatigue damage) for a rotor speed of 23 rpm, but only modest damage elsewhere within the CSR. These values are readily adjustable as new information is developed from ongoing SNL tests. Because the normal fatigue damage rate is very low for rotor speeds near 23 rpm, there is not a great deal of fatigue damage in total from operation in this CSR. However, it is still a speed range that should be avoided.

Figure 4 is a schematic diagram that represents the elements in the portion of the ASYM controller that modulates rotor rpm for speeds that might excite a critical structural resonance centered at 23 rpm. WT control for rotor speeds close to 23 rpm is expected to be in the coasting mode - producing zero net energy. Therefore, the speed of the rotor is governed only by the balance between the rotor torque applied by the wind and the drivetrain loads as follows:

$$P(rotor)/\Omega_R = P(GB)/\Omega_R + T(CB) \qquad (2)$$

where P(rotor) is the wind-induced rotor power, P(GB) is the constant level of parasitic power loss due to gearbox drag, T(CB) is the drag torque applied by the main column bearings associated with the rotor, and Ω_R is the rotor rpm. Because all spurious drivetrain torques are either constant or vary with rpm, the only controllable torque that is capable of modulating the rotor rpm is that from the generator, and it is not normally applied while the WT is coasting. However, for speed control it can be introduced as a positive torque (for rpm increases) or a negative torque (for rpm decreases) on the right side of equation (2). The former is a motoring torque and the latter is braking action that leads to positive generation (regenerative braking). Based on a desire to minimize the level of transient torques introduced by the generator, rotor accelerations that are controlled by modulating generator torque are currently limited to 0.15 rpm/s.

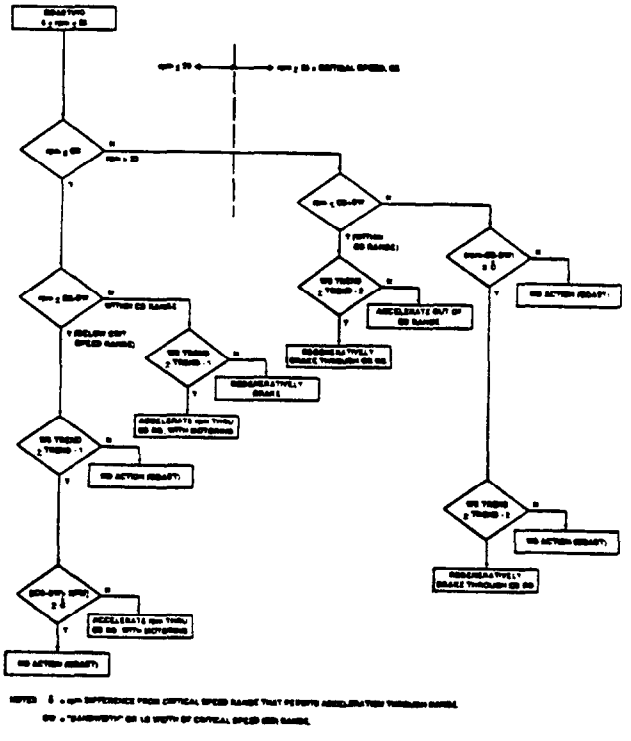

Figure 4. Schematic Diagram of ASYM Controller Operation in Critical Speed Range

Reference to Figure 4 is useful in following the discussion on the control sequence below. While operating within the coasting speed range, the first controller decision is whether the rpm is above or below the critical speed (CS). Subsequently, the controller evaluates whether the rpm is within the "bandwidth" of the CSR, within which accelerated damage is more severe. Whether the controller finds that the rotor rpm is within the band or not, it evaluates a wind speed trend criterion (discussed below), that if satisfied would permit the speed of the rotor to accelerate up through or down through the CSR. If the prior decision had determined that the rpm was within the CSR, the controller must take action to control rotor rpm so that it is in the CSR for a minimum time.

If the wind speed trend is not satisfied, the WT regeneratively brakes to reduce rpm (if rotor speed is lower than the CS), or reduces generator torque to allow rotor rpm to increase to a value higher than the CSR (if rotor speed is initially higher than the CS). If the trend is not satisfied, and the speed is outside of the CSR, no control action is required and coasting continues. If, however, the wind speed trend is satisfied, and the rotor speed is outside of the CSR, the controller evaluates whether it still makes sense to accelerate through the CSR if the rpm is close enough to the boundary of the CSR to allow the controlled speed change to occur. The criterion for being close to the CSR boundary is defined as δ in Figures 3 and 4. A later section of this paper will discuss the merits of various trend levels and values for δ.

Wind Speed Trend

A simple mathematical function has been developed to determine a crude trend in wind speed. The objective of employing a wind trend estimation is to minimize the number of times that the rotor rpm must cross through a CSR, thus minimizing associated fatigue damage. The trend measure currently employed in ASYM is the difference in two moving average wind speeds with different averaging periods. The long-term trend is determined by the wind speed averaged over a range of several minutes to 4 hours. A short-term trend is similarly calculated with a shorter averaging period. For the simulations discussed here, the averaging periods have been varied with ratios up to 18:1.

If the short-term average exceeds the long-term average by a specified level, the wind speed trend is defined as positive. Based on satisfying a trend criterion for increasing wind speeds (i.e., Trend-1 in Figure 4), the controller would permit the rotor to speed up and cross through the CSR. Similarly, if the rotor speed is higher than the CSR, and the wind trend for decreasing wind speeds is sufficiently strong (i.e., Trend-2), the controller would regeneratively reduce the rotor rpm through the CSR.

SIMULATION RESULTS

Controller Effectiveness in CSR

To evaluate the effectiveness of the CSR controller portion of ASYM described in Figure 4, several simulations were carried out with different criteria for wind speed trend and rpm criteria for controller action.

The measures of effectiveness are (1) operational time spent in the CSR, (2) associated fatigue damage from operation in the CSR, and (3) regenerative braking or motoring energy required to control rotor speed. Some of the key results are discussed below.

Damage Rate vs. RPM. Fatigue damage rates vary with either (1) the wind speed in general (irrespective of rotor speed) or (2) modal vibration within a CSR. To obtain a first-order estimate of the sensitivity of damage rate to rotor speed in a VSCF WT, the damage distribution function (vs. rpm) is developed and plotted in Figure 5. The figure, estimated for the case of a mean annual wind speed of 8 m/s and a wind-stress function (WSF) of 40 RMS(psi)/m/s, indicates the two factors that lead to accelerated damage. Operation in the constant-speed range at 38 rpm produces high fatigue damage, but is a necessary part of generating high power output. The fatigue damage for operation within the CSR is shown as a small fraction of the damage at higher rpms, but the analytical estimate of structural response for operation within the CSR is only an estimate based on equation (1) and assumptions described earlier. The actual response may be far greater. The estimates in Figure 5 do not show the effect of operation at high wind speeds at constant or variable rpm. These factors will be included in later project efforts.

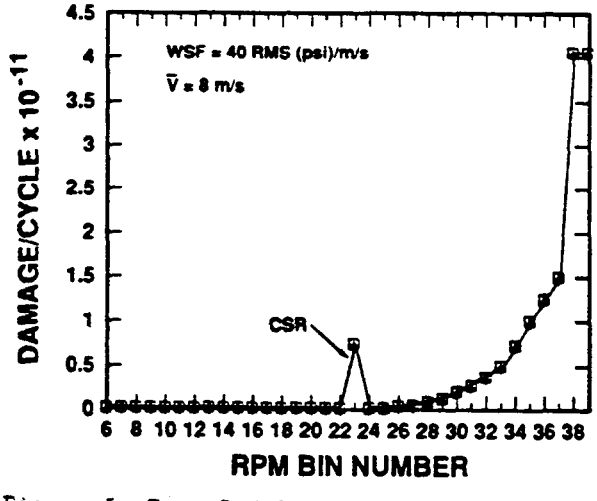

Figure 5. Test Bed Damage Distribution Function vs. rpm

RPM Distributions. Figure 6 is a plot of the results of simulations that compare the number of hours per year that the WT spends in various rpm bins over the whole operating envelope. The average wind speed conditionand the cutin algorithm criterion are listed above the figure. The baseline simulation is for the case of no active speed control during WT coasting (box symbols), and the other case is for the use of active "smart" controls with wind-trend filters specified in the figure. The CSR crossing criterion, δ, that defines how close to the CSR boundary the actual rpm must be to initiate a crossing through the CSR, has been chosen as 0 rpm. It should be noted that for rotor speeds higher than 25 rpm, there appears to be no difference in the number of hours in each bin between the controlled and uncontrolled case. The major difference arises due to the CSR controller that affects the operation in low-rpm bins.

The key results of the simulation are summarized in Figure 7, which is an expanded-scale view of the plot for rotor

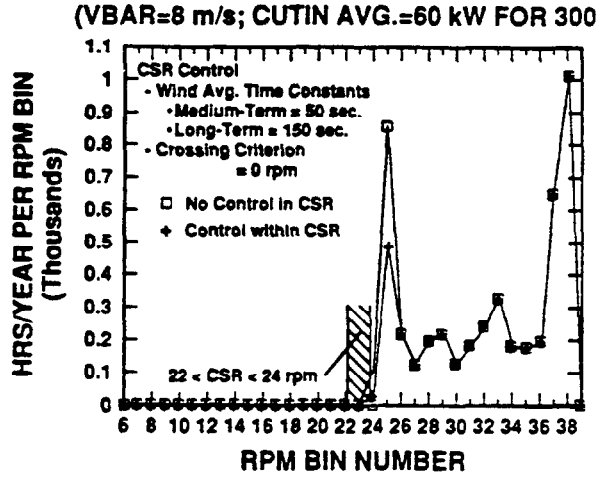

Figure 6. On-Time Distribution vs. rpm Bins

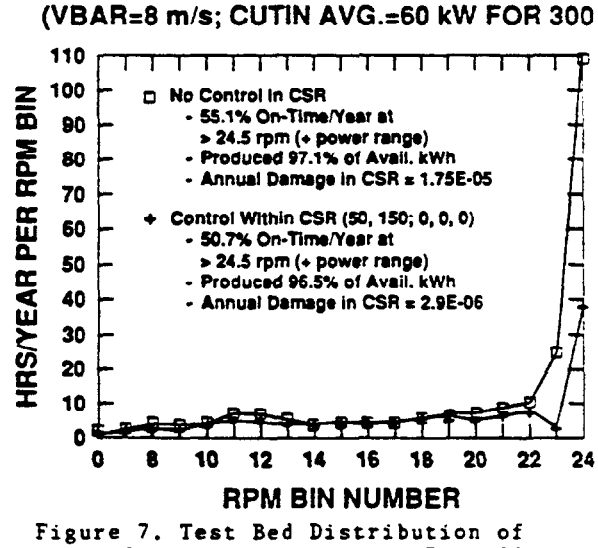

Figure 7. Test Bed Distribution of On-Time for rpm Less Than 25

speeds less than 25 rpm. The notes in the figure define the parameters of the control system in the CSR. In the order listed, these include 50-sec. medium-term and 150-sec. long-term wind speed trend moving average window time constants, values of 0 m/s for the required values of the medium-term and long-term trends to permit the rotor rpm to cross through the CSR, and finally a 0 value for delta, the difference between the actual rpm and that at the nearest boundary of the

CSR. The energy production and damage results, also shown in Figure 7, indicate that for the case of no CSR control, the WT stays within the power-producing rotor speed range (i.e., > 25 rpm) approximately 5 percent more time than for the controlled case. Thus, it permits the machine to generate approximately 0.6 % more energy. A detailed examination of the simulation results indicates that the major source for on-time variations is in the 25-rpm speed bin. However, the case for no CSR speed control leads to approximately 6 times as much fatigue damage in the CSR. In each case studied, the fatigue damage estimated for operation in the CSR is less than one percent of the total fatigue damage for operation over the entire operating envelope. However, the results show the effectiveness of the control approach.

Evaluation of Wind Speed Trend Criteria

Figure 8 is a plot of results from five cases in which the wind speed trend values were varied. The simulations explored the sensitivity of three key parameters to the wind speed trend level that must be exceeded in order to enable the WT rotor speed to cross through the CSR. The wind speed trend conditions assumed are listed within parenthesis as two wind speed values (in m/s) that appear below the bar graph for operating time and fatigue damage. The first figure is the amount that the short-term average must exceed the long-term average to permit a speed increase through the CSR. The second figure is the amount that the long-term trend must exceed the short-term trend to allow a speed decrease through the CSR.

All cases employed a 10-second filter on the dynamic wind speed that is driving the rotor speed variations. The key parameters studied include (1) the operating time in the CSR, (2) associated fatigue damage when rotor speeds coincide with the CSR, and (3) regenerative and motoring energies. Regenerative braking and/or motoring energies were applied to bring about transient or short-term rotor speed corrections (limited to accelerations of 0.15 rpm/s) to (1) move the rotor speed away from the CSR if the wind speed trend criterion was not satisifed, or (2) accelerate through the CSR if the rpm was within the CSR (or sufficiently close to the boundary) and the wind speed trend criterion was met. As discussed previously, regenerative braking energy is also produced when (1) the rotor speed is in excess of the envelope value shown in Figure 1 and (2) when the WT is stopped in an emergency manner from a high wind speed condition.

The results, shown in Figure 8, indicate the following:

(1) The rotor speed coincides with the CSR for a minimum number of hours per year if no wind speed difference between short and long-term averages is required for rotor speed increases, but that a wind speed trend of 1 m/s is required for rotor speed decreases. This is the (0,1) wind speed trend criterion shown in Figure 8, and resulted in operation in the CSR for approximately 2.3 hours per year. The (1,1) wind trend criterion produced similar results.

(2) There is substantially more fatigue damage associated with the control approach that produced the lowest dwell times in the CSR because, during light winds the rotor speed is often dropping into the middle of the CSR, and requires motoring to bring it back to higher rotor speeds while it waits to satisfy the wind trend criterion for reducing rotor speeds. This conclusion is evident in the high motoring energy required each year for the two cases with minimum dwell time in the CSR (see bottom portion of Fig. 8).

Another way to view this anomalous finding is as follows. During a normal startup sequence, when the wind speed trend is satisfied, the machine is motored up to 25 rpm. At this time, it is allowed to either (1) coast down in speed if winds are dropping, or (2) begin generating useful power at rpms above 25 if winds are sufficient. Thus, there is a preponderance of conditions where the rpm is entering the CSR from speeds above it as apposed to below it. If the controller establishes stringent guidelines for permitting the rpm to pass down through the CSR, it will bounce in (due to down gusts) and be motored out of the upper end of the CSR frequently. Such transient events result more frequently in rotor speeds close to 23 rpm - the peak of the damage function within the CSR (see Figure 3). Therefore, it may be concluded that it is better to readily permit control of the rotor speed through the CSR when the rotor speed approaches the critical range from higher values than to hinder rpm reductions.

(3) The best balance of minimizing time in the CSR and fatigue damage is associated with no wind speed trend. This is the (0,0) criterion listed on the left portion of the figure. It should be noticed that this case also produces the least braking or motoring as well. It indicates that the dynamic wind speeds, on a second-to-second basis, are very random. It may indicate that the use of the wind filter for dynamic response of the rotor may be all that is required to assure that the rotor speeds do not vary too violently in gusty winds and enter the CSR too often based on wind-induced, transient rpm swings. The results mean that once the rotor speed enters the CSR from either lower or higher rpm the speed controller should take over, and carry the rpm through the range as rapidly as permitted.

Several other cases were studied in which the wind speed trend was varied from the 50-second, short-term wind speed average and compared to averages over periods as long as 4 hours. Various ratios of the averaging

time constants were examined. The results were generally found to be consistent with those summarized in Figure 8.

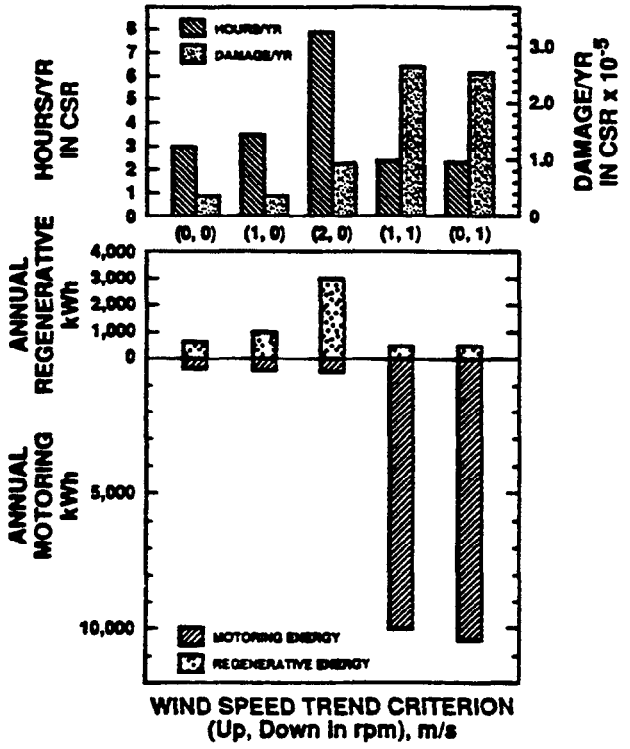

Figure 8. Summary of Five Cases of Wind Speed Trend Evaluation for the Case of Comparing 50-sec. & 150-sec. Averages

Comparison with No CSR Control

To explore the merits of CSR rotor speed control further, a base case of no CSR control was evaluated and compared to the cases presented in Figure 8 and to other similar cases. The overall results are listed in Table 1 for the conditions summarized in the table. The wind speed criterion in each case was the difference between the wind speed averaged with the medium-term, wind-speed filter listed, and a value averaged over a period three times that of the medium-term filter. The top row of data lists the results for the case of no CSR speed control. The group of the five top rows of data for the controlled cases is the same group the performance of which is summarized in Figure 8. The rows below that are for cases in which the medium-term wind speed filter time constant or the rpm difference criterion, δ , were varied to explore the sensitivity to each. By examining the results in the table, the following conclusions can be drawn:

(1) The use of no CSR speed control leads to over 24 hours of operating time in the CSR, but the associated annual fatigue damage is no worse than for the case of (0,1) or (1,1) wind speed criteria discussed above. Therefore, it appears that the controller is marginally useful for the damage rates studied here for the CSR, but could be substantially more valuable for CSRs that produce a great deal of fatigue damage.

(2) There appears to be no benefit in employing the rpm difference criterion, δ , because the time spent in the CSR, and any associated damage does not vary with the value of δ .

(3) Longer wind speed averaging periods lead to longer times spent in the CSR for those cases that are the most appealing (i.e., the 0,0 and 1,0 wind speed trend cases). However, for the cases that have the least dwell time in the CSR, but high associated fatigue damage (i.e., the 1,1 and 0,1 cases), the longer averaging periods lead to slightly less dwell time, but no change in the fatigue damage. Thus, it appears that the best approach is to use no wind speed trend criterion, but to exercise active rotor speed control when the rotor speed enters the CSR during coasting operation.

Table 1. Results of Simulation of "Smart" Controls in 23-rpm Critical Speed Range (CSR)

Simulation Conditions
- Wind Speed Dynamic Control Filter Time Const. = 10 Sec.
- VBAR = 8 m/s; Surface Roughness Length (Z_o) = 0.1 m
- 60-MW Low WS Cutin Avg. Per. 300-Sec. Low WS Avg. Window

Tau (s) of Medium Rg. WS Filter	WS Trend for Incr. rpm,m/s	WS Trend for Decr. rpm,m/s	rpm diff, δ to Allow rpm Chg.	Hrs/Yr in 23-rpm Bin	Annual Fat.Damage in CSRx10^6
Apply No Dynamic Rotor Speed Control					
50	0	0	0	24.22	17.5
Apply WS Trends and Dynamic Rotor Speed Control in CSR					
50	0	0	0	3.00	2.9
50	1	0	0	3.46	2.9
50	2	0	0	7.85	8.7
50	1	1	0	2.42	26.2
50	0	1	0	2.30	26.2
50	0	0	0.2	3.00	2.9
50	1	0	0.2	3.44	2.9
50	2	0	0.2	7.85	8.7
50	1	1	0.2	2.40	26.2
50	0	1	0.2	2.20	26.2
100	0	0	0.2	3.36	2.9
100	1	0	0.2	4.79	5.8
100	2	0	0.2	8.56	5.8
100	1	1	0.2	2.35	5.8
100	0	1	0.2	2.14	5.8
300	0	0	0.2	4.15	5.8
300	1	0	0.2	8.37	5.8
300	2	0	0.2	8.37	5.8
300	1	1	0.2	2.32	17.5
300	0	1	0.2	2.13	17.5

SUMMARY

Based on the application of a VSCF version of ASYM applied to the SNL 34-m VAWT Test Bed, the following summary conclusions can be drawn based on the findings discussed above:

(1) The value of the CSR controller is demonstrated by the results that show that there are reduced operating time and fatigue associated with its application (see Table 1). It is also expected to be a useful tool for controlling braking action from high wind speeds, when the rotor rpm must pass through the 1st edgewise mode, and for control of rotor speed "overshoots" at 38 rpm. While operating in the vicinity of the "corners" of the operating envelope at which control shifts from VSCF to the constant-speed mode

at 38 rpm, the rotor speed may experience gust-induced rpm excursions that could cause the rotor speed to coincide with the 1st tower in-plane mode that begins at approximately 39.5 rpm. In this instance, the controller will be invoked to reduce fatigue damage.

(2) The use of wind speed trends as a means of enhancing the effectiveness of the CSR controller appears to have no value in conjunction with the ASYM code. The use of Markov chains to develop hourly average wind speeds provides a means of structuring the hour-by-hour average wind speeds to be correlated. However, any "persistence" that may be found in high frequency wind speed traces may not be properly taken into account in the application of the Shinozuka Method to develop wind speed dynamics (turbulence effects). Thus, the use of wind speed filters with different time constants may be an inappropriate way to develop trends if the second-by-second simulated wind speed data are truly random.

(3) There appear to be no benefits from beginning a traverse through the CSR when an rpm difference criterion is met (when a wind speed trend is also met). Thus, simpler controls produce the best results for the cases studied. For CSRs that have a broader rotor speed range, and the potential for more severe fatigue damage, the more sophisticated speed controls may still be warranted.

ACKNOWLEDGEMENT

The work described in this paper has been sponsored by the U. S. Department of Energy, Wind/Ocean Technology Division through the Wind Energy Research Division of the Sandia National Laboratories.

REFERENCES

Carne, T. G. et al, "Modal Validation of the Sandia 34-Meter Test Bed Turbine Using Substructured Modal-Testing," 8th ASME Wind Energy Symposium, Houston, TX, Jan. 22-25, 1989, pp. 277-283.

Frost, W., Long, D. H., and Turner, R. E., "Engineering Handbook on the Atmospheric Environment Guidelines for Use in Wind Turbine Generator Development," NASA Technical Paper Number 1359, December 1979.

Hinrichsen, E. N., "Integration of Wind Turbine and Power System Controls," Sixth Biennial Wind Energy Conference and Workshop, Minneapolis, MN, June 1-3, 1983, American Solar Energy Society, Boulder, CO.

Kaimal, J. C., Wyngaard, J. C., Izumi, Y., and Cote, O. R., "Spectral Characteristics of Surface Layer Turbulence," Quart. J. Roy. Meteorol. Soc., V. 98, 1972, pp. 563-589.

Kaimal, J. C., Gaynor, J. E., and Wolfe, D. E., "Turbulence Statistics for Design of Wind Turbine Generators," NOAA/ERL Wave Propagation Laboratory, Boulder, CO, Report to DOE Under Interagency Agreement No. DE-A106-79ET23115, December 1980.

Mc Nerney, G. M., "Control Algorithm Investigations," Proc. of Vertical-Axis Wind Turbine (VAWT) Design Technology Seminar for Industry, April 1-3, 1980, Report SAND80-0984, August 1980, Albuquerque, NM.

Mc Nerney, G. M., "Vertical Axis Wind Turbine Control Strategy," Report SAND81-1156, August 1981, Sandia National Laboratories, Albuquerque, NM.

Mc Nerney, G. M., and Veers, P. S., "A Markov Method for Simulating Non-Gaussian Wind Speed Time Series," Report SAND84-1227, January 1985, Sandia National Laboratories, Albuquerque, NM.

Miner, M. A., "Cumulative Damage in Fatigue," ASME J. of Applied Mechanics, 67:A159-A164, 1945.

Ralph, M. E., "Control of the Variable-Speed Generator on the Sandia 34-meter Vertical Axis Wind Turbine," Proc. of AWEA/DOE Windpower '89, San Francisco, CA, September 24-27, 1987.

Shinozuka, M., "Simulation of Multivariate and Multidimension Random Processes," J. of the Acoustical Society of America, V. 49, No. 1, (Part 2), 1957, p.357.

Sutherland, H. J., and L. Schluter, "The LIFE Computer Code - Numerical Formulation and Input Paramters," Proc. of AWEA/DOE Windpower '89, San Francisco, CA, September 24-27, 1989.

Vachon, W. A., "A Design Code to Study Vertical-Axis Wind Turbine Control Strategies," Report SAND87 - 7012, July 1987, Sandia National Laboratories, Albuquerque, NM.

Vachon, W. A., "The Effects of Control Algorithms on Fatigue Life and Energy Production of Vertical Axis Wind Turbines," Seventh ASME Wind Energy Symposium, New Orleans, LA, January 10-13, 1988, pp. 149-158.

Vachon, W. A., "The Effect of Controls on Life and Energy Production of the 34-m VAWT Test Bed", 8th ASME Wind Energy Symposium, Houston, TX, Jan. 22-25, 1989, pp. 209-218.

Veers, P. S., "Modelling Stochastic Wind Loads on Vertical Axis Wind Turbines," Report Number SAND83-1909, September 1984, Sandia National Laboratories.

Veers, P. S., "A General Method for Fatigue Analysis of Vertical Axis Wind Turbine Blades," Report SAND82-2543, October 1983, Sandia National Laboratories.

Proceedings of the Ninth ASME Wind Energy Symposium
D. E. Berg (ed.), SED-Vol. 9, ASME, January 1990

PERFORMANCE PREDICTIONS FOR AN INTERMEDIATE-SIZED VAWT BASED ON PERFORMANCE OF THE 34-m VAWT TEST BED*

H. M. Dodd
Wind Energy Research Division
Sandia National Laboratories
Albuquerque, New Mexico

ABSTRACT

The DOE/Sandia 34-m Vertical Axis Wind Turbine (VAWT) Test Bed is a research turbine that has been in operation for over a year. With the advanced technology components incorporated in the turbine (including airfoils, structures and variable speed operation), its performance can be used to predict next generation commercial VAWT potential. This paper begins with the predicted and measured performance results obtained from the Test Bed and applies these results to a hypothetical commercial machine of the same size.

The effects of a number of parameters are included in the performance analyses. First, the importance of siting considerations are presented, including wind frequency distributions (both real and Rayleigh) and mean wind speed and wind shear effects. Next, the paper shows the relative contribution of variable speed operation to improved performance and discusses other aspects of variable speed. The predicted performance of a 34-m VAWT is compared to existing machines, with annual energy capture per unit of swept area being the primary comparative metric. Finally, some cost of energy considerations associated with these technological advances are covered.

INTRODUCTION

The DOE/Sandia 34-m VAWT Test Bed is a unique research machine whose primary function is to develop advanced technologies which may lead to the next generation of commercially viable wind turbines. The Test Bed was formally dedicated in May of 1988, and detailed performance testing began shortly thereafter. Primary emphases of this research and development effort center on improvements in aerodynamics, structural response, component fatigue, variable speed operation and utility interfacing. Earlier papers have discussed the design and fabrication process(1) as well as the general test plan(2). More recently, results from the first year of testing were presented(3) with special attention given to problems encountered and the resolution of those problems.

In the area of structural dynamics, recent results(4) from the Test Bed program demonstrate considerable promise that VAWT analytical codes can now accurately predict turbine responses, including the effects of aeroelastic and structural damping and, more importantly, the effects of turbulence contained in the incident wind. Similarly, fatigue codes now exist(5,6) that, when applied to the Test Bed stress responses(7), yield results that can help quantify the effects of variable speed operation on component lifetimes. Control aspects of variable speed operation of the Test Bed have also been reported(8) with the pros and cons discussed. Finally, and of most direct importance to this report, the Test Bed's initial aerodynamic performance has been defined(9) and serves as the experimental basis for the results of this study. Collectively, the above references indicate that our ability to describe and understand VAWT phenomenologies has improved dramatically, with the Test Bed providing the substantiating data. More importantly, we are very close to being able to explicitly prescribe the configuration of a new generation, commercial VAWT. This paper will provide a first-order look at the performance potential of such a machine.

MEASURED PERFORMANCE

One of the primary features of the Test Bed is that its blades are composed of airfoil shapes that represent the first VAWT-specific designs ever implemented(10). The predicted versus measured performance comparisons of these SAND 0018/50 Natural Laminar Flow (NLF) profiles are a key element in establishing the future potential of VAWT technology. One of the inherent advantages of a Darrieus wind turbine is that, except for the movement of the rotor

*This work is supported by the U.S. Department of Energy at Sandia National Laboratories under contract DE-AC04-76DP00789.

assembly about its (vertical) axis of rotation, there are no moving parts above ground level. However, a past difficulty with the concept has been the tendency to produce very high power in high winds, which requires oversizing of drivetrain components - a costly "solution." To alleviate this problem, the NLF airfoils were specifically designed to be very efficient at low and moderate winds, while producing a flat power curve in higher winds, through stall regulation, in order to improve energy capture while decreasing hardware costs. In addition, variable speed operation holds the promise of improved performance through increased energy capture and adaptability of turbine operation to local conditions. Taken together, improved airfoils and variable speed are often considered to hold the key to future commercial viability.

Test Bed performance data, taken during 1989 and discussed in detail in reference 9, are compared with predictions (made before the turbine was ever built) in Figure 1. At the time of this writing, complete experimental data were available for only two rotational speeds, 28 and 34 rpm. From the figure it is clear that stall regulation is in fact occurring and that the measured data agree fairly well with predictions. The most important discrepancy occurs at wind speeds from cut-in to about 9 m/s (20 MPH), where measured results consistently fall below analytical values. Reference 9 discusses these differences in detail; here it is sufficient to note that most of the differences can be attributed to a unique feature of the Test Bed: aerodynamically "dirty" blade-to-blade joints that would not be present on a commercial design. Therefore, this paper assumes that the analytical results can justifiably be used to simulate a commercial turbine's performance, particularly when comparing various operational strategies of the turbine.

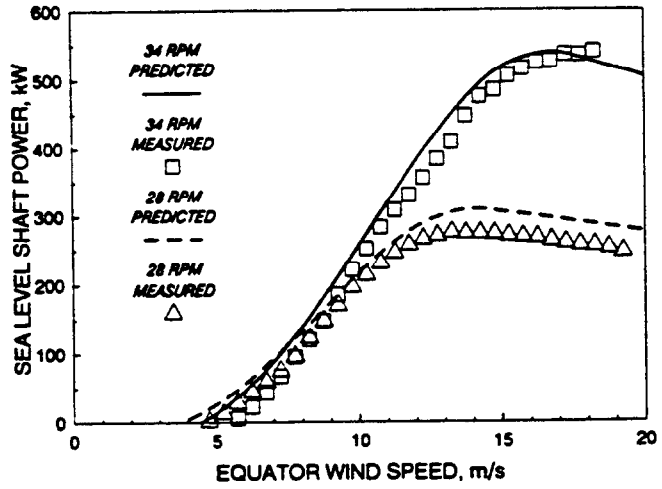

Figure 1. DOE/Sandia 34-m Test Bed performance comparisons measured vs. analytical

PERFORMANCE PROJECTIONS

This section presents the performance projections for various configurations of a hypothetical commercial VAWT whose size matches that of the VAWT Test Bed (i.e., 34-m diameter). Nothing in this study addresses the issue of what the optimum-sized VAWT would be from a cost of energy standpoint. Rather, the 34-m diameter and 955 square meter swept area of the Test Bed are used because of the extensive analytical and experimental data base supporting the performance projections.

Wind Resource

The performance of any wind turbine is certainly a function of its design; but the extreme nonlinearity of the resource (i.e., available wind power is directly proportional to the velocity cubed) makes siting an equally important contributor to performance. Two important factors in siting concern the frequency distribution of wind speeds and the variation of winds with height above ground. The simplest commonly-used analytical representation for wind speed frequency distribution is the Rayleigh distribution. The Rayleigh distribution is compared to three "real" data sets in Figure 2 (the data were provided by USDA for the Amarillo Airport site and FloWind Corporation for the other two sites). It can be seen that while there are noticeable differences, particularly with respect to the Altamont distribution, the Rayleigh representations are as similar to the real sites as the real sites are to each other. Thus, this study will focus on the Rayleigh representation, particularly since mean wind speed variations are an important consideration.

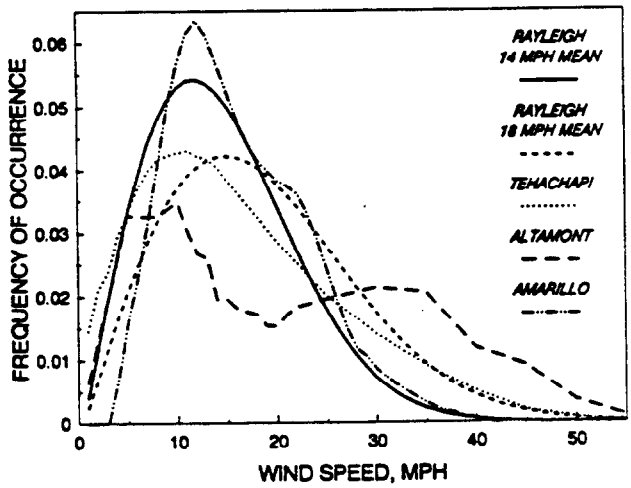

Figure 2. Wind speed occurrences Rayleigh vs. actual data

The other important parameter is the effect of wind shear, which is usually represented by allowing the wind to increase exponentially as height increases above a reference height, usually 10m. The height ratio exponent is normally assumed to be positive and is typically less than 0.2 (although negative exponents have been observed at Altamont and Solano County in California). For this study wind shear effects on performance will be bracketed by considering only two values for the exponent: zero (i.e., no shear effects) and one-seventh, a commonly used value. In the case of the Test Bed, equatorial height is 30m, so the turbine reference wind speed is 1.17 times the reference wind speed at 10m for the one-seventh wind shear exponent. This means that, neglecting high wind cut-out effects, there is 60%

more energy available for a turbine at 30m than for one at 10m (or for one at a zero exponent site). Similar to the statement made above concerning optimum diameter, this study does not consider the cost effectiveness of raising the turbine's equatorial height to values greater than the nominal 30m minimum. Such a strategy may deserve consideration, but is beyond the scope of this paper.

Turbine Performance

Three hypothetical 34m diameter commercial VAWTs are considered: a fully variable speed unit (20-40 rpm), a two-speed unit (20/40 rpm), and a single-speed unit (35 rpm). The single speed was chosen to be 35 because that rpm was found to be generally as efficient as other single-speed options in the 25-40 rpm range, particularly at the moderate wind sites with mean wind speeds of 6.3 m/s (14 MPH) or less. Figure 3 shows the predicted mechanical power output and efficiencies as functions of equatorial wind speed for these three configurations. In Figure 3a, note the very minor difference between variable and two-speed power in the 5-9 m/s range; otherwise the two curves coincide. While the 35 rpm curve looks dramatically different at high winds (up to 250 kW less power), the more important difference is in the 10-15 m/s range, because more annual energy is available in this region at moderate wind sites. Figure 3b gives the mechanical conversion efficiencies (also as a function of wind speed), and the difference between two speed and variable speed is more obvious.

Electric output was then determined by taking the shaft power predictions(3), subtracting a 5 kW assumed tare loss, and then assuming a mechanical to electrical efficiency of 90%. In addition, all cases assume an equatorial cut-out wind speed of 20 m/s (45 MPH); this is certainly not restrictive from a net energy capture perspective, particularly at moderate mean wind speed sites. The assumption is further justified if it is assumed that high wind fatigue damage is of concern, which it appears to be, so operations in higher winds will probably be restricted anyway. Also, while variable speed generators are expected to be somewhat less efficient than one- or two-speed systems, this potential difference is neglected in this comparative study.

Next, combining these power curves with 10m Rayleigh wind speed distributions typified in Figure 2, and taking wind shear effects into account, annual energy capture curves can be generated. Figures 4a and 4b present the results for zero wind shear and the one-seventh shear exponent, respectively. Note that energy capture is expressed in KWh per square meter of swept area; this is to allow direct comparisons with other wind turbines having differing swept areas. Clearly, the performance of all three configurations is quite good, with the variable speed machine outperforming the other two. Quantifying the results at a moderate mean wind speed site of 6.3 m/s (14 MPH): 1) for zero shear, two-speed and variable-speed operations increase energy capture over one-speed operation by 12% and 15%, respectively; 2) for the one-seventh exponent sites, these values increase to 14% and 16%; and 3) for one-speed operation, including wind shear effects increases energy capture by 46%.

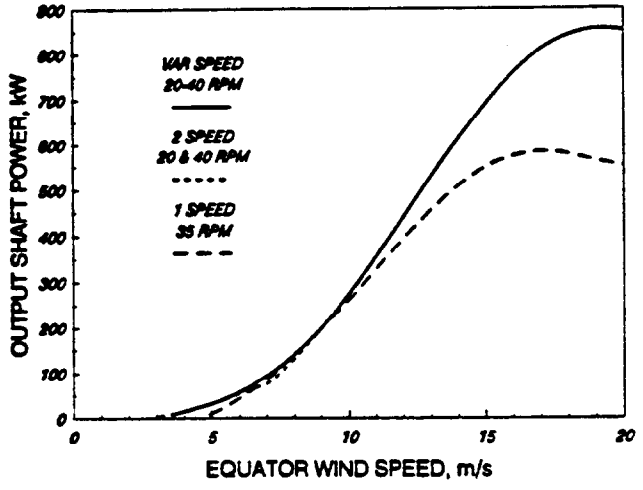

(a) Mechanical power output (based on CARDAA models)

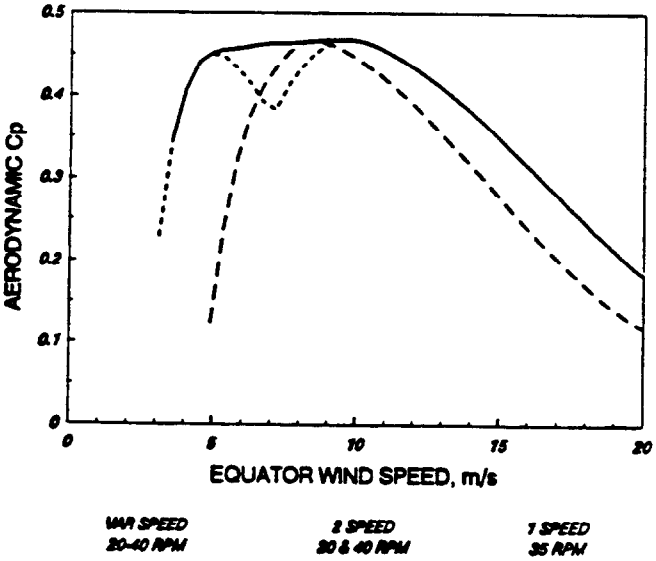

(b) Mechanical efficiency (based on CARDAA models)

Figure 3. 34-m VAWT performance

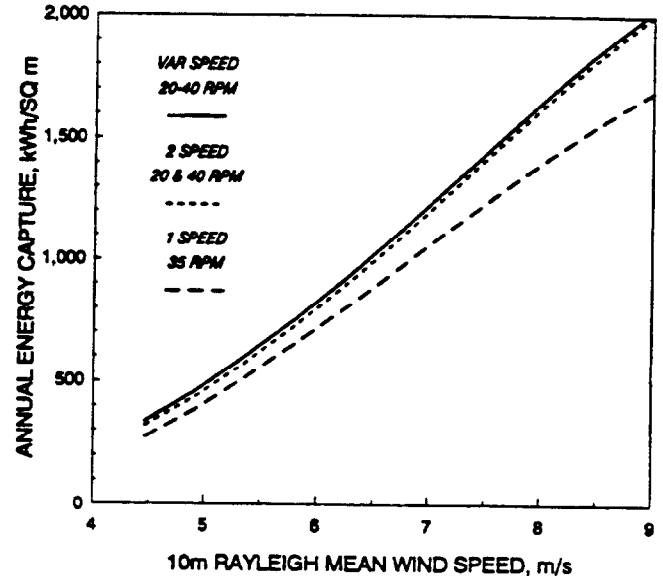

(a) Zero wind shear

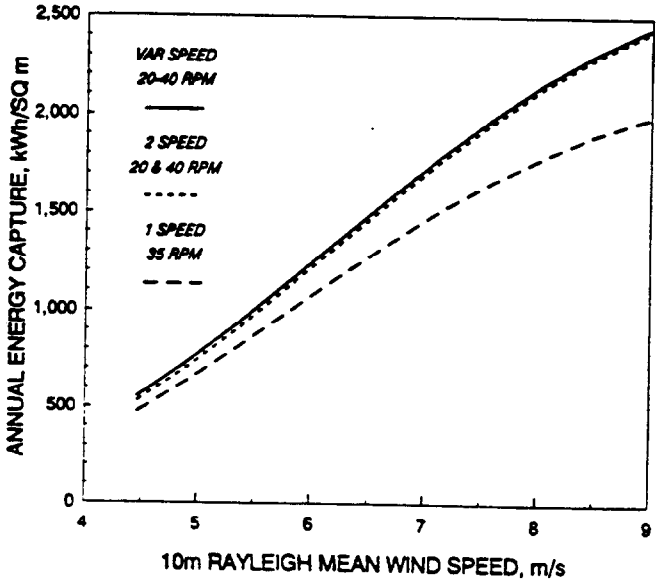

(b) 1/7 wind shear exponent

Figure 4. VAWT energy capture projections

Finally, in order to quantify the effects of the lower power outputs actually measured in the Test Bed program to date (when compared to the analytical predictions presented above), two hypothetical VAWTs were "flown" against each other at various Rayleigh mean wind speed sites at both 28 and 34 rpm. One machine was assumed to perform according to the analytical predictions, while the other followed the measured performance curve. The results in the primary wind speed range of interest (i.e., 6.3-8.1 m/s means), for wind shear exponents of zero and one-seventh, can be summarized as follows. At the lowest mean wind speed of 6.3 m/s (14 MPH), energy capture deficits ranged from 13.8% to 17.9%; at the higher mean sites of 8.1 m/s (18 MPH), the deficits dropped to 9.4% to 13.5%. While these values are certainly nontrivial, they are in all cases less than the effect of going from a zero shear site to a one-seventh shear site at the same two rpm's. Since we fully expect to be able to correct most of these discrepancies through the use of fairings on the "dirty" joints(9), these deficits can justifiably be neglected at this time.

COMPARISONS

The most important aspect of this study is not how closely predictions and current measurements of Test Bed performance agree, but rather how much performance improvement may reasonably be expected from this next generation technology. This section considers this issue by comparing the relative projected performance of a 34-m diameter VAWT with the best performing current commercial VAWTs - the FloWind F-17 and F-19 machines. With over 500 of these two machines installed in California (the F-19 was an evolutionary improvement on the F-17), their performance is well documented and has consistently been near the top of California turbines in annual energy capture per square meter. It is useful in this study to include both machines in order to contrast evolutionary changes with generational ones.

The relative electrical output of the three machines is presented in Figure 5. The large differences in power can be quite misleading, however, since the 34-m machine has a swept area about three times larger (955 versus 316 and 242 square meters). The figure does illustrate the stall regulation characteristics of the NLF-bladed 34-m VAWT. It should also be noted that the output powers from the F-17 and F-19 continue to increase, even in winds exceeding 20 m/s, so that drivetrain sizing becomes an issue. In this regard, an additional potential advantage of the 34-m variable speed configuration is the ability to combine stall regulation with minor rpm adjustments to further reduce peak power with very little impact on energy capture results. For example, a reduction in peak power from about 750 kW_e to 600 kW_e (a 20% reduction) can be achieved by about a 2 rpm speed reduction; the corresponding reduction in annual energy capture at a 6.3 m/s (14 MPH) Rayleigh site was found to be only 1.5%!

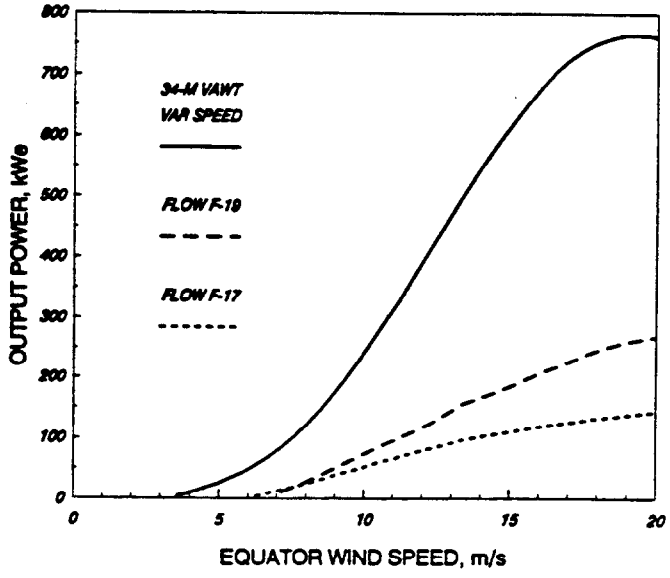

Figure 5. VAWT power curves
Electric power output

In order to accurately compare the performance of existing and next-generation VAWTs, Figure 6 presents results for projected annual energy capture in kWh_e per square meter, thus eliminating the issue of relative machine size. Furthermore, Figure 6(a) ignores wind shear effects while 6(b) includes them so that performance improvements from simply being higher in the earth's boundary layer can be separated from the technological improvements of the next generation design. From these comparisons it is clear that the advanced technology VAWT significantly outperforms either of the existing machines; i.e., the generational improvements are far greater than the earlier evolutionary ones. For example, at the 6.3 m/s Rayleigh site with zero shear, energy capture per square meter of the F-19 is 3.4% better than the F-17, while the 34-m performance is 38.6% higher. In the one-seventh wind shear exponent case, these increases grow to 12.8% and 69.1%, respectively. Thus, wind shear effects can be very important (if a candidate site has them), but even without the wind shear, very dramatic improvements appear possible.

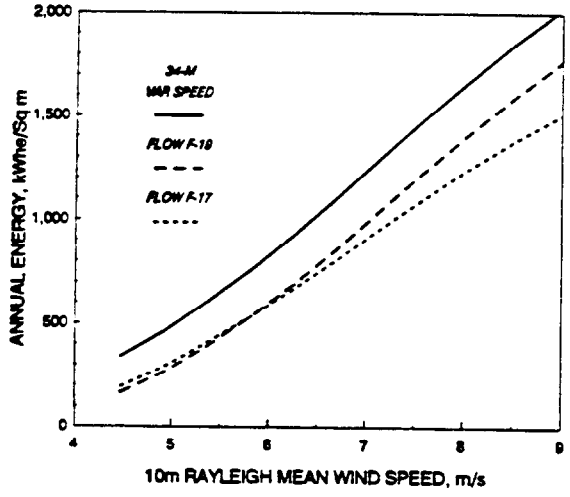

(a) Zero shear

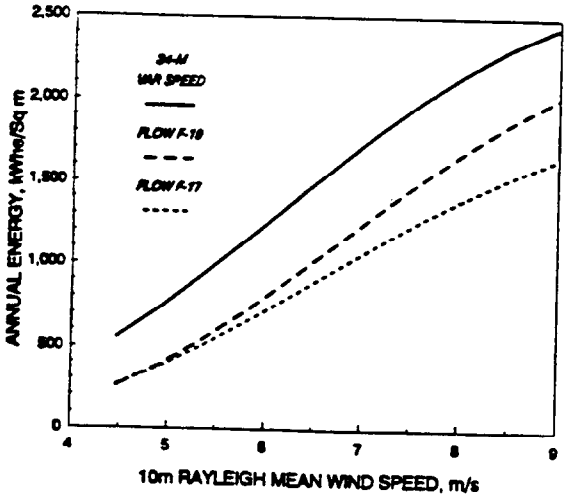

(b) 1/7 Wind shear exponent

Figure 6. VAWT energy capture comparisons

CONCLUSIONS

From the above comparisons, it is clear that the next generation VAWT should be a significantly better performer than existing machines; this is primarily attributable to increases in size (higher Reynolds Number effects) and improved airfoils. Additional, significant benefits accrue from the increased height above ground (wind shear effects), but this is separate from the generational improvement. From the Turbine Performance section, it is also clear that the cost effectiveness of variable speed cannot be deduced from this study. It may well be that considerations other than the issue of increased generator/power conditioning costs versus increased energy capture and reduced drivetrain costs will be decisive. For example, fatigue performance, siting flexibility, and utility interfacing issues may become the deciding factors.

ACKNOWLEDGMENTS

The results presented in this paper represent the combined efforts of many Sandia staff members with able assistance from the USDA in Bushland, Texas, and numerous contractors. Without their hard work on and dedication to the Test Bed, this paper would contain only analytical projections, with the results subject to all the uncertainties of such a study. With their efforts, the performance figures cited herein must take on significant meaning, and provide considerable optimism for the future of wind power.

REFERENCES

1. Klimas, P. C., Dodd, H. M. and Clark, R. N., "An Overview of the DOE/Sandia/USDA Vertical Axis Wind Turbine Test Bed Project," Proceedings of Windpower '87, American Wind Energy Association, October 5-8, 1987, San Francisco, California, SERI/CP-217-3315, pp. 35-40.

2. Stephenson, W. A., "Test Plan for the 34 Meter Vertical Axis Wind Turbine Test Bed Located at Bushland, Texas," SAND86-1623, Dec. 1986, Sandia National Laboratories, Albuquerque, NM.

3. Dodd, H. M., Ashwill, T. D., Berg, D. E., Ralph, M. E., Stephenson, W. A., and Veers, P. S., "Test Results and Status of the DOE/Sandia 34-m VAWT Test Bed," Proceedings of the Canadian Wind Energy Conference '89, Canadian Wind Energy Association, Sept. 1989.

4. Ashwill, T. D. and Veers, P. S., "Structural Response Measurements and Predictions for the Sandia 34-Meter Test Bed," Proceedings of the Ninth ASME Wind Energy Symposium, ASME, Jan. 1990, New Orleans, Louisiana.

5. L. L. Schluter and H. J. Sutherland, "Reference Manual for the LIFE2 Computer Code," SAND89-1396, Sandia National Laboratories, Albuquerque, NM, Sept. 1989.

6. H. J. Sutherland, "Analytical Framework for the LIFE2 Computer Code," SAND89-1397, Sandia National Laboratories, Albuquerque, NM, Sept. 1989.

7. Ashwill, T. D., Sutherland, H. J. and Veers, P. S., "Fatigue Analysis of the Sandia 34-Meter Vertical Axis Wind Turbine," Proceedings of the Ninth ASME Wind Energy Symposium, ASME, Jan. 1990, New Orleans, Louisiana.

8. Ralph, M. E., "Control of the Variable Speed Generator on the Sandia 34-Metre Vertical Axis Wind Turbine," Proceedings of Windpower '89, American Wind Energy Association, Sep. 25-27, 1989, San Francisco, CA.

9. Berg, D. E., Klimas, P. C. and Stephenson, W. A., "Aerodynamic Design and Initial Performance Measurements for the Sandia 34-Metre Diameter Vertical Axis Wind Turbine," Proceedings of the Ninth ASME Wind Energy Symposium, ASME, Jan. 1990, New Orleans, Louisiana.

10. Klimas, P.C., "Tailored Airfoils for Vertical Axis Wind Turbines,"SAND84-1062, Nov. 1984, Sandia National Laboratories, Albuquerque, NM.

☆ U.S. GOVERNMENT PRINTING OFFICE 1992—774-122/80076